ABSTRACT

Title of dissertation: PNEUMATIC ARTIFICIAL MUSCLE ACTUATORS FOR COMPLIANT ROBOTIC MANIPULATORS

Ryan M. Robinson
Doctor of Philosophy, 2014

Dissertation directed by: Professor Norman M. Wereley
Department of Aerospace Engineering

Robotic systems are increasingly being utilized in applications that require interaction with humans. In order to enable safe physical human-robot interaction, light weight and compliant manipulation are desirable. These requirements are problematic for many conventional actuation systems, which are often heavy, and typically use high stiffness to achieve high performance, leading to large impact forces upon collision. However, pneumatic artificial muscles (PAMs) are actuators that can satisfy these safety requirements while offering power-to-weight ratios comparable to those of conventional actuators. PAMs are extremely lightweight actuators that produce force in response to pressurization. These muscles demonstrate natural compliance, but have a nonlinear force-contraction profile that complicates modeling and control.

This body of research presents solutions to the challenges associated with the implementation of PAMs as actuators in robotic manipulators, particularly with regard to modeling, design, and control. An existing PAM force balance model

was modified to incorporate elliptic end geometry and a hyper-elastic constitutive relationship, dramatically improving predictions of PAM behavior at high contraction. Utilizing this improved model, two proof-of-concept PAM-driven manipulators were designed and constructed; design features included parallel placement of actuators and a tendon-link joint design. Genetic algorithm search heuristics were employed to determine an optimal joint geometry; allowing a manipulator to achieve a desired torque profile while minimizing the required PAM pressure. Performance of the manipulators was evaluated in both simulation and experiment employing various linear and nonlinear control strategies. These included output feedback techniques, such as proportional-integral-derivative (PID) and fuzzy logic, a model-based control for computed torque, and more advanced controllers, such as sliding mode, adaptive sliding mode, and adaptive neural network control. Results demonstrated the benefits of an accurate model in model-based control, and the advantages of adaptive neural network control when a model is unavailable or variations in payload are expected. Lastly, a variable recruitment strategy was applied to a group of parallel muscles actuating a common joint. Increased manipulator efficiency was observed when fewer PAMs were activated, justifying the use of variable recruitment strategies.

Overall, this research demonstrates the benefits of pneumatic artificial muscles as actuators in robotics applications. It demonstrates that PAM-based manipulators can be well-modeled and can achieve high tracking accuracy over a wide range of payloads and inputs while maintaining natural compliance.

PNEUMATIC ARTIFICIAL MUSCLE ACTUATORS FOR COMPLIANT ROBOTIC MANIPULATORS

by

Ryan Michael Robinson

Dissertation submitted to the Faculty of the Graduate School of the
University of Maryland, College Park in partial fulfillment
of the requirements for the degree of
Doctor of Philosophy
2014

Advisory Committee:
Prof. Norman Wereley, Chair/Advisor
Prof. Robert Sanner
Prof. Inderjit Chopra
Prof. Derek Paley
Prof. Balakumar Balachandran
Dr. Curt Kothera

© Copyright by
Ryan M. Robinson
2014

Acknowledgments

I would like to gratefully acknowledge the support of my advisors, Dr. Norman Wereley and Dr. Curt Kothera. Dr. Wereley has been my advisor for nine years, and I could not hope for a better mentor. He has been incredibly supportive, providing guidance, inspiration, and ideas that were vital to my success. Dr. Wereley gave me the freedom to be creative and explore topics that I found interesting. Even with his responsibilities as aerospace chair, he continued to take a deep interest in his students' work and always worked tirelessly to keep us on track. Dr. Kothera is a great mentor, colleague, and friend. It has been my pleasure to work with him on numerous projects which now constitute the majority of this dissertation. Dr. Kothera motivated me to make steady progress every week, and he was always there to listen carefully and provide fresh insights. He is an excellent writer and proofreader; I hope that I was able to absorb some of those skills.

I would also like to thank Dr. Sanner, Dr. Chopra, Dr. Paley, and Dr. Balachandran for their support, patience, and flexibility as my doctoral committee members. Their interest in my work was motivation to ???, and their willingness to share their expertise has been greatly appreciated.

I must thank Dr. Wei (Peter) Hu for taking me on as an undergraduate lab assistant in Dr. Wereley's group seven years ago. From my humble beginnings cleaning magnetorheological fluid dampers to my later work designing them, Dr. Hu taught me a great deal about how high-level research is conducted. He was always patient and more than willing to devote his time to support my work.

To my colleagues and good friends in the lab, you all have given me so much help over the years; I truly appreciate it. We've also had a lot of fun, which helped keep me sane and motivated. Special thanks to Robbie, Harinder, Andrew, Ami, Tom, Steve, Pablo, Ben and Dr. Choi. It's crazy that five of us doctors are graduating together–truly the end of an era. To my colleagues that still have a few more years, all my best...also, I highly recommend my tranquil back cubicle, which kept me insulated from distractions (with the exception of the occasional Nerf dart).

I would like to acknowledge the support of my family and friends. Mom, Dad, Tim, Kelli, and Kerri, your encouragement, kindness, humor, and love are always present in my life. To my lifelong friends, you guys are the best, thanks for believing in me, listening to me babble on about my work, and for understanding when I had to go into dissertation mode.

And to Janene: The past three years of my life have been amazing and unforgettable because of you. I am ridiculously lucky to have found such a talented, compassionate, and beautiful woman. You are my constant inspiration through the incredible, hard work you do as you pursue your doctorate in psychology. Thank you for being there for me through every step of my dissertation. I'm so glad that finally, our lives, which have been on parallel tracks for so long, are beginning to merge. I can't wait to build our future together.

Table of Contents

List of Tables vii

List of Figures viii

1 Introduction 1
1.1 Problem Statement . . . 1
1.2 Compliant and Human-Friendly Robotics . . . 4
1.2.1 Conventional Actuation Systems . . . 5
1.2.2 Smart Material Actuators . . . 7
1.2.3 Series Elastic Actuators . . . 8
1.2.4 Active Safety Control . . . 10
1.3 Pneumatic Artificial Muscle Actuators . . . 14
1.3.1 Background and Motivation . . . 14
1.3.2 PAM Literature Review . . . 17
1.3.2.1 Modeling of Pneumatic Artificial Muscles . . . 17
1.3.2.2 Control of PAM-Actuated Systems . . . 20
1.3.2.3 Robotics Applications . . . 24
1.3.2.4 Orthotics Applications . . . 31
1.3.2.5 Aerospace Applications . . . 36
1.4 Contributions of Dissertation . . . 39
1.5 Overview of Dissertation . . . 41

List of Abbreviations 1

2 Quasi-Static Modeling and Analysis of Pneumatic Artificial Muscles 45
2.1 Introduction . . . 45
2.2 Improvements to Force Balance Model . . . 49
2.2.1 Original Force Balance Model . . . 49
2.2.2 Non-constant Bladder Thickness Modification . . . 54
2.2.3 PAM Extension . . . 56
2.2.4 Elliptic Toroid Shape for Bladder Ends . . . 57
2.2.5 Braid Length along the Surface of the Elliptic Toroid . . . 60

2.2.6 Linear Relationship between Hyperelastic Constants and Pressure 67
2.3 Results and Analysis . . . 69
2.4 Conclusion . . . 74

3 Structural Design of PAM-Based Robotic Manipulators 77
3.1 Introduction . . . 77
3.2 Design Requirements and Simulation . . . 80
3.2.1 Design Requirements . . . 80
3.2.2 Actuator Development and PAM Characterization . . . 81
3.2.3 PAM Comparison . . . 85
3.2.4 Robot Arm Simulation . . . 85
3.2.5 Proof-of-Concept Manipulator Construction . . . 95
3.3 Test Setup . . . 97
3.3.1 Fabrication of Test Setup . . . 97
3.3.2 Testing and Experimental Results . . . 97
3.4 Analysis . . . 101
3.5 Optimization of Joint Geometry via Genetic Algorithms . . . 104
3.5.1 Optimization Problem . . . 104
3.5.2 Optimization Results . . . 109
3.6 Conclusion . . . 112

4 Control of PAM-Based Robotic Manipulators 115
4.1 Introduction . . . 115
4.2 PAM-Actuated Robotic Manipulator . . . 120
4.2.1 Design and Experimental Setup . . . 120
4.2.2 System Model . . . 122
4.3 Control Strategies . . . 125
4.3.1 Output Feedback Control . . . 125
4.3.1.1 Proportional-Integral-Derivative Control . . . 125
4.3.1.2 Fuzzy Control . . . 126
4.3.2 Model-Based Feedforward Control . . . 128
4.3.2.1 Model-Based Control without Feedback . . . 129
4.3.2.2 Model-Based Control Augmented with Output Feedback . . . 131
4.4 Control Analysis Via Simulation . . . 132
4.4.1 PID and Fuzzy Control . . . 132
4.4.1.1 Gain Tuning Metrics . . . 132
4.4.1.2 Simulated Trajectory Following . . . 134
4.4.2 Model-Based Control with Output Feedback . . . 135
4.5 Experimental Evaluation . . . 137
4.5.1 PID and Fuzzy Control . . . 137
4.5.1.1 Experimental Validation . . . 137
4.5.1.2 Experimental Gain Tuning . . . 138
4.5.1.3 Comparison of Output Feedback Controllers . . . 140
4.5.2 Model-Based Control with Output Feedback . . . 143

4.5.2.1 Model Validation . . . 143
4.5.2.2 Experimental Analysis of Feedforward Gain . . . 145
4.5.3 Discussion of Controllers . . . 146
4.6 Conclusions . . . 147

5 Advanced Control of PAM-Based Robotic Manipulators 150
5.1 Introduction . . . 150
5.2 Robotic Manipulator . . . 153
5.3 Control Strategies . . . 156
5.3.1 Sliding Mode Control . . . 157
5.3.2 Adaptive Sliding Mode Control . . . 159
5.3.3 Adaptive Neural Network Control . . . 161
5.4 Position Control Results . . . 164
5.4.1 Sliding Mode Control . . . 165
5.4.2 Adaptive Sliding Mode Control . . . 166
5.4.3 Adaptive Neural Network Control . . . 170
5.5 Discussion and Comparison of Controllers . . . 175
5.6 Conclusion . . . 184

6 Variable Recruitment 186
6.1 Introduction . . . 186
6.2 Preliminary Characterization and Analysis of Bladder Effects . . . 189
6.3 Variable Recruitment on a Robotic Manipulator . . . 192
6.4 Variable Recruitment Simulations . . . 195
6.4.1 Dynamic Modeling . . . 195
6.4.2 Simulation Procedure . . . 199
6.4.3 Simulation Results . . . 201
6.5 Variable Recruitment Experiments . . . 204
6.5.1 Experimental Procedure . . . 204
6.5.2 Experimental Results . . . 205
6.6 Discussion . . . 207
6.7 Conclusion . . . 210

7 Conclusion 213
7.1 Summary of Research and Key Conclusions . . . 213
7.1.1 Pneumatic Artificial Muscle Modeling . . . 213
7.1.2 Manipulator Proof-of-Concept and Joint Optimization . . . 214
7.1.3 Proof-of-Concept Manipulator Control Study . . . 215
7.1.4 Adaptive Control Study . . . 215
7.1.5 Variable Recruitment . . . 216
7.2 Contributions to Literature . . . 217
7.3 Future Work . . . 218

Bibliography 222

List of Tables

1.1 Comparison of actuation technologies (adapted from [1–4]). 16

3.1 Prototype design goals. 81
3.2 Comparison of different-sized PAMs. 86
3.3 Geometric parameters for PAM force model. 91
3.4 Joint design requirements and PAM characteristics. 105
3.5 Optimal parameters of candidate designs, determined by genetic algorithm-based optimization. 113

4.1 Fuzzy ruleset. 127

5.1 Parameter values of sinusoids in desired trajectory. 165
5.2 Adaptation gains for adaptive sliding mode control. 168

6.1 Geometric and material parameters for test PAMs. 191
6.2 Test matrix for variable recruitment, 50 deg max. angle. 200
6.3 Test matrix for variable recruitment, 90 deg max. angle. 200

List of Figures

1.1 Geared motor (Maxon). 6
1.2 Robot finger actuated by SMA (Bundhoo, 2009). 9
1.3 Electroactive polymer legged robot (Pei, 2003). 9
1.4 Series elastic actuator concept. 11
1.5 Baxter robot (Rethink Robotics). 14
1.6 Miniature PAM (Hocking and Wereley, 2013). 17
1.7 Bridgestone "Rubbertuator" arm. 25
1.8 7 DOF robot (Tondu, 2005). 25
1.9 FESTO AirArm (Eichorn, 2009). 26
1.10 "OctArm" continuum robot (Walker, 2005). 28
1.11 Shadow Robotic Hand (Shadow Robot Company). 29
1.12 Walking Robots, (a) PAM-based leg (Colbrunn, 2000), (b) Lucy bipedal walking robot (Verrelst et al., 2005). 30
1.13 Human-lifting robots (a) Robotic nursing assistant (HStar Technologies [5]), and (b) Battlefield extraction assist robot (Vecna Technologies [6]). 31
1.14 McKibben muscle orthosis with CO_2 tank. 32
1.15 7 DOF rehabilitation exoskeleton (Caldwell and Tsagarakis, 1994). . . 34
1.16 "Power assist wear" (Noritsugu, 2008). 34
1.17 Ankle orthosis (Park et al., 2014). 35
1.18 PAM-actuated trailing edge flap (Woods et al., 2011). 37
1.19 Active camber airfoil (Peel et al., 2009). 37
1.20 Morphing skin test article (Bubert, 2009). 38
1.21 MiniPAM cartridge (Vocke et al., 2012). 38

2.1 PAMs grouped in an antagonistic pair, actuating a rotating joint. . . 49
2.2 Force balance model [25]. 51
2.3 Force-contraction profile comparing model and experiment; 1.9 cm (0.75-in) diameter, 18.5 cm (7.3-in) length PAM with a 76.5 deg braid angle. 54
2.4 Nonlinear modulus values as determined by optimization procedure; 1.9 cm (0.75-in) diameter, 1.5 cm (7.3-in) length PAM with a 76.5 deg braid angle. 54

2.5 Blocked force vs. pressure; 1.9 cm (0.75-in) diameter, 18.5 cm (7.3-in) length PAM with a 76.5 deg braid angle. 56
2.6 Geometric model of PAMs in (a) contraction, (b) extension. 59
2.7 Cross-section showing estimated bladder thickness during (a) contraction and (b) extension; 1.9 cm (0.75-in) diameter, 18.5 cm (7.3-in) length PAM with a 76.5 deg braid angle. 64
2.8 Comparison of cylindrical and elliptic tip models (a) radius vs. contraction and (b) thickness vs. contraction; 1.9 cm (0.75-in) diameter, 18.5 cm (7.3-in) length PAM with a 76.5 deg braid angle. 65
2.9 Elliptic tip model parameters (a) tip eccentricity and (b) braid length along the elliptic tip; 1.9 cm (0.75-in) diameter, 18.5 cm (7.3-in) length PAM with a 76.5 deg braid angle. 66
2.10 Force vs. contraction, nonlinear force balance model with non-constant thickness and elliptic tip geometry; 1.9 cm (0.75-in) diameter, 18.5 cm (7.3-in) length PAM with a 76.5 deg braid angle. 68
2.11 Force vs. contraction with hysteresis estimates, nonlinear force balance model with non-constant thickness and elliptic tip geometry; 1.9 cm (0.75-in) diameter, 18.5 cm (7.3-in) length PAM with a 76.5 deg braid angle. 68
2.12 Modulus values optimized to vary linearly with pressure using nonlinear force balance model with non-constant thickness, (a) first-order, (b) second-order, (c) third-order, and (d) fourth-order polynomial model for strain; 1.9 cm (0.75-in) diameter, 18.5 cm (7.3-in) length PAM with a 76.5 deg braid angle. 70
2.13 Normalized mean squared error of model force predictions for Mth-order polynomial strain models; 1.9 cm (0.75-in) diameter, 18.5 cm (7.3-in) length PAM with a 76.5 deg braid angle. 71
2.14 Force vs. contraction, nonlinear force balance with non-constant thickness, (a) first-order, (b) second-order, (c) third-order, and (d) fourth-order polynomial model for strain; 1.9 cm (0.75-in) diameter, 18.5 cm (7.3-in) length PAM with a 76.5 deg braid angle. 72
2.15 Stress-strain relationship in the (a) axial and (b) circumferential directions, as determined by polynomial fitting; 1.9 cm (0.75-in) diameter, 18.5 cm (7.3-in) length PAM with a 76.5 deg braid angle. 73
2.16 Experiment vs. model using fourth-order polynomial model for strain and $E_k(P)$ interpolated from data of three experimental pressure levels ; 1.9 cm (0.75-in) diameter, 18.5 cm (7.3-in) length PAM with a 76.5 deg braid angle. 75
2.17 Normalized mean squared error of model predictions, comparing $E_k(P)$ interpolated from data of all eight experimental pressure levels vs. only three experimental pressure levels (0.14, 0.41, and 0.83 MPa [20, 60, and 120 psi]); 1.9 cm (0.75-in) diameter, 18.5 cm (7.3-in) length PAM with a 76.5 deg braid angle. 76

3.1 Characterization of a 2-in OD, 13-in long PAM. 83

3.2 Testing of a 2-in OD, 13-in long PAM (a) resting, (b)contracted. . . . 84
3.3 Characterization of a 0.625-in OD, 7.8-in long PAM. 84
3.4 Parameters for design analysis. 86
3.5 Concept for variable moment arm joint. 87
3.6 Geometry of robotic arm joint. 88
3.7 Torque output vs. angle of rotation. 90
3.8 Simulation of step input, elbow joint. 95
3.9 CAD model of PAM manipulator. 96
3.10 PAM arm extended during testing. 98
3.11 PAM arm contracted during testing. 98
3.12 Elbow PAM pressure and rotation vs. time. 100
3.13 Elbow joint torque vs. pressure. 100
3.14 Experimental and predicted force vs. displacement. 102
3.15 Experimental and predicted static torque vs. angle of rotation. 103
3.16 Dynamics of upper arm contraction. 103
3.17 Second-generation, two degree-of-freedom manipulator. 106
3.18 Joint parameters for optimization. 107
3.19 Torque vs. range of motion, illustrating regions to be minimized. . . . 109
3.20 Fitness value vs. generation, genetic algorithm-based optimization. . 110
3.21 Joint dimensions vs. generation, genetic algorithm-based optimization. 111
3.22 Torque vs. range of motion, initial and final generations. 111
3.23 Torque vs. range of motion, shoulder joint. 112
3.24 Torque vs. range of motion, elbow joint. 113

4.1 Schematic of PAM-Actuated Manipulator System. 121
4.2 PAM-actuated joint holding 50 kg (110 lb). 121
4.3 Fuzzy membership functions for input/output variables. 128
4.4 Model-based feedforward (a) without output feedback, (b) with PID or fuzzy feedback control. 131
4.5 Performance metrics as g_1 and h vary ($g_2 = 0.6$) with a 23 kg (50 lb) payload (a) error metric; (b) smoothness metric; (c) combined metric. 135
4.6 Simulated control, feedforward with fuzzy feedback 136
4.7 Simulated control, feedforward with PID feedback 137
4.8 PID control, integral gain selection with a 23 kg (50 lb) payload (a) error metric; (b) smoothness metric; (c) combined metric; (d) time response for best cases. 141
4.9 Experimental vs. simulated optimal gains (a) PID; (b) fuzzy. 141
4.10 PID control with optimized gains. 143
4.11 Fuzzy control with optimized gains. 144
4.12 Comparison of optimized experimental PID and fuzzy control, 23 kg (50 lb) payload. 144
4.13 Simulated and experimental results using feedforward control with fuzzy feedback, 45 kg (100 lb) payload. 145
4.14 Lift-hold-return trajectory while varying model gain k_M, 23 kg (50 lb) payload. 146

4.15 Comparison of lift-hold-return trajectories, 11 kg (25 lb) payload. . . 147

5.1 One degree-of-freedom robotic arm with 50 lb payload. 154
5.2 Torque vs. angle, comparison of models with experimental data. . . . 156
5.3 Diagram of a cascaded controller. 157
5.4 Diagram of sliding mode controller. 159
5.5 Diagram of adaptive sliding mode controller. 161
5.6 Single layer neural network structure. 163
5.7 Diagram of adaptive neural network controller. 164
5.8 Sliding mode control results: (a) angle, (b) angle error, and (c) mean squared error. 167
5.9 Adaptive sliding control results: (a) angle, (b) angle error, and (c) mean squared error. 168
5.10 Parameter adaptation for three experiments, varying adaptation gains. 169
5.11 Adaptive neural network control for two distinct initial conditions; (a) angle, (b) angle error, and (c) mean squared error. 171
5.12 Neural network adaptation over 100 s, 50 lb payload, no prior information. 172
5.13 Neural network adaptation over 100 s, 50 lb payload, with model. . . 173
5.14 Adaptive neural network control, varying payloads; (a) angle, (b) angle error, and (c) mean squared error. 174
5.15 Neural network adaptation over 100 s, 15 lb payload, no prior information. 175
5.16 Neural network adaptation over 100 s, 50 lb payload, with network initialized from 100 s of training with 15 lb payload. 176
5.17 Adaptive neural network control, varying initial network structure; (a) angle, (b) angle error, and (c) mean squared error. 177
5.18 Diagram of a cascaded PID controller. 177
5.19 Comparison of control strategies, compound sinusoidal trajectory; (a) angle, (b) angle error, and (c) mean squared error. 179
5.20 Comparison of control strategies, lift-hold-return trajectory; (a) angle, (b) angle error, and (c) mean squared error. 180
5.21 Adaptive neural network control, 0 lb payload, Gaylord model vs. no information. 182
5.22 Neural network adaptation over 100 s, 0 lb payload, with Gaylord model. 183

6.1 Comparison of single-PAM (full pressure) vs. dual-PAM (half pressure) force, PAM A. 191
6.2 Comparison of single-PAM (full pressure) vs. dual-PAM (half pressure) force, PAM B. 193
6.3 Robotic arm holding a 95 kg (210 lb) payload. 194
6.4 Exploded view of shoulder joint. 194
6.5 Diagram of PAM-based robotic system. 196
6.6 Diagram of cascaded PI control system. 200

6.7 Efficiency of manipulator with variable recruitment, 50 deg max. angle. 202
6.8 Efficiency of manipulator with variable recruitment, 90 deg max. angle. 202
6.9 Maximizing efficiency through variable recruitment, simulations, 90 deg max. angle. 203
6.10 Efficiency of variable recruitment with and without bladder elasticity, simulations, 90 deg max. angle. 204
6.11 Angle and torque vs. time, 2 PAMs, 18 kg (40 lb) payload, 90 deg max. angle. 206
6.12 Torque vs. pressure, experiment and simulation, 2 PAMs, 18 kg (40 lb) payload. 206
6.13 Efficiency of manipulator with variable recruitment, 90 deg max. angle. 207
6.14 Work output of manipulator with variable recruitment, 90 deg max. angle. 208
6.15 Energy input of manipulator with variable recruitment, 90 deg max. angle. 208
6.16 Two non-activated PAMs. 211
6.17 Four non-activated PAMs. 212

Chapter 1: Introduction

1.1 Problem Statement

Although decades have passed since the adoption of robotic systems in industry, the modern concept of the robot continues to evoke thoughts of rigid and clunky machines, echoing the "mechanical knight" envisioned by Leonardo da Vinci at the turn of the 16th century [7]. High impedance robots—systems that are heavy and stiff—have secured a niche in industrial operations because of their precision, speed, and task repeatability. However, these characteristics that improve accuracy also prevent safe human-robot interaction. High impedance systems do not yield in the presence of an obstacle or disturbance, and upon impact can damage the surrounding environment or injure the operator. Often, "safety cages" must be erected, limiting the robot to a highly structured, undisturbed environment [8].

Interest in robots outside of the industrial arena has begun to blossom, as evidenced by the success of small, mobile domestic robots for tasks like floor cleaning. Nevertheless, systems that perform manipulation tasks have not gained popularity in domestic applications. Among problems such as prohibitive cost and limited autonomy, safety hazards are a major obstacle to wide adoption that must be overcome in order for robotic systems to interact with humans in unstructured

environments.

There is growing interest in biologically-inspired robotic systems that exhibit lower impedance, and there is currently a research thrust in the new field of soft robotics. These compliant systems will deform at the joints in the event of a disturbance, allowing for greater safety. Compliant motion with minimal trade-offs in other aspects of performance would pave the way for robots in the home and in a wide variety of other applications.

The research described in this dissertation explored the concept of human-safe robotic manipulation, specifically through the employment of lightweight, naturally compliant, biologically-inspired actuators known as pneumatic artificial muscles. These muscles utilize the energy stored in compressed air to produce mechanical work. Pneumatic artificial muscles are capable of high specific force and force density. This enables lifting of massive payloads, including humans themselves—something that other soft actuators cannot achieve without prohibitively high mass, volume, or pressure. Specific applications for lifting humans include patient placement in hospitals, casualty extraction in combat situations or disaster relief efforts. Related applications which could benefit from high-specific-work, compliant muscles include orthotics for rehabilitation and exoskeletons for strength augmentation.

Challenges exist that currently inhibit the widespread use of PAMs in robotic systems. Foremost is their inherently nonlinear static and dynamic behavior, a byproduct of hyperelastic bladder deformation, bladder-braid interaction, and compressible fluid dynamics. In order to effectively design manipulators to meet specifications of torque, speed, volume, and range of motion, an accurate model of actuator force

behavior is required. Similarly, control of these nonlinear actuators must enable accurate trajectory following and high power output while maintaining predictable, smooth motion. The controller must also demonstrate robust, stable recovery in the presence of disturbances.

Researchers, especially within the past two decades, have studied pneumatic artificial muscle behavior and proposed numerous architectures for reliable actuator control in a variety of applications. These applications include robotic manipulators and legs, orthotics, exoskeletons, and morphing aerospace surfaces. However, certain demanding applications have remained out of reach. One of these applications is a lightweight PAM-based robotic manipulator that is able to lift a wide range of payload weights (including weights over 150 lb) along a desired trajectory over a wide range of motion (90 deg), while compensating for disturbances. The present manipulators take full advantage of the high strength-to-weight ratio of PAMs, maximizing the payload it can lift. The application is "demanding" for two major reasons: (1) The limit to the mass flow rate of air into the actuators often introduces time delay in reaching desired pressure, and (2) the system must be able to safely react to large changes in inertia, from payloads that can reach several times the mass of the manipulator itself.

The purpose of the research, therefore, is to investigate the use of PAMs as actuators in robotic manipulators, specifically heavy-lift manipulators. The major goals are to precisely model PAM behavior, maximize manipulator torque output, and maximize trajectory tracking performance. Furthermore, a variable recruitment strategy is evaluated to improve efficiency for lightweight payloads. More broadly, this

dissertation aims to complement and improve upon the existing knowledge of PAM-based human-friendly robotics. As compliant manipulation technology improves and proliferates, a new paradigm in human-robot interaction will be achievable.

1.2 Compliant and Human-Friendly Robotics

High inertial force is the result of a high-mass system being slowed down from a high velocity. In order for a robotic manipulator to operate safely with humans, the system must have low mass such that an impact with the robot moving at high speed will not cause severe damage. Injury can also occur if a human (in motion with his or her own inertia) impacts a robotic manipulator that is stiff and resists deformation. Sharp edges and hard surfaces are problematic as well.

Some clues for the design of human-friendly manipulators can be found in human arms themselves (which obviously interact with humans). The average adult arm is soft, highly dexterous, and can manipulate payloads several times its own weight, traits that are highly desirable in a manipulator. To achieve these feats, the human arm employs lightweight, soft (biological) muscles that possess naturally compliant characteristics. Hence, light weight and compliance are factors that would be useful to emulate in the design of human friendly systems.

The remainder of this section overviews current actuation technology, including "smart" actuators, compliant actuators, and active control algorithms meant to improve the safety characteristics of a manipulator.

1.2.1 Conventional Actuation Systems

Conventional robotic actuation systems fall into two a major categories: electromechanical and hydraulic. Both technologies offer high overall efficiency and static positioning accuracy. However, these systems fall short in many ways when safe human interaction is a consideration. Hydraulics and geared electric motors are naturally rigid and can only be made to act compliant through complex control strategies (and even then, bandwidth is limited).

Electric motors produce mechanical force through the interaction of a magnetic field with the current passed through wound coils. In practical robotics applications, motors must be geared because of their poor torque density in a direct drive configuration. Gearing leads to very high stiffness and backdrive friction, characteristics which can cause injury to humans or damage the surrounding environment. Further disadvantages of geared systems include backlash, torque ripple, and noise [9]. Shock loads to the system can cause high stress on gear teeth, which could easily damage the system.

Hydraulic systems are known for their superior specific work, primarily due to the high operating pressure of the hydraulic fluid (commonly between 20-35 MPa [3000-5000 psi]). The incompressibility of hydraulic fluid leads to high actuator efficiency. Nevertheless, there are major drawbacks to using hydraulic systems in certain applications. Hydraulic fluid is typically a synthetic oil, which is prone to leakage at high pressures, and can be hazardous to humans and the environment. Hydraulic systems are also inherently very stiff because of the incompressibility of

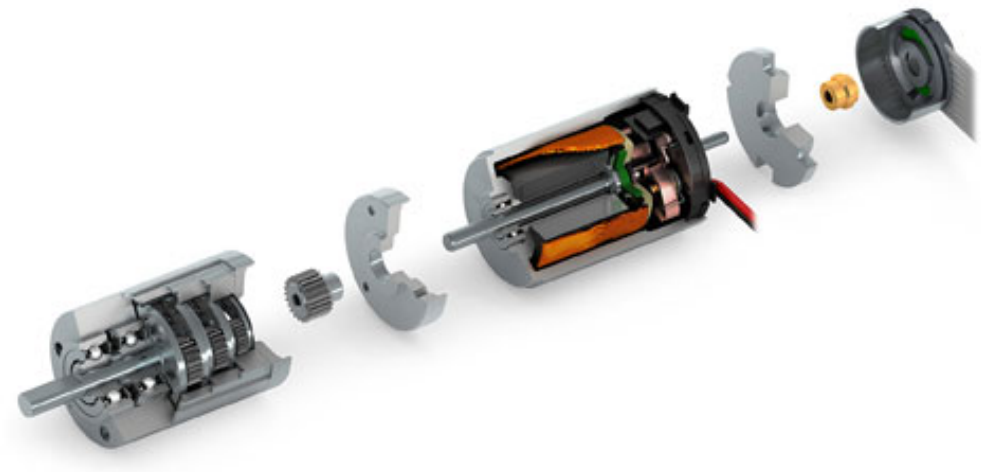


Figure 1.1: Geared motor (Maxon).

the fluid. The volumetric flow rate of a hydraulic pump dictates the bandwidth at which a hydraulic system can successfully implement compliant control (which will be discussed in Section 1.2.4), but in many instances, the system cannot react quickly to sudden disturbances (impacts).

A widely used alternative to hydraulics and electric motors is the traditional pneumatic cylinder. Pneumatic cylinders take advantage of the compressibility of air to provide natural compliance. However, the cylinder is typically heavy in order to ensure pressurized air cannot escape. The maximum pressure used in pneumatics is typically an order of magnitude less than in hydraulics due to efficiency losses and hazards associated with highly compressed gas. Subsequently, work density is at least an order of magnitude lower than hydraulics. Furthermore, the friction introduced by the piston seal can be problematic.

1.2.2 Smart Material Actuators

Several "smart" actuators exist that have gained major attention over the past three decades. This category of actuators encompasses material alloys that exhibit controllable induced strain under various types of fields. Smart actuators include piezoelectrics, shape memory alloys, magnetostrictives, and electroactive polymers. Despite their utility and popularity in certain applications, these materials each have significant drawbacks that disqualify them in most robotic manipulator applications.

Piezoelectrics, such as lead zirconium titanate (PZT), strain when an electric field is applied, and can react at a very high bandwidth. However, the maximum induced strain from these materials is too low to be useful in a robot joint requiring large range of motion. A miniature piezoelectric motor was devised that weighed 70 g, but could only reach torques of 0.07 Nm [**?**]. Rather than act as the primary actuators for the robot, piezoelectric devices have been more successfully used to control the vibrations of a flexible robotic manipulator [10].

Shape memory alloys (SMA), which extend or contract in response to thermal fields (often by running current through the material to generate resistive heat) are capable of high specific work and moderate strain, but exhibit low bandwidth and very low thermal efficiency. In research by Bundhoo [11], a robot finger actuated by SMA was developed, but there was a delay of 5 to 10 s before joint motion occurred. Another study conducted by Dilibal created an SMA-actuated robotic hand; however, the complete system is complex and bulky, requiring water or freon to dissipate heat energy quickly [12]. Precise control of SMA is difficult, and many systems can only

reliably switch between "on" and "off" states [4].

Magnetostrictives strain in response to magnetic fields, yet require a prohibitively large, heavy electromagnet around the material to generate the desired field [4].

Electroactive polymer (EAP) muscles are soft, compliant actuators that mimic the properties of muscle, but the technology has not reached maturity for high-force, high-strain robotic manipulator applications [13]. Some versions of these muscles are capable of high strains and stresses, but require high driving electric fields, which could pose danger to humans. A set of dielectric elastomer muscles have been used as robot legs in work by Pei et al. [14] that bend in response to a driving voltage of 5.5 kV.

1.2.3 Series Elastic Actuators

One method of implementing natural compliance is the addition of an elastic component (i.e., a spring) in series with a high stiffness actuator. There are several benefits to this configuration. The high stiffness actuator can be controlled to great accuracy, while the elastic component deforms as a known function of the applied force. The compound stiffness of the series results in a low impedance system that can be tuned through proper selection of the spring. Furthermore, energy can be temporarily stored in the elastic component for repetitive motions such as walking [15].

There are some disadvantages to this configuration, however. First, the elastic

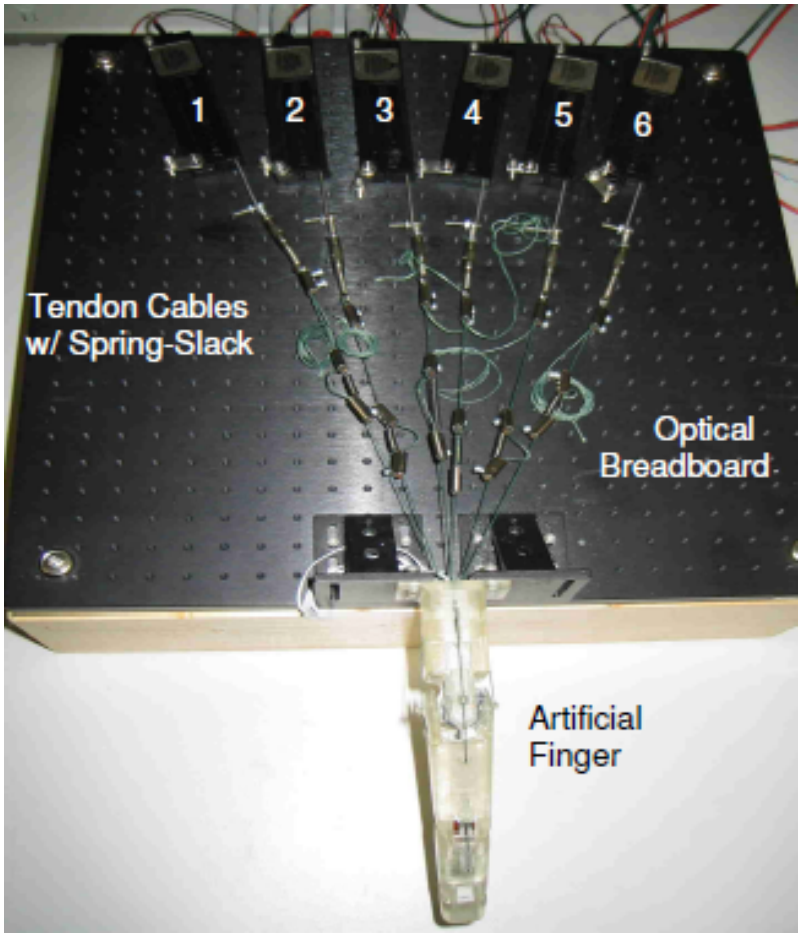


Figure 1.2: Robot finger actuated by SMA (Bundhoo, 2009).

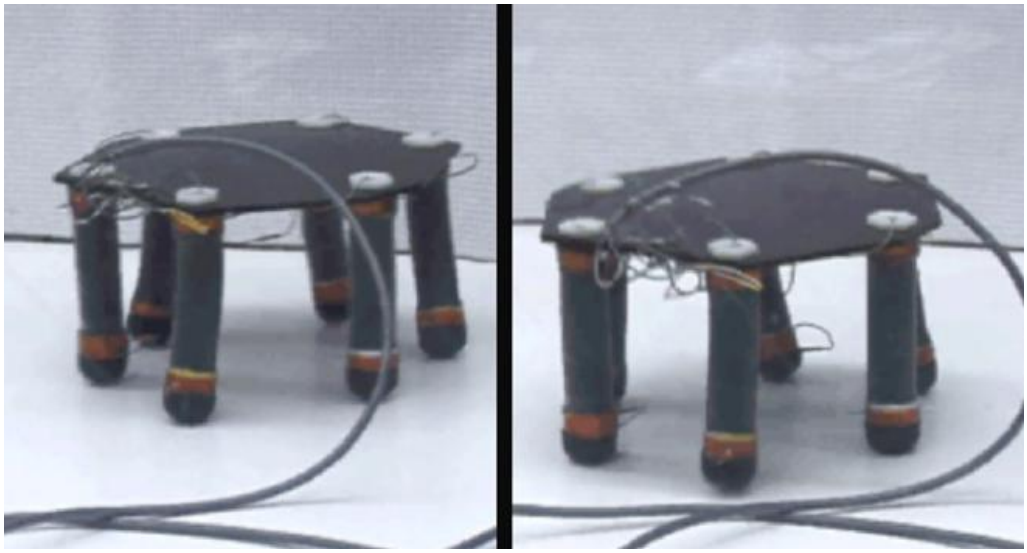


Figure 1.3: Electroactive polymer legged robot (Pei, 2003).

spring is passive, and may not be tuned for all necessary functions. A very low stiffness system under limited actuator authority will respond slower to torque inputs and, below a certain stiffness, requires more time to reach a new desired position than a moderately stiff system moving slowly enough to minimize injury. Therefore, there is a minimum limit to achievable positioning time [16]. Second is low actuator performance when the load inertia is small compared to the motor's reflected inertia. In this case, an impulse applied to the load can cause high frequency oscillations, instability, and contact chatter. A damper is recommended to handle small load inertias, and the system should be critically damped for the lowest expected load [17]. However, damping increases the impedance of the actuator. Additions to the actuator will increase the overall system weight, decreasing specific work.

1.2.4 Active Safety Control

Compliant manipulation can be obtained with traditional actuators through the application of an impedance control strategy. The term impedance control is widely used, but in this strategy, position and orientation are actually being commanded, while impedance is modulated. The objective of impedance control is to make the system exhibit target dynamics, including stiffness and damping properties chosen by the designer, about the commanded trajectory.

Injury criteria exist to estimate the consequences of a collision. The severity of a head impact is related to the acceleration of the head and the pulse duration. To measure collision severity in car accidents, Versace [18] proposed a metric known as

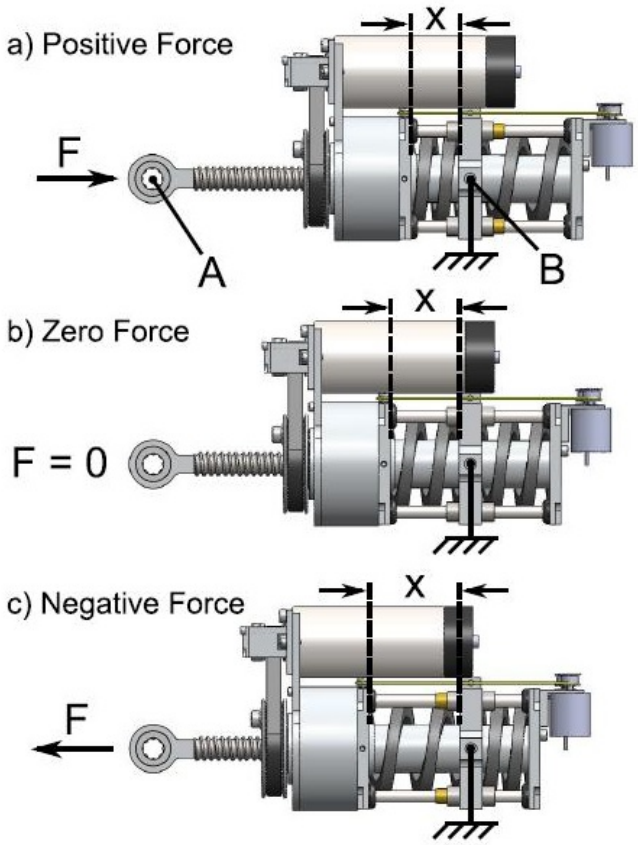


Figure 1.4: Series elastic actuator concept.

the Head Injury Criterion (HIC):

$$HIC = T\left(\frac{1}{T}\int_0^t a(\tau)d\tau\right)^{2.5} \tag{1.1}$$

where T is impact duration, a is head acceleration, and τ is a variable of integration representing time. HIC values of 1000 or greater are associated with severe injury. The HIC can be extended to other parts of the body [19]. In robotics research, this metric has been employed to measure the severity of injury imparted by a robotic manipulator [16] and to evaluate the safety of different actuation strategies.

Kazerooni [20] developed a controller with variable impedance, where the robotic system was designed to provide compensation such that the end effector position was proportional to the interaction force (within a given operating frequency range). The stiffness of the system could be chosen by the designer to allow human-friendly interaction. However, depending on the actuator and system properties, high frequency external forces, such as sudden impacts, may not be possible to fully compensate. Furthermore, an accurate model of the system is required for high performance. In demanding applications, the designer must accept a certain trade-off between performance and robustness to modeling uncertainty. Another issue with employing a naturally stiff actuator is fail safety, in which the system can no longer be controlled as desired. In this case, the system may revert to stiff, potentially unsafe behavior.

Collision detection and reaction is another form of active safety control. Haddadin [21] demonstrated how reactive control strategies can significantly contribute

to safety. The system was able to distinguish between desired physical interaction with the robot and unexpected collisions with the potential to cause injuries. Upon detection of a dangerous collision, the robot would react with one of several strategies tested, including zero-gravity compliance control and admittance control (which led to the robot "fleeing" from the disturbance). The system can compensate when there is enough time to categorize the disturbance, but in some cases, impacts with rigid surfaces (e.g., the human head) may result in a hard shock before reactive strategies can be implemented.

Bicchi and Tonietti [16] proposed a variable stiffness transmission (VST) concept for enhanced safety. In this strategy, the joint actuation scheme consists of compliant components that can be tuned on-line. The authors suggest tuning for high stiffness during low velocity motion and lower stiffness during high velocity motion. In this way, a variable stiffness "trajectory" can be implemented in tandem with a motion trajectory planner. The authors state that pneumatic artificial muscle (PAM) actuators arranged in an antagonistic pair are "among the best candidates" for this task.

A combination of active and passive safety features are most likely to produce the safest systems. Baxter, by Rethink Robotics [22] is advertised as a low cost industrial robot that can be trained by humans and work in close proximity with humans. Its passive safety features include series elastic actuators, back-drivable motors, and padded surfaces. Active control features include visual object detection, collision detection, and emergency stop mechanisms. However, Baxter is only rated to handle payloads up to 5 lb. This limits the type of tasks that can be performed.

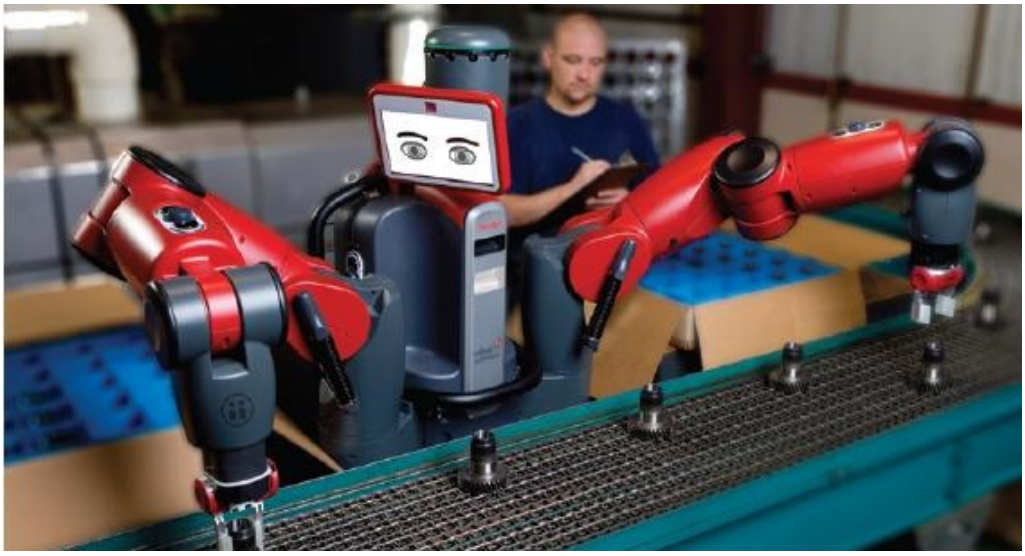


Figure 1.5: Baxter robot (Rethink Robotics).

Moreover, the system has a maximum speed below that which would injure humans, limiting task completion times.

1.3 Pneumatic Artificial Muscle Actuators

The background and motivation for employing pneumatic artificial muscles will be discussed in further detail in this section. Research performed to date and the evolution of PAM-based design will be examined.

1.3.1 Background and Motivation

Pneumatic artificial muscles (PAMs) are lightweight, soft actuators that employ pressurized air to generate axial force. The term "pneumatic artificial muscle" encompasses a range of designs. The common components of these actuators are an elastomeric "bladder" material and an inextensible fiber material. The fiber can be embedded inside the elastomer, or can surround and move freely on the bladder

surface. The latter is traditionally known as a McKibben actuator, named after Joseph McKibben, who popularized these devices as orthotics for polio patients in the 1950s [23]. The invention of the McKibben-type pneumatic muscle is generally attributed to R. H. Gaylord, who patented the "Fluid actuated motor system and stroking device" in 1958 [24]. A similar "Elastic diaphragm" patented by A. H. Morin [25], awarded in 1953, is cited in the Gaylord patent. Pressurization of a soft bladder causes the stiff braid fibers to reorient, generating stroke in one direction. Typically, McKibben-type PAMs are contractile, meaning that pressurization causes the PAM to shorten axially, while expanding radially. Resistance to this contraction generates a tensile force.

PAMs have several appealing features for use in robotic systems. They are capable of excellent power-to-weight ratios and high specific work when highly pressurized. Additionally, they are easily scaled to different sizes; in fact, many researchers have focused on "miniature" PAMs, roughly denoting muscles with diameters less than 0.25-in [26, 27]. These compliant actuators are damage tolerant [2,28], and have been endurance-tested for as many as 125 million cycles with minimal wear [2] and little change in force characteristics. Table 1.1 displays important metrics for comparison between types of actuators, including specific work, work density, maximum frequency, and efficiency [1–4].

In some applications, PAMs are employed in antagonistic pairs. This arrangement is widely observed in biological systems. A commonly cited agonist-antagonist pair is the biceps-triceps pair of muscles on the human arm. As the agonist contracts, the antagonist extends, preserving the stiffness of the joint.

Table 1.1: Comparison of actuation technologies (adapted from [1–4]).

Actuation Technology	Max Strain	Actuation Stress (MPa)	Specific Work (J/kg)
Hydraulic	1.0	70	35000
Electromechanical	0.5	1	300
Pneumatic Cylinder	1.0	0.9	1200
Piezoelectric	10^{-4}	10	1
Shape Memory Alloy (SMA)	0.1	700	4500
Magnetostrictive	0.002	10	20
Electroactive Polymer (Gel)	0.4	0.3	1
Pneumatic Artificial Muscle	0.4	16	5000
Human Muscle	0.5	0.4	0.8

Actuation Technology	Work Density (kJ/m^3)	Max Frequency (Hz)	Efficiency
Hydraulic	10^5	100	0.95
Electromechanical	10^3	100	0.35
Pneumatic Cylinder	250	100	0.40
Piezoelectric	10	10^7	0.95
Shape Memory Alloy (SMA)	10^4	7	0.02
Magnetostrictive	15	10^7	0.80
Electroactive Polymer (Gel)	0.4	100	0.30
Pneumatic Artificial Muscle	10^3	100	0.40
Human Muscle	0.8	100	0.25

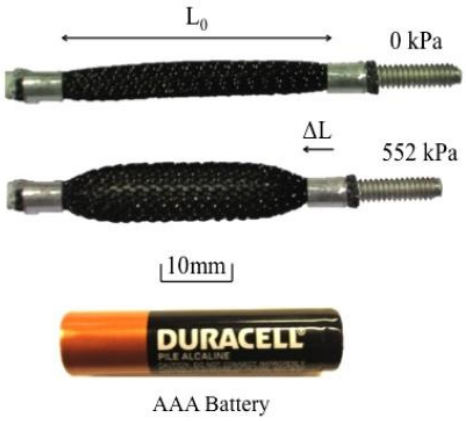


Figure 1.6: Miniature PAM (Hocking and Wereley, 2013).

1.3.2 PAM Literature Review

A large body of literature exists on the subject of pneumatic artificial muscles. Included are nonlinear modeling studies, design and characterization of systems employing PAMs for actuation, and control studies of PAM-based systems. Thorough reviews on PAM modeling and control are available [29, 30]. The following sections will briefly overview the history and state-of-the-art in these areas, as well as provide examples of PAM applications in robotics, orthotics, and aerospace.

1.3.2.1 Modeling of Pneumatic Artificial Muscles

Since the inception of PAM-actuated systems, researchers have relied upon complex mathematical models to help characterize their nonlinear behavior. PAM size, shape, and material characteristics affect force and strain characteristics. PAMs also exhibit hysteresis; which implies force is dependent on the history of the actuator state. For any PAM, the axial force of the actuator is dependent on the internal pressure and the level of strain. As the PAM radius expands and length contracts,

braid fibers reorient, and the angle θ_b between the braid fibers changes. Gaylord [24] first modeled the relationship between actuator force, pressure, and strain with a simple geometric model that ignores bladder elasticity, hysteresis, and non-cylindrical effects:

$$F = \frac{P\pi D_{45^\circ}^2}{2}\left(3\cos^2\theta_b - 1\right) = \frac{P}{4\pi N^2}\left(3L^2 - B^2\right) \tag{1.2}$$

In this equation, P is pressure differential, D_{45° is the actuator diameter when braid angle is 45 deg, N is number of turns a single braid makes around the circumference, L is the strained actuator length, and B is braid length. Subsequent studies have improved upon this model using energy balance, force balance, or large deformation theory approaches that do incorporate the losses caused by bladder elasticity.

Schulte [23] improved upon Gaylord's original equation to include effects of bladder elasticity and friction, but the equation was not derived. Schulte postulated that friction and elasticity were highly nonlinear. Thirty-five years later, Chou and Hannaford [31] introduced a PAM modeling approach based on the principle of virtual work, which results in a force equation similar to the formula in Schulte's work. Klute and Hannaford [32] then introduced a nonlinear Mooney-Rivlin mathematical description of the bladder to this model, improving force estimates at high contraction. The Mooney-Rivlin constants can be known *a priori* based on the material selected, or determined empirically. Using the same methodology, Tsagarakis and Caldwell [33] incorporated a conical surface profile at the actuator ends to compensate for the non-cylindrical shape and accounted for the initial "activation" pressure required to

overcome the radial elasticity of the bladder.

Ferraresi et al. [34] developed an alternative approach to PAM modeling known as force balancing. This model accounts for geometry and bladder elasticity by summing forces in the axial and circumferential directions, but also assumes that the PAM shape is always fully cylindrical. Interestingly, both force and energy balance derivations uncover Gaylord's original geometric force term. The force balance model was modified by Kothera et al. [35] to incorporate non-constant bladder thickness into the formulation, significantly improving results. Hocking and Wereley [27] used the Ferraresi model to characterize miniature PAMs with stiff silicone bladders, but replaced the elastic modulus of the bladder with a nonlinear hyperelastic function that could be empirically fit to the data. However, these models could not accurately obtain PAM force during extension past resting length because they assumed a fully cylindrical PAM shape.

Large deformation theory can be used to precisely model the extreme shape change undergone by a bladder during expansion. Rivlin [36] laid the groundwork for this theory in the late 1940s. Adkins and Rivlin [37] modeled large elastic deformations of thin shells composed of isotropic materials. Kydoniefs [38] used this modeling approach for an elastomeric cylinder reinforced with inextensible fibers. Further extending this work, Shan et al. [39] developed a finite axisymmetric deformation model that predicts the changing shape of a flexible matrix composite membrane under different conditions. However, large deformation theory requires a complex numerical procedure for convergence. Likewise, it is assumed in these studies that the inextensible braid fibers are embedded in the material, and thus cannot

fully account for free braid movement on the surface of McKibben-type actuators.

Despite decades of research [40], an all-encompassing model that reliably estimates PAM nonlinear force-contraction behavior over the operational envelope of actuator strain and pressure has been elusive. The existing models have not demonstrated sufficient accuracy and scalability for demanding applications such as model-based control of a variable-payload robotic manipulator. Accuracy in most models decreases at high bladder strains ($\varepsilon \geq 1$) due to the nonlinear stress-strain relationship of these actuators. Most actuator models also assume a fully cylindrical shape, and those that do consider shape change simplify the geometry of the rounded ends and do not account for the new path that the braid must travel. Absent from the literature is a model that can precisely capture the nonlinear stress-strain relationship of the artificial muscle while accounting for shape change.

1.3.2.2 Control of PAM-Actuated Systems

The nonlinearities present in dynamic PAM-based systems lead to difficulties in smooth, responsive control. These nonlinearities are not limited to PAM force behavior; compressible airflow dynamics and the mechanics of the overall system must also be considered in many applications. While simple output feedback strategies (such as proportional-integral-derivative control) are often able to achieve stable trajectory following with proper gain tuning, problems such as phase delay, undesired oscillation, and overshoot are common. Therefore, several advanced control algorithms have been studied for PAM-based systems.

Past efforts to control pneumatic artificial muscles span a wide range of established techniques. Caldwell et al. [41] used adaptive control based on model estimation, demonstrating accuracy for lightweight payloads (0.325 kg [0.7 lb]) over 9 deg of arm rotation. However, PAM-based systems do not reach their full potential unless they can handle payloads exceeding their own weight and can operate over a much larger range of motion. Ahn and Nguyen [42] developed an intelligent switching algorithm using a learning vector quantization neural network for various payloads, showing experimental data for step inputs. This controller requires training the neural network for an extended amount of time before the system could reliably lift different payloads. Wu et al. [43] developed a self-tuning fuzzy PID controller for a hand exoskeleton actuated by PAMs. The experiments showed undesired oscillation about the reference trajectory, though there was a time-varying disturbance due to human input. Yeh et al. [44] designed an optimal controller using loop transfer recovery (LTR) for a leg exoskeleton, which was deemed successful, but limited to only 15 deg of rotation.

When manipulator joint trajectories require high speed and acceleration, the tracking capabilities of pure output feedback control are degraded. Moreover, oversimplified computed torque controllers or adaptive controllers with slow parameter updating may not have the capability to track fast nonlinear dynamics. To address this problem, several approaches to PAM-based control have incorporated highly detailed models of the system. Zhu et al. [45] designed an adaptive robust controller for a parallel manipulator with only a few degrees of movement, incorporating a model of the flow dynamics and valve. Ganguly et al. [46] introduced static and dynamic

empirical models of PAM actuation and valve characteristics in a model-based PID controller for a rotary joint. The adoption of feedforward compensation was shown to improve system response in work by Nho and Meckl [47], who demonstrated neuro-fuzzy and inverse dynamics feedforward control on a two-link manipulator. Fateh and Izadbakhsh [48] employed a hybrid computed torque approach to a two-link manipulator and found that feedforward control reduces tracking error. These model-based feedforward strategies influenced the design of the control system in the present work.

Control studies on PAM-based systems have often employed sliding mode control, a robust nonlinear control strategy that drives the dynamics of the system to that of an exponentially stable system [49]. Many sliding control algorithms have been proven to be globally stable when model errors and system disturbances are bounded [50]. Carbonell et al. [51], Cai and Dai [52], and Lilly [53] performed simulations of PAM-actuated systems using sliding mode controllers. However, these second-order controllers assume that the PAM pressure or force being used as a control input is instantaneous, which cannot be assumed in a practical system with large PAM volume. Similarly, Nouri et al. [54] designed an adaptive controller with a sliding component which neglected airflow dynamics for low payloads (0.6 kg [1.3 lb]). Xing et al. [55] applied sliding mode control with a disturbance observer to a PAM in linear motion experiments with a 1 kg (2 lb) load. While the controller showed good performance, airflow dynamics were neglected and commanded pressure was assumed to be instantaneous, which is not realistic in more demanding applications. In order to address such problems, Shen [56] designed a model-based sliding mode controller

including a dynamic airflow model, and applied it to a linear table actuated by PAMs. Aschemann and Schindele [57] developed a cascaded sliding mode controller for a high-speed linear axis with a detailed empirical model of valve dynamics for pressure feedback and a model of the linear axis for position feedback. As in other model-based control strategies, detailed physical models were necessary to achieve satisfactory performance. Tondu et al. [58] applied sliding mode control with twisting and super-twisting algorithms to two degrees-of-freedom of a PAM-based manipulator, noting that the equivalent force control term was not helpful on the link farther from the base because of model uncertainty. Overall, studies that have successfully applied sliding mode control to experimental PAM-actuated systems have used systems with high stiffness, low inertial loads, and minimal time delays. However, the robotic manipulators in the present study exhibit relatively low stiffness, highly variable inertial loads, and substantial time delay. Moreover, sliding mode control can be negatively affected by measurement noise and low resolution sensors, which are present in the current systems.

While past research has demonstrated smooth and accurate motion control, the systems were simple and the payloads were much less than the mass of the manipulator. The control of a PAM-actuated manipulator with both high range of motion and high tip payload variations has not yet been attempted.

1.3.2.3 Robotics Applications

As a result of their functional similarity to natural muscles, numerous studies have focused on applicability to robotic systems, including manipulation and joint control of robotic arms and legs, or human assistance and rehabilitative devices. PAMs are especially suitable for use in robots intended to physically interact with human subjects because their inherent compliance increases safety.

One of the first PAM-actuated robotic manipualtors was developed by Bridgestone and Hitachi in 1984 [59]. The creators dubbed their actuator the "Rubbertuator" and their system the "SoftArm." Linear motion from the actuators was transmitted through steel cables and pulleys to bend the arm at its joints. The arm had seven degrees-of-freedom, and could lift up to 4.4 lb.

In 1994, Tondu et al. [60] employed McKibben muscles in a naturally compliant two degree-of-freedom SCARA arm actuated by PAMs in an antagonistic configuration, using a constant radius pulley to convert linear motion to rotational motion. About a decade later, Tondu et al. extended their work to a seven degree-of-freedom robot arm [40]. In this manipulator, gears were used to change the axis of rotation and to allow the two shoulder joints to operate independently. By varying the average pressure of the antagonistic pair, variable stiffness could be achieved. The greatest peak torque produced by this robot was 67 Nm (50 ft-lb) in the shoulder abduction joint, but because constant-radius pulleys were employed at the joints, this torque quickly trailed off as the actuators contracted. The robot was able to lift and maneuver delicate objects through tele-operation.

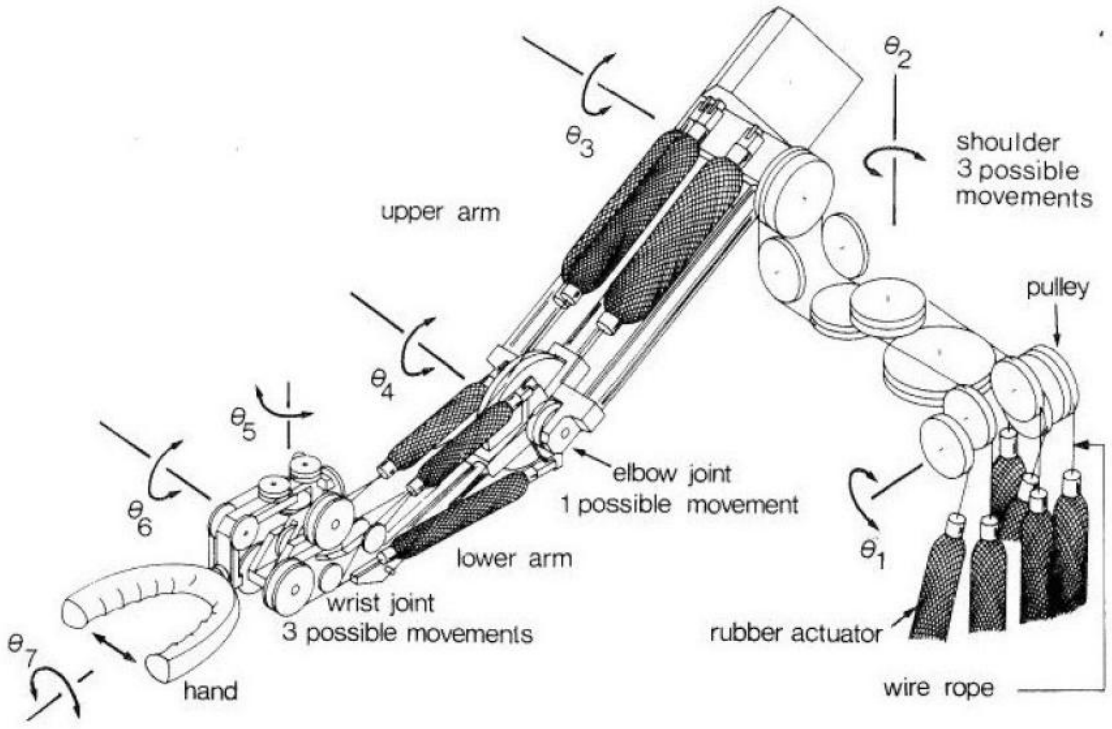


Figure 1.7: Bridgestone "Rubbertuator" arm.

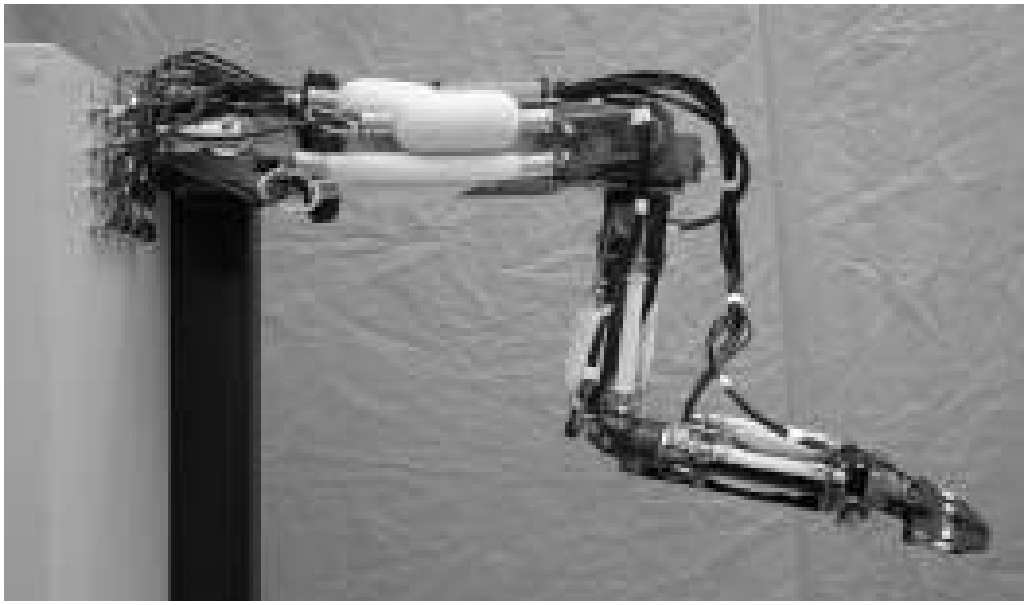


Figure 1.8: 7 DOF robot (Tondu, 2005).

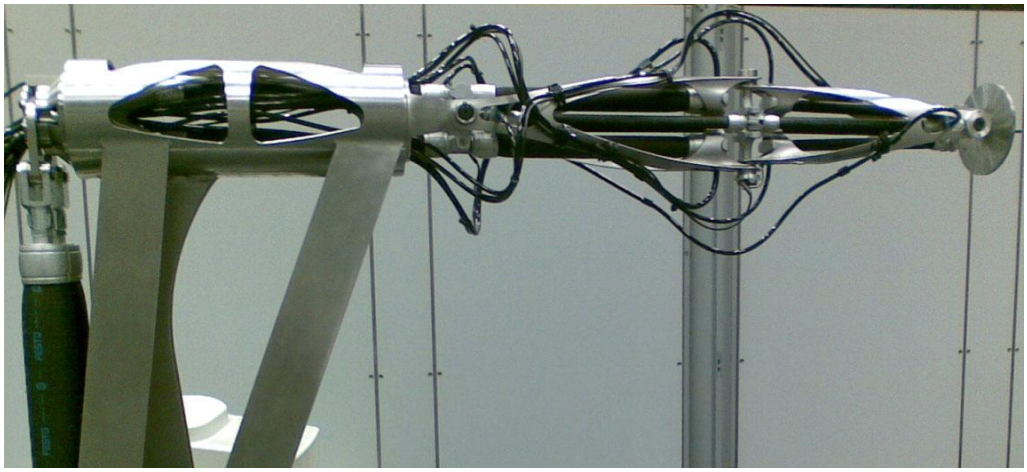


Figure 1.9: FESTO AirArm (Eichorn, 2009).

Eichorn et al. [61] designed and constructed Festo's four degree-of-freedom PAM-actuated manipulator called AirArm. Instead of attempting to transmit shoulder abduction torque from a stationary frame to a rotating frame, as in Tondu's work, the designers placed the shoulder abduction PAMs in a cylindrical column that rotates along with the arm when the other shoulder degree-of-freedom (extension) is actuated. Experiments demonstrated that the arm could reach tip velocities of up to 4 m/s. However, payload lifting was not studied.

Tuijthof and Herder designed a unique four-degree-of-freedom manipulator that they claim is inherently safe because the arm uses pneumatic artificial muscles and a gravity equilibrator system [62]. Springs and masses positioned and tuned so as to keep the potential energy of the system constant.

Anthropomorphic manipulators have been constructed in order to study and emulate human anatomy and to increase manipulator dexterity. Caldwell et al. [63] created a robotic arm and tested PAM-actuated elbow control with adaptive control. The manipulator was meant to replicate the layout and dimensions of the human

arm, with three degrees-of-freedom in the shoulder, one in the elbow, and three in the wrist. However, the shoulder joint was actuated by motors. Departing from the conventional method of single-degree-of-freedom joints, Yaegashi et al. [64] employed a spherical (ball and socket) joint to demonstrate high torque and range of motion within a compact volume. H-infinity motion tracking control was demonstrated with fair results. A similar parallel manipulator was designed by Zhu et al. [45], which used three PAMs to pivot a plate about a ball joint. This setup had limited range of motion, but high accuracy and controllable stiffness.

Not all PAM-based robotic manipulators have used discrete joints. In fact, their flexibility and light weight characteristics are ideal for non-discrete jointed, "continuum" robots. Walker et al. [65] created a robotic arm modeled from an octopus appendage. A cross-section of the robot reveals three PAMs surrounding a central flexible rod. Pressure in each PAM can be varied independently, allowing omni-directional bending along the main axis. Advantages to this configuration are high dexterity and ability to conform to surroundings. The arm can curl and constrict around objects of varying sizes and shapes in order to lift them. Trivedi [66] determined an exact geometric model for this type of manipulator. This was useful for calculating the controllable force throughout the workspace.

Other research groups have focused on PAM-actuated robotic hands. Shadow Robot Company [67] created a robotic hand that has 20 degrees-of-freedom. The PAMs and valves required for the many degrees-of-freedom reside outside the hand itself, packed along the forearm. The inherent compliance in PAMs is useful in delicate grasping tasks. Nagase [68] developed PAM-like actuators called pneumatic



Figure 1.10: "OctArm" continuum robot (Walker, 2005).

balloons for a compliant robotic hand, and used force sensing to grasp delicate objects like paper cups (maximum force was less than 5 N [1 lbf]). The pneumatic balloons were internal to the hand, but only four actuators were used.

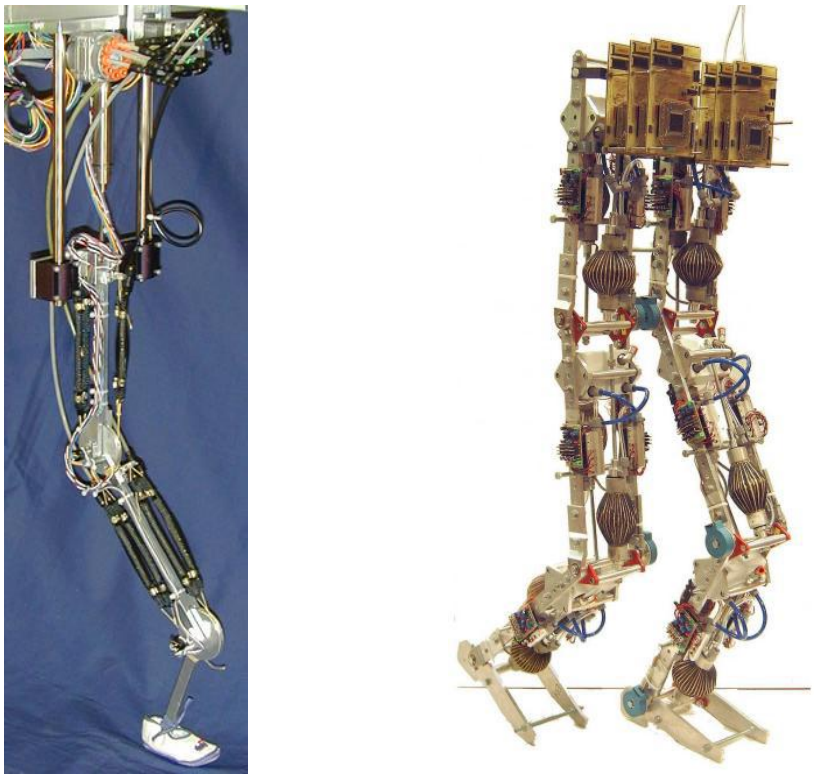
Robotic legs intended for walking have also been actuated by pneumatic artificial muscles. van der Linde [69] designed a PAM-based low power joint for walking robots. PAM stiffness could be quickly varied in order to enhance ballistic movement with cycle adjustability and orbital control. Colbrunn [70] designed a robot leg intended for walking that could produce stable, repeatable forward walking motion. The system was able to take advantage of the passive damping and elasticity characteristics of PAMs—valves could be closed between 66% and 94% of the walking motion. However, the full desired range of motion was not achievable with an



Figure 1.11: Shadow Robotic Hand (Shadow Robot Company).

antagonistic configuration. Additionally, tracking error was high. This may have been a result of using a solenoid valve with pulse-width-modulation instead of a more precise proportional valve. A similar walking design was created by Verrelst et al. [71]. PAM leg muscles were connected to rods which rotated the joints, and the attachment points could be varied to change the joint torque profile. The system demonstrated slow walking motions with basic PID control.

As previously stated, pneumatic artificial muscles have many advantages that make them desirable in portable, heavy-lift robotic systems intended for interaction with humans [72, 73]. Robots with the strength and dexterity to lift humans could be used for nursing assistance [5] and in casualty extraction [6]. However, there is very little research into PAM-based manipulators designed to lift heavy payloads



(a) (b)

Figure 1.12: Walking Robots, (a) PAM-based leg (Colbrunn, 2000), (b) Lucy bipedal walking robot (Verrelst et al., 2005).



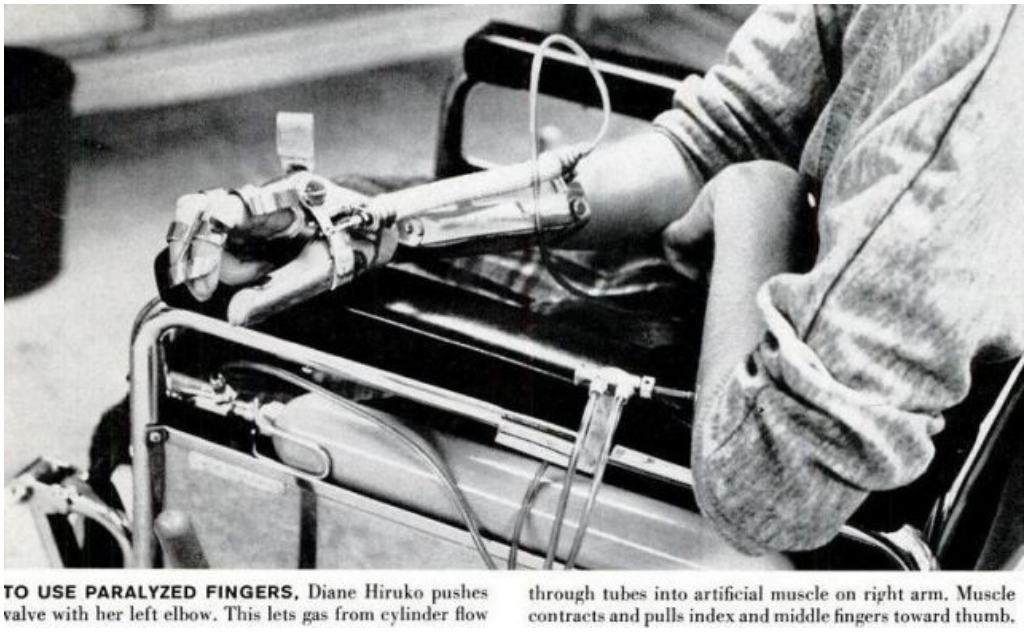
(a) (b)

Figure 1.13: Human-lifting robots (a) Robotic nursing assistant (HStar Technologies [5]), and (b) Battlefield extraction assist robot (Vecna Technologies [6]).

(greater than 20 lb), or control studies where payloads have greater mass than the manipulator itself. No known studies to date consider optimization of the manipulator joint structures to maximize torque output over the full range of motion with minimal operating pressure. This type of research would provide a more accurate and valuable assessment of PAM-based manipulator abilities in comparison to manipulators equipped with other actuation technologies such as electric motors and hydraulics.

1.3.2.4 Orthotics Applications

The objective of many orthotic devices is to prevent muscular degeneration and the development of abnormal motions resulting from neuromuscular disorders such as cerebral palsy, amyotropic lateral sclerosis, multiple sclerosis, or stroke [74]. These systems not only prevent degeneration, but are often able to assist muscle re-education. Active orthotic devices that interact with humans, especially wearable systems, must be safe, compliant, and lightweight. Traditional systems using electric



TO USE PARALYZED FINGERS, Diane Hiruko pushes valve with her left elbow. This lets gas from cylinder flow through tubes into artificial muscle on right arm. Muscle contracts and pulls index and middle fingers toward thumb.

Figure 1.14: McKibben muscle orthosis with CO_2 tank.

motors are too inflexible, causing a loss of smooth motion [75].

Due to their light weight, flexibility, low friction, and inherently safe actuation, PAMs have been employed in active orthotic devices. The first PAM orthotics were developed in 1957 at Los Ranchos Hospital [76] in collaboration with Joseph L. McKibben (coincidentally, the physicist who made the final connections to trigger the first atomic bomb [77]). The impetus for the design was McKibben's daughter, Karan, who had been afflicted by polio and had lost the ability to move her fingers. The pneumatic muscle was the perfect size and weight to actuate a wrist-hand orthotic device, allowing a patient to pinch objects with three fingers. The pneumatic valve supplying air from a CO_2 tank was controlled by a manual lever.

While the concept was abandoned for some time because of poor valve technology and heavy air tanks, PAMs began to reappear in orthotics research during the 1990s. Winters [78] carried out an investigation of McKibben and other types of

pneumatic artificial muscles for applications in orthotics. Prior et al. [79] described the design of a wheelchair-mounted rehabilitation robot using their "Flexator" pneumatic muscle, although no information was given describing how rehabilitation would be performed.

Caldwell and Tsagarakis [80] developed an arm exoskeleton orthosis with seven degrees-of-freedom (Figure 1.15), each using an antagonistic PAM configuration. The system could be used for strength augmentation or resistance exercise. The overall mass of the manipulator, which was primarily composed of an aluminum structure, was only 2 kg. However, maximum joint torque was only 2 Nm. Torque feedback was studied in an elbow joint impedance control scheme. In a subsequent study [81], torque was boosted to up to 30 Nm in the shoulder and 6 Nm in the elbow. Although lightweight, the system was not designed to be wearable.

Noritsugu developed a power assist glove and upper body strength augmentation suit based on "pneumatic rubber muscles" [82]. These actuators are somewhat different than McKibben muscles because they are composed of an asymmetric fiber bellows instead of a helical braid. Normally, the fiber is restricted on one side, causing the muscle to extend and curl in one direction during pressurization. The power assist glove is capable of 4 N pinch force. The upper body suit (Figure 1.16) does not require a solid structure, and is therefore claimed to provide more comfort than a cable and pulley system.

In order to provide enhanced rehabilitation, Ueda et al. [83] developed an upper body PAM-actuated exoskeleton system that purposefully activates specific muscles of the wearer in a systematic manner. The influence of exoskeleton torques



Figure 1.15: 7 DOF rehabilitation exoskeleton (Caldwell and Tsagarakis, 1994).

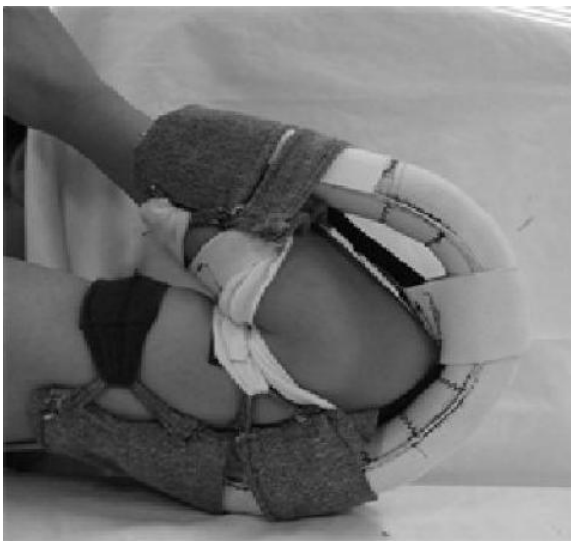


Figure 1.16: "Power assist wear" (Noritsugu, 2008).

was predicted using a human musculoskeletal model.

Wearable PAM systems have also been used in lower body rehabilitation. A knee joint was constructed by Jordan et al. [84] for soft fluidic actuators with rotary elastic chambers. Jamwal et al. [85] created a wearable parallel robot for three degrees-of-freedom in an ankle orthosis. A multi-objective genetic algorithm was used to find a family of optimal designs. Chandrapal [86] designed an intelligent PAM-based knee orthosis that was capable of recognizing user intent from electromyography (EMG) signals. The nonlinearities of the PAM system were compensated through an intelligent self-organizing fuzzy controller.

The design and control of a wearable PAM-based ankle-foot rehabilitation system was studied by Park et al. [74]. A unique feature was the absence of rigid mechanical linkages. PAM placement was inspired by human anatomy; each individual PAM was placed on top of the muscle it was intended to augment.

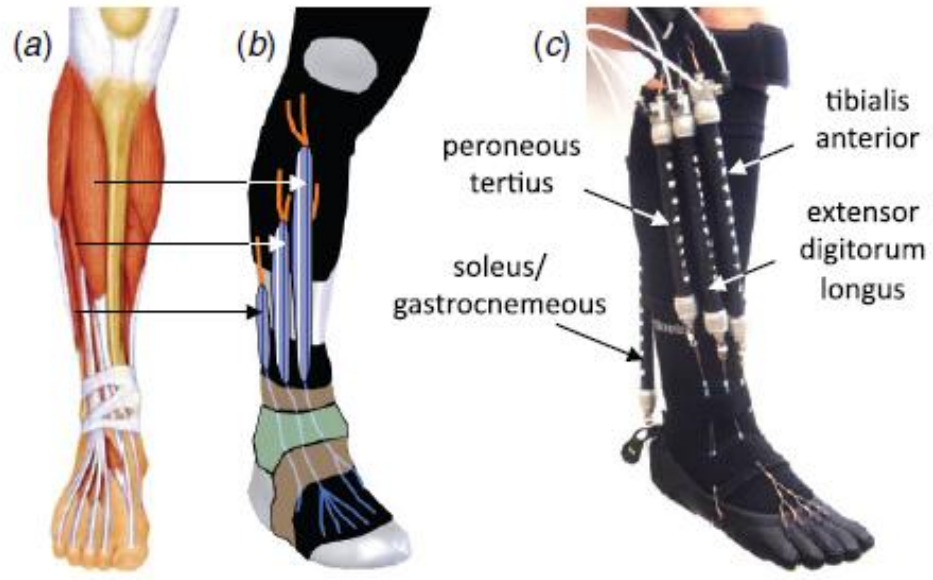


Figure 1.17: Ankle orthosis (Park et al., 2014).

The orthosis successfully assisted dorsiflexion/plantarflexion, and inversion/eversion movements.

1.3.2.5 Aerospace Applications

Recently, the aerospace field has begun to explore unconventional, bio-inspired methods for task-specific wing morphing and enhanced control of aerodynamic surfaces. As a result, innovative research has been undertaken using PAMs as actuators in aerospace applications.

Woods et al. [87] performed several experiments with a helicopter rotor trailing edge flap using PAMs. A bellcrank linkage system was devised in order to place PAMs near the root of the rotor blade, where the centrifugal force was lowest. Wind tunnel tests determined that PAMs could produce the necessary torques to resist aerodynamic loads and are controllable at the high frequencies necessary in rotor applications. Tests in rotation proved that the pneumatic components could operate normally in the rotating environment [88].

Peel et al. [89] developed an active camber airfoil actuated by lightweight PAMs. The nose and tail of the structure were able to deform by 25 deg and 20 deg, respectively. The wing structure was specifically designed to eliminate buckling of the lower skin.

Bubert [90] designed a highly extensible skin elongation system for a morphing aircraft wing that employed PAMs as actuators. Skin elongation of 100% was achieved in the span direction while maintaining a constant chord, thereby doubling

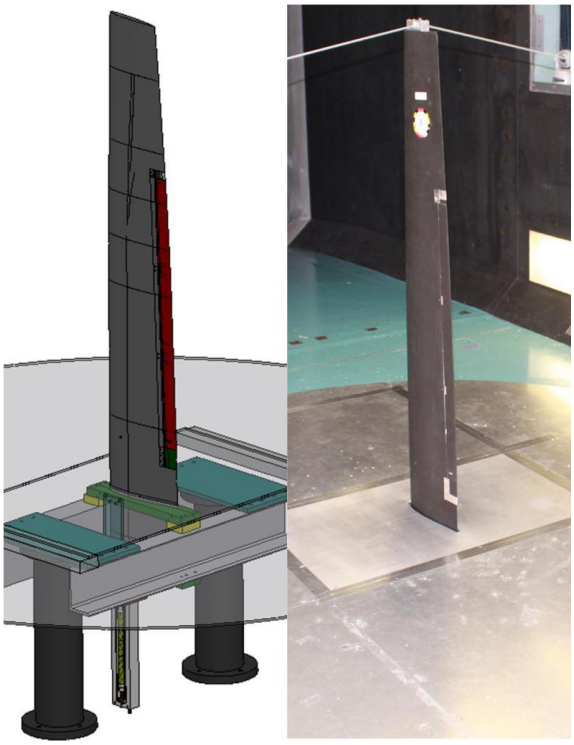


Figure 1.18: PAM-actuated trailing edge flap (Woods et al., 2011).

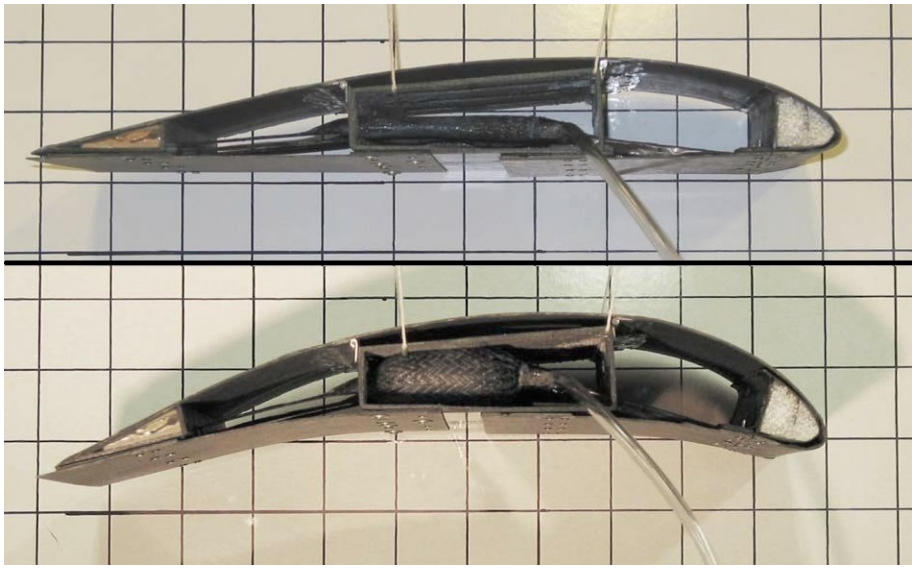


Figure 1.19: Active camber airfoil (Peel et al., 2009).

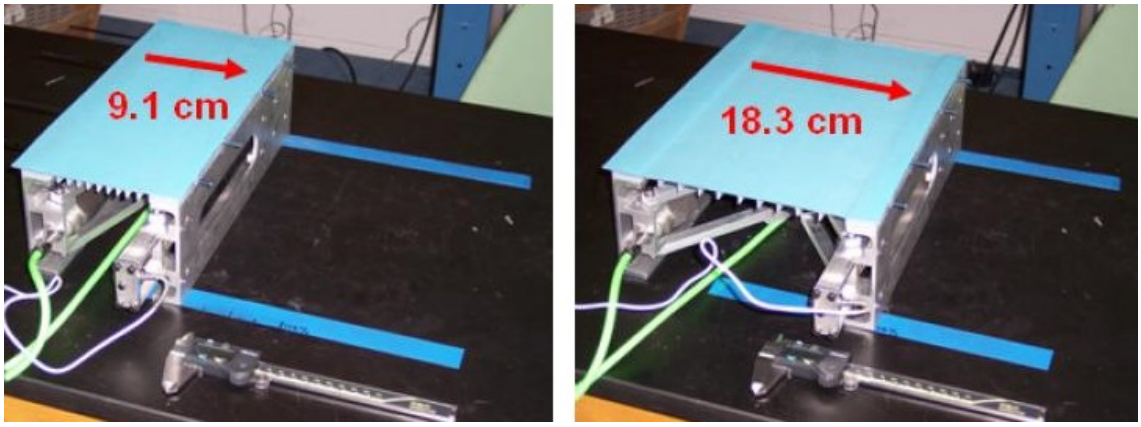


Figure 1.20: Morphing skin test article (Bubert, 2009).

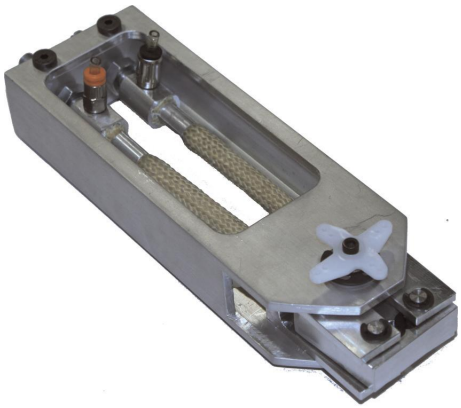


Figure 1.21: MiniPAM cartridge (Vocke et al., 2012).

the effect area, with PAMs operating an X-frame structure. A simple PID controller was sufficient for the linear motion.

Vocke et al. [91] designed and tested a miniature PAM actuation package (Figure 1.21) for use in a micro-air-vehicle (MAV). Findings included that well-designed miniature PAM mechanisms can generate a greater static torque than similarly-scaled conventional servo motors, leading to superior specific torque, while torque density of the PAM device was on par with the servos.

1.4 Contributions of Dissertation

The objective of this research was to design and evaluate manipulators actuated by lightweight, compliant pneumatic artificial muscles and intended to lift a large range of payload masses over a large range of motion. Special emphasis was placed on a compact design and smooth, accurate motion control. Several original contributions were made to the state of the art in PAM modeling, design, and control.

Prior to this research, most PAM models assumed a fully cylindrical PAM shape in contraction and extension when, in fact, the actuator ends form an elliptic shape when deformed. Some models attempted to account for these tip effects by including conical tip surfaces [63] or assuming a reduction in active length [35]. Furthermore, existing models have not sufficiently accounted for the complex, nonlinear actuator stress-strain relationship generated by the interaction between the bladder and braid. In the present work, an existing PAM model (Ferarresi, 2001) was refined to improve force estimates over the full range of actuator strain and operating pressure. First, a new method was devised to account for the path a braid fiber travels around the elliptical ends of the PAM, leading to a better approximation of geometric shape change, and thus, PAM force behavior. Additionally, the actuator stress-strain relationship was changed from linear to fourth order to account for nonlinear bladder-braid interaction in both positive and negative strain. The empirically-fit constitutive relationship was shown to accurately predict force-contraction curves at untested pressures.

While dexterous multi-degree-of-freedom robotic manipulators have been de-

veloped in past work, the payload capacity of these systems is low. The highest reported payloads on PAM-based manipulators working against gravity is 2 kg (4.5 lb) [40, 59]. These low maximum payloads are mainly a result of two design choices: (1) employing antagonistic actuation, which allows bi-directional torque, but forces a trade-off between torque and range of motion; and (2) ignoring optimization of joint geometry. While one study has attempted to optimize antagonistic actuation on a knee orthotic [92], the dual four-bar-linkage design is not optimal for a uni-directional system. This work is the first known study to design PAM-based manipulators with the specific intention of maximizing uni-directional torque over a large angular range of motion (90+ deg) in order to lift payloads an order of magnitude greater than current PAM-actuated manipulators (over 70 kg [150 lb]). To achieve this goal, the manipulators were constructed with unique design features, including parallel PAM arrangements and a novel joint design optimized for uni-directional actuation. The genetic algorithm optimization procedure used for kinematic design of a PAM-actuated manipulator is an original approach in PAM literature, adopted to ensure that the joint can maintain high torque output from PAM actuators even as their force reduces with contraction.

Numerous control strategies have been applied in PAM literature. Among these are model-based controllers, which attempt to account for the complex pneumatic and mechanical dynamics of the PAM-actuated system [56] but do not have the ability to adapt to changes in system parameters. Alternatively, adaptive neural network controllers that utilize a "black box" model of the system [93] have also been applied. A neural network structure does not take advantage of the known system

dynamics. In the present work, an ideal combination of modeling and adaptation is determined for PAM-based manipulator control. The controller incorporates neural networks within expressions of the known system dynamics to create a hybrid neural network control law. In this controller, the neural networks are nonlinear functions of angle involving the payload parameters and the quasi-static relationship between angle and torque. The new model structure assumes a linear relationship between pressure and joint torque, as well as a common equation of motion for an open-chain manipulator. Including these relationships preserves controller structure without requiring knowledge of nonlinear PAM dynamics, joint kinematics, or payload.

Lastly, this work investigates a novel variable recruitment strategy—activating the minimum number of PAMs necessary to meet torque requirements—on a PAM-actuated robotic manipulator. While previous research tested variable recruitment to measure force, this is the first study to quantify the efficiency benefits of PAM variable recruitment. The improved PAM force model was leveraged to accurately simulate variable recruitment.

1.5 Overview of Dissertation

This dissertation is organized into seven chapters, each presenting a different aspect of the research performed.

Chapter 1: Introduction. This chapter presents the motivation for soft actuation, specifically the use of pneumatic artificial muscles in robotic applications that require human-robot interaction. Current technologies, including conventional

actuators, series elastic actuators, and compliant control strategies are discussed, and their limitations are explained. Pneumatic artificial muscles are introduced as a solution to these limitations, and a broad literature review on the modeling and control of PAMs, as well as applications in robotics, orthotics, and other areas is presented.

Chapter 2: Quasi-Static Modeling and Analysis of Pneumatic Artificial Muscles. This chapter investigates modifications to an existing PAM modeling approach. The first original modification is a detailed model of the elliptic ends of the actuator. The second is a reformulation of the stress-strain relationship that accounts for braid and bladder interaction, even in extension beyond resting length. These improvements provide higher-accuracy force-contraction predictions than previous models. The constitutive relationship is found to be nearly linear with pressure, allowing straightforward extension to untested pressure levels.

Chapter 3: Structural Design of PAM-Based Robotic Manipulators. The design of a two degree-of-freedom PAM-based manipulator is discussed. Important features for compact design, such as multi-PAM actuator groups, tendon-based joints, and pressure manifolds are described in detail. Simulations, which include dynamics of the PAM actuators and airflow components, are conducted to predict performance, followed by open-loop experiments to validate performance. Constrained optimization is employed to determine joint geometry that minimizes the PAM pressure required to satisfy a torque profile over a given range of motion.

Chapter 4: Control of a Heavy Lift Robotic Manipulator with Pneumatic Artificial Muscles. Two output feedback controllers (proportional-integral-derivative

and fuzzy logic) are applied to a PAM-based manipulator in the pursuit of smooth and accurate motion tracking. Due to the limitations of pure output feedback control, a model-based feedforward controller is developed and combined with output feedback to achieve improved closed-loop performance. Simulations are performed in order to validate the control algorithms, guide controller design, and predict optimal gains. Using real-time interface software and hardware, the controllers are implemented and experimentally tested on the manipulator.

Chapter 5: Advanced Control of PAM-Based Robotic Manipulators. Building upon the work in Chapter 4, advanced control strategies are implemented. A sliding mode controller is employed in conjunction with a model-based sliding mode observer, yielding the highest accuracy of all the control strategies when payload is known *a priori*. To achieve high performance regardless of payload, an adaptive controller based on neural networks is designed and implemented. Tests are conducted with real-time payload modification under different waveforms, validating the effectiveness of the controller.

Chapter 6: Variable Recruitment in PAM Groups. This chapter presents a bio-inspired variable recruitment strategy to improve system efficiency. Efficiency gains arise from a lower total bladder resistance and a diminished air "throttling" effect when fewer PAMs are employed. Quasi-static characterization data is analyzed to compare single vs. multiple PAM force output for a constant air mass, and the effect of bladder material selection is explored. Dynamic tests are performed on a PAM-based manipulator, and muscle recruitment is varied to determine its effect on efficiency at different levels of payload and muscle contraction. Considerations

for the proper addition and subtraction of activated muscles in real-time control applications are discussed.

Chapter 7: Conclusions. This final chapter summarizes the key conclusions from this research. The original work contributed to literature is identified, and several topics worthy of future work are discussed.

Chapter 2: Quasi-Static Modeling and Analysis of Pneumatic Artificial Muscles

2.1 Introduction

Pneumatic artificial muscles (PAMs) are lightweight, compliant actuators composed of a helically braided sleeve surrounding an elastomeric bladder, which are held together at each end by a fitting [29, 40]. Pressurization of the soft bladder inflates the muscle and causes the stiff braid fibers to reorient, generating a contractile stroke and a pulling force. PAMs were originally devised by Joseph McKibben to actuate orthotic devices for polio patients in the 1950's [23]. Similar applications have been studied more recently, including PAM-powered devices for orthotics and rehabilitation [29, 30, 69] and bio-inspired humanoid robotic devices, such as robotic hands [68, 94] and haptic devices [75]. These compliant actuators are particularly desirable in portable, heavy-lift robotic systems intended for interaction with humans [72, 73], specifically those envisioned for nursing assistance and in battlefield casualty extraction, or in soft robotic applications [95]. In addition, these compliant actuators are damage tolerant [2, 28], and have been endurance-tested for as many as 125 million cycles with minimal wear [2].

In many applications, PAMs are employed in antagonistic pairs. This arrangement, illustrated in Figure 2.1, is widely observed in biological systems. A commonly cited agonist-antagonist pair is the biceps-triceps pair of muscles on the human arm. As the agonist contracts, the antagonist extends past resting length, preserving the stiffness of the joint. Antagonistic PAM configurations have been applied to robotics [96], trailing edge flaps [87], and miniature servo-motors [91].

Although several models have been proposed to capture static and dynamic PAM behavior as described in a review by Tondu [40], these models have not demonstrated sufficient accuracy and scalability for demanding applications such as model-based control of a robotic manipulator in high-speed conditions [97]. The accuracy of most physical models is often poor at low pressures due to the pressure deadband effect, a phenomenon in which the applied pressure must exceed a threshold (activation) pressure before PAM contraction begins [27]. Additionally, accuracy decreases at high bladder strains ($\varepsilon \geq 1$) due to the nonlinear stress-strain relationship in the bladder as it deforms from its resting state as a hollow cylinder to a shorter, larger-diameter hollow cylinder with rounded ends. The internal pressure, actuator strain, and geometry of the braid dictate this complex shape. However, most PAM models assume a fully cylindrical shape, neglecting the boundary constraints that produce rounded ends, or subtracting the rounded portions from the active length.

Gaylord [24] first modeled the relationship between actuator force, pressure, and strain with a simple geometric model that completely ignores bladder effects. Subsequent studies have improved upon this model with energy balance and force balance approaches that incorporate the losses caused by bladder elasticity. Klute

and Hannaford [32] introduced a nonlinear Mooney-Rivlin term based on the principle of virtual work, improving the force estimates at high contraction. Tsagarakis and Caldwell [33] proposed a model that incorporates a simple model of tip deformation and compensates for the activation pressure required to overcome the radial elasticity of the bladder. Ferraresi et al. [34] developed the force balance approach, which was modified by Kothera et al. [35] to account for bladder thickness change. Shan et al. [39] developed a finite axisymmetric deformation model that could predict the changing shape of a flexible matrix composite membrane under different conditions, but force generation was not explored in detail. Despite decades of research [40], an all-encompassing model that reliably estimates nonlinear force-contraction behavior over the operational envelope of actuator strain and pressure for PAMs of different sizes has not yet been developed.

While the behavior of an individual PAM can be determined through exhaustive experimental tests, this is often impractical. In our prior work [27] with a miniature PAM (4.16 cm [1.64-in] length, 0.41 cm [0.1625-in] diameter, composed of a silicone bladder and polyethylene terephthalate [PET] braid), the nonlinear elasticity of the bladder was captured by modeling stress as a polynomial function of the strain, in which coefficients were determined empirically at many pressure levels. This model was found to be highly accurate at the tested pressures, predicted blocked force with high accuracy, and accounted for hysteresis in quasi-static experiments. However, this model was not applicable to PAMs undergoing extension, that is, when a PAM is stretched past its resting length. Inaccuracy of the extensile force predictions resulted from assuming a fully cylindrical PAM shape and neglecting curvature at

the actuator ends. Furthermore, attempts to interpolate force-contraction profiles to untested pressures often yielded low-accuracy results, rendering the model only useful at or near the tested pressures. Other models, such as those presented by Liu and Rahn [98] and Shan et al. [39] are able to capture extension beyond resting state, but the models are complex and require a numerical procedure for convergence. Additionally, these studies assume that the inextensible braid fibers are embedded in the material, rather than allowing free movement on the surface of the bladder.

The present work addresses these issues by developing a new model that improves blocked force predictions, characterizes PAMs in extension, and decreases the amount of empirical data required to accurately characterize this type of actuator. Several improvements to the current model were considered. First, this work incorporates non-constant bladder thickness, a phenomenon resulting from volume conservation as the bladder expands circumferentially. Then, a detailed geometric model is introduced, which preserves the boundary conditions at the bladder ends and better approximates the observed shape of the actuator. The improved model is applied in extension, where it is found to well-predict the dramatic increase in force. Finally, the constants of the stress-strain polynomial are constrained to vary linearly with pressure during the curve-fitting procedure, dramatically improving the predictive ability of the final model.

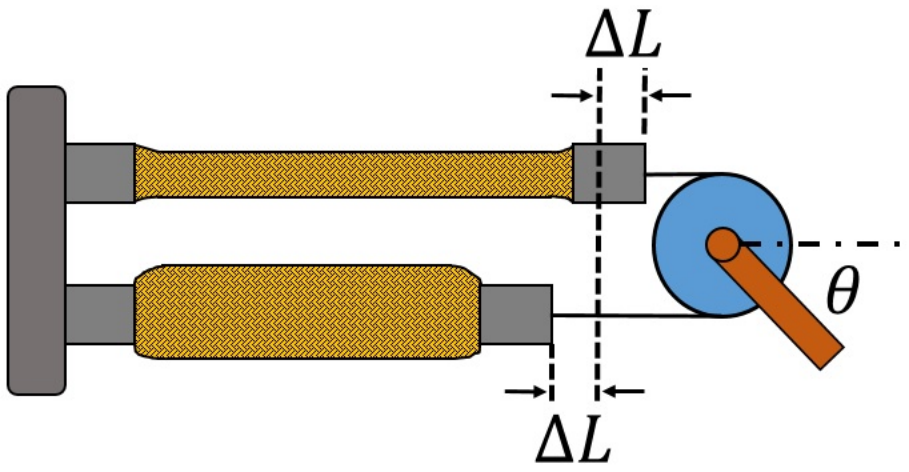


Figure 2.1: PAMs grouped in an antagonistic pair, actuating a rotating joint.

2.2 Improvements to Force Balance Model

2.2.1 Original Force Balance Model

A free-body diagram for the PAM force balance model that was originally derived by Ferraresi et al. [34] and improved upon by Hocking and Wereley [27] is shown in Figure 2.2. The actuator is modeled as a cylinder that expands and contracts as the actuator strain is varied. The braided fibers which wind helically around the bladder are assumed to have constant length B (a valid assumption as the Kevlar fiber modulus is four to five orders of magnitude higher than the latex bladder modulus), so that braid length is determined by:

$$B = \frac{L}{\sin \alpha} \tag{2.1}$$

where L is the length of the actuator and α is the angle that the actuator braid makes

with the circumferential plane on the actuator surface. Geometric constraints also dictate the number of turns, N, completed by the braid around the circumference of the bladder, which is given by:

$$N = \frac{L}{2\pi R \tan\alpha} \tag{2.2}$$

The outer radius of the PAM, R, is given by:

$$R = \frac{\sqrt{B^2 - L^2}}{2\pi N} \tag{2.3}$$

The thickness of the bladder, t, is calculated under the assumptions that bladder volume V_B, is a constant determined from the initial bladder geometry as a uniform hollow cylinder, and that the bladder remains a uniform hollow cylinder but with changing length and outer radius:

$$t = R - \sqrt{R^2 - \frac{V_B}{\pi L}} \tag{2.4}$$

Applying the concept of force balance to a quasi-static PAM, we obtain equations in the circumferential (c) and axial (z) directions, respectively:

$$PRL = \sigma_c t L + NT\cos\alpha \tag{2.5}$$

$$F + \pi R^2 P = \sigma_z A_B + T\sin\alpha \tag{2.6}$$

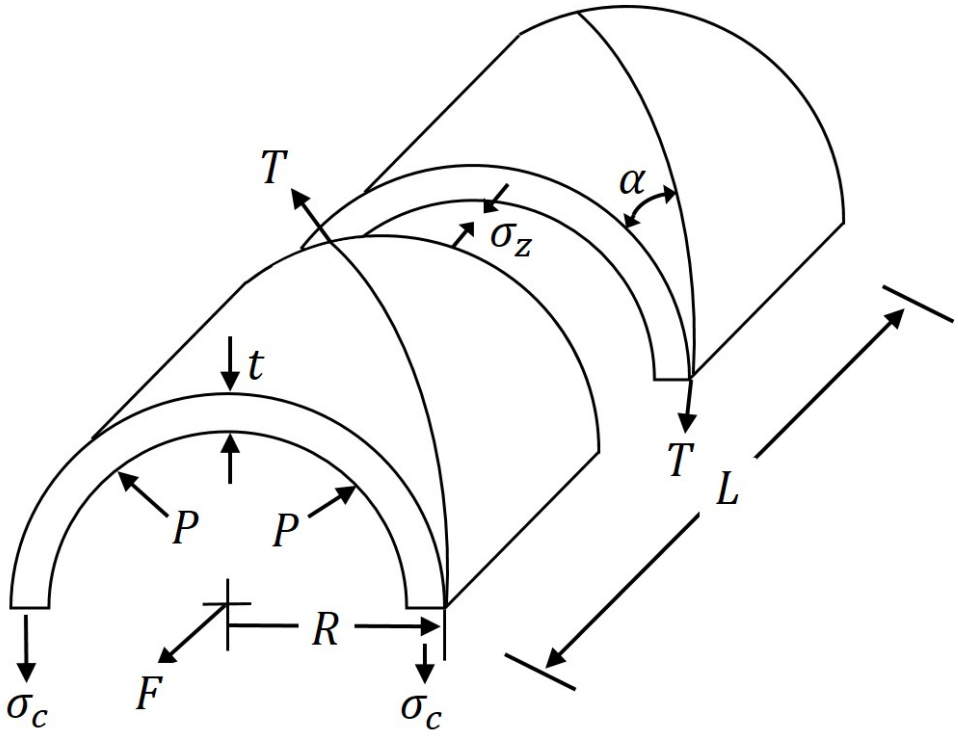


Figure 2.2: Force balance model [25].

where P is internal pressure, T is tension in the braid, A_B is bladder cross-sectional area, σ_z is axial bladder stress, σ_c is circumferential bladder stress, and F is the actuator force produced in the axial direction. By solving for T in Eqn. 2.5 and substituting the result into Eqn. 2.6, we obtain an expression for actuator force:

$$F = -\pi R^2 P + \sigma_z \frac{V_B}{L} + \frac{PRL - \sigma_c tL}{N} \tan\alpha \tag{2.7}$$

Substituting Eqns. 2.2 and 2.3 into Eqn. 2.6, the expression simplifies to:

$$F = \frac{P}{4\pi N}(3L^2 - B^2) + \sigma_z \frac{V_B}{L} - \sigma_c \frac{tL^2}{2\pi R N^2} \tag{2.8}$$

The total actuator force includes the Gaylord force term (the first term shown) and terms dependent on bladder stress in the axial and circumferential directions.

While a number of methods can be used to determine these stresses, such as finite elasticity theory [39, 99], we have elected to treat the nonlinear bladder stress as a polynomial function of strain [27] and use system identification techniques to determine the unknown coefficients. Yeoh []Yeoh1993 stated that the strain energy density function of a nearly incompressible, nonlinear elastic material can be expressed as a polynomial function; we use these findings as the inspiration for our approach. Employing a polynomial stress-strain relationship relieves the restrictions imposed by defining specific material properties or elasticity relations that would not be able to account for the complex interactions that occur as the braid slides freely along the outer surface of the bladder, including strain stiffening and softening effects at high radial strains, as well as the pressure-dependent stiffness that was observed experimentally.

The unknown coefficients of the constitutive polynomial function are the modulus values E_k:

$$\sigma = \sum_{k=1}^{M} E_k \varepsilon^k \tag{2.9}$$

The axial and circumferential strains are given respectively by:

$$\varepsilon_z = \frac{L}{L_0} - 1 \tag{2.10}$$

$$\varepsilon_c = \frac{R}{R_0} - 1 \tag{2.11}$$

The curve-fitting optimization procedure from [27] was applied to experimental data. At each pressure level, we choose E_k values in an M-th order nonlinear force-balance model that minimize the mean squared error ϵ_F between experimental measurements and model estimates (using Matlab's *fmincon* function) summed over the n data points on the curve:

$$\epsilon_F = \sum_{i=1}^{n} |F_{a,i} - F_{m,i}|^2 \tag{2.12}$$

Figure 2.3 displays the model and experimental data for a 1.9 cm (0.75-in) diameter, 18.5 cm (7.3-in) length PAM with a 76.5 deg braid angle, using an optimized 4th-order polynomial stress-strain relation. Note that this particular PAM size will be used throughout the remainder of the analysis as the illustrative example of the model improvements. F_{AVG} refers to the averaged data sets at each pressure level (from 0.07 to 0.8 MPa [10 to 120 psi]), and F_{NLFB} refers to the force predicted by the nonlinear force balance model assuming constant bladder thickness. The model matches very well with the data at high contraction; however, the blocked force is overestimated at each pressure. Moreover, the model cannot accurately capture the extensile behavior of the actuator that occurs during negative contraction. Figure 2.4 shows the values of E_k at each of the tested pressures. Note that there is a clear linear trend between the pressure and the modulus values at pressures greater than 0.2 MPa (30 psi).

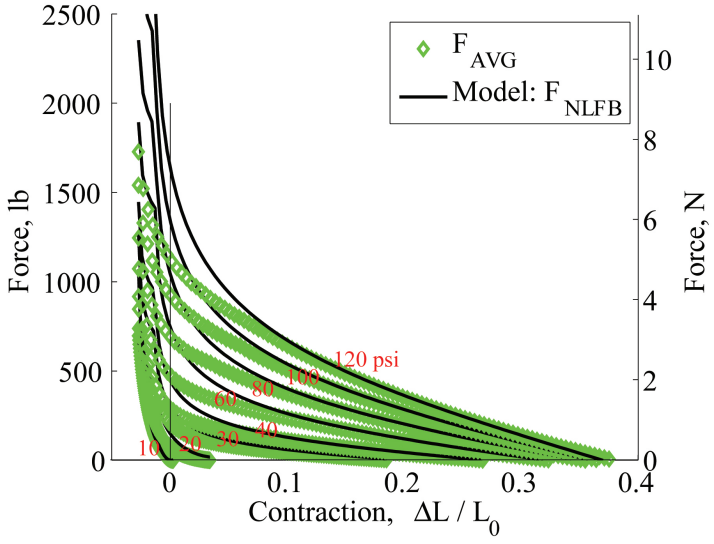


Figure 2.3: Force-contraction profile comparing model and experiment; 1.9 cm (0.75-in) diameter, 18.5 cm (7.3-in) length PAM with a 76.5 deg braid angle.

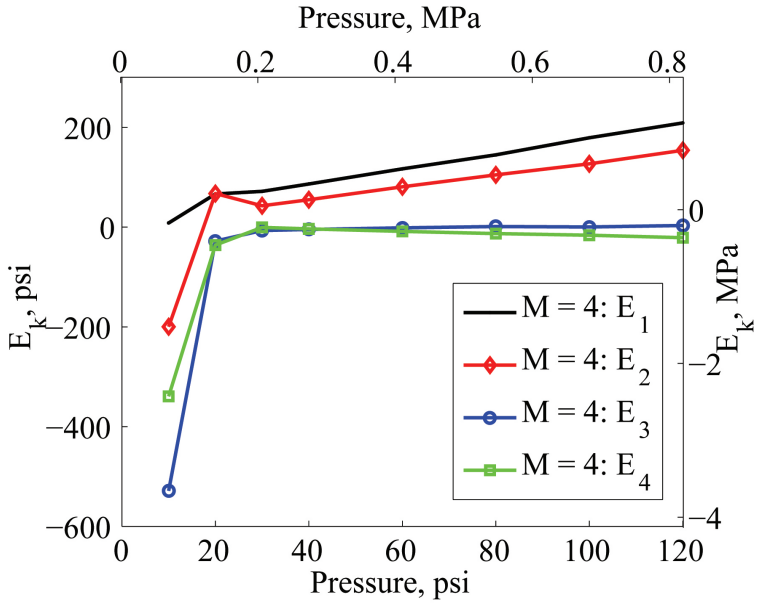


Figure 2.4: Nonlinear modulus values as determined by optimization procedure; 1.9 cm (0.75-in) diameter, 1.5 cm (7.3-in) length PAM with a 76.5 deg braid angle.

2.2.2 Non-constant Bladder Thickness Modification

A modification to Ferraresi's original force balance model was proposed by Kothera et al. [35], incorporating the change in thickness of the bladder into the

formulation. Eqns. 2.5 and 2.6 are changed to reflect how the change in thickness of the bladder affects static equilibrium:

$$P(R-t)L = \sigma_c tL + NT\cos\alpha \tag{2.13}$$

$$F + \pi(R-t)^2 P = \sigma_z A_B + T\sin\alpha \tag{2.14}$$

Additionally, the average circumferential strain in the bladder is more accurately modeled with thickness change:

$$\varepsilon_c = \frac{R - t/2}{R_0 - t_0/2} - 1 \tag{2.15}$$

This leads to a modified equation for the actuator force (e.g., compare to Eqn. 2.8):

$$F = \frac{P}{4\pi N}(3L^2 - B^2) + P\left(\frac{V_B}{L} - \frac{tL^2}{2\pi RN^2}\right) + \sigma_z\frac{V_B}{L} - \sigma_c\frac{tL^2}{2\pi RN^2} \tag{2.16}$$

where we observe a new pressure-dependent term.

Figure 2.5 displays blocked force models assuming constant and non-constant thickness for the sample PAM, compared with experimental measurements at tested pressures. In the figure, F_{NLFBnc} refers to the force predicted by assuming non-constant bladder thickness. The model with the non-constant thickness assumption clearly fits experimental data more closely than the model derived assuming constant bladder thickness. Both models account for the fact that the PAM begins to produce

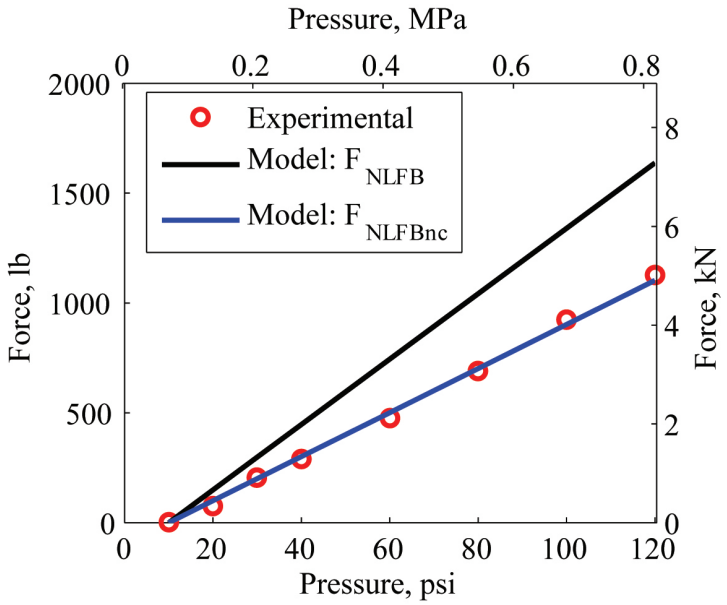


Figure 2.5: Blocked force vs. pressure; 1.9 cm (0.75-in) diameter, 18.5 cm (7.3-in) length PAM with a 76.5 deg braid angle.

force at non-zero pressure. This pressure deadband is caused by bladder resistance, and varies with bladder material and thickness. For the actuators tested in this work, the activation pressure was found to be approximately 0.07 MPa (10 psi).

Note that the accuracy of both of these models is dependent upon braid angle, which is somewhat difficult to measure and carries some uncertainty. Even small variations in braid angle can produce large changes in force output. For instance, if a lower braid angle was estimated on the PAM data shown in Figure 2.5 (74 deg instead of 76.5 deg), the constant-thickness model would be more accurate than the non-constant thickness model.

2.2.3 PAM Extension

As mentioned previously, PAMs are often used in antagonistic pairs. In some cases, a bias contraction is applied and both PAMs are pressurized to continuously

maintain a desired hinge stiffness. However, in many systems, the agonist muscle contracts while the antagonist extends past resting length (acting as a nonlinear spring) to maintain high stiffness, eliminating the need for dual pressurization. In such applications, an accurate model PAM extension is necessary for proper control design and simulation.

Extension past resting length causes the braided sleeve to constrict around the bladder until the PAM "necks down" at the ends. As mentioned earlier, previous models have assumed a fully cylindrical shape. This assumption produces fairly good estimates of PAM radius and bladder thickness (and hence, PAM force) during contraction. However, during high bladder extension, this simple model calculates bladder thickness to be greater than the predicted PAM radius, which cannot occur as it is physically impossible. This inconsistency motivates a more detailed method of calculating PAM radius and bladder thickness.

2.2.4 Elliptic Toroid Shape for Bladder Ends

McKibben-type PAMs display a physical shape characterized by a cylindrical section in the axial center, encapsulated by two rounded ends. The braid and bladder are clamped down at the ends so that the radius at each end of the active length region is constant. When a pressurized PAM is in the contracted state, the ends of the bladder exhibit convex curvature between the end fittings and the cylindrical shape in the center. The outer area of the curved surface can be approximated by the partial surface area of an elliptic toroid. An elliptic toroid is a surface of

revolution, similar to a ring torus, and is formed when an ellipse is fully revolved around a central axis. The equation for such an ellipse is given by:

$$\begin{aligned} x(u,v) &= \cos u(a\cos v + c) \\ y(u,v) &= \sin u(a\cos v + c) \\ z(u,v) &= b\sin v, \end{aligned} \tag{2.17}$$

where v is the angle inside the two-dimensional ellipse shape beginning at the minor axis, and u is the angle as the ellipse rotates around the axis of revolution. As illustrated in Figure 2.6(a), the cross section of a PAM between the end fitting and the central cylindrical section can be closely approximated as a half-ellipse with minor axis a and major axis b, offset from the longitudinal axis of the PAM by a distance c. Experimental observations of multiple PAMs suggest that the part of the braided surface at the edge where it protrudes from the end fitting is usually sloped. The boundary angle of $\pi/3$ rad (60 deg) with respect to the coordinate system of the ellipse was selected as a reasonable approximation of the slope at the bladder ends. Therefore, in this work we assume the surface of the ellipse shared by the PAM surface runs from $v \in [0, \pi/3]$.

Alternatively, in extension, PAMs exhibit concave curvature near the ends while maintaining the initial radius at the end fitting boundary. The radius of the central cylindrical section is less than the resting radius, and the curvature at the ends produces a different elliptic pattern. The outer surface of the PAM in the curved region is now approximated by a part of the internal section of an elliptic toroid. Figure 2.6(b) illustrates this cross-section.

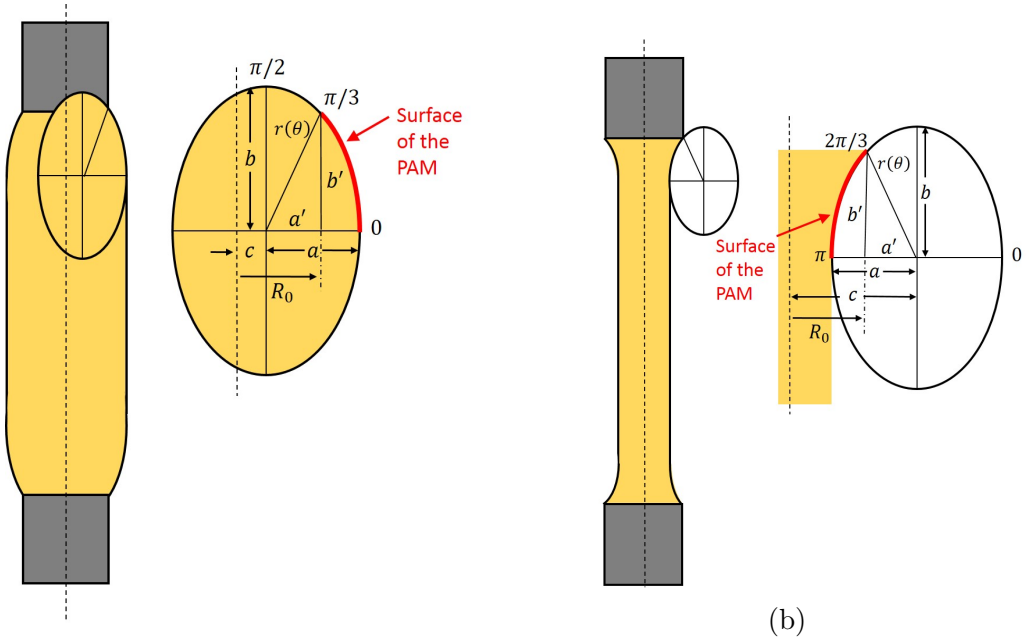


Figure 2.6: Geometric model of PAMs in (a) contraction, (b) extension.

In both cases, the length from the center of the ellipse to the resting radius is denoted as a'. The vertical distance from the end fitting edge to the center of the ellipse is denoted as b'. These terms are a function of the ellipse radius r. Radius is a function of the major and minor axes, and the angle with respect to the minor axis; it is given by:

$$r = \sqrt{\frac{a^2 b^2}{b^2 \cos^2 v + a^2 \sin^2 v}} \tag{2.18}$$

Substituting the proportionality constant $k = b/a$ and solving for $v = \pi/3$ or $v = 2\pi/3$, the radius is

$$r = a\sqrt{\frac{4k^2}{k^2 + 3}} \tag{2.19}$$

Using trigonometric relationships, we determine a', b', and c:

$$a' = \pm a\sqrt{\frac{k^2}{k^2+3}} \tag{2.20}$$

$$b' = a\sqrt{\frac{3k^2}{k^2+3}} \tag{2.21}$$

$$c = R_0 - a' = R - a \tag{2.22}$$

By rearranging the expression for c and substituting for a', we can find a:

$$a = \pm\frac{R_0 - R}{1 - \sqrt{k^2/(k^2+3)}} \tag{2.23}$$

2.2.5 Braid Length along the Surface of the Elliptic Toroid

The aforementioned force balance model requires a good approximation of the central radius as PAM length varies to produce accurate results. Since braid length B is constant, we can determine the radius R by finding a PAM shape for which the braid length over the deformed PAM is equivalent to the resting braid length. The total braid length is the sum of the braid length over each elliptic end and the cylindrical center. First, the arc length s of the braid wrapping around the elliptic ends is calculated. The length of a squared line element for a curve on a

three-dimensional surface is given by:

$$ds^2 = dx^2 + dy^2 + dz^2 \tag{2.24}$$

Differentiating the equations of motion for an elliptic toroid, we determine the infinitesimally small elements in rectangular coordinates as a function of those in angular coordinates:

$$\begin{aligned} dx &= -\sin u(a\cos v + c)du - a\cos u \sin v dv \\ dy &= \cos u(a\cos v + c)du - a\sin u \sin v dv \\ dz &= b\cos v dv \end{aligned} \tag{2.25}$$

leading to a total squared line element length in terms of angular coordinates:

$$ds^2 = (a\cos v + c)^2 du^2 + (a^2 \sin^2 v + b^2 \cos^2 v)dv^2 \tag{2.26}$$

The slope of the braid as it wraps around the PAM bladder is assumed to be constant, rotating a total of N times over the entire length. Hence, over one elliptic end, the braid rotates $N(b'/L)$ times, and the braid length in the u-direction is $2\pi N(b'/L)$. Therefore, the average braid slope over the end arc ($v = 0$ to $\pi/3$) is given by:

$$\frac{du}{dv} = \frac{2\pi N(b'/L)}{\pi/3} = \frac{6Nb'}{L} \tag{2.27}$$

In numerical simulations, v is varied over n small increments Δv, and the

corresponding values of Δu are determined from Eqn. 2.27. By calculating Δs for each increment from Eqn. 2.26, and summing over the curve, we obtain a good approximation of s, the length of braid fiber over the curved surface:

$$s^2 = \sum_{i=1}^{n} \left[(a\cos v_i + c)^2 (\frac{6Nb'}{L})^2 + (a^2 \sin^2 v_i + b^2 \cos^2 v_i) \right] \Delta v \tag{2.28}$$

The total braid length estimate, B_{est}, is given by

$$B_{est} = \frac{L_c}{L} \sqrt{L^2 + (2\pi RN)^2} + 2s \tag{2.29}$$

where $L_c = L - 2b'$ is the length of the central cylindrical portion. By minimizing the error ϵ_B between the estimated braid length and the known resting braid length, we numerically solve for PAM radius at a given strain:

$$\epsilon_B = |B - B_{est}(R)| \tag{2.30}$$

Due to the non-cylindrical shape of the PAM, the thickness of the bladder can only be loosely approximated by Eqn. 2.4. Instead, we use numerical integration of the curved surface to find the deformed bladder volume for a given thickness. From the assumption of an incompressible bladder, the deformed thickness is the thickness at which deformed volume is equal to resting volume. The integration is performed using two curves corresponding to the inner and outer surface of the bladder, and

completing a solid of revolution about the longitudinal z-axis:

$$V_{est} = \pi \int_0^L \left| f^2(z) - g^2(z) \right| dz \tag{2.31}$$

where $f(z)$ and $g(z)$ are piecewise-continuous functions described by:

$$f(z) = \begin{cases} c + a\sqrt{1 - (\frac{z+b'}{b})^2} & z \leq b' \\ & L \leq L_0 \\ c + a\sqrt{1 - (\frac{z-(L-b')}{b})^2} & z > L - b' \\ & L \leq L_0 \\ c + 2a' + a\sqrt{1 - (\frac{z+b'}{b})^2} & z \leq b' \\ & L > L_0 \\ c + 2a' + a\sqrt{1 - (\frac{z-(L-b')}{b})^2} & z > L - b' \\ & L > L_0 \\ R & b' < z \leq L - b' \\ & L \in \mathbb{R} \end{cases} \tag{2.32}$$

$$g(z) = f(z) - t \tag{2.33}$$

The error ϵ_V between the resting volume and the deformed volume must be zero at the exact deformed thickness. The error is given by:

$$\epsilon_V = |V - V_{est}(t)| \tag{2.34}$$

Typical cross-sections of the bladder with calculated thicknesses are shown in

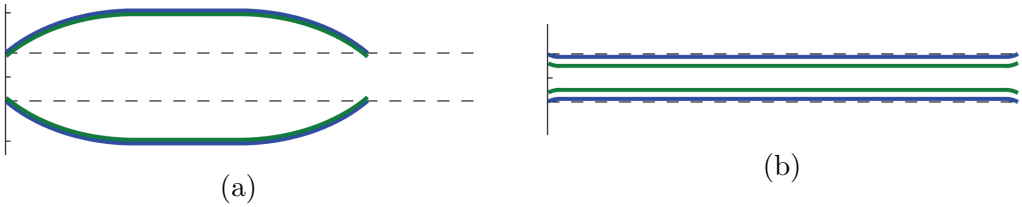
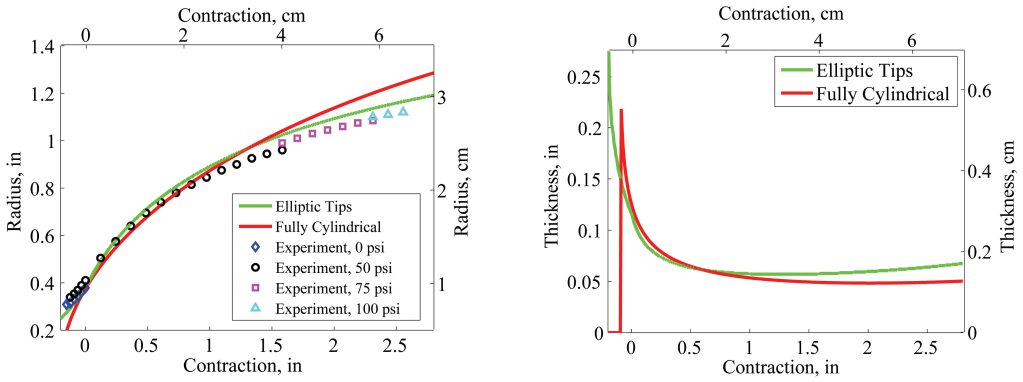


Figure 2.7: Cross-section showing estimated bladder thickness during (a) contraction and (b) extension; 1.9 cm (0.75-in) diameter, 18.5 cm (7.3-in) length PAM with a 76.5 deg braid angle.

Figure 2.7, with the dashed black lines denoting the outer diameter at rest.

Using this procedure, the radius was calculated as a function of contraction, shown in Figure 2.8(a). This new model is compared with radius estimates from the fully cylindrical model and experimental data. To obtain experimental radius measurements, the sample PAM was displaced (extended past resting length and contracted) by a load frame and radius was measured along the central cylindrical portion with calipers. The experimental data matches with the elliptic ends model more accurately than the fully cylindrical model in both extension and contraction. In extension, the central radius of the PAM under the elliptic tip model remains above 0.76 cm (0.3 in). This allows the bladder thicken, as shown in Figure 2.8(b), without being physically restricted by the braid. On the other hand, the fully cylindrical PAM model predicts that PAM radius collapses so quickly that at around 0.1 in of extension past resting length, there is not enough space for the bladder to fit inside.

It is important to note that the bladder radius and thickness measurements are dependent on the ellipse axis ratio k, which defines the eccentricity of the ellipse. The most accurate results are produced when k is not simply a constant, but a function of actuator strain. The optimal relationship was determined empirically,



(a) (b)

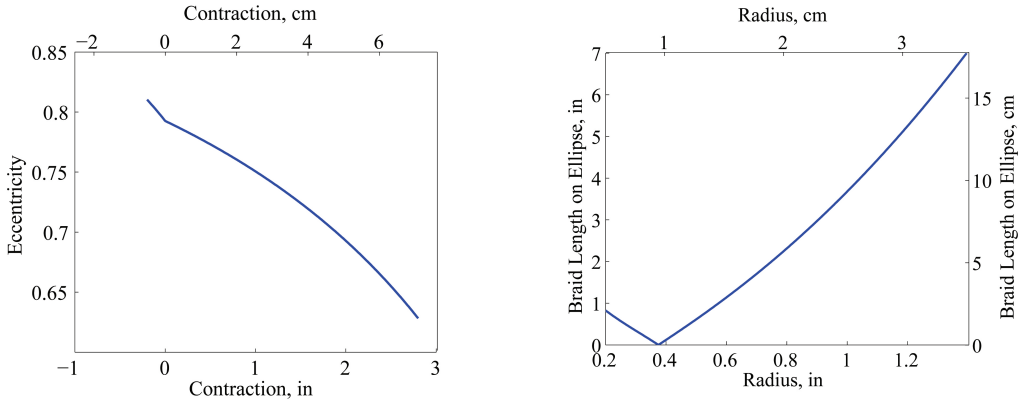
Figure 2.8: Comparison of cylindrical and elliptic tip models (a) radius vs. contraction and (b) thickness vs. contraction; 1.9 cm (0.75-in) diameter, 18.5 cm (7.3-in) length PAM with a 76.5 deg braid angle.

and was found to follow the piecewise linear relationship:

$$k = \begin{cases} 1.64 - 0.13\Delta L & L \leq L_0 \\ 1.64 - 0.33\Delta L & L > L_0 \end{cases} \tag{2.35}$$

Figure 2.9(a) displays the eccentricity as a function of actuator strain for the sample PAM. Note that the decreasing eccentricity with increasing contraction is observed experimentally, with the ends becoming more hemispherical as the PAM radius expands. Figure 2.9(b) illustrates the length of the braid following the elliptic curve changing with PAM radius. The braid length on the ellipse is zero at resting radius (0.95 cm [0.375 in]) because the PAM is assumed perfectly cylindrical. The predicted braid length on the elliptic surface is higher during radius expansion than radius contraction of an equal amount because the braid traverses a larger-area inflated surface during radius expansion, as opposed to a necked down surface when the radius contracts.

Applying this new PAM geometry to the force balance model derived by



(a) (b)

Figure 2.9: Elliptic tip model parameters (a) tip eccentricity and (b) braid length along the elliptic tip; 1.9 cm (0.75-in) diameter, 18.5 cm (7.3-in) length PAM with a 76.5 deg braid angle.

Hocking and Wereley [27] produces a force vs. contraction profile that is much more accurate in both extension and contraction. Figure 2.10 shows the modeled force vs. contraction cycles for a range of pressures (0.07 to 0.8 MPa [10 to 120 psi]) compared to experimental data of the averaged force. Figure 2.11 shows the same data, but in its original, non-averaged form that contains hysteresis. The model can easily capture this hysteresis with the addition of a friction term to the total force. The friction force is given by:

$$F_F = -c_F F \tag{2.36}$$

where c_F is a friction coefficient determined empirically as in Hocking and Wereley [27]. The friction coefficient is a function of pressure, where for this example PAM $c_F = 0.16 - 0.145P$, P in MPa. It should be noted that other approaches for modeling such hysteresis, based on viscoelastic mechanisms such as the Maxwell-slip model [118], also add similar friction or slip terms to the analysis.

2.2.6 Linear Relationship between Hyperelastic Constants and Pressure

The practicality of this analytical model is important. While pure interpolation of results can lead to fairly good estimates when there is enough data available, a great deal of characterization data and computational power is required. Even after accounting for non-constant bladder thickness and complex PAM geometry, the current force balance model is not suitable for interpolation without exhaustive characterization data at small increments of pressure and contraction because the relationship between elastic moduli E_k and pressure can be nonlinear. However, if the optimization procedure is modified to guarantee a linear relationship between the elastic moduli and pressure, smooth transitions between experimental pressure values could be found, and interpolation would require less experimental data. Observation of previous data (Figure 2.4) illustrates that a linear fit between the E_k constants and pressure is nearly optimal at higher pressures. In the low pressure range, the linear constraint will no longer produce optimal results; however, as the next section illustrates, results were found to retain most of their accuracy.

A modified optimization procedure was adopted in order to achieve a linear relationship between the elastic moduli and pressure. Instead of directly optimizing E_k values for each pressure level and subsequently choosing a linear fit, a new set of parameters were employed to optimize for all pressure levels simultaneously. The parameters were the $2M$ constants m_k and b_k, which correspond to the slope and y-intercept of the $E_k = m_k P + b_k$ functions of an Mth-order polynomial. The

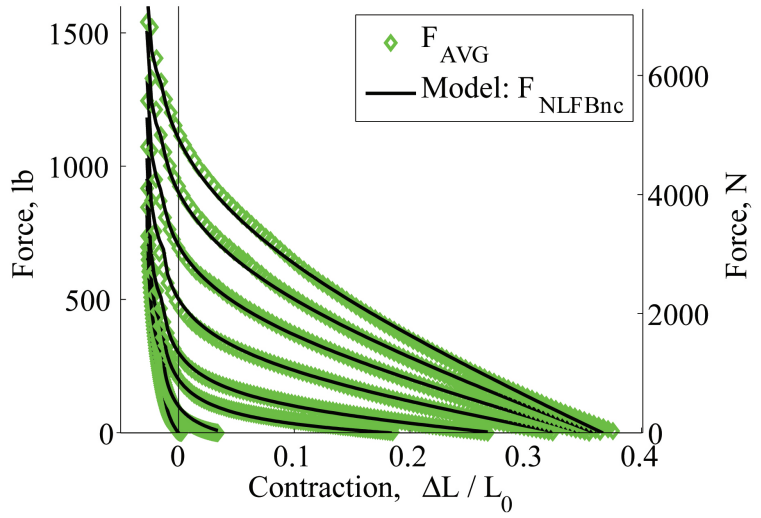


Figure 2.10: Force vs. contraction, nonlinear force balance model with non-constant thickness and elliptic tip geometry; 1.9 cm (0.75-in) diameter, 18.5 cm (7.3-in) length PAM with a 76.5 deg braid angle.

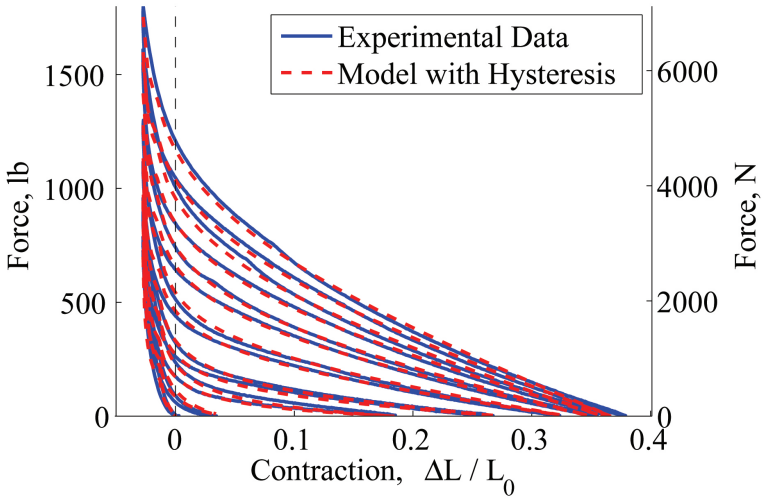


Figure 2.11: Force vs. contraction with hysteresis estimates, nonlinear force balance model with non-constant thickness and elliptic tip geometry; 1.9 cm (0.75-in) diameter, 18.5 cm (7.3-in) length PAM with a 76.5 deg braid angle.

constants were varied using the *fmincon* optimization function in MATLAB until the mean squared error was minimized for the entire set of experimental data.

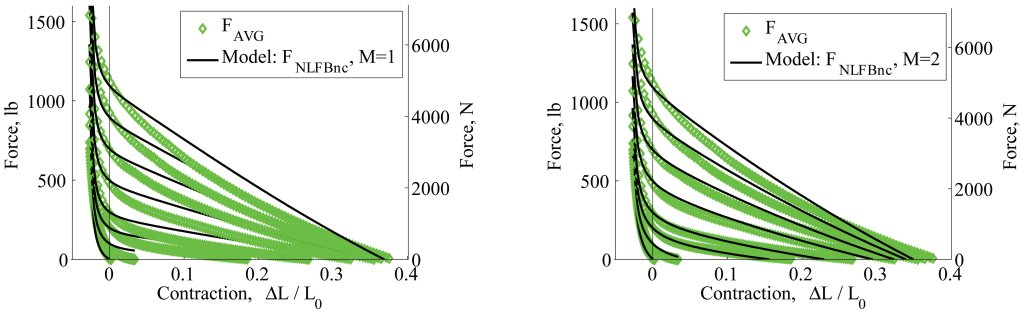
2.3 Results and Analysis

Employing each of the improvements from the previous section, Model predictions of force vs. contraction using stress-strain relationships from first-order to fourth-order are shown in Figure 2.12. The model is shown to accurately capture all the extension behavior, while the predictive ability becomes increasingly more accurate as the order of the stress-strain polynomial is increased. Figure 2.13 more clearly illustrates the model error for each experimentally-tested pressure level. The normalized mean squared error $\epsilon_{F,norm}$ is given by:

$$\epsilon_{F,norm}(P) = \frac{\sqrt{\frac{1}{n}\sum_{i=1}^{n} F_{a,i}(P) - F_{m,i}(P)}}{F_{-2.75\%}(P)} \tag{2.37}$$

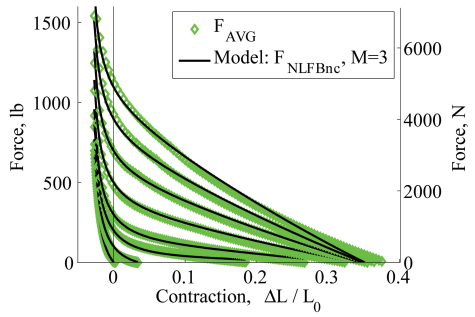
where n=100 is the number of data points for each pressure level, $F_{a,i}(P)$ is the averaged experimental force, $F_{m,i}(P)$ is the model-predicted force, and $F_{a,-2.75\%}(P)$ is the experimental force at 2.75 % extension, i.e. the maximum force obtained, for each pressure level. In nearly all cases, increasing polynomial order decreases error. Furthermore, the fourth-order polynomial error is the lowest for each tested pressure except 30 psi. Also notable is that the first- and second-order functions exhibit higher error at high pressures, while the fourth-order model exhibits higher model error at low pressures. Clearly, a fourth-order polynomial is much better at capturing PAM force-contraction behavior at high pressure.

Figure 2.14 displays the empirically-determined modulus values, E_k, as a function of pressure. The E_1 term has a fairly consistent slope and y-intercept in

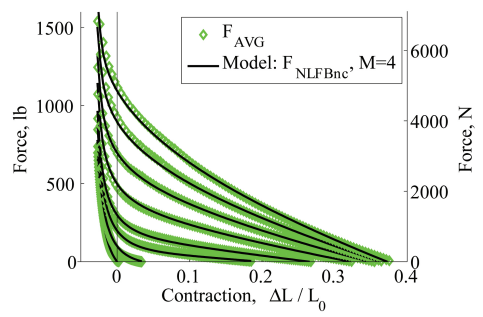


(a) $M = 1$

(b) $M = 2$



(c) $M = 3$



(d) $M = 4$

Figure 2.12: Modulus values optimized to vary linearly with pressure using nonlinear force balance model with non-constant thickness, (a) first-order, (b) second-order, (c) third-order, and (d) fourth-order polynomial model for strain; 1.9 cm (0.75-in) diameter, 18.5 cm (7.3-in) length PAM with a 76.5 deg braid angle.

each of the plots, indicating the fundamental actuator characteristics are captured with a linear stress-strain relationship. In fact, uniaxial tests of the bladder alone indicated a linear stress-strain relationship at strains up to 200%. However, the higher-order terms play an important role in accurately modeling high pressure and biaxial high strain behavior. The improvement in force prediction gained by increasing the order of the polynomial suggests there are complex bladder-braid interactions being lumped into the bladder stress-strain relationship. These interactions are separate from those that cause the hysteretic behavior displayed in Figure 2.11 and warrant future investigation.

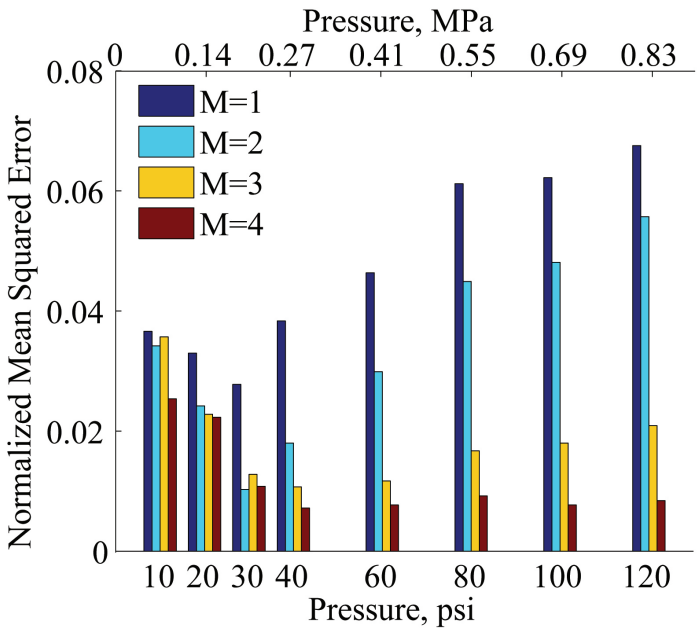
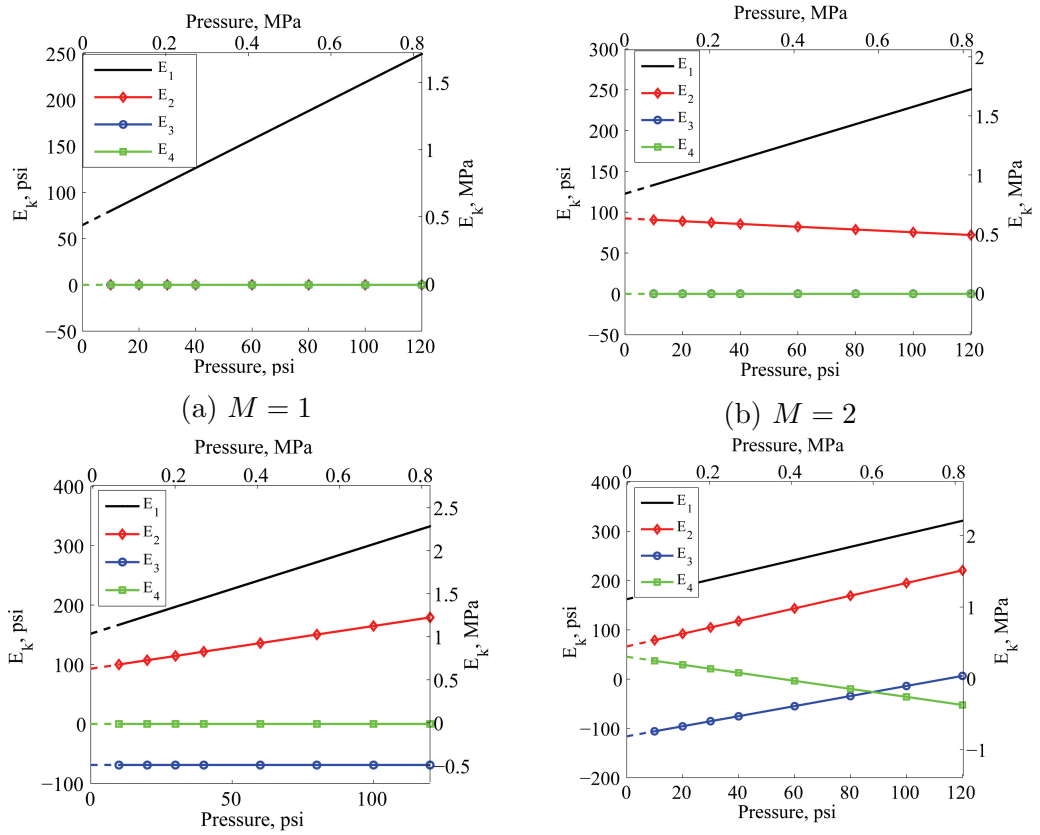


Figure 2.13: Normalized mean squared error of model force predictions for Mth-order polynomial strain models; 1.9 cm (0.75-in) diameter, 18.5 cm (7.3-in) length PAM with a 76.5 deg braid angle.

Figure 2.15 illustrates the stress-strain curves produced by the fourth-order polynomial fitting of the example actuator at multiple pressure levels, showing that increasing pressure increases the slope of the curve for low strains ($\varepsilon < 2$). The intrinsic properties of the bladder material do not change in the presence of pressure; however, this increased pressure, which increases contact force with the braid, may cause the bladder to form a high-friction quasi-bond with the braid, stiffening the actuator and resisting bladder expansion until high contraction is reached. Then, when the PAM actuator is undergoing very large circumferential strains ($\varepsilon \geq 2$), a softening in the bladder material is observed, including a negative stiffness at high pressure. Modeling this softening effect requires higher order E_k terms to correctly match force-contraction data. This phenomenon is not expected in a hyperelastic material, because while hyperelastic models often display a temporary



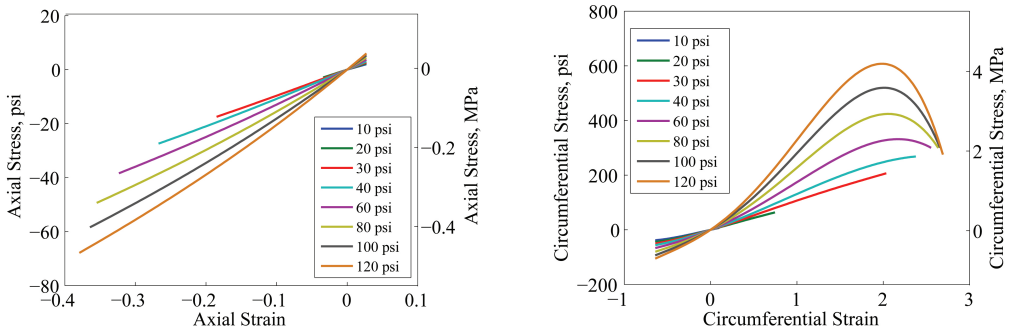
(a) $M = 1$ (b) $M = 2$

(c) $M = 3$ (d) $M = 4$

Figure 2.14: Force vs. contraction, nonlinear force balance with non-constant thickness, (a) first-order, (b) second-order, (c) third-order, and (d) fourth-order polynomial model for strain; 1.9 cm (0.75-in) diameter, 18.5 cm (7.3-in) length PAM with a 76.5 deg braid angle.

plateau in stress levels, no known models predict stress decreasing with increasing strain. Therefore it is likely that this effect is caused by the braid interacting with the bladder. Further study is required to gain a better physical understanding of this phenomenon.

Lastly, the improved model (including non-constant thickness, modified PAM geometry, and a linear relationship between elastic moduli and pressure) can be shown to accurately predict force vs. contraction curves at a wide range of pressures using data at only a few pressure levels, thereby substantially reducing the experi-



(a) (b)

Figure 2.15: Stress-strain relationship in the (a) axial and (b) circumferential directions, as determined by polynomial fitting; 1.9 cm (0.75-in) diameter, 18.5 cm (7.3-in) length PAM with a 76.5 deg braid angle.

mental time required to parameterize an accurate model. Figure 2.16 illustrates this predictive ability. The linearly-varying E_k values were calculated using experimental data at 0.14, 0.41, and 0.83 MPa (20, 60, and 120 psi), shown in black. The model was then interpolated to other pressures (0.07, 0.2, 0.28, 0.55, and 0.69 MPa [10, 30, 40, 80, and 100 psi]), shown in red. As the figure illustrates, the force is still predicted extremely well for all pressures. Figure 2.17 compares the normalized mean squared error, as calculated in Eqn. 2.37, for the model based on a linear $E_k(P)$ function from the full set of force-contraction data against the model based on a linear $E_k(P)$ function from the reduced set. By reducing the set of experimental pressures used in the fit, error only increases significantly at 0.07 MPa (10 psi) (likely because the curve was extrapolated rather than interpolated) and shows little change at the other tested pressure levels. This data suggests that the model can be used in a predictive manner once a PAM has been initially characterized.

2.4 Conclusion

An improved model of pneumatic artificial muscle behavior was developed for antagonistic actuation schemes. Several refinements were applied to the force balance model in order to capture nonlinear PAM force behavior in contraction and extension. The new model combines the effect of non-constant bladder thickness with a hyperelastic bladder stress-strain relationship. A detailed geometric representation of PAM shape incorporating elliptic deformation at the ends was developed to improve model force predictions, particularly for PAM extension. Lastly, the polynomial coefficients of the stress-strain relationship were constrained to vary linearly with pressure, augmenting the ability to predict behavior at untested pressure levels while preserving high model accuracy.

Analysis of the optimized PAM modulus terms suggests a stiffening effect as pressure increases; however, the effect begins to weaken at around 200% circumferential strain, where a softening effect takes hold. While the original force balance model accounts for the shape of the braid and energy storage in the bladder, it does not attempt to model complex bladder-braid interactions (besides hysteresis effects). Therefore, the nonlinear phenomena in the actuator stress-strain relationship are likely attributable to these unmodeled interactions. Further studies must be undertaken to better understand these effects and to pursue additional modeling improvements.

Given that this improved model demonstrates high accuracy in quasi-static experiments, it can be reliably employed into a model-based control strategy in

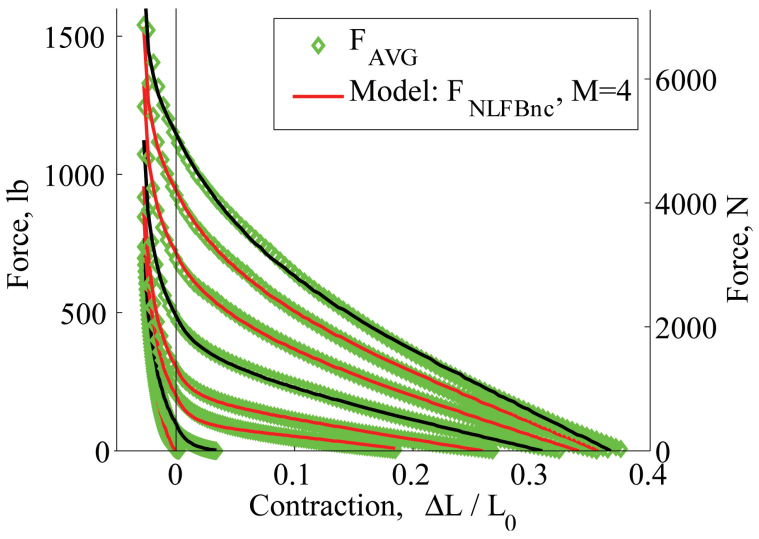


Figure 2.16: Experiment vs. model using fourth-order polynomial model for strain and $E_k(P)$ interpolated from data of three experimental pressure levels ; 1.9 cm (0.75-in) diameter, 18.5 cm (7.3-in) length PAM with a 76.5 deg braid angle.

PAM-based applications. While high frequency, demanding applications may include unmodeled dynamics that were not captured by this model, such as nonlinear airflow dynamics and damping behavior at high velocity, the model can be augmented with additional terms, or the control strategy can incorporate closed-loop feedback.

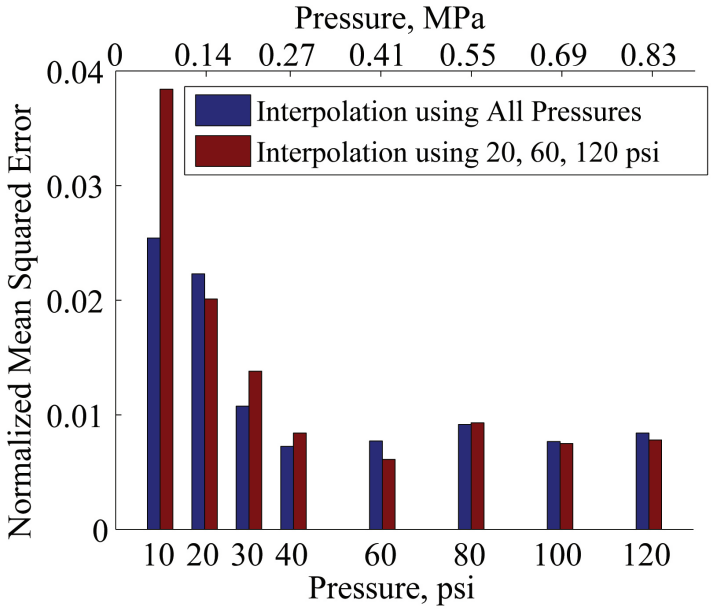


Figure 2.17: Normalized mean squared error of model predictions, comparing $E_k(P)$ interpolated from data of all eight experimental pressure levels vs. only three experimental pressure levels (0.14, 0.41, and 0.83 MPa [20, 60, and 120 psi]); 1.9 cm (0.75-in) diameter, 18.5 cm (7.3-in) length PAM with a 76.5 deg braid angle.

Chapter 3: Structural Design of PAM-Based Robotic Manipulators

3.1 Introduction

Pneumatic artificial muscles (PAMs) are compliant actuators featuring an elastomeric bladder surrounded by a braided sleeve. Applying pressure inside the soft bladder (i.e., inflation) increases the diameter and decreases the length of the actuator through reorientation of the stiff braid fibers, generating a contractile stroke and pulling force similar to human muscle. Also known as McKibben actuators, these were initially developed as orthotic devices for polio patients [23].

PAMs have several advantages over other forms of conventional actuation technology. For example, they are extremely lightweight (10s of grams) and simple, as they are only composed of a thin bladder, braid fibers, and small lightweight end fittings. Accordingly, they are highly scalable to various physical sizes and force-stroke requirements with a host of inexpensive, commercially available materials. Additionally, PAMs can achieve much higher power-to-weight ratios than electrical and hydraulic actuators [155]. They are capable of producing high forces at high speed [162]. No gears are necessary, thus there is no inertia or backlash added to the system. Other benefits of these devices include durability, reliability [2], operation without precise mechanical alignment, and high force capability at comparably low

operational pressures (0 to 1.4 MPa [0 to 200 psi]). Operating with air also enables use of an open fluid circuit, where return air is vented to the atmosphere and a small compressor may be employed to extract air from the outside environment to replenish the air lost.

As a result of their functional similarity to natural muscles, there have been numerous studies that focused on applicability to robotic systems, including manipulation and joint control of robotic arms [40, 157, 160] and legs [69, 132], or human assistance and rehabilitative devices [75, 80, 152]. PAMs are especially suitable for use in robots intended to physically interact with human subjects because their inherent compliance increases safety.

The development of PAM-actuated systems required mathematical models to help characterize PAM behavior. In 1958, Gaylord derived a simplified model which considers only the geometric parameters of the actuator and assumes that the actuator retains a cylindrical shape. More recently, studies have introduced a nonlinear Mooney-Rivlin term to account for elastic energy storage [32], and other terms to describe tip effects resulting from the non-cylindrical shape at the ends of the actuator [33]. Other models employ a force-balance approach [34]. Due to their compliance (from gas compressibility) and nonlinear behavior, PAMs have the disadvantage of being difficult to accurately position in open-loop, but recent advancements in modeling have enabled more reliable positioning and control [35, 156].

Presently, there is significant interest in deploying robotic platforms to perform duties that could be hazardous for humans. One particular application is casualty extraction. In this case, the substitution of a robot for recovery personnel eliminates

the threat of harm to the rescuer(s). Some casualty extraction concepts employ existing military robots to tow a casualty laid on a stretcher [154]. However, in some situations, it may not be possible for the injured person to board the stretcher without additional assistance. Furthermore, dragging the casualty across rugged terrain may cause even more injury. A different approach is a robotic system that can lift and carry the casualty with minimal or no required support from the casualty. The benefits of using PAMs in this type of platform include the weight savings accrued by utilizing lightweight PAM components as opposed to conventional hydraulic actuators and systems, low pressure air (90-150 psi) as opposed to high pressure (on the order of 20 MPa [3000 psi]), no hydraulic fluid, and reduced maintenance requirements. As mentioned previously, the compliance of PAM actuators is also beneficial for interacting with humans, such as lifting and carrying them to safety. Other applications for such a robot include manipulating or moving heavy packages, explosives, and hazardous substances, and patient placement in hospitals.

The goal of the present work is to identify requirements for a lightweight, high force robotic manipulator actuated with pneumatic artificial muscles, design the system for heavy lifting capability, and assemble a prototype arm that demonstrates its abilities in a laboratory environment. Two actuation approaches are considered using different sizes and numbers of PAMs for each, and they are compared to determine the more efficient actuation scheme. A demonstrator arm is designed, fabricated, and experimentally tested. A model characterizing PAM behavior is coupled with a kinematic model for the manipulator and is validated by experimental measurements in quasi-static and dynamic tests.

3.2 Design Requirements and Simulation

3.2.1 Design Requirements

Key requirements for a high-force robotic manipulator are torque, speed, and range of motion. Many robotic arms currently used in military applications have relatively low payload capacities, though they are typically smaller robotic platforms than what is currently under consideration. An example is the Foster-Miller TALON Engineer robot, a four degree-of-freedom bomb disposal robot that can handle a maximum payload of 30 kg (65 lb) [161]. The latest version of the un-fielded Battlefield Extraction Assist Robot (BEAR) by Vecna Robotics, whose primary duty is casualty extraction, can lift over 225 kg (500 lb) using its two hydraulic arms [6]. The arm designed in the present study was intended to be a proof-of-concept demonstrator of similar lifting capabilities using PAM actuation. The manipulator prototype was chosen to have two degrees-of-freedom (elbow pitch and wrist pitch) across three links (upper arm, lower arm, hand). Elbow and wrist torque of 200 ft-lb per arm was estimated to be sufficient for two arms to lift a 95th percentile male soldier [159] wearing an additional 100 lb of gear, totaling 316 lb. The range of motion was chosen to be that of a full lifting motion, or 90 deg of rotation. The desired speed is 57 deg/s (1 rad/s), or enough to complete this lifting motion in less than 2 seconds. Design goals for both degrees-of-freedom are summarized in Table 3.1. The first two (arm) links are 13 inches long, and the hand manipulator is 7 inches long.

Table 3.1: Prototype design goals.

Torque at max pressure	Range of Motion	Angular Rate
200 ft-lb (271 Nm)	90 deg	57 deg/s

A secondary objective of the joint actuation system design was to minimize volume, as space is a valuable commodity in robotic systems, and some PAMs can inflate to more than triple their resting diameter during operation near their free contraction limit. No specific values of arm cross-sectional area were chosen, but design comparisons included minimizing volume as an important goal.

3.2.2 Actuator Development and PAM Characterization

Once the design goals were determined, PAMs of varying size were fabricated and characterized in order to compare key actuation characteristics, where the leading solution would be chosen to maximize force and speed capabilities while minimizing weight and volume. It is commonly known that larger diameter PAMs produce higher force capability than smaller diameter PAMs [35]. Likewise, design guidelines from past experimental studies indicated that braid fibers aligned closer to the longitudinal axis (high braid angle) lead to larger contraction and force [138]. Although this increased force does come at the expense of larger radial expansion, which could lead to larger volume, the first approach considered implementation of a few larger diameter PAM actuators. This is also due to fact that the heavy-lift robot arm would demand higher forces than any previously constructed by the research team or any that are available commercially. An outer diameter (OD) of

2-in was selected for this case, also having high braid angle. These PAMs were fabricated in-house with commercial braid, but a custom bladder had to be fabricated to match desired stiffness at that size. The bladder was constructed by pouring a low-viscosity addition-cure silicone rubber (Bluestar V330) into a cylindrical tube mold and allowing it to cure at room temperature. Two end fittings were integrated onto the ends of the bladder, where one had a thru-hole to allow the passage of air and the other was closed. The braided sleeve (fiberglass) was placed around the bladder and end fittings and hose clamps were used to hold the bladder and braid onto the end fittings. Epoxy was also applied to seal and strengthen the ends. Note that this hose-clamp construction method is only used on preliminary laboratory prototypes. The second approach was to consider several smaller diameter PAMs, whose combined force would be on the same order as the fewer larger diameter PAMs of the first approach. In this case, 0.625-in outer diameter PAMs were fabricated using existing in-house techniques. Much higher braid angles were briefly considered with these smaller diameter PAMs, but as studies have shown, this led to braid instability and lower fatigue life [104]. Therefore, a more moderate braid angle was selected to ensure actuator reliability.

Force vs. displacement cycles for one of the 2-in OD PAMs are shown in Figure 3.1. The behavior is nonlinear and increases with applied pressure. There is also a distinct hysteresis; higher forces are produced during axial extension than during contraction. This PAM, with a braid angle of approximately 77 deg, attained a blocked force of over 4000 lb at 90 psi. The blocked force is defined as the force generated in the actuator from the internally applied fluid pressure when the two ends

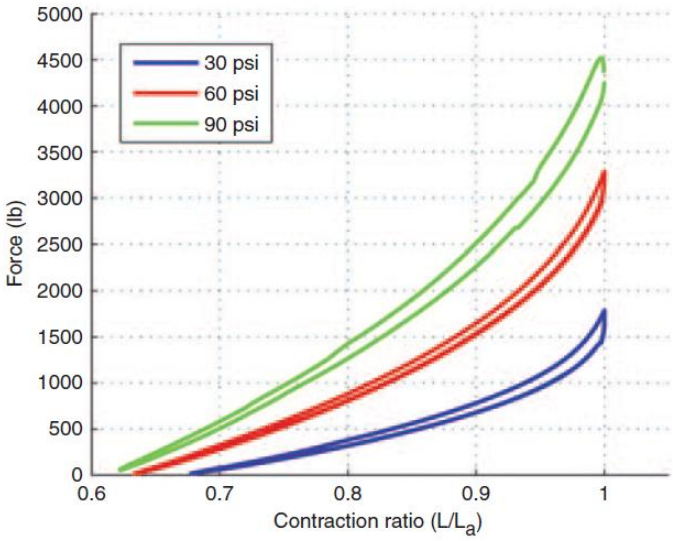


Figure 3.1: Characterization of a 2-in OD, 13-in long PAM.

are held in place at the resting length of the actuator; it is a common performance metric. As the PAM is allowed to contract, force decreases nonlinearly until reaching full contraction (where force equals zero). This point is defined as the free contraction for a given actuator and is used as another performance metric. This 2-in OD PAM contracted to 61 percent of its original resting length. Figure 3.2 shows the 2-in OD PAM in (a) its blocked condition and (b) in a contracted/inflated state.

The 0.625-in OD PAMs were inflated to a maximum of 150 psi instead of 90 psi. This was allowable because mature end fitting production technologies were available with 0.625-in OD PAMs, and previous burst tests demonstrated no catastrophic failure up to 1000 psi. To validate the robustness at 150 psi, one of these full-braid PAMs was pre-tested at 150 psi with full contraction for over 3,000 cycles, and exhibited no change in braid structure or force characteristics. The blocked force for the 0.625-in OD PAM was approximately 820 lb at 150 psi. Free contraction length was 63 percent of the resting length. These test results are shown in Figure 3.3.



(a) (b)

Figure 3.2: Testing of a 2-in OD, 13-in long PAM (a) resting, (b)contracted.

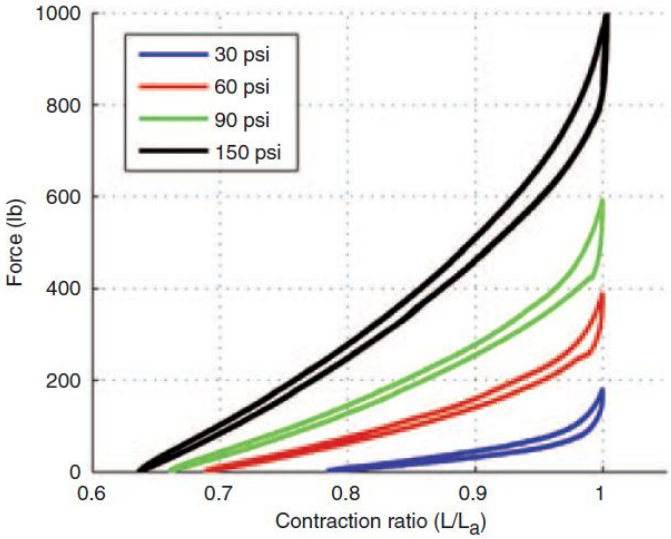


Figure 3.3: Characterization of a 0.625-in OD, 7.8-in long PAM.

3.2.3 PAM Comparison

A summary of the details for the two PAM actuator configurations considered in this study are listed in Table 3.2. This is largely due to the weight of the end fittings, which were not weight-optimized for the 2-in OD PAM. In order to meet torque requirements, it was estimated that at least six 0.625-in OD PAMs and at least two 2-in OD PAMs would be needed based on the force and contraction profiles. Six 0.625-in OD PAMs have a lower total air volume (both resting and fully inflated) than two 2-in OD PAMs, which implies a faster response time and a lower volume requirement on the compressed air source during operation. When packed in a circular arrangement around the center of the arm, six 0.625-in OD PAMs will occupy a smaller volume than two 2-in OD PAMs, leading to a more compact design. Increasing the number of PAMs also allows for more redundancy; if one PAM fails, an emergency valve could close and the other PAMs would still be able to support their proportion of the load. These factors help highlight the advantages of using multiple 0.625-in OD PAMs in the prototype device. Despite the increased complexity of using a larger number of PAMs, the benefits of increased speed, better packaging, and lower air requirements were significant enough to warrant the use of 0.625-in OD PAMs in the prototype design.

3.2.4 Robot Arm Simulation

In order to approximate the speed and response capabilities from a particular robot arm or joint, an analysis of arm kinematics was performed based on the design

Table 3.2: Comparison of different-sized PAMs.

Parameter	0.625-in OD PAM (150 psi)	2-in OD PAM (90 psi)
Braid Angle (deg)	72.5	78
Max Diameter (in)	1.75	4.5
Blocked Force (lbf)	820	4280
Mass (lbm)	0.17	2.2
Specific Blocked Force (lbf/lbm)	4280	1950

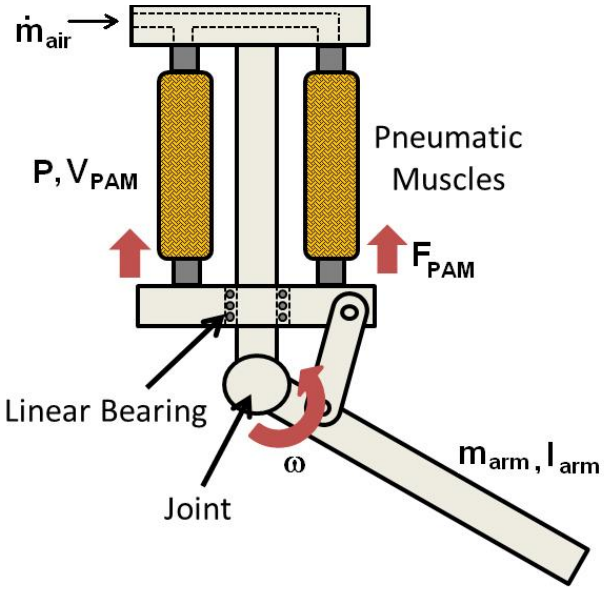


Figure 3.4: Parameters for design analysis.

shown in Figure 3.4. There are two links connected by a one degree-of-freedom joint and the angular velocity of the extended forearm is of interest, as it is rotated at the elbow joint by PAMs located in the upper arm region. The PAMs create the force responsible for accelerating the forearm link as internal pressure builds up, and this pressure increase is driven by the flow rate of air into the actuator. As pressure increases in the PAMs, they contract and produce force.

A joint was devised in which an L-shaped member rotates around a hinge and is connected to another L-shaped member by a "tendon," as illustrated in Figure

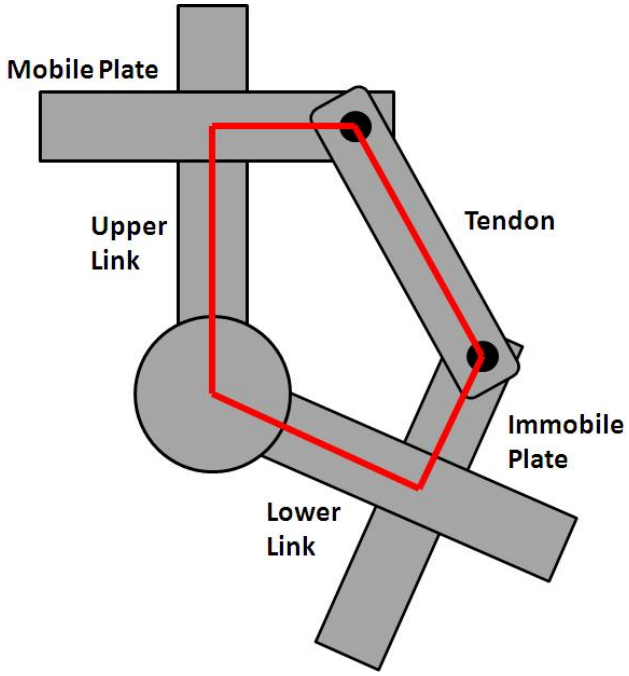


Figure 3.5: Concept for variable moment arm joint.

3.5. The member on the same side as the PAM elongates by a distance of Δl as the PAM contracts by that same amount on the other side of the mobile plate. Force is transmitted by the tendon from the mobile PAM side to the other immobile side of the joint. From this geometry, the length of the moment arm increases as PAM force decreases, which allows the joint to generate torque at a relatively constant force level over the large range of angular motion.

From Figure 3.6, the hypotenuses of the right triangles formed between each L-shaped member are given by:

$$AO = \sqrt{(l_0 + \Delta l)^2 + r_0^2} \tag{3.1}$$

$$BO = \sqrt{l_0^2 + r_0^2} \tag{3.2}$$

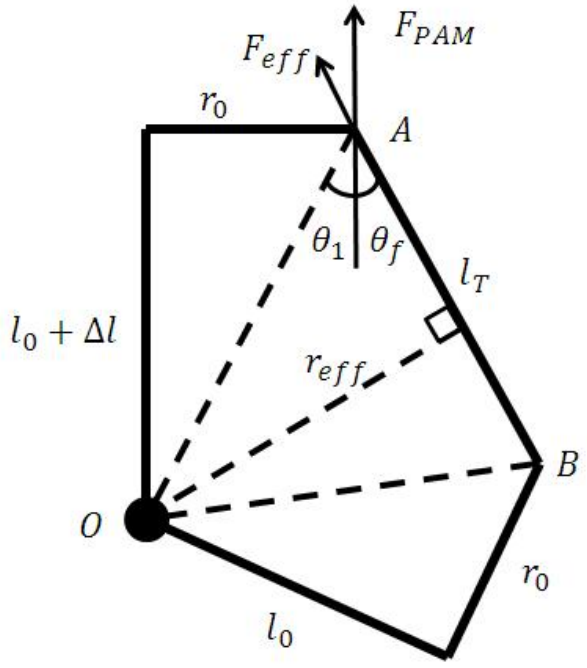


Figure 3.6: Geometry of robotic arm joint.

where it should be noted that AO changes with Δl as the PAM actuators contract and BO is constant. The angle between AO and the upper link is:

$$\theta_1 = \tan^{-1}\left(\frac{r_0}{l_0 + \Delta l}\right) \tag{3.3}$$

where l_0 is the constant length between the joint pivot and the actuator plates at rest and r_0 is the linkage offset distance on the actuator plates from the aligned arm link axis.

To determine the component of the PAM force that acts to rotate the joint, we begin by using the above quantities to solve for the angle of the AOB triangle,

which is given by:

$$\cos\left(\theta_1 + \theta_f\right) = \frac{l_T^2 + AO^2 - BO^2}{2 l_T AO} \tag{3.4}$$

From here, the angle through which the PAM force acts is computed as:

$$\theta_f = \cos^{-1}\left(\frac{l_T^2 + AO^2 - BO^2}{2 l_T AO}\right) - \theta_1 \tag{3.5}$$

which leads to the component of the PAM force that is available to rotate the joint:

$$F_{eff} = F_p \cos\theta_f \tag{3.6}$$

where F_p is the pulling force of the PAM actuators, and this force leads to the effective radius about which the force component acts

$$r_{eff} = AO \sin\theta_1 + \theta_f \tag{3.7}$$

This is then used to compute the torque in the joint:

$$\tau_{PAM} = r_{eff} F_{eff} \tag{3.8}$$

Having established these expressions, a joint torque analysis was conducted. Various geometries for each member dimension were simulated for the purpose of maximizing the range of motion between 0 and 90 deg where torque is above 200 ft-lb (the typical range of motion of the robot under consideration here). The final

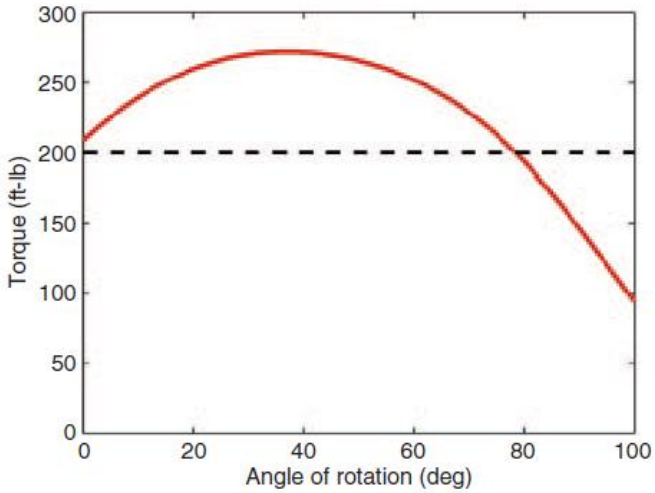


Figure 3.7: Torque output vs. angle of rotation.

lengths were chosen as $l_0 = 1.56$-in, $r_0 = 0.42$-in, and $l_T = 3.04$-in. The analysis estimated that this was achievable from 0 to 78 deg when using six 0.625-in diameter PAMs, as shown in Figure 3.7. It was decided that this torque output was adequate for the demonstrator. Using greater than six PAMs was considered, but it only modestly increased joint range of motion.

For dynamic response analysis, the volume of the PAM was assumed to be of cylindrical shape, with an increasing diameter and decreasing length as follows:

$$V_{PAM} = \frac{\pi D^2 L}{4} \tag{3.9}$$

L is the contracted length given by

$$L = \lambda L_0 \tag{3.10}$$

Table 3.3: Geometric parameters for PAM force model.

L_0 (in)	D_0 (in)	N	B (in)	θ_b (deg)
7.785	0.625	1.25	8.16	72.5

where $L0$ is the resting length, and D is the inflated diameter, given by:

$$D = \frac{\sqrt{B^2 - L^2}}{N\pi} \tag{3.11}$$

In this equation, N is the number of circumferential turns of a braid fiber around the actuator, given by:

$$N = \frac{L_0}{\pi D_0 \tan\theta_b} \tag{3.12}$$

where D_0 is the resting diameter, θ_b is braid angle, and B, the length of a single braid fiber, is given by:

$$B = \frac{L_0}{\sin\theta_b} \tag{3.13}$$

Values for the numerical parameters used in this model are listed in Table 3.3.

Note that PAM volume does not remain completely cylindrical as the PAM contracts, so the values resulting from this first analysis were conservative estimates of performance. The following equation predicts steady mass flow rate of the air

through a round orifice [163]:

$$\dot{m}_{air} = \begin{cases} AC_d P_{us}\sqrt{\frac{2}{RT}}C_1, & \frac{P_{ds}}{P_{us}} < P_{cr} \\ AC_d P_{us}\sqrt{\frac{2}{RT}}C_2, & \frac{P_{ds}}{P_{us}} \geq P_{cr} \end{cases} \tag{3.14}$$

where A is the valve orifice area, P_u and P_d are absolute pressures upstream and downstream of the valve, respectively, R is the gas constant for the medium (air), and T is the temperature upstream of the valve, though the process was assumed to be adiabatic. The term C_d is a discharge coefficient, capturing the losses in the orifice. Critical pressure is given by:

$$P_{cr} = \frac{2}{\gamma + 1}^{\frac{\gamma}{\gamma-1}} \tag{3.15}$$

where C_1 and C_2 are pressure and medium-dependent flow terms for subsonic and sonic flow, respectively:

$$\begin{aligned} C_1 &= \sqrt{\frac{\gamma}{\gamma-1}\left[\left(\frac{P_{ds}}{P_{us}}\right)^{\frac{2}{\gamma}} - \left(\frac{P_{ds}}{P_{us}}\right)^{\frac{\gamma-1}{\gamma}}\right]} \\ C_2 &= \left(\frac{2}{\gamma+1}\right)^{\frac{1}{\gamma-1}}\sqrt{\frac{\gamma}{\gamma+1}} \end{aligned} \tag{3.16}$$

Richer and Hurmuzlu [158] derive an expression for pressure change in a container of changing volume using the ideal gas law, conservation of mass, and conservation of energy:

$$\dot{P} = \frac{RT}{V_{air}}(\alpha_{in}\dot{m_{in}} - \alpha_{out}\dot{m_{out}}) - \alpha P\frac{\dot{V}_{air}}{V_{air}} \tag{3.17}$$

where V is the actuator volume, and the coefficients a, a_{in}, and a_{out} are specific heat ratios for the different processes. Pressure at any time can then be calculated by integration:

$$P(t) = \int_0^t \dot{P}(\sigma) d\sigma \tag{3.18}$$

Knowledge of the pressure inside the PAM actuator is required to determine the force. Various quasi-static models have been proposed in order to capture the force-contraction behavior of PAMs, and a comprehensive review of these models is available [35]. The model employed in the present work takes into account the Gaylord force with additonal Mooney-Rivlin correction terms to represent elastic energy storage in the elastomeric bladder. The model estimates force-contraction behavior as a function of the material properties of the component parts (Kevlar braid and latex bladder), PAM geometry, braid angle, and input pressure. As previously mentioned, the Gaylord force only considers the kinematic relationships of the braid and assumes there is no loss or energy storage:

$$F_{Gaylord} = \frac{P}{4\pi N} \left(3 \left(\lambda L_0 \right)^2 - B^2 \right) \tag{3.19}$$

When the Mooney-Rivlin term is included, the equation for the PAM force is given as:

$$F = F_{Gaylord} - F_{M-R} \tag{3.20}$$

$$F = \frac{P}{4\pi N}\left(3\left(\lambda L_0\right)^2 - B^2\right) - V_b\frac{dW}{dL} \tag{3.21}$$

where V_b is the volume of the bladder material and W is the nonlinear relationship between stress and strain based on geometric and material properties of the rubber. Angular acceleration is given by:

$$\alpha(t) = \frac{\sum_i \tau_i(t)}{I} \tag{3.22}$$

where τ_i are the torques and I is the moment of inertia. Once the angular acceleration is known, the angular velocity can be computed through integration:

$$\omega(t) = \int_0^t \frac{\sum_i \tau_i(t)}{I} dt \tag{3.23}$$

Using this speed analysis development, open-loop simulations were performed on the elbow joint for the chosen robot arm configuration. In the present case, the wrist joint was assumed to be non-rotating and elbow rotation was the only active degree-of-freedom. Figure 3.8 is a simulated time history of a pressure step response for the lower limb with a 100 lb tip payload. The limb rotated 90 deg with a maximum pressure of 150 psi. The data indicates a maximum angular velocity of 200 deg/s, and the average angular velocity in completing the motion is 60 deg/s, which meets the criterion for angular velocity greater than 57.3 deg/s (1 rad/s).

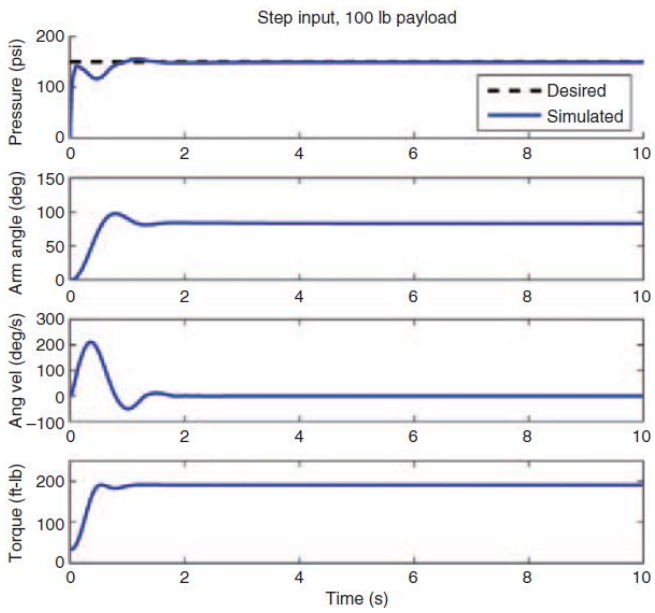


Figure 3.8: Simulation of step input, elbow joint.

3.2.5 Proof-of-Concept Manipulator Construction

Figure 3.9 depicts a computer-aided design (CAD) model of the manipulator when the wrist joint is fully extended and the elbow joint is fully contracted. Only one PAM is shown installed for each degree-of-freedom to highlight other details of the design. The prototype consists of two steel main arm links that are connected by hinge joints. Around the arm links are flat plates. The upper plate is stationary (immobile), while the lower plate is mobile due to linear bearings that make contact with the arm. PAMs are attached to each plate, so that, as the PAMs contract, the mobile plate, which is connected to the next arm link by a "tendon," pulls the link and forces it to rotate. The plates have attachment areas for up to 10 PAMs on each degree-of-freedom. Besides satisfying range of motion, velocity, and torque requirements, the manipulator should be as compact as possible and must withstand

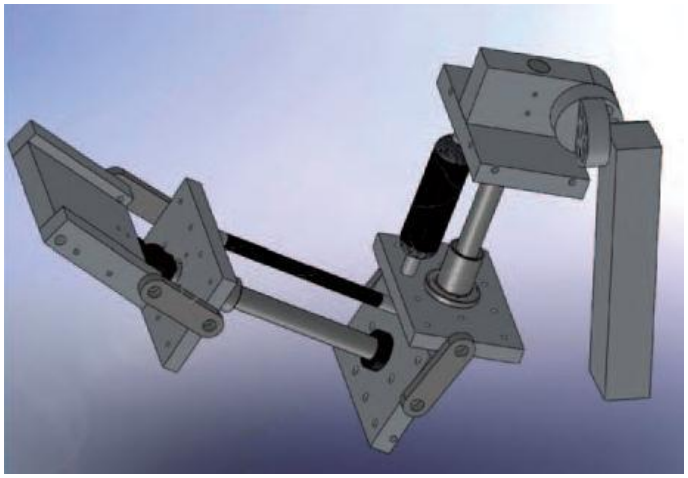


Figure 3.9: CAD model of PAM manipulator.

the stresses of lifting heavy payloads. The 0.625-in OD PAMs were packed in a tight arrangement around the steel rods, but given enough space to safely inflate to their maximum diameter (1.75-in). All of the links are sized to avoid over-stressing the joints at maximum torque with a safety factor of over 1.5. Additionally, the main arm links are sized so that the arm will not bend more than 0.5-in when extended in the horizontal direction and under a 500 lb tip payload. The hand link has a 0.5-in diameter hole at the tip through which Kevlar rope can be passed, which can connect a hanging payload to the arm for testing.

A simple, volume-efficient method for delivering air to the multiple PAMs was achieved by fabricating manifolds. A series of holes was bored through the upper stationary plates connecting each set of PAMs to the arm. All of the inlet holes except one were sealed. The manifolds allowed for only one air hose per degree-of-freedom. The shoulder was composed of two rotating plates and could be adjusted in the pitch and yaw directions. The shoulder on this prototype allows for manual adjustments in 45 deg increments, but remains stationary during arm manipulation.

3.3 Test Setup

3.3.1 Fabrication of Test Setup

A total of twelve PAMs were fabricated with six PAMs being installed around each of the two arm links in a hexagonal arrangement. The fully assembled prototype hardware is shown in Figures 3.10 and 3.11 in the deflated/extended and inflated/contracted conditions, respectively. The arm was constructed such that when fully extended, the upper arm link was hanging 0 deg from vertical, the lower arm link was directed 10 deg forward from vertical, and the hand link was directed 20 deg forward from vertical. For testing purposes, additional control and sensor components were added to the system. Angular rotation sensors (Midori, QPC series) were attached to the elbow and wrist joints to measure the rotation angle, and a pressure transducer (Omega, PX-209 series) was connected to the incoming air line to measure PAM pressure. Voltage-controlled pressure regulators (Parker, P3HP series and Festo, MPPES-3-1) were controlled separately for both degrees-of-freedom.

3.3.2 Testing and Experimental Results

Operational experiments were conducted to examine the manipulator performance

about the wrist joint only, actuating the lower arm about the elbow joint only, and actuating both links simultaneously. In these experiments, different loads were hung from the tip of the hand manipulator. The maximum payload tested was 380 lb. In

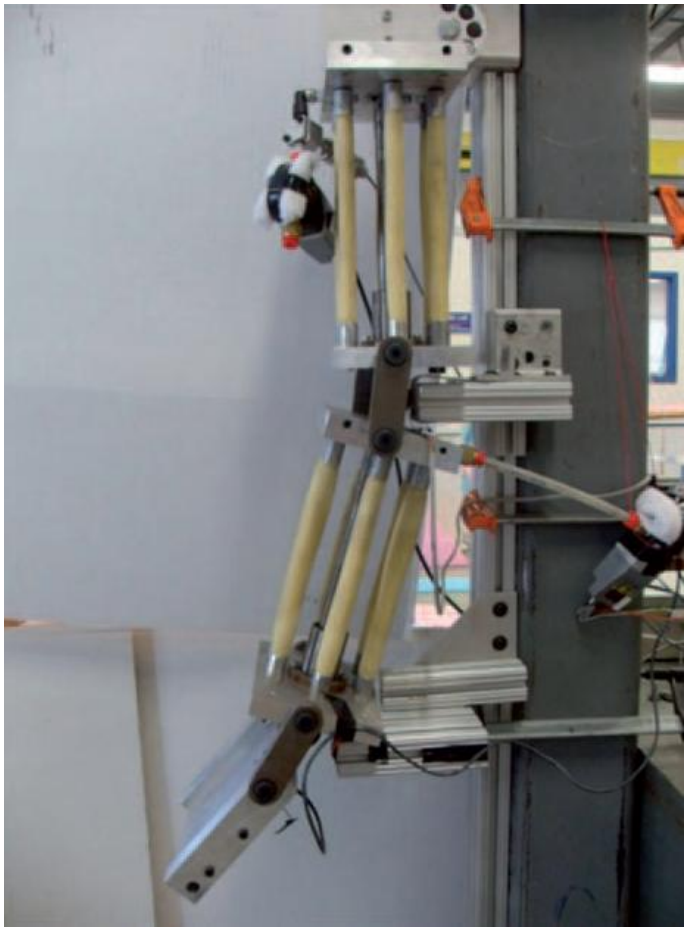


Figure 3.10: PAM arm extended during testing.



Figure 3.11: PAM arm contracted during testing.

each test, rotation data was gathered as the pressure to the PAMs was increased. At maximum pressure, the maximum rotation angle was observed. Torque was determined at this angle. With multiple tests, torque was experimentally determined over most of the range of motion for both joints. It should be noted that due to limits on the pressure regulators and air tubing used in the test setup, the maximum pressure available in quasi-static experiments was 150 psi and the maximum torque was limited accordingly.

Figure 3.12 shows measured time histories for PAM pressure and joint rotation angle with a tip payload of 135 lb. The pressure was controlled open-loop by a triangular wave function of 0.05 Hz input to the corresponding pressure regulator. As pressure increases to approximately 150 psi, joint rotation increases as well. Note that the figure shows data collected from actuating the elbow joint only. The rate of rotation increases significantly once the bladder begins to expand radially (as the pressure overcomes its elastomeric stiffness) and decreases to zero as the PAM reaches maximum contraction. Due to hysteresis present in the PAM force-contraction behavior, it can also be noticed that the rotation between the two sides of the triangular wave is slightly asymmetrical.

Figure 3.13 shows the torque generated as a function of the time-varying pressure in the elbow joint. Static torque in the joint was calculated by

$$\tau = F_{payload} r_{payload} \sin\phi \tag{3.24}$$

where ϕ is the angle between the arm link direction and the gravity vector, $F_{payload}$

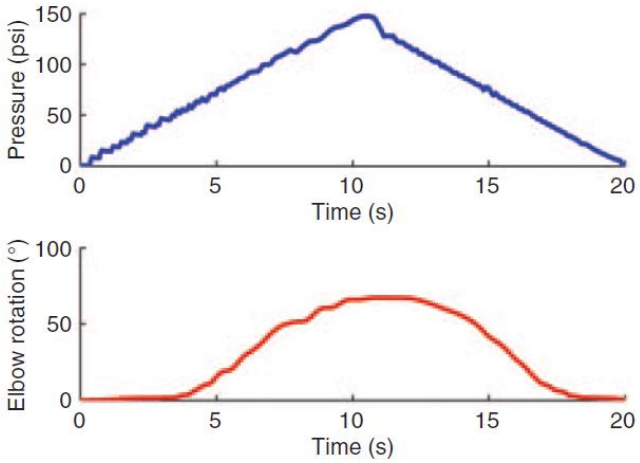


Figure 3.12: Elbow PAM pressure and rotation vs. time.

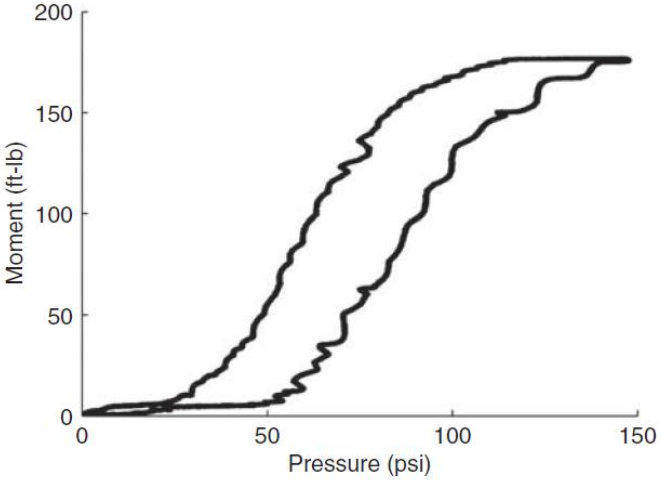


Figure 3.13: Elbow joint torque vs. pressure.

is the force exerted on the hand link due to the payload mass, and $r_{payload}$ is the moment arm extending from the joint center to the point of payload attachment. The figure shows that the available torque increases with pressure. As expected, there is also hysteresis between the contraction and extension portions of this curve.

3.4 Analysis

The accuracy of the system model relies heavily on its ability to predict Pneumatic Artificial Muscle behavior. Thus, experimental results from PAM characterization were compared with the actuator model. Figure 3.14 depicts the experimental and model-predicted PAM force at various pressures. The force-contraction profile of the model at 150 psi matched with the lower (contractile) part of the curve. However, the model of PAM force at lower pressures (30, 60, 90 psi) followed or slightly over-predicted the upper (extensile) part of the curve. This model does not account for hysteresis in the experimental data, which exists because of increased braid and bladder friction during the extension/reducing diameter phase of the test, as well as reduced resistance in the bladder. A PAM undergoing inflation has more elastic energy stored than a PAM undergoing deflation, a characteristic not accounted for in the Mooney-Rivlin term, which predicts force only for inflation/contractile motion. Therefore, the model is more accurate at 150 psi than at lower pressures. If future applications for this manipulator demand higher accuracy at low pressure, corrections to the model should be considered.

As validation of the kinematic model for the robot arm, the maximum torque

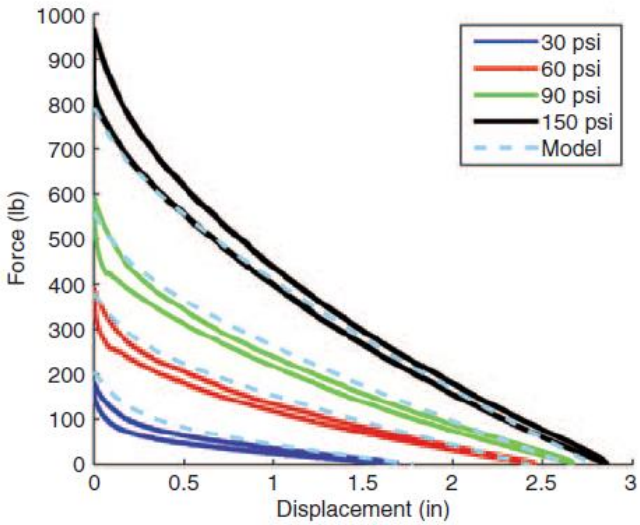


Figure 3.14: Experimental and predicted force vs. displacement.

output from the experiments was compared to model predictions. As shown in Figure 3.15, the experimentally measured values for torque in both the elbow and wrist joints are well-predicted by the model. Note also that the difference between the torque curves for the elbow and wrist joints arises from the resting angle in relation to the vertical direction.

Experiments were also performed to validate the dynamics of the system model. These tests consisted of a 4 s ramp input followed by a 6 s hold of maximum pressure. Figure 3.16 shows the model-predicted and experimental results using a 100 lb payload. In the first graph, "desired" pressure is the ramp/hold signal sent to the pressure regulators in both simulated and experimental tests. PAM pressure vs. time in the experiment matches well with the simulation. Pressure did not reach the desired 150 psi because of the limitations of the pressure regulators in dynamic tests (145 psi maximum).

The system attained a maximum torque of 190 ft-lb at 83 deg of rotation,

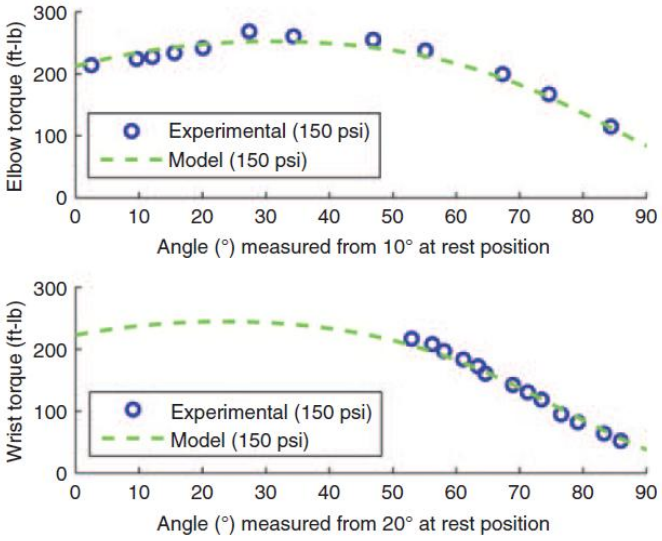


Figure 3.15: Experimental and predicted static torque vs. angle of rotation.

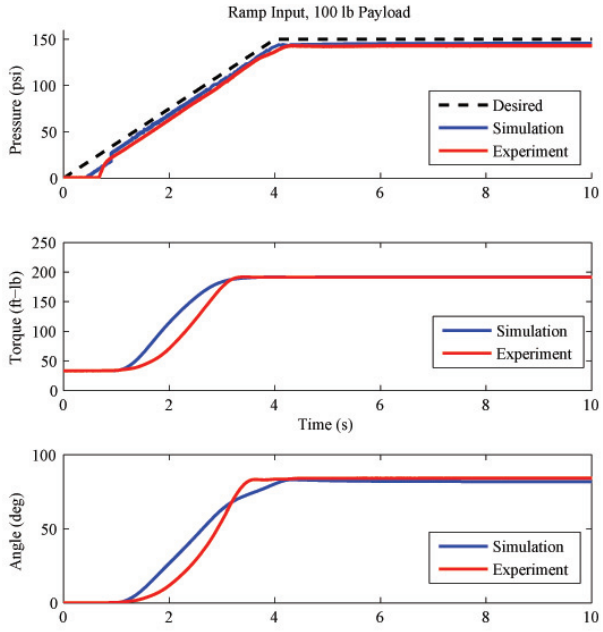


Figure 3.16: Dynamics of upper arm contraction.

which was in agreement with the model. However, experimental data showed a more gradual increase to the maximum torque than was predicted because the actuator model does not predict force as accurately at lower pressures. The discrepancy in the torque curves led to a similar discrepancy in angular rotation curves. An undesired characteristic of the experiment is the significant delay (0.5 - 1 s) before the PAM pressure rises above zero, causing the arm to remain stationary. This is caused by the deadband in the regulator, blocking the passage of air until a voltage threshold (corresponding to about 10 psi) is reached. This is an undesired characteristic of the regulator that will lead to replacement in future revisions and more precise control studies.

3.5 Optimization of Joint Geometry via Genetic Algorithms

3.5.1 Optimization Problem

The manipulator joint design on the first-generation proof-of-concept robot arm presented above (Section 3.2.4) was the product of human trial-and-error, and only two independent joint parameters were varied to determine a satisfactory torque profile at maximum pressure. However, for the development of a second-generation robot arm with greater lifting capability (Figure 3.17), joint parameters were determined using constrained multi-variable optimization. Design requirements and pre-determined PAM characteristics (limited by volume requirements and commercially-available materials) are listed in Table 3.4.

In the two-dimensional tendon-link arrangement described previously, there

Table 3.4: Joint design requirements and PAM characteristics.

Joint	Shoulder	Elbow
Torque (ft-lb)	788	362
Min Angle (deg)	15	10
Max Angle (deg)	120	80
Number of PAMs	6	8
PAM Diameter (in)	1	0.75

are four geometric parameters available for variation, as shown in Figure 3.18: These are the length along the upper limb axis l_u, perpendicular offset from the upper limb axis r_u, length along the lower limb axis l_l, and perpendicular offset from the lower limb axis r_u. It should be noted that when the initial arm angle is known (as is the case in this study), the length of the tendon link l_T is not an independent variable in the joint design, but its length does change as the other parameters vary. Due to the complex joint geometry, an analytical solution was not feasible.

A detailed optimization procedure was devised to ensure that the selected configuration could satisfy torque requirements over the full range of motion without excess pressure. In each individual optimization step, the goal was to minimize the area of the region(s) in a torque vs. angle profile where predicted joint torque falls below a desired torque threshold. An example of this type of region is shown in Figure 3.19. The objective function J was a weighted sum of this area below the curve A_b, the area above the curve A_t (weighted very low, used simply to help guide the optimization), and a penalty function PF to heavily penalize configurations which cannot rotate the full range of motion within 15% of PAM stroke (otherwise

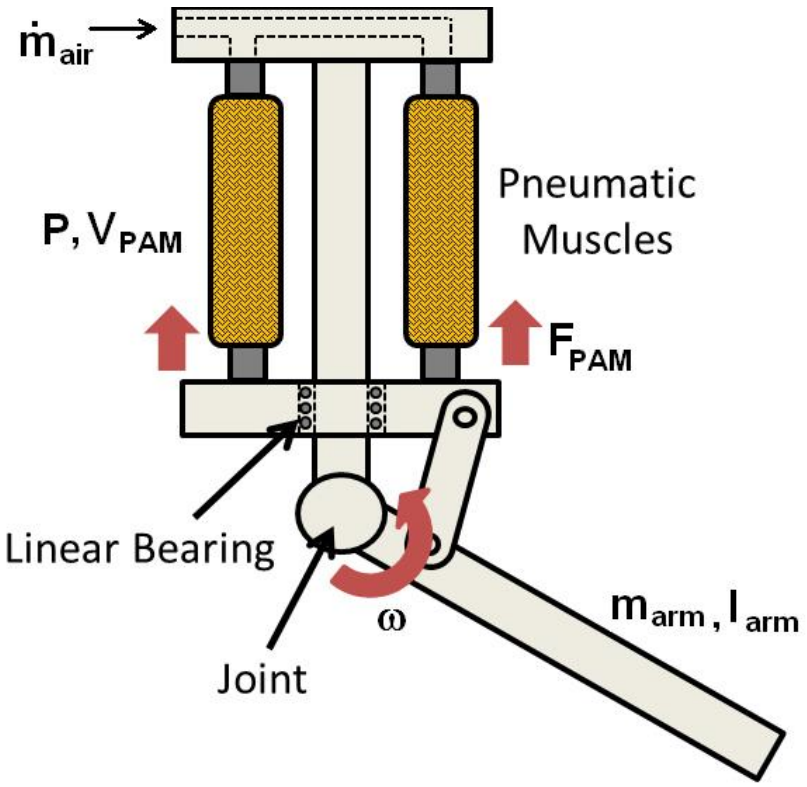


Figure 3.17: Second-generation, two degree-of-freedom manipulator.

PAM inflation would be prohibitively high). The function is given by:

$$J = A_b + 0.01A_t + PF \tag{3.25}$$

$$PF = \begin{cases} 0, & \theta_{max,a} \geq \theta_{max} \\ 10000, & otherwise \end{cases} \tag{3.26}$$

where $\theta_{max,a}$ is the maximum available angle and θ_{max} is the maximum required angle. PAM size, PAM number, and pressure level were held constant (though manual effort was made to minimize the size and number of PAMs needed prior to initiating this procedure). Constraints were placed on the design variables in order to ensure

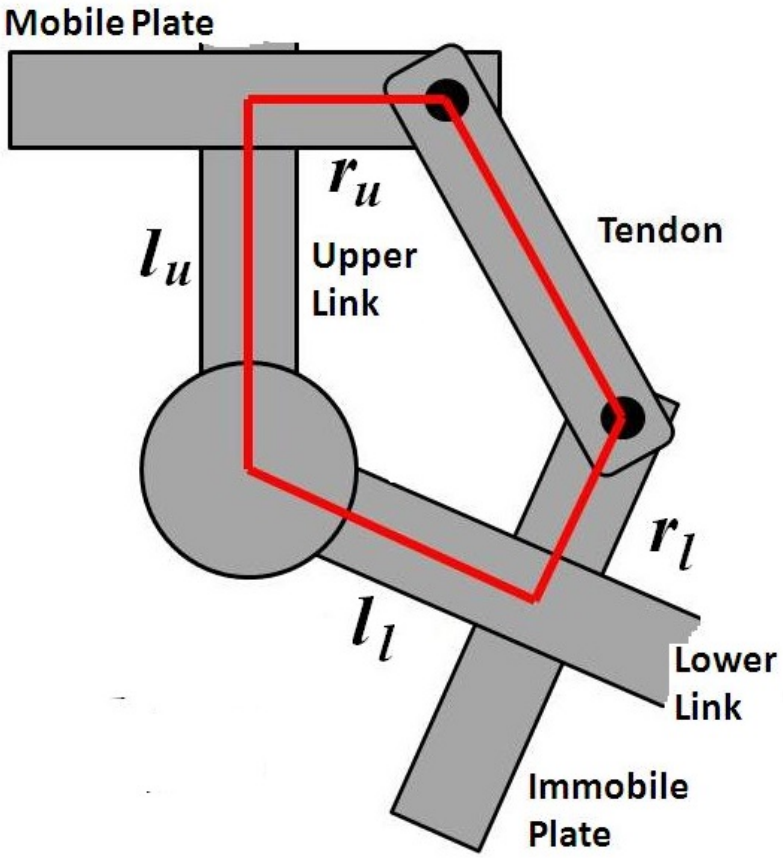


Figure 3.18: Joint parameters for optimization.

sufficient space for PAMs and to accommodate physical limits to the proximity of each joint (parts were sized to withstand the expected stresses).

A genetic algorithm was selected to perform a heuristic search for the optimal joint dimensions. Genetic algorithms emulate the process of natural evolution. The general principle is selection of the "fittest" designs, and "mating" these designs so that the next generation inherits the desirable characteristics of the former generation. Mutation, the random changing of one gene (variable), prevents the algorithm from remaining stuck at local minima. As a result, this structured process of learning by trial-and-error is very robust. While achieving a global minimum is not necessarily guaranteed with this approach, it is more probable than other standard optimization routines. The MATLAB function "*ga()*" was employed to perform this optimization.

To begin the design process, an initial population of 20 designs (sets of the variables l_u, r_u, l_l, and r_u) was selected at random, though the randomness was limited to parameter values that fell within preset upper and lower bounds. Based on the objective of meeting the required torque over the range of motion (with minimal pressure and within volume constraints), a score was given to each of the initial random starting points. The two sets of design parameters from the initial 20 with the lowest scores were selected and converted to a binary "gene" form. Then these sets were "mated" by cutting the genes at a random point and trading parts of one design with parts of another to form a new design. This was done 18 times to create a new population. This new population of 18, along with the 2 best designs from the previous generation, then formed a new generation of 20 designs. This evolution process was set to be repeated for either 100 generations or until the system

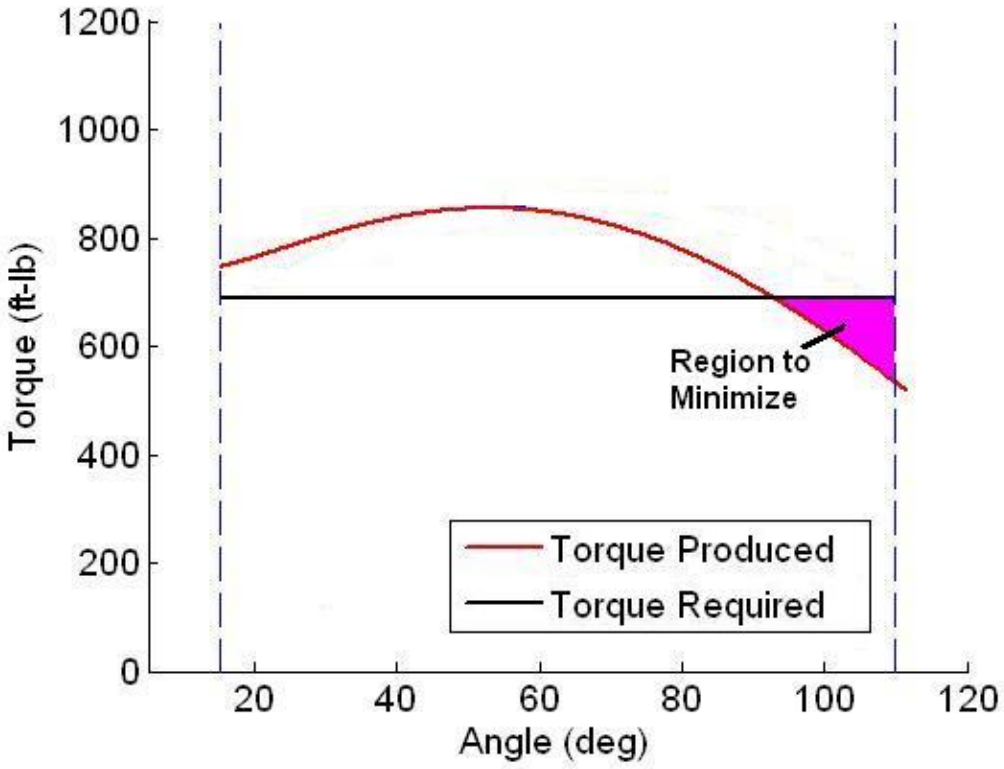


Figure 3.19: Torque vs. range of motion, illustrating regions to be minimized.

converged to within established error tolerance bounds.

After each optimization, the area under the torque threshold was evaluated. PAM pressure was adjusted and the optimization was repeated until the area under the curve was essentially zero; therefore, the design corresponded to the minimum pressure necessary to meet torque requirements.

3.5.2 Optimization Results

Results demonstrated convergence to joint configurations that met optimization goals when pressure levels were sufficient. Figure 3.20 illustrates the gradual improvement in minimizing the objective function as generation number increases and

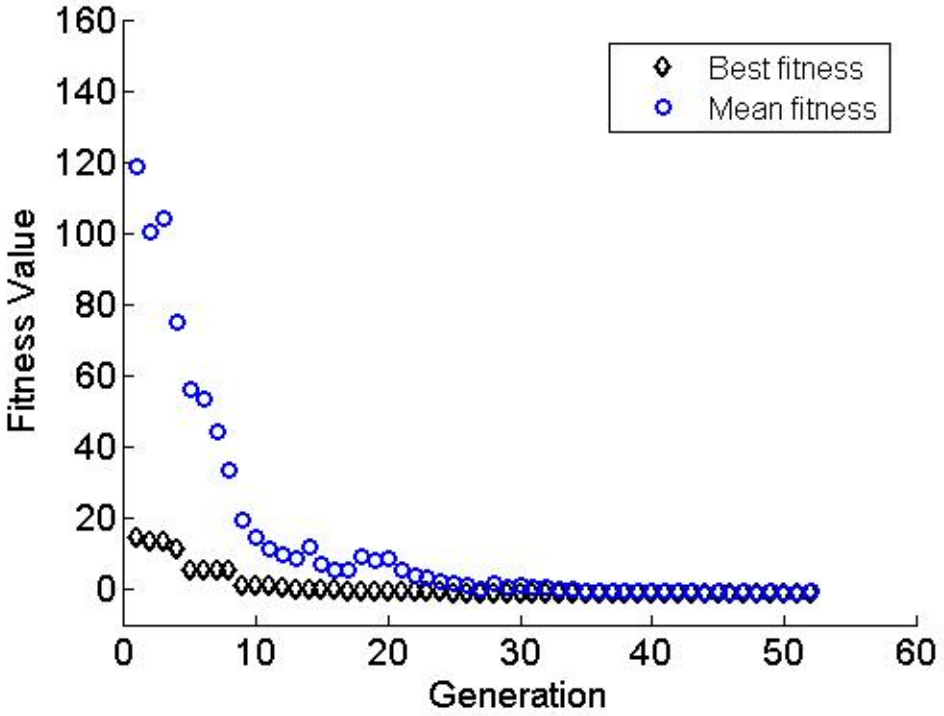


Figure 3.20: Fitness value vs. generation, genetic algorithm-based optimization.

eventual convergence to an optimal solution. Figure 3.21 shows a typical optimization history for the shoulder joint of the PAM-based manipulator. The desired joint torque was 788 ft-lb between an initial angle of 15 deg and a final angle of 120 deg. Figure 3.22 illustrates the difference between initial and final torque curves. Several runs were performed with different initial conditions in order to validate that the system consistently converged to the same final values.

Due to additional unforseen constraints on joint geometry, optimization for each joint was performed a second time. Specifically, the joint shafts, tendon links, and supporting structure were enlarged and redesigned to improve the structural integrity (increase the safety factor) of the system. This forced the minimum allowable values of some link parameters on each joint to increase. The final torque profiles are shown

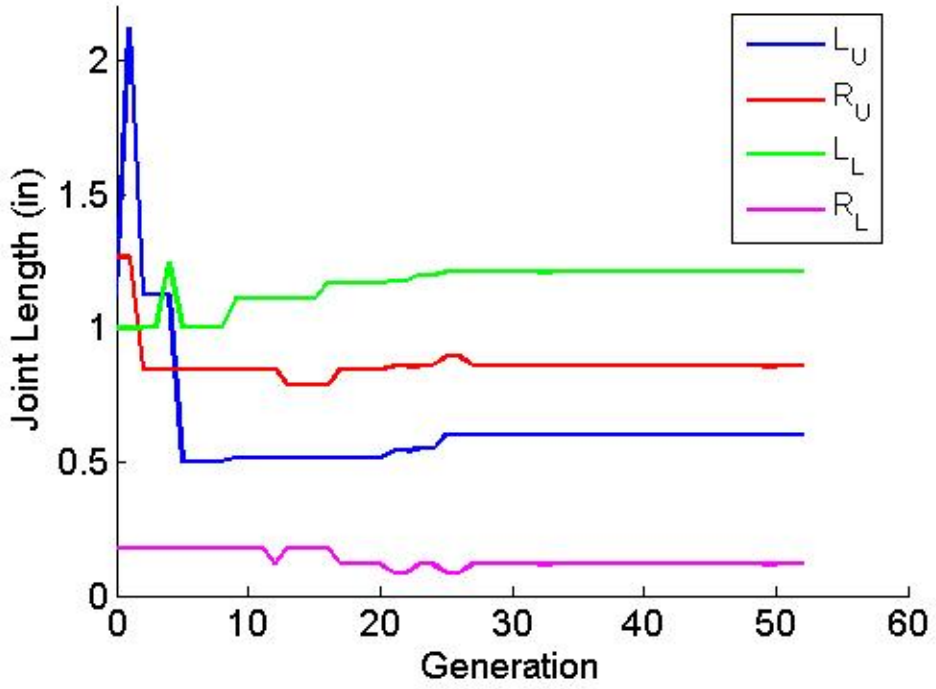


Figure 3.21: Joint dimensions vs. generation, genetic algorithm-based optimization.

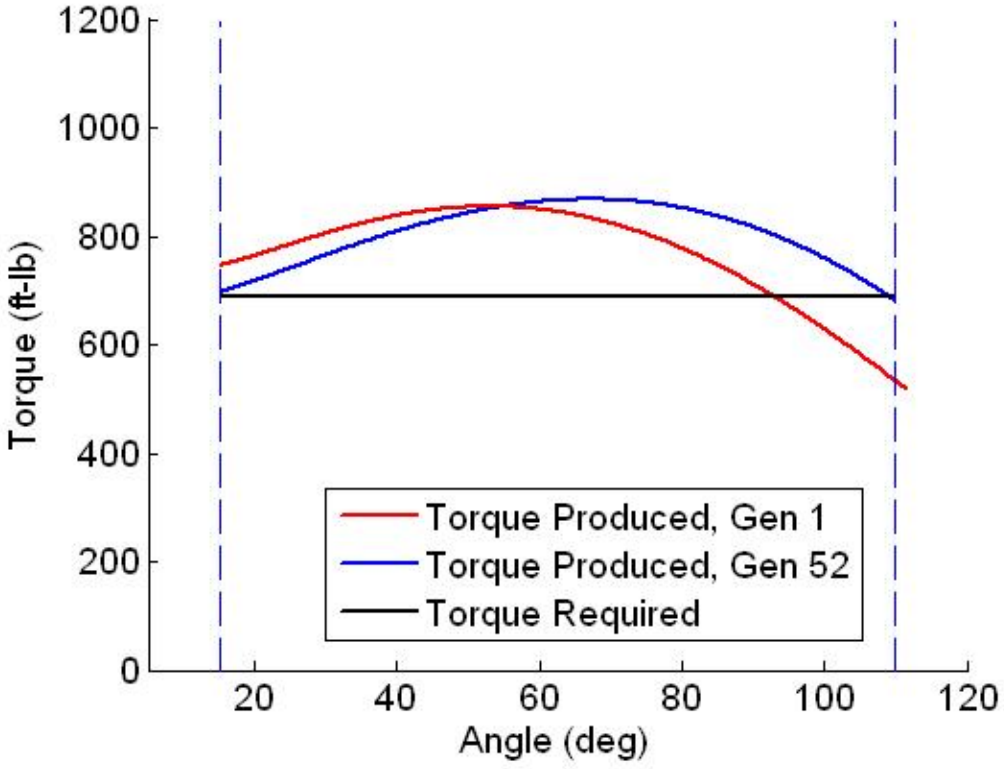


Figure 3.22: Torque vs. range of motion, initial and final generations.

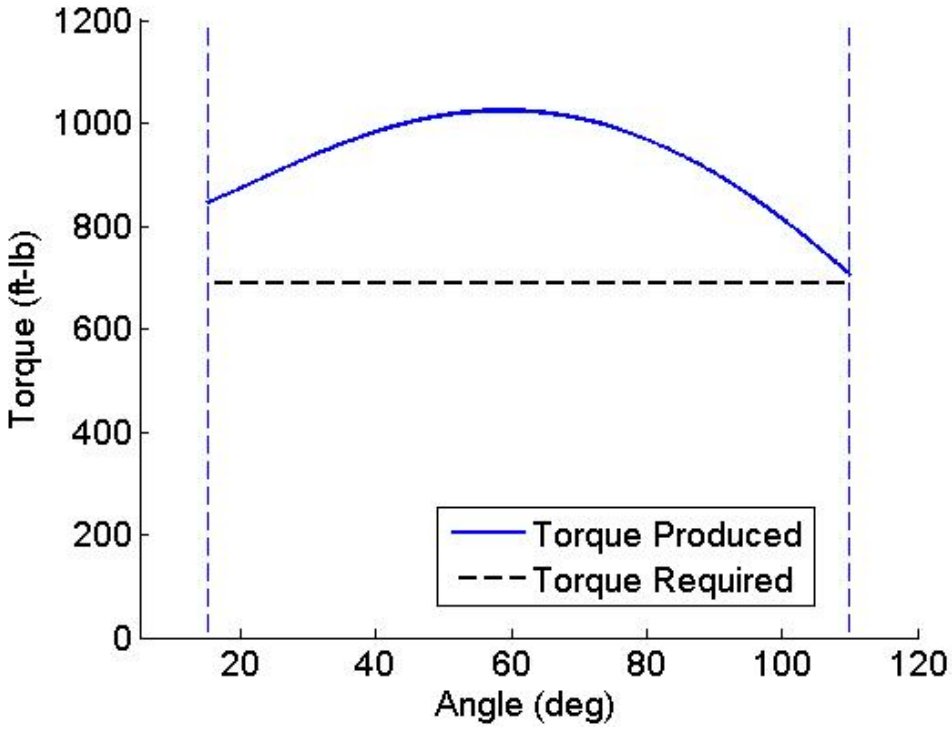


Figure 3.23: Torque vs. range of motion, shoulder joint.

in Figures 3.23 and 3.24. The final parameter values are given in Table 3.5. Note that the torque generated at the minimum angles are well above the desired torque; this is a consequence of the new geometric constraints.

3.6 Conclusion

A proof-of-concept demonstrator of a pneumatic artificial muscle-actuated robotic manipulator intended for lifting heavy payloads was built and tested, showing the potential that PAM actuators have for this type of application. The two degree-of-freedom system with links that approximate the lengths of a typical human arm was able to achieve joint torques in excess of 200 ft-lb for each joint of the initial proof-of-concept demonstrator, and nearly 800 and 400 ft-lb for the shoulder and

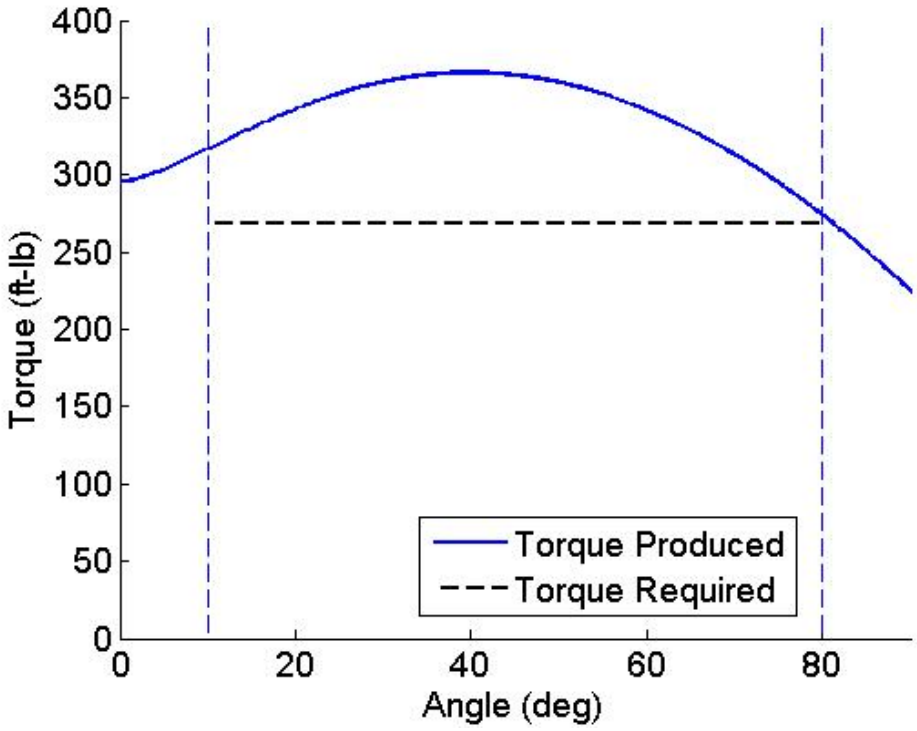


Figure 3.24: Torque vs. range of motion, elbow joint.

Table 3.5: Optimal parameters of candidate designs, determined by genetic algorithm-based optimization.

Joint	Shoulder	Elbow
Pressure (psi)	190	150
PAM Length (in)	10.88	4.94
l_u (in)	1.00	0.70
r_u (in)	1.08	0.70
l_l (in)	1.08	1.15
r_l (in)	0.19	-0.20

elbow, respectively, of a refined manipulator. A system model was devised that took into account PAM behavior, arm dynamics, and airflow through the pneumatic subsystem. The actuator model considered the Gaylord force from pressure effects on the braid, as well as the Mooney-Rivlin energy storage term.

Error between quasi-static torque experimental values and model predictions at 150 psi was on the order of a few percent. Dynamic testing uncovered some discrepancy at low pressure, suggesting that the model may need adjustment for precise, low pressure applications. Although the effects of experimentally observed hysteresis in the PAMs were neglected, this actuator model overall showed good accuracy of the system model when simulated predictions were compared to experimental measurements, indicating that the simplified PAM model is sufficient for initial performance predictions and design analysis.

Lastly, design optimization was performed on the joints of a second-generation, two degree-of-freedom manipulator. The dimensions of the joints were selected using genetic algorithms with the objective of minimizing the joint torque under a threshold torque over the desired range of motion, while minimizing the required pressure. This design method was found to be superior to simple trial-and-error. While the initial joint designs were found to be optimal, they did not fully account for structural integrity requirements; therefore, a second optimization was performed with strict constraints on joint dimensions. The resulting joints required higher pressures than the original joints and demonstrated torque levels considerably higher than the desired torque at low angles; however, this was necessary to reach the desired torque at high angles.

Chapter 4: Control of PAM-Based Robotic Manipulators

4.1 Introduction

Commercial and domestic applications for mobile robots continue to expand into areas that require human-robot interaction. Often, the design objectives considered in mobile robotic applications are low weight, high range of motion, high torque, and low power. However, interaction with humans warrants additional safety measures, including compliant manipulation. This requirement is problematic for many conventional actuators, which typically use high stiffness to achieve high performance, thereby increasing inertia, and leading to large impact forces upon collision [166].

One type of actuator that can satisfy these competing requirements is the pneumatic artificial muscle (PAM). PAMs are extremely lightweight, compliant, and capable of higher specific work than comparably-sized hydraulic actuators and electric motors [155]. They are composed of a helically braided sleeve surrounding an elastomeric bladder and are held together by end fittings. Pressurization of the soft bladder inflates the muscle and causes the stiff braid fibers to reorient, generating a contractile stroke and pulling force similar to human muscle. Also known as McKibben actuators, PAMs were initially developed as orthotic devices

for polio patients [23]. Similar applications have dominated the field over the years, with PAM-powered devices for orthotics and rehabilitation [75, 80, 152] and biologically-inspired humanoid robotic devices [40, 69]. Looking to other applications, these actuators are particularly desirable in portable robotic systems intended for interaction with humans [166], such as those envisioned for nursing assistance and in casualty extraction.

While being considered in robotics for several decades, work still remains to develop an all-encompassing PAM model formulation. Many modeling approaches exist, including energy balance [32], force balance [34] and finite elasticity theory [39], but precise modeling of the nonlinear behavior has proven difficult. Moreover, scalability to different sizes, length-to-diameter ratios, and bladder thickness-to-diameter ratios has seen limited success. Modeling error is compounded farther in PAM systems when considerations for the flow and compressibility of air are included, making precise control difficult. Control is especially difficult for a PAM-based manipulator with payload weights ranging from zero to several times the mass of the manipulator itself.

Past efforts to control pneumatic artificial muscles span a wide range of established techniques. Caldwell et al. [41] used adaptive control based on model estimation, demonstrating accuracy for lightweight payloads (0.325 kg [0.7 lb]) over 9 deg of arm rotation. However, it is important that manipulators intended to lift humans can handle payloads exceeding their own weight and can operate over a much larger range of motion. Ahn and Nguyen [42] developed an intelligent switching algorithm using a learning vector quantization neural network for various payloads,

showing experimental data for step inputs. This controller requires training the neural network for an extended amount of time before the system could reliably lift different payloads. Wu et al. [43] developed a self-tuning fuzzy PID controller for a hand exoskeleton actuated by PAMs. The experiments showed undesired oscillation about the reference trajectory, though there was a time-varying disturbance due to human input. Yeh et al. [44] designed an optimal controller using loop transfer recovery (LTR) for a leg exoskeleton, which was deemed successful, but limited to only 15 deg of rotation.

When manipulator joint trajectories require high speed and acceleration, the tracking capabilities of pure feedback control are degraded [165]. Moreover, over-simplified computed torque controllers or adaptive controllers with slow parameter updating may not have the capability to track fast nonlinear dynamics. To address this problem, several approaches to PAM-based control have incorporated highly detailed models of the system. Zhu et al. [45] designed an adaptive robust controller for a parallel manipulator with only a few degrees of movement, incorporating a model of the flow dynamics and valve. Ganguly et al. [46] introduced static and dynamic empirical models of PAM actuation and valve characteristics in a model-based PID controller for a rotary joint. The adoption of feedforward compensation was shown to improve system response in work by Nho and Meckl [47], who demonstrated neuro-fuzzy and inverse dynamics feedforward control on a two-link manipulator. Fateh and Izadbakhsh [48] employed a hybrid computed torque approach to a two-link manipulator and found that feedforward control reduces tracking error. These model-based feedforward strategies influenced the design of the control system in

the present study.

Control studies on PAM-based systems have often employed sliding mode control, a robust nonlinear control strategy that drives the dynamics of the system to that of an exponentially stable system [49]. This methodology has been extended to adaptively control robot manipulators [151], improving the response to unmodeled dynamics or payload variations. Many sliding control algorithms have been proven to be globally stable when model errors and system disturbances are bounded [50]. Carbonell et al. [51], Cai and Dai [52], and Lilly [53] performed simulations of PAM-actuated systems using sliding mode controllers. However, these second-order controllers assume that the PAM pressure or force being used as a control input is instantaneous, which cannot be assumed in a practical system with large PAM volume. Similarly, Nouri et al. [54] designed an adaptive controller with a sliding component that neglected airflow dynamics for low payloads (0.6 kg [1.3 lb]). Xing et al. [55] applied sliding mode control with a disturbance observer to a PAM in linear motion experiments with a 1 kg (2 lb) load. While the controller showed good performance, airflow dynamics were neglected and commanded pressure was assumed to be instantaneous, which is not realistic in more demanding applications. In order to address such problems, Shen [56] designed a model-based sliding mode controller including a dynamic airflow model, and applied it to a linear table actuated by PAMs. Aschemann and Schindele [57] developed a cascaded sliding mode controller for a high-speed linear axis with a detailed empirical model of valve dynamics for pressure feedback and a model of the linear axis for position feedback. As in other model-based control strategies, these detailed physical models were necessary to

achieve satisfactory performance. Tondu et al. [58] applied sliding mode control with twisting and super-twisting algorithms to two degrees-of-freedom of a PAM-based manipulator, noting that the equivalent force control term was not helpful on the link farther from the base because of model uncertainty. Overall, studies that have successfully applied sliding mode control to experimental PAM-actuated systems have used systems with high stiffness, low inertial loads, and minimal time delays. However, the robotic arm in the present study, as outlined in the following section, exhibits relatively low stiffness, highly variable inertial loads, and substantial time delay. Moreover, sliding mode control can be negatively affected by measurement noise and low-resolution sensors, which are present in the system. The authors intend to investigate the implementation of an adaptive sliding mode controller on a system better suited to this strategy in future work.

While many of these studies have demonstrated smooth and accurate motion, control of a PAM-actuated manipulator with both high range of motion (90 deg) and high tip payload variations (0 to 45 kg [0 to 100 lb]) has not been attempted. It should be noted that the manipulator arm in question weighs 7 kg (15 lb), several times less than the maximum payload. The objective of the present work is to develop a control algorithm for this manipulator that satisfies accuracy and smooth motion requirements. This began first by considering proportional-integral-derivative (PID) and fuzzy logic controllers, but moved toward a model-based feedforward structure to achieve improved performance. In this study, the controllers were simulated and experimentally tested on the manipulator. System performance was evaluated for different trajectories and payloads. Additionally, the effect of varying the gain in the

feedforward model was analyzed.

4.2 PAM-Actuated Robotic Manipulator

4.2.1 Design and Experimental Setup

The heavy-lift, PAM-actuated, proof-of-concept manipulator was designed and constructed in Chapter 3. Figure 4.1 illustrates the components of the actuator system, including a high pressure air source, pneumatic valves, and manipulator. As illustrated, the actuators provide torque in only the positive direction, and gravity provides a restoring force in the opposing direction. In other words, the system is not operating in an antagonistic configuration. The manipulator design allows for a compression spring to provide antagonistic force; however, a spring was not used in this study. Figure 4.2 shows the arm in operation, holding 50 kg (110 lb). Throughout experimentation, angular Hall-effect sensors (Midori Precisions) were attached to each joint to measure rotation angles that typically varied from 0 to 100 deg. Pressure transducers (Omegadyne Inc.) were attached to incoming air lines to monitor PAM pressure. Each degree-of-freedom can be fed compressed air through a proportional servo-valve (Festo MYPE-type). However, in these experiments, only the elbow joint was actuated. The cross-sectional area of the valve inlet and outlet are a function of the voltage sent from the controller. Hence, the controller was capable of directly manipulating the flow rate of air.

The sensors and control valves were connected to a dSPACE®real-time interface, which allowed for quick implementation and modification of controllers modeled

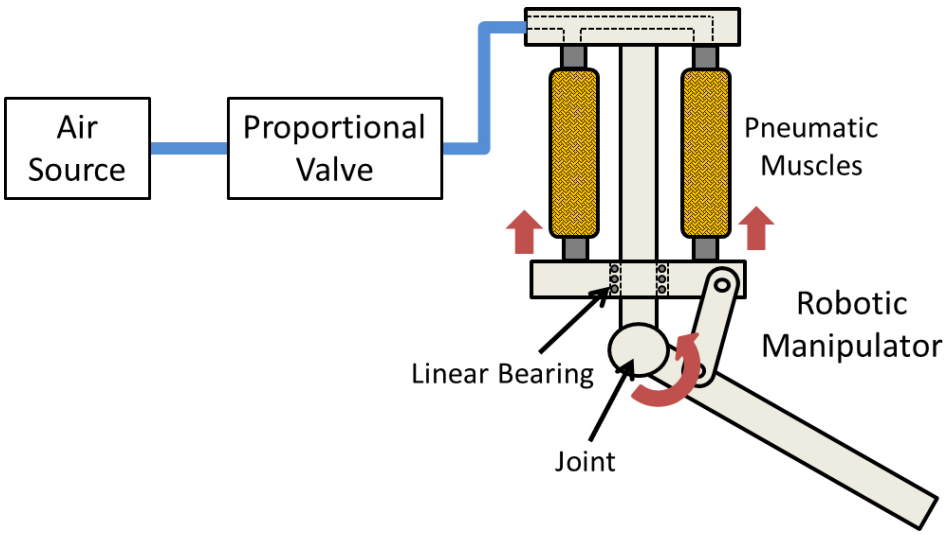


Figure 4.1: Schematic of PAM-Actuated Manipulator System.



Figure 4.2: PAM-actuated joint holding 50 kg (110 lb).

in Simulink®. In these single-degree-of-freedom (SDOF) control experiments, a single-input, single-output (SISO) controller was employed for elbow rotation. Output error between the measured (actual) angle and the reference (desired) angle was used to compute a voltage to the control valve. The pressure supply was set to 0.83 MPa (120 psi).

4.2.2 System Model

A complete model of the elbow degree-of-freedom consists of three major components: the airflow through the valve, the response of the PAM actuators, and the manipulator dynamics. The control valve regulates air pressure in the actuators, which is used to calculate PAM force. PAM force is then translated to actuator motion. Airflow is regulated by the control voltage to the valve, whose orifice area A is a nonlinear function of the control voltage. Orifice area is calculated by interpolating values from a lookup table.

The mass flow rate of air depends on both upstream and downstream pressures, P_{us} and P_{ds}, and the orifice area:

$$\dot{m}_{air} = \begin{cases} AC_d P_{us}\sqrt{\frac{2}{RT}}C_1, & \frac{P_{ds}}{P_{us}} < P_{cr} \\ \\ AC_d P_{us}\sqrt{\frac{2}{RT}}C_2, & \frac{P_{ds}}{P_{us}} \geq P_{cr} \end{cases} \tag{4.1}$$

The term C_d is a discharge coefficient capturing the losses in the orifice, $P_{cr} = (2/(\gamma+1))^{\gamma/(\gamma-1)}$ is the critical pressure separating subsonic and supersonic flow, and C_1 and C_2 are given by:

$$C_1 = \sqrt{\frac{\gamma}{\gamma-1}\left[\left(\frac{P_{ds}}{P_{us}}\right)^{\frac{2}{\gamma}} - \left(\frac{P_{ds}}{P_{us}}\right)^{\frac{\gamma-1}{\gamma}}\right]}$$

$$C_2 = \left(\frac{2}{\gamma+1}\right)^{\frac{1}{\gamma-1}}\sqrt{\frac{\gamma}{\gamma+1}} \tag{4.2}$$

where γ is the specific heat ratio of air.

Richer and Hurmuzlu [158] derived an expression for pressure change in a container of changing volume using the ideal gas law, conservation of mass, and conservation of energy:

$$\dot{P} = \frac{RT}{V_{air}}(\alpha_{in}\dot{m_{in}} - \alpha_{out}\dot{m_{out}}) - \alpha P\frac{\dot{V}_{air}}{V_{air}} \tag{4.3}$$

where R is the specific gas constant for air, T is air temperature, V_{air} is air volume in the PAMs, $\alpha_{in} = 1.4$ and $\alpha_{out} = 1$ are the respective specific heat ratios of the gas flow into and out of the PAMs, and $\alpha = 1.2$ is the approximate specific heat ratio due to volume change. From this expression of pressure rate, the time-varying pressure inside the PAM actuators can be determined by integration.

Quasi-static PAM actuator models relating force to contracted length and applied pressure can be derived using a number of approaches [35]. Experimental data was found to best match the force balancing method derived initially by Ferraresi et al. [34]. In this model, corrected for the effect of non-constant bladder thickness, PAM force is given by:

$$F = \frac{P}{4\pi N^2}\left[3(L_0 - \Delta L)^2 - B^2\right] + P\left[\frac{V_B}{L_0 - \Delta L} - \frac{(t_0 - \Delta t)(L_0 - \Delta L)}{2\pi(R_0 - \Delta R)^2 N^2}\right] + F_L + F_T \tag{4.4}$$

where L_0 is resting length, ΔL is contraction, V_B is bladder volume, B is braid length, N is number of braid turns around the circumference of the PAM, t_0 is the resting bladder thickness, Δt is the change in bladder thickness, R_0 is the

resting bladder radius, and ΔR is the change in radius. The forces F_L and F_T are pressure-independent terms governed by the elasticity of the bladder E_R, and are as follows:

$$F_L = E_R V_B \left(\frac{1}{L_0} - \frac{1}{L_0 - \Delta L} \right) \tag{4.5}$$

$$F_T = \frac{E_R (L_0 - \Delta L)}{2\pi (R_0 - \Delta R) N^2} [(t_0 - \Delta t)(L_0 - \Delta L) - t_0 L_0] \tag{4.6}$$

This formulation was found to be accurate for PAMs undergoing contraction, but there is an inherent hysteresis that alters the force-contraction profile in extension. In extension, the resistive force preventing the PAM bladder from expanding increases the PAM force. Also, there is friction both between the braid and bladder and between the braid fibers themselves. This hysteresis is captured in the model by adding empirical constants to the terms:

$$F_2 = \frac{P}{4\pi N^2} \left[3(L_0 - \Delta L)^2 - B^2 \right] + 0.3P \left[\frac{V_B}{L_0 - \Delta L} - \frac{(t_0 - \Delta t)(L_0 - \Delta L)}{2\pi (R_0 - \Delta R)^2 N^2} \right] + 0.8F_L + 0.8F_T \tag{4.7}$$

Force from the PAM group is translated into an arm torque, defined as $\tau = F r_{eff} \cos\theta_f n_{PAM}$, where r_{eff} is the effective length of the moment arm (nonlinear function of joint angle), θ_f is the angle between the stationary upper link and the joint tendon, and n_{PAM} is the number of parallel PAMs in the muscle group.

PAM torque is resisted by the weight and inertia of the arm and payload. The

arm dynamics for single degree-of-freedom motion are related to PAM torque by:

$$\tau = I_z\ddot{\theta}_d + m_{pld}l_{arm}^2\ddot{\theta}_d + (m_{arm}l_{c,arm} + m_{pld}l_{arm})g\sin\theta_d \tag{4.8}$$

where θ_d is desired angle, I_z is the link inertia, m_{arm} is the arm mass, $l_{c,arm}$ is the distance between the joint and the link center of mass, m_{pld} is the payload mass, l_{arm} is the link length, and g is gravitational acceleration. With the previous equation, joint angle can be determined and continuously monitored by the controller.

4.3 Control Strategies

4.3.1 Output Feedback Control

4.3.1.1 Proportional-Integral-Derivative Control

Proportional-integral-derivative (PID) control is a feedback strategy widely used in industrial applications. The controller input, voltage to the pneumatic valve, is given by:

$$u(t) = k_P e(t) + k_I \int e(t)dt + k_D\dot{e}(t) \tag{4.9}$$

The control signal can be manipulated by three user-defined gains: the proportional gain, k_P, integral gain, k_I, and derivative gain, k_D. Additional improvement was achieved by adding a low-pass filter to the controller output to eliminate high-frequency content and provide a smoother response, while only slightly increasing

total error.

4.3.1.2 Fuzzy Control

As an alternative to PID control, a fuzzy logic controller was designed and implemented based on the approach described by Passino and Yurkovich [164], which is briefly described in this section. Fuzzy control employs membership functions and a ruleset established by the designer to translate controller inputs into a desired output in a smooth, non-discrete manner. A fuzzy controller categorizes a numerical input value using linguistic variables such as "positive big" and "negative medium." Each linguistic variable i has its own membership function $\mu_i(x)$, which quantifies the "certainty" that the numerical input x can be classified as that variable (on a scale from 0 to 1). Triangular-shaped membership functions are most common and were used here [164].

In this fuzzy controller, the input variables were angle error and error rate, and the output variable was valve voltage. Each of the inputs was scaled by gains g_1 and g_2, and the output was scaled by gain h. Note that in this study, the inputs were divided by g_1 and g_2, meaning that higher values of g_1 and g_2 decrease the system sensitivity. However, the output was multiplied by h; therefore, higher values of h increased the system reaction.

Figure 4.3 shows the seven membership functions associated with each linguistic variable with unity gains. It is clear from the overlapping membership functions that a numerical input can be categorized as more than one linguistic variable simultaneously.

Table 4.1: Fuzzy ruleset.

	Error							
Error Rate		NB	NM	NS	ZO	PS	PM	PB
	NB	PB	PB	PM	PS	ZO	ZO	NS
	NM	PB	PM	PM	PS	ZO	NS	NM
	NS	PB	PM	PS	ZO	NS	NM	NB
	ZO	PB	PM	PS	ZO	NS	NM	NB
	PS	PB	PM	PS	ZO	NS	NM	NB
	PM	PM	PS	ZO	NS	NM	NM	NB
	PB	PS	ZO	ZO	NS	NM	NB	NB

This leads to the "fuzzy" combinations that enable smooth transitions between different outputs.

Table 4.1 displays the user-defined ruleset for the fuzzy controller. The control logic combines the linguistic input variables that are given non-zero membership values and prescribes the output based on this ruleset. For example, IF the angle error is "negative small," AND the error rate is "positive small," THEN the output will be "positive small." However, the membership of a given numerical value is often split between two membership functions. To determine the weight given to a particular rule, we define:

$$\mu_{p,ij} = min(\mu_{e_i}, \mu_{\dot{e},j}) \tag{4.10}$$

as the "premise" membership to rule ij, where $\mu_{e,i}$ and $\mu_{\dot{e},j}$ are the membership values of error with respect to membership function i and error rate with respect to membership function j. Since multiple linguistic variables can be activated, multiple

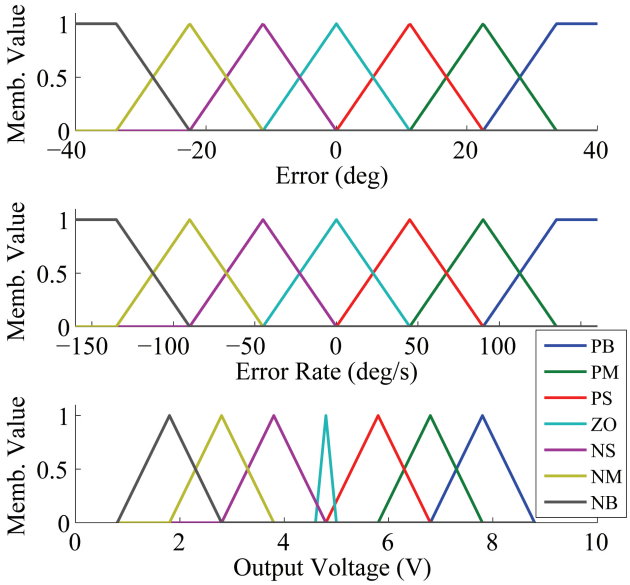


Figure 4.3: Fuzzy membership functions for input/output variables.

outputs from the ruleset are combined and weighted using the "center of gravity" defuzzification method. This final combination is then multiplied by gain h to produce the total output. It should be noted that, as with PID control, a low-pass filter was added to the output to reduce oscillatory content.

4.3.2 Model-Based Feedforward Control

Although output feedback controllers, such as PID and fuzzy logic, can be tuned for smooth trajectory following and good disturbance rejection, neither take advantage of the known system dynamics to improve control. Therefore, a model-based feedforward controller was designed and implemented. The system model described in the last section was used previously for control studies [97]. These simulations accurately predicted dynamic behavior of the arm when subjected to an

arbitrary input. Thus, a controller was designed with a feedforward control element based on an inverse of the system model.

4.3.2.1 Model-Based Control without Feedback

Figure 4.4(a) depicts the structure of the basic model-based feedforward controller. The system contains an inverse model of the arm, pneumatic muscles, and airflow dynamics to help negate the nonlinear dynamics of the plant. This feedforward element samples the commanded trajectory and calculates desired PAM pressure at each time interval. If desired pressure is greater than actual pressure, the system exhausts air until it reaches the desired pressure, and vice versa. Note that actual PAM pressure must be known in order to calculate the desired airflow rate in the valve, which could be considered a feedback component within the feedforward controller. Given the desired state of the system, inverse dynamics are used to calculate desired torque using Eqn. 6.6, though payload mass must be known a priori to achieve accurate trajectory tracking.

By rearranging the PAM group torque equation, desired force can be determined as:

$$F_d = \frac{\tau_d}{r_{eff} \cos \theta_f} \tag{4.11}$$

Then, desired pressure in each PAM is calculated by rearranging Eqn. 4.3 as:

$$P_d = \left(\frac{F_d}{n_{PAM}} - F_L - F_T\right)\left[\frac{(3(L_0-\Delta L)^2 - B^2}{4\pi N^2} + \frac{V_B}{L_0-\Delta L} - \frac{(t_0-\Delta t)(L_0-\Delta L)}{2\pi(R_0-\Delta R)^2}\right] \tag{4.12}$$

(or alternatively, Eqn. 4.7 for PAM extension). Simply differentiating desired pressure to find the desired pressure rate does not produce good results because initial pressure error would not be compensated and model inaccuracy may cause the error to compound. Therefore, actual PAM pressure P is monitored by the feedforward controller and pressure error $\Delta P = P_d - P$ is determined. The goal of the controller now is to minimize the pressure error, by proportionally adjusting desired pressure rate, $\dot{P}_d = -k_M \Delta P$, where gain k_M is introduced to adjust the speed of convergence of the actual pressure to the desired pressure. Therefore, $\dot{m}_d$, the desired mass flow rate of air to the PAM group, is estimated as:

$$\dot{m}_d = \begin{cases} \frac{\dot{P}_d V + \alpha P \dot{V}}{RT\alpha_{out}} & \dot{P}_d < 0 \\ \\ \frac{\dot{P}_d V + \alpha P \dot{V}}{RT\alpha_{in}} & \dot{P}_d > 0 \end{cases} \tag{4.13}$$

From this flow rate, a desired valve orifice size A_d is calculated by rearranging

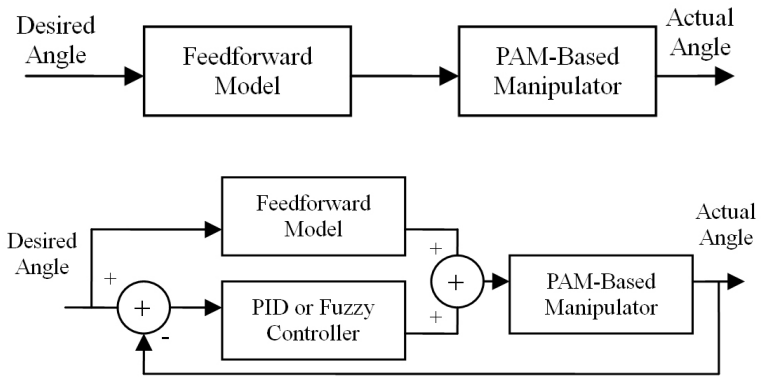


Figure 4.4: Model-based feedforward (a) without output feedback, (b) with PID or fuzzy feedback control.

Eqn. 4.1 as:

$$A_d = \begin{cases} \frac{\dot{m}_d}{C_d C_1 P_{us}} & \frac{P_{ds}}{P_{us}} < P_{cr} \\ \\ \frac{\dot{m}_d}{C_d C_2 P_{us}} & \frac{P_{ds}}{P_{us}} \geq P_{cr} \end{cases} \tag{4.14}$$

Ideally, the gain would be very high in order to obtain the desired pressure nearly instantaneously, but problems with oscillation and model inaccuracies require that the gain be tuned for an optimal combination of accuracy and smoothness.

4.3.2.2 Model-Based Control Augmented with Output Feedback

If the joint is following a commanded trajectory with only model-based feedforward control, minor inaccuracies in the model can produce significant steady-state error, and major inaccuracies may lead to instability. Therefore, the model-based feedforward controller can be augmented with a stabilizing feedback controller, such as a PID or fuzzy controller, as illustrated in Figure 4.4(b). A desired joint angle

is passed into the model and the feedback controller in parallel. Their outputs are summed, creating a total control voltage that is sent to the PAM manipulator. The arm dynamics are sensed and used in feedback to ensure the arm closely follows the trajectory.

4.4 Control Analysis Via Simulation

4.4.1 PID and Fuzzy Control

The two output feedback control strategies that were implemented on the manipulator use distinct approaches to provide smooth, stable, and accurate motion. However, both rely on gain tuning to achieve optimal results. This section details the metrics used to evaluate controller performance in trajectory-following exercises as the gains were varied.

4.4.1.1 Gain Tuning Metrics

For simulations and experiments, performance metrics were established to ensure that the best set of gains was chosen. The first was an integration of the squared error in angular position as a function of time, giving a total error metric:

$$\nu = \int_0^{T_f} (y_d - y)^2 dt \tag{4.15}$$

where y is the measured joint angle, y_d is the desired joint angle, and T_f is the final time of the test run. Note that the input to the controller is the error signal,

$e = y_d - y$. While it may seem that this metric is sufficient in tuning the gains since it minimizes angle deviation, it became quickly apparent that some responses with a lower value of ν also had substantial oscillation about the desired profile y_d. Hence, another error metric was considered to highlight smoothness of the response. This metric was based on the local curvature of the measured angle:

$$\kappa = \frac{y''}{(1 + y'^2)^{3/2}} \tag{4.16}$$

where y is the first time derivative of the measured angle and y'' is the second time derivative. With the local curvature at each time step, an error metric was computed by integrating κ with respect to time, giving the total curvature:

$$\omega = \int_0^{T_f} \kappa dt \tag{4.17}$$

This integration provides a single value for comparison where the response with minimal curvature, or oscillation in the response, is easily identifiable. Having two error metrics now, one based on minimal overall error and one based on minimal oscillation, a combined metric was established drawing on contributions from both individual metrics. Each individual metric was normalized with respect to the minimum value of that metric and weighted with W_i as:

$$J = W_\nu \frac{\nu}{min\nu} + W_\omega \frac{\omega}{min\omega} \tag{4.18}$$

such that the minimum possible combined value was $J = 1$. The weights were chosen

as $W_\nu = 0.25$ and $W_\omega = 0.75$ to give more precedence to smoothness of the controlled response than total error, which tended to be undesirably oscillatory alone.

4.4.1.2 Simulated Trajectory Following

Prior to experimental testing, simulations of the feedback controllers were performed. In each simulation, the elbow joint was commanded to follow a lift-hold-return trajectory with 5 s segments, the error and smoothness were monitored, and a combined metric score was calculated. Each of the control gains was varied iteratively, and the set of gains that produced the lowest score was determined to be optimal. Both PID and fuzzy controllers were simulated for various payload weights hung from the tip of the end effector.

Figure 4.5 shows surface contour plots of the performance metrics from fuzzy gain tuning simulations (similar results were also obtained for the PID controller). These plots allow g_1 and h to vary, while $g_2 = 0.6$ is held fixed at the value determined to be optimal for some of the cases. The two individual metrics are shown, along with the combined metric. It is clear that the optimal gain set according to the error metric and smoothness metric are different, producing a combined metric that includes characteristics of both individual metrics and returns a new optimal value ($g_1 = 0.45, h = 0.65$). Note that the area directly surrounding this minimum is smooth, meaning that small deviations from these gains will not cause abrupt changes in behavior. This is important because a future controller may incorporate gain scheduling in order to account for changes in payload, and as the controller

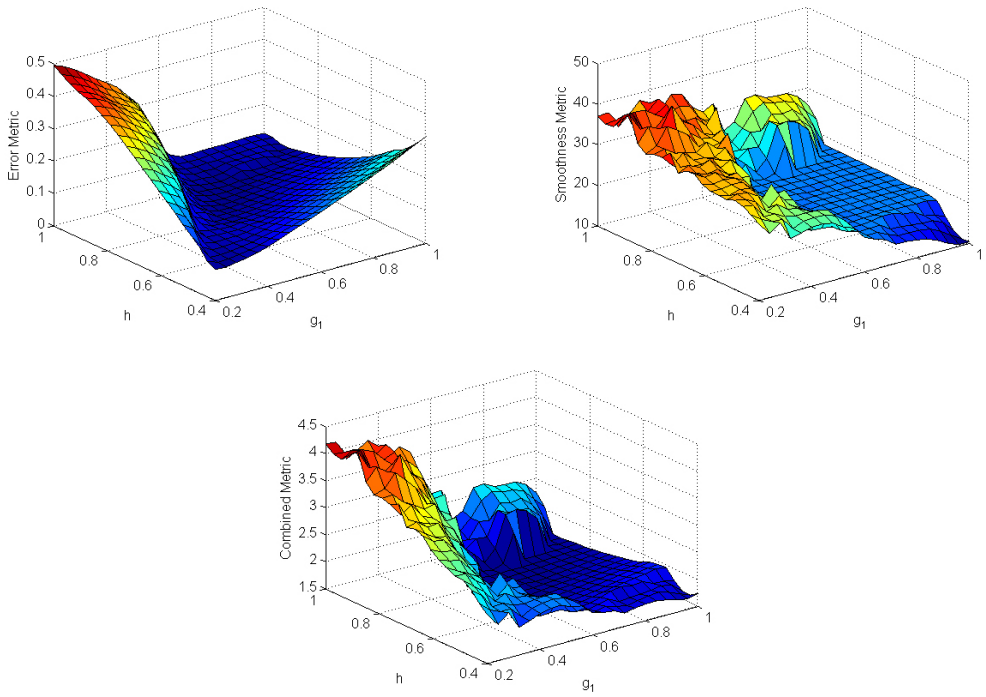


Figure 4.5: Performance metrics as g_1 and h vary ($g_2 = 0.6$) with a 23 kg (50 lb) payload (a) error metric; (b) smoothness metric; (c) combined metric.

transitions from one set of gains to another, gains may not be at their exact optima at all times.

4.4.2 Model-Based Control with Output Feedback

Model-based feedforward control was also evaluated in simulation. Some plant parameters (PAM force, friction, and arm inertia) were intentionally made slightly different from the controller parameters so the model would not match perfectly. Figure 4.6 shows the trajectory and pressure response for the feedforward controller with fuzzy feedback. It can be seen that both the reference trajectory and pressure are closely followed in all three cases. Control gains are identical for each simulation ($g_1 = 0.4, g_2 = 0.3, h = 0.7, k_M = 1.0$). As predicted, larger payloads require higher

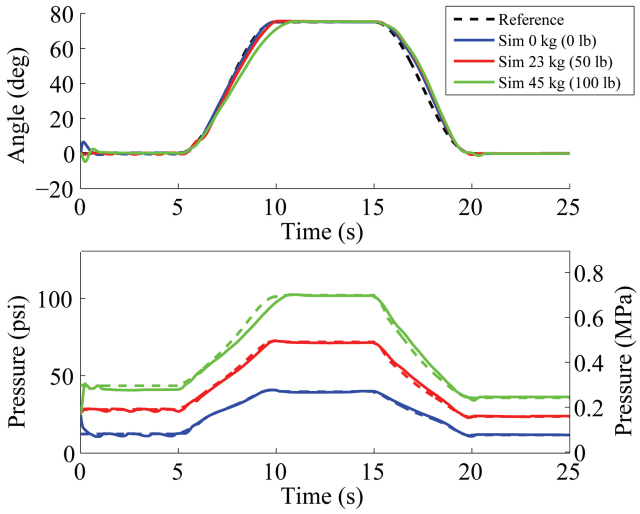


Figure 4.6: Simulated control, feedforward with fuzzy feedback

pressure to achieve the maximum angle. Error during the lift ramp is seen to increase with increasing payload because the maximum mass flow rate of air decreases as upstream pressure and downstream pressure converge. This effect could be reduced with higher source pressure.

Figure 4.7 shows the same trial simulations with PID feedback in place of fuzzy feedback. Again, controller gains are identical for each simulation ($k_P = 5.0, k_I = 2.0, k_D = 0.0, k_M = 1.0$). Operation is similar to feedforward control with fuzzy feedback; however, there is slightly increased error in the return stage, which is likely an effect of the integral term delaying a change in direction because of accumulated prior error.

In both trials, the operation of the model-based controller is smooth and accurate across a large range of payloads, and no overshoot is present. The simulations provided a good case for implementation and evaluation on the manipulator hardware.

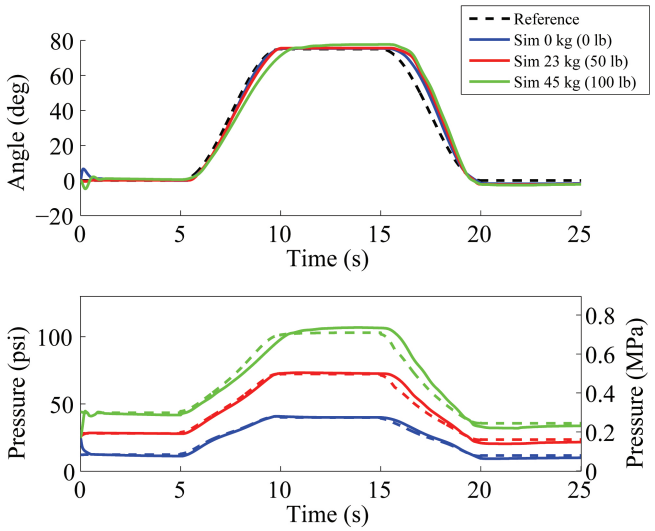


Figure 4.7: Simulated control, feedforward with PID feedback

4.5 Experimental Evaluation

4.5.1 PID and Fuzzy Control

4.5.1.1 Experimental Validation

Guided by optimal results from simulation, experimental tests were performed and compared with simulation data. There was generally good correlation between model predictions and experimental measurements, providing validation that the simulation model is sufficient for closed-loop design with the noted PID and fuzzy controllers. Validation of the predicted joint behavior suggested that the simulation model could be extended to other manipulator configurations and control strategies, such as model-based approaches.

4.5.1.2 Experimental Gain Tuning

Although simulations with optimal gains showed good correlation with experiments, the differences between the model and actual system indicated that experimental gain tuning could improve performance. Unlike in simulation, evaluating an exhaustive set of gain combinations was not practical, so experimental gain tuning began with the predicted optimal gains and varied these in search of experimental optima. Tuning of the PID controller was performed for three payloads: 11, 23, 34 kg (25, 50, 75 lb). The process began with k_P. Next, k_I was varied while a highly rated value of k_P was held constant. Then, k_D was added and incremental adjustments were made again. Fuzzy controller gains were tuned similarly, in the order of g_1, h, and then g_2.

Figure 4.8 shows an example of how the different error metrics guided the selection of different gains as being "optimal" in the experiments. This example is with 23 kg (50 lb) and considers variations in k_I with two different values of k_P, while $k_D = 0$. As can be seen for the two individual metrics in Figure 4.8(a)-(b), each gives a best response (minimum value) with a different value of k_P and that minimum metric value occurs at a different gain value of k_I. This is the main purpose for considering the combined (normalized and weighted) metric in Figure 4.8(c). With the weights discussed above, this figure shows that the best overall closed-loop response with respect to these metrics and weights occurs when $k_P = 1.4$ and $k_I = 2.5$. To help show the differences in the actual measured time response of the joint rotation angle, Figure 4.8(d) has been included to show the responses

for the best gains according to each metric in Figure 4.8(a)-(c). As shown, "Best Error" follows the "Desired Angle" the closest, but it also has the largest oscillations. "Best Smoothness" and "Best Combined" are much closer to each other, though slightly less accurate than "Best Error," but both have less oscillatory behavior. This provides an example of the trade-offs considered in tuning the gains.

Two data points corresponding to $k_I = 2.5$ in Figure 4.8(a) seem to be outliers, potentially caused by factors that are specific to this system and the chosen reference trajectory. For instance, this integral gain value could have led to a buildup of steady state error that started to rebound just as reference angle began to increase/decrease, causing the arm to closely follow the reference angle in its upward/downward movement, in effect anticipating the systems motion and cancelling out time delay. Another possibility is that this specific integral gain value causes swaying of the payload in a manner that helps the controller follow the path. The most obvious outlier ($k_P = 2.6$, $k_I = 2.5$) was weeded out because of less impressive performance in terms of the "smoothness metric." The use of a combined metric helps to reduce anomalies in the data, especially because low error often corresponds with high oscillation. It is possible that the point ($k_P = 1.4$, $k_I = 2.5$) would no longer correspond to the optimal set of gains if a different trajectory was chosen, but because it is close to the other local minimum in Figure 4.8(c), ($k_P = 1.4$, $k_I = 3.0$), it should be safe to assume good performance for other similar lifting trajectories.

Figure 4.9 compares the optimal gains determined from simulation and experiment. Figure 4.9(a) shows that the PID experimental gains are within a reasonable range of those simulated. The derivative gain is zero or near zero at each payload

and the proportional gain starts just above $k_P = 1$ at 11 kg (25 lb) and decreases with increasing payload. At the minimum payload, the integral gains for both cases are near $k_I = 4$, but above this payload there is some deviation with the experiment showing a downward trend and the simulation showing an upward trend initially before turning downward. Optimal fuzzy control gains are displayed in Figure 4.9(b). The g_1 values and trend from 23 to 34 kg (50 lb to 75 lb) are close, but there is a large difference in the preferred values at 11 kg (25 lb). Both g_2 and h follow experimental trends better, where g_2 stays relatively constant with payload (the values differ up to 2x), and h shows an increasing trend with payload, with nearly equivalent values at 23 and 34 kg (50 lb and 75 lb). The difference with small payload may be caused by system parameters involved with the dynamics that were not well-modeled, but were not critical factors at heavy payloads or for PID control. These parameters (damping, friction, or payload swinging) are difficult to estimate. The discrepancy in modeling created an optimal region in simulated gain tuning that did not exist for the physical system. Overall, it can be stated that the experimentally determined optimal gains are fairly similar to the optimal gains predicted by the simulation model, though future model refinement may be beneficial.

4.5.1.3 Comparison of Output Feedback Controllers

Figure 4.10 shows the time histories of lift-hold-return trajectory-following experiments using the experimentally-optimized PID gains for three payload weights. In each case, the joint initiated positive rotation with about 1 s of delay and quickly

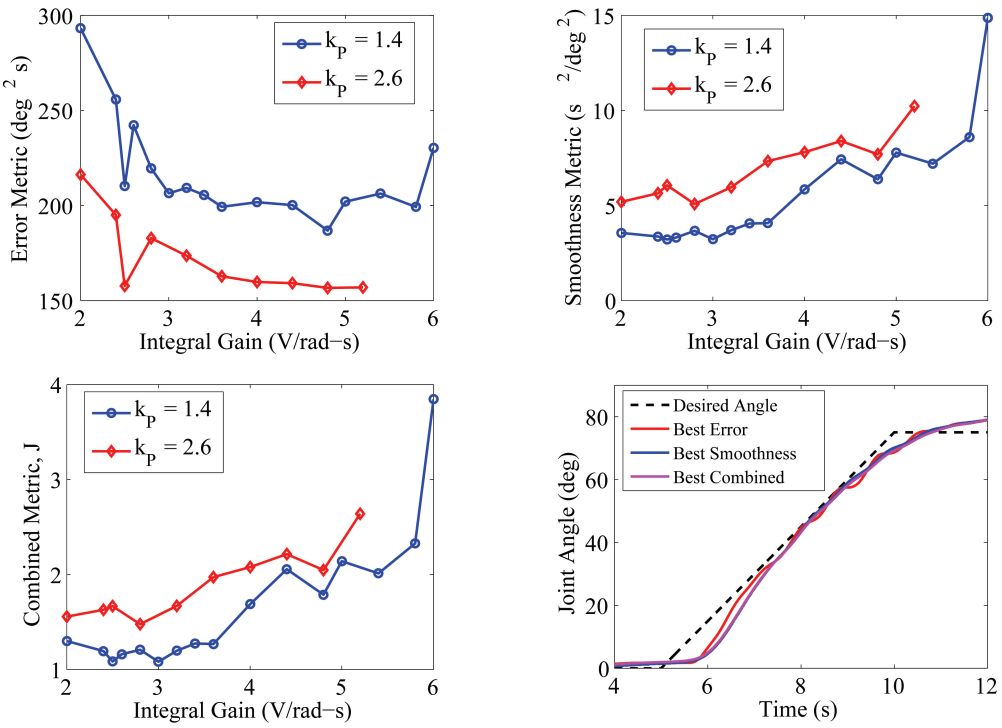


Figure 4.8: PID control, integral gain selection with a 23 kg (50 lb) payload (a) error metric; (b) smoothness metric; (c) combined metric; (d) time response for best cases.

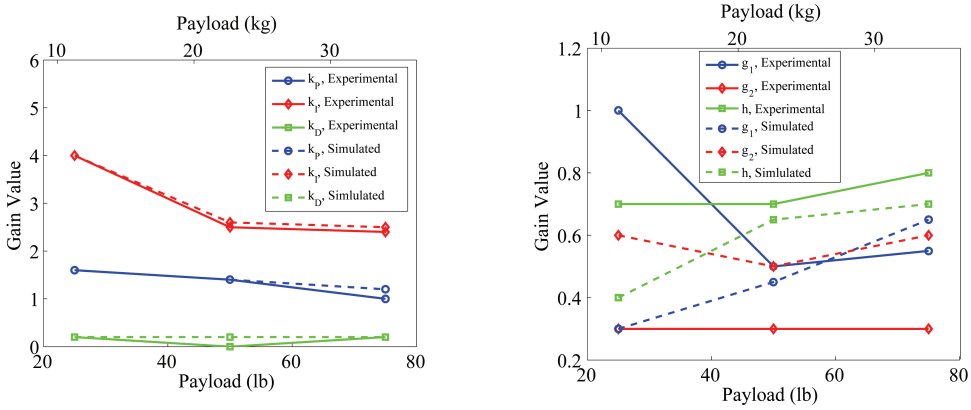


Figure 4.9: Experimental vs. simulated optimal gains (a) PID; (b) fuzzy.

converged to a steady-state during the hold stage. Additional payload prevented contraction until pressure increased, which slightly added to the delay. Due to the larger weighting on the smoothness metric, oscillations reached acceptable levels, but the total error was slightly larger. The cumulative angle error over the trajectory

also increases with payload. Most visible with the PID controller is the undesirably large error in the return stage (arm lowering). With 34 kg (75 lb), this is attributable to integrator windup, when the integral term accumulates high error because the arm cannot produce required torque in this case. Consequently, when the reference changes, the integrator must unwind before the arm can change position. This also causes a considerable overshoot past the rest position when the arm is lowered. This problem could be mitigated by preventing the integral term from increasing over certain bounds. However, an anti-integrator windup will not remove this overshoot phenomenon completely unless the integral gain is set to zero. Some integral gain is needed to allow PID control to remain smooth, reactive, and able to settle to steady-state. Hence, this is a drawback of the PID control strategy for this system.

Figure 4.11 displays results of optimal gains using the fuzzy controller under the same experimental conditions. All three joint angle trajectories are similar in shape, implying minimal change in lifting behavior with changes in payload weight. There is some undesirable low-frequency oscillation during the lift stage, and the arm, while close, does not quite reach the desired hold angle. There is no overshoot, however, and more gradual movement during the return stage, making the closed-loop tracking appear better overall with the fuzzy controller than the PID controller.

Figure 4.12 presents a direct comparison of the PID and fuzzy experiments with the 23 kg (50 lb) payload. In lifting the payload, fuzzy control produces more oscillation, but the overshoot seen with the PID controller does not self-correct until after the return stage has begun. The fuzzy controller lags during the lift stage more than with PID, but PID generally reacts more slowly to the return stage (mainly

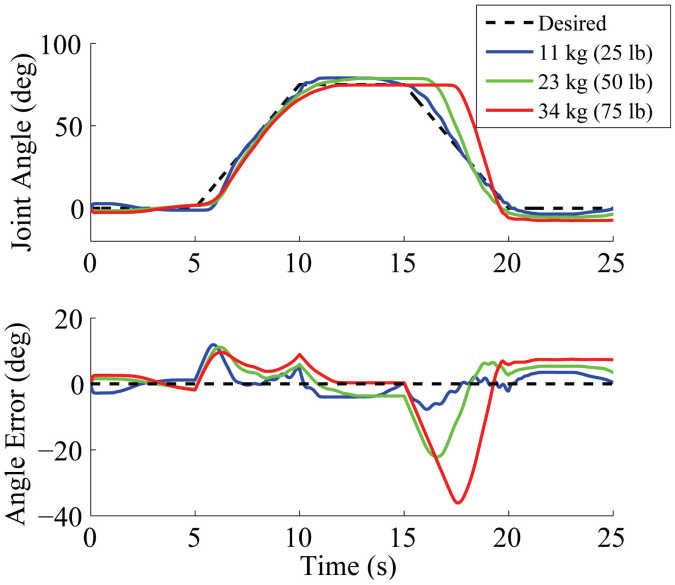


Figure 4.10: PID control with optimized gains.

due to integrator windup). The consistent lag of about 0.75 s in each fuzzy control case indicates that introducing a time-shift in the "Desired Angle" to account for the characteristic delay in the system as a type of feedforward correction could decrease error, thereby artificially improving the tracking capability of the joint. It should also be noted that this type of correction would likely be less beneficial to the PID controller because it can better track the lift slope and its major delay is only at the start of the return stage.

4.5.2 Model-Based Control with Output Feedback

4.5.2.1 Model Validation

Following successful simulations, the feedforward controller with PID/fuzzy feedback was implemented on the PAM-based manipulator using dSPACE real-time control hardware and software. Figure 4.13 displays both simulated and experimental

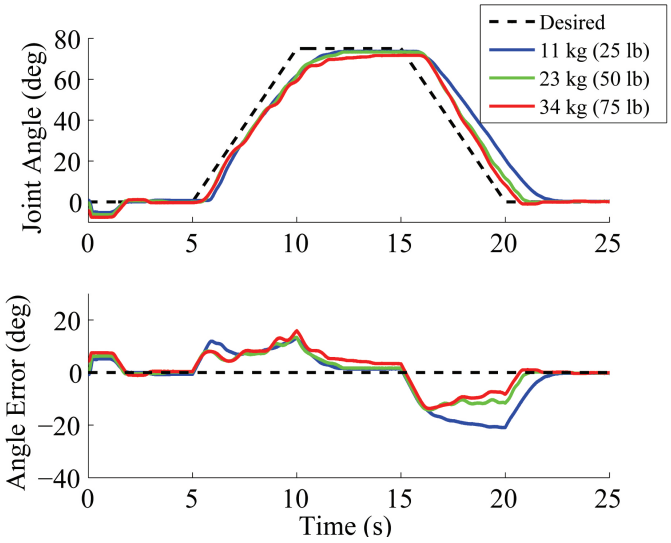


Figure 4.11: Fuzzy control with optimized gains.

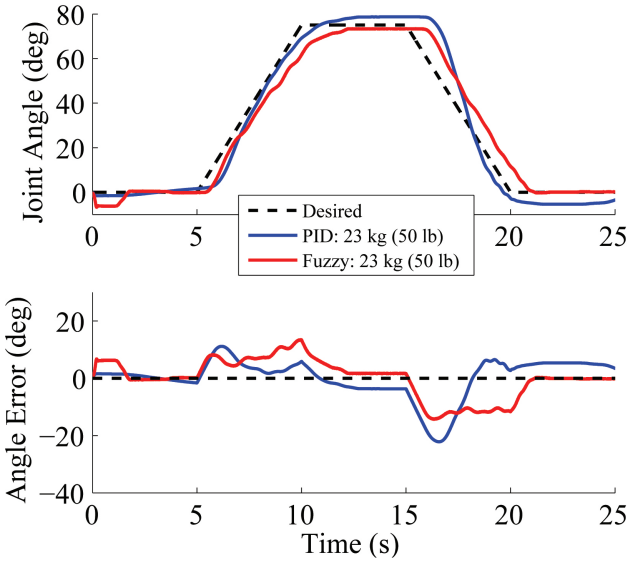


Figure 4.12: Comparison of optimized experimental PID and fuzzy control, 23 kg (50 lb) payload.

results for the same lift-hold-return trajectory with 45 kg (100 lb) and identical system gains ($g_1 = 0.4, g_2 = 0.3, h = 0.7, k_M = 0.5$). The only major difference between simulation and experimental results is the final resting angle after the return stage, which maintains a steady-state error even after 5 s. The major cause of the discrepancy is that the PAM model is inaccurate at low pressures ($<$ 40

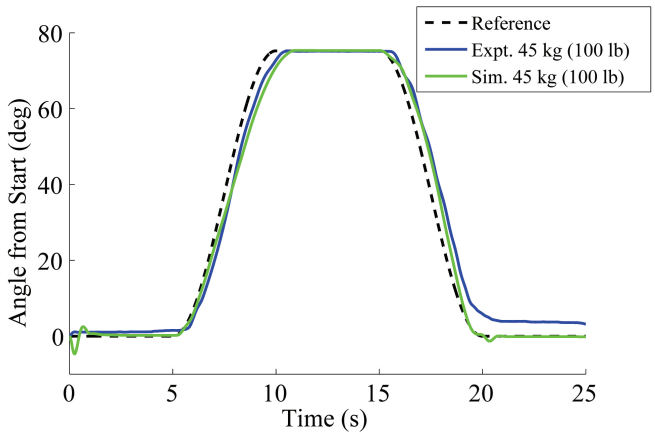


Figure 4.13: Simulated and experimental results using feedforward control with fuzzy feedback, 45 kg (100 lb) payload.

psi). Additionally, friction in the joint and hysteresis in the actuators that was not accurately described by the model exaggerate the error.

4.5.2.2 Experimental Analysis of Feedforward Gain

Significant variations in the system response with changing feedforward gain k_M warrant a more detailed analysis of this relationship. Figure 4.14 shows desired trajectory of several experimental trials varying k_M, while the feedback controller gains were fixed ($g_1 = 0.45, g_2 = 0.3, h = 0.7$). With $k_M = 0$ (pure fuzzy feedback), the responsiveness is low, and the lag increases error. However, this case has the lowest steady-state error at the initial/final angle, where the model is inaccurate. In terms of pressure, trials with higher k_M follow the predicted pressure (dotted line) more closely. This pressure trajectory, representing model calculation of needed pressure, is accurate at high pressures, but inaccurate lower. As k_M increases, the model aids the system in quickly responding to changes in direction, but the steady-state error at low angles (i.e., low pressures) increases. The optimal gain based on

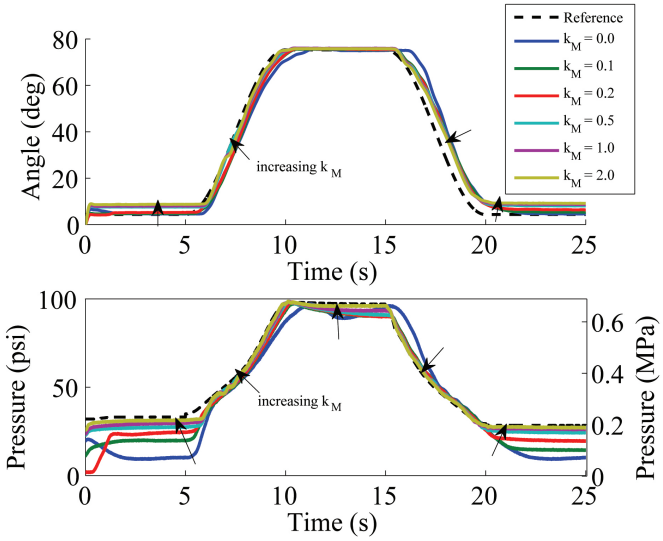


Figure 4.14: Lift-hold-return trajectory while varying model gain k_M, 23 kg (50 lb) payload.

RMS error over the 25 s interval is $k_M = 0.5$.

4.5.3 Discussion of Controllers

Figure 4.15 compares the response of the four controllers investigated. Two are simple output feedback controllers (PID and fuzzy) and two are model-based feedforward controllers augmented with PID and fuzzy feedback ($k_M = 0.5$). It is clear that the feedforward term increases accuracy in all stages of the response. Feedforward with PID control also decreases oscillation in comparison to PID control alone.

Responsiveness to change in direction is also improved with model-based feedforward control. In this manner, the feedforward term is similar to an increase in the feedback gains. Unlike increasing feedback gains, however, the system does not exhibit more oscillation. While there is a large time delay in arm angle, there is

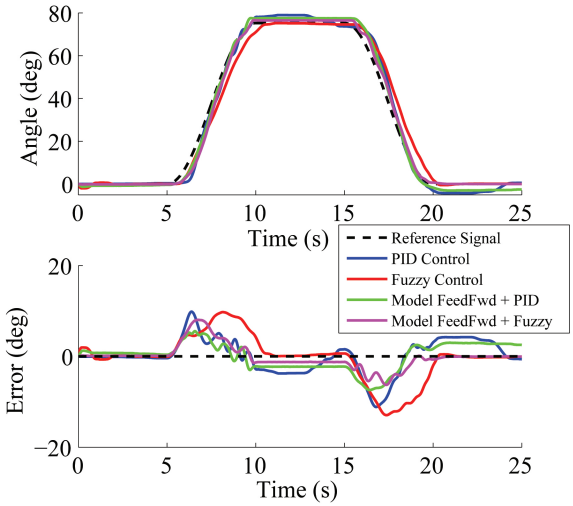


Figure 4.15: Comparison of lift-hold-return trajectories, 11 kg (25 lb) payload.

significantly less time delay in achieving desired pressure. Therefore, the convergence of actual and predicted pressure occurs smoothly and without overshoot.

4.6 Conclusions

This study investigated the use of several controllers on the elbow joint of a heavy-lift two degree-of-freedom manipulator actuated by pneumatic artificial muscles. Each method was designed, simulated, and implemented on experimental hardware. Output feedback (PID and fuzzy) controllers were examined, as well as model-based feedforward controllers augmented with output feedback. A model of the manipulator, actuators, and airflow dynamics was developed to enable simulation control studies and gain optimization. Trajectory-following experiments were conducted through simulation, as were preliminary gain optimizations, where it was determined that a combined performance metric weighing angle error and smoothness was necessary to achieve the desired response.

Using real-time interface software and hardware, the controllers were experimentally tested. Refinement of each technique was performed through an experimental gain tuning procedure, where it was learned that the predicted optimal gains were fairly accurate for PID and fuzzy control. When optimized, output feedback controllers demonstrated robustness to variations in payload weight over a large range of motion, and were shown to follow basic lift-hold-return trajectories with low oscillation, lag, and overshoot. PID control demonstrated higher accuracy and smoothness than fuzzy control during the lifting phase, but was more susceptible to overshoot and lag while holding or lowering the weight. The overall performance with output feedback alone suggested the need for improvement.

To improve closed-loop performance, model-based feedforward control augmented with output feedback was implemented. This approach was shown to produce smooth and precise motions with low error for varying payloads, even without changing control gains. The feedforward gain was also varied to demonstrate its effect on the response, where it was shown that there is an optimal gain setting. There is room for improvement in model accuracy at low pressures, which would allow for higher feedforward gain values and further improve the tracking ability of this control strategy.

Due to the complicated control structure and the unmodeled or unanticipated dynamics in the system, it is difficult to formally establish the stability of the system. When the open loop system is in static equilibrium at any point between the joint limits, the system is stable because of the large passive damping component inherent to pneumatic muscles. This damping helps to ensure that PAMs are stable in well-

tuned closed loop feedback systems. However, to guard against potential instability when a controller is employed, one should perform a careful analysis to determine a stable range of control gain values over the known range of payloads.

Future improvements to consider include a dynamic PAM model that better accounts for nonlinearities such as hysteresis, an adaptive element that responds to abrupt changes in payload in real-time, and automated trajectory planning. Another challenge is to extend this system to multiple degrees-of-freedom, where coupling between joints and three-dimensional motion increases complexity and small model errors may propagate to links farther down the manipulator.

Chapter 5: Advanced Control of PAM-Based Robotic Manipulators

5.1 Introduction

Pneumatic artificial muscles (PAMs), also known as McKibben muscles, are lightweight, compliant actuators composed of an elastomeric bladder surrounded by a helically-braided fiber sleeve. Internal air pressurization causes the bladder to make contact with the braid fibers, typically generating a contractile stroke as the bladder expands radially and fibers reorient. When prevented from freely contracting, these actuators generate axial force. As a result of their natural compliance and high specific force/power capabilities, PAMs are desirable in lightweight robotic manipulators, particularly those intended for interaction with humans. However, control of PAM-actuated systems, including PAM-based manipulators, has proven difficult due to the highly nonlinear nature of the actuators and the pneumatic systems supporting their actuation.

Past efforts to control pneumatic artificial muscles span a broad range of established techniques. In order to address the nonlinear behavior of these PAM-based systems, many approaches to PAM-based control have incorporated detailed empirical models of the system. The adoption of feedforward compensation was shown to improve the system response in Nho and Meckl [47] through the use of

inverse dynamics feedforward control. Fateh and Izadbakhsh [48] employed a similar hybrid computed torque approach. Vo Minh et al. [169] developed cascade position control with hysteresis compensation for a robotic manipulator, using a Maxwell slip model to characterize hysteretic behavior. Pure model-based control strategies rely heavily on the accuracy of the model to cancel nonlinearities, which can be a detriment to controller implementation, particularly in regard to development time and effort.

Several PAM control studies have employed model-based sliding mode control, a robust nonlinear control strategy intended to drive the dynamics of the system to that of an exponentially stable system [49]. Carbonell [51], Cai and Dai [52], and Lilly [53] each performed simulations of PAM-actuated systems using model-based sliding mode controllers. These above studies assumed that PAM pressure or force are instantaneous control inputs and must be regulated. In most practical applications, however, PAM pressure is subject to inherent delays from airflow dynamics (i.e., not instantaneous). To this end, Aschemann and Schindele [57] developed a model-based cascaded sliding mode controller with pressure feedback for a PAM-actuated rotary joint in a linear table. Shen [56] designed a model-based sliding mode controller including a dynamic airflow model, and applied it to a linear table actuated by PAMs. While sliding mode control is able to compensate for some uncertainty, model accuracy significantly impacts performance. Unfortunately, in some scenarios, the PAM actuator dynamics, system dynamics, and payload characteristics are unknown or time-varying, and the model employed is a poor approximation, which adversely affects closed-loop performance.

To better accommodate uncertainties in system dynamics, including large variations in payload, adaptive techniques may be employed. Caldwell et al. [63] employed adaptive control based on model estimation, but the closed-loop performance was sensitive to errors in the feedforward term. Rezoug et al. [170] developed an adaptive fuzzy nonsingular terminal sliding mode controller for a manipulator actuated by PAMs that requires no knowledge of the system. However, this controller requires torque sensing and an accurate estimate of acceleration, which may be difficult to obtain due to sensor noise.

An alternative approach that requires little or no prior knowledge is control with artificial neural networks. Neural networks are computational models that consist of a set of adaptive weights that are tuned by a learning algorithm. These models are capable of approximating a wide range of nonlinear functions of their inputs. Ahn and Nguyen [42] developed an intelligent switching algorithm for a PAM-based robot arm using a learning vector quantization neural network. The single degree-of-freedom system was restricted to low speeds and slowly varying inertial loads to remain stable. In a subsequent study, Ahn and Ahn [93] implemented an adaptive recurrent neural network on a PAM-actuated manipulator that was capable of compensating for payload mass and time-varying parameters on-line. The authors reported a 2000% change in system inertia between minimum and maximum loading (0.5 kg to 10 kg). However, in some high-loading cases, undesired oscillations were present. Furthermore, the stiffness of the system was high due to the antagonistic actuator arrangement, and was limited to only 20 deg of motion. Lastly, the system was actuated in the horizontal plane and was not subject to gravitational effects.

The objective of the present work is to develop control algorithms that allow a single degree-of-freedom PAM-based manipulator to smoothly and accurately track desired motions regardless of model quality and prior development effort. Studies that have successfully applied control to experimental PAM-actuated systems thus far have exhibited high stiffness, which generally reduces tracking error. However, the robotic manipulator employed in the present study is a uni-directionally actuated, low-stiffness system; PAMs lift the arm, but gravity provides the return force. Combined with highly variable inertial loads (an over 2500% increase from the unloaded condition) and a large (90 deg) range of motion, the problem of accurate position control becomes even more difficult.

In order to investigate the effects of different advanced control strategies on a heavy-lift PAM-actuated robotic manipulator, three concepts are developed for position control: sliding mode control, adaptive sliding mode control, and adaptive neural network control. These controllers are all partially based upon work by J.-J. Slotine concerning passivity and sliding control [50, 151]. Numerous simulations and experiments are performed to evaluate and compare closed-loop performance.

5.2 Robotic Manipulator

The manipulator employed in this study is a one degree-of-freedom version (shoulder joint only) of the two degree-of-freedom arm designed and tested in Section 3.5; the new configuration is displayed in Figure 5.1. Important features include uni-directional actuation (gravity provided the return force), a parallel arrangement of

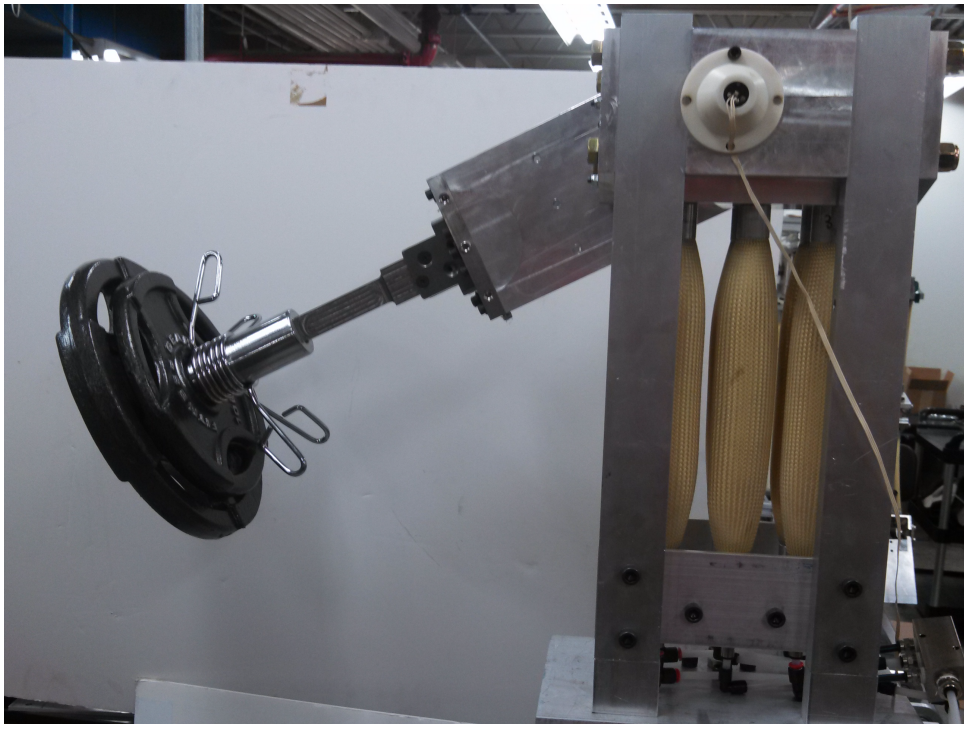


Figure 5.1: One degree-of-freedom robotic arm with 50 lb payload.

PAMs, and a nonlinear joint geometry that was optimized for torque generation over the full range of motion. The sensors on the manipulator are only capable of measuring angular position and PAM pressure signals, both of which have measurement noise.

Due to the PAMs' nonlinear force behavior and the aforementioned nonlinear joint geometry, the equation of motion relating PAM pressure to joint torque is complex. While a complete, highly detailed model of the pneumatic system was employed in Chapter 4, quasi-static manipulator torque may be approximated by a third-order polynomial function of angle and a linear function of pressure to simplify the controller structure:

$$\tau(P, \theta) = C_1(\theta)P + C_2(\theta) \tag{5.1}$$

$$C_1(\theta) = k_1\theta^3 + k_2\theta^2 + k_3\theta + k_4 \tag{5.2}$$

$$C_2(\theta) = k_5\theta^3 + k_6\theta^2 + k_7\theta + k_8 \tag{5.3}$$

The coefficients k_i were determined by a least-squares fit to best match the original model.

Figure 5.2 displays the original and simplified models, as well as experimental values of joint torque. The torque during contraction is different than during extension, which is a result of PAM hysteresis. Both models are fairly accurate within the range of expected manipulator angles and pressures (indicated by the vertical dashed lines at 15 deg and 110 deg).

Using the simplified model, the equation of motion for the present one degree-of-freedom manipulator is given by:

$$C_1(\theta)P + C_2(\theta) = I\ddot{\theta} + b\dot{\theta} + mgr\sin\theta \tag{5.4}$$

where I is inertia of the rotating arm link, b is viscous damping, m is the mass of the link, g is the gravitational constant, and r is the distance from the joint to the link center of mass. This formulation was applied in all three of the control strategies outlined in the next section.

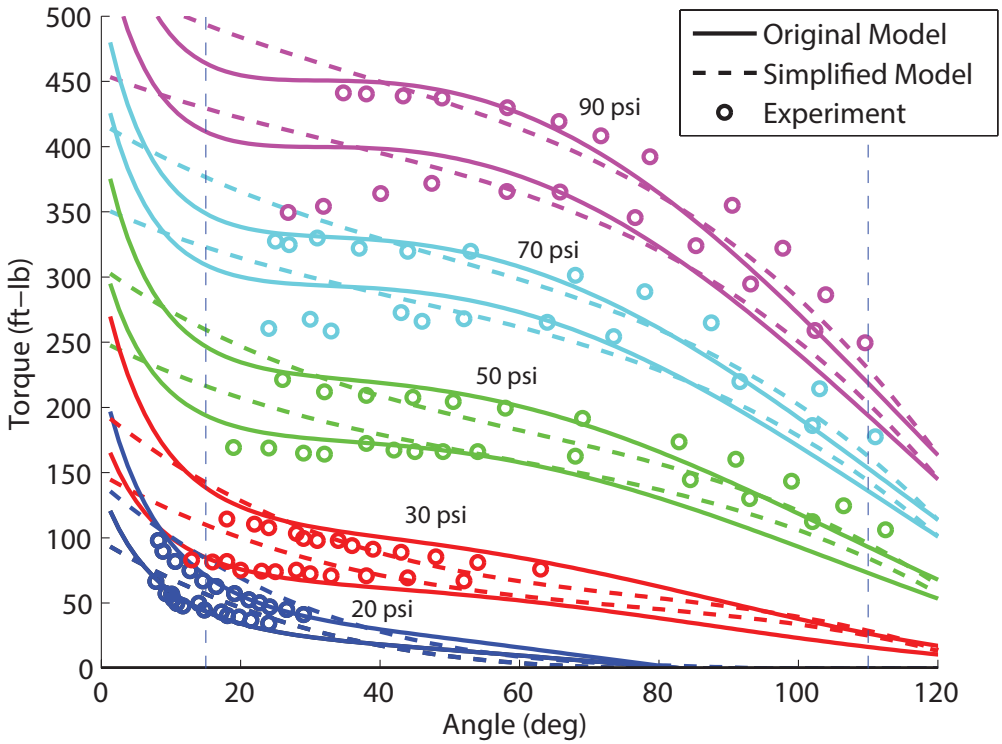


Figure 5.2: Torque vs. angle, comparison of models with experimental data.

5.3 Control Strategies

This section describes the design of three distinct nonlinear controllers. Each control strategy takes pressure and angle as sensor inputs, and ultimately outputs a voltage to the pneumatic valve controlling the airflow from a pressure source to the PAMs. It was determined in preliminary experiments that an inner pressure feedback loop is highly desirable; therefore, a cascaded structure was implemented. In this arrangement, angle feedback outputs a desired pressure, which is then used for pressure feedback. An example of a cascaded controller is shown in Figure 5.3. For the purposes of comparison, the controllers outlined below have identical PI controllers for pressure feedback. This work focuses on the angle feedback component,

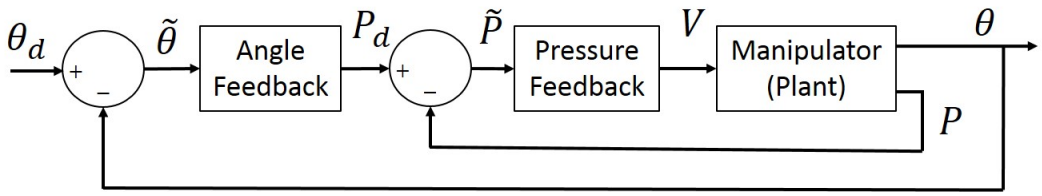


Figure 5.3: Diagram of a cascaded controller.

which simplifies the control problem, but relies on a high pressure loop tracking bandwidth.

5.3.1 Sliding Mode Control

Sliding mode control attempts to send the state of the system to a "sliding surface," from which the system will exponentially converge. This sliding surface is typically defined as $s = 0$, where s is an error metric given by $s = \dot{\theta} + \lambda\theta$. In order to drive the dynamics of a given system to that of an exponentially stable system, a signum function is applied. Slotine and Li [151] developed a control law specific to robotic manipulators:

$$\tau_d = \hat{H}(\theta)\ddot{\theta}_r + \hat{C}(\theta, \dot{\theta})\dot{\theta}_r + \hat{G} - K_D \text{sgn}(s) \tag{5.5}$$

where H, C and G are the inertial, Coriolis, and gravitational components of a general manipulator, respectively. The terms $\ddot{\theta}_r = \ddot{\theta}_d - \lambda\dot{\tilde{\theta}}$ and $\dot{\theta}_r = \dot{\theta}_d - \lambda\tilde{\theta}$ are used to simplify the expression. This control law is guaranteed stable, assuming instantaneous torque and a sufficiently high controller gain K_D. Slotine and Li show

this by defining a Lyapunov function candidate:

$$V = \frac{1}{2} s^T H s \tag{5.6}$$

Differentiating this expression yields

$$\dot{V} = s^T H \dot{s} + \frac{1}{2} s^T \dot{H} s = s^T (H\ddot{\theta} + H\ddot{\theta}_r) + \frac{1}{2} s^T \dot{H} s \tag{5.7}$$

By substituting in the system dynamics from Eqn. 5.4 and the control law, Eqn. 5.5, rearranging terms, and noting that the matrix $\dot{H} + 2C$ is skew-symmetric, the equation [151]

$$\dot{V} = s^T (\tilde{H}\ddot{\theta}_r + \tilde{C}\dot{\theta} + \tilde{G}) - \sum_1^n K_{D,i} |s_i| \tag{5.8}$$

is obtained, where $\tilde{H}$,$\tilde{C}$, and $\tilde{G}$ represent model error in the corresponding matrices. So long as the second term is greater than the first (i.e., K_D is sufficiently high), $\dot{V}$ is negative, and the system reaches the sliding surface in finite time, and then converges to θ_d exponentially.

For a single degree-of-freedom manipulator with damping, as is the case for the present work, the control law Eqn. 5.5 simplifies to:

$$\tau_d = \hat{I}\ddot{\theta} + \hat{b}\dot{\theta}_r + \hat{mgr}\sin\theta + C_2(\theta) - K_D \mathrm{sgn}(s) \tag{5.9}$$

Torque cannot be commanded or monitored for direct feedback control in the present system, but pressure can be regulated. Therefore, desired pressure is treated as the

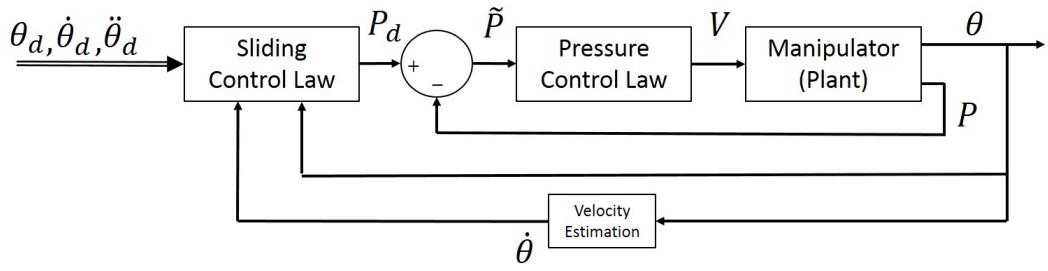


Figure 5.4: Diagram of sliding mode controller.

controller output (system input). Eqn. 5.4 can be rearranged as:

$$P = \frac{1}{C_1(\theta)}\{I\ddot{\theta} + b\dot{\theta} + mgr\sin\theta - C_2(\theta)\} \tag{5.10}$$

With the addition of a sliding term, the sliding mode control law then becomes:

$$P_d = \frac{1}{C_1(\theta)}\{I\ddot{\theta} + b\dot{\theta} + mgr\sin\theta - C_2(\theta)\} - K_D\text{sgn}(s) \tag{5.11}$$

Figure 5.4 illustrates the sliding mode control strategy. Note the inner pressure feedback loop, which employs proportional-integral (PI) control. The desired and actual pressure signals are filtered to ensure smoothness, which improves the performance of the PI controller without reducing the tracking bandwidth.

5.3.2 Adaptive Sliding Mode Control

The sliding control methodology presented above can be extended to permit adaptive updating of system parameters, potentially improving the response to unmodeled dynamics and payload variation. Slotine and Li [50, 151] provide a modification to the sliding controller to permit adaptation of certain parameters such

as inertia, damping, and gravitational terms. When the manipulator dynamics are well known and equations are structured in a simple manner, parameter convergence and good trajectory-following is possible.

In many applications, the model might be only partially known or the system payload may change over time. We can define a matrix of "known" parameters (functions of angular position and velocity) $Y = Y(\theta, \dot{\theta}, \theta_r, \dot{\theta}_r)$ such that the control law becomes

$$\begin{aligned} \tau_d &= \hat{H}(\theta)\ddot{\theta} + \hat{C}(\theta, \dot{\theta})\dot{\theta} + \hat{G} - K_D \text{sgn}(s) \\ &= Y(\theta, \dot{\theta}, \theta_r, \dot{\theta}_r)\hat{a} - K_D \text{sgn}(s) \end{aligned} \tag{5.12}$$

where $\hat{a}$ is the set of parameters to be updated. In the present case, we choose $\hat{a} = [\hat{I} \;\; \hat{b} \;\; \hat{mgr}]$.

Reformulating the equation in terms of a desired pressure, as in 5.11:

$$P_d = \frac{1}{C_1(\theta)}\{Y(\theta, \dot{\theta}, \theta_r, \dot{\theta}_r)\hat{a} - K_D \text{sgn}(s)\} \tag{5.13}$$

The parameter estimates $\hat{a}$ can be updated using a number of methods. In this study, we choose a simple gradient-based method:

$$\dot{\hat{a}} = -\Gamma Y^T s_\Delta \tag{5.14}$$

where Γ is a user-defined (normally diagonal) adaptation gain matrix and s_Δ is the

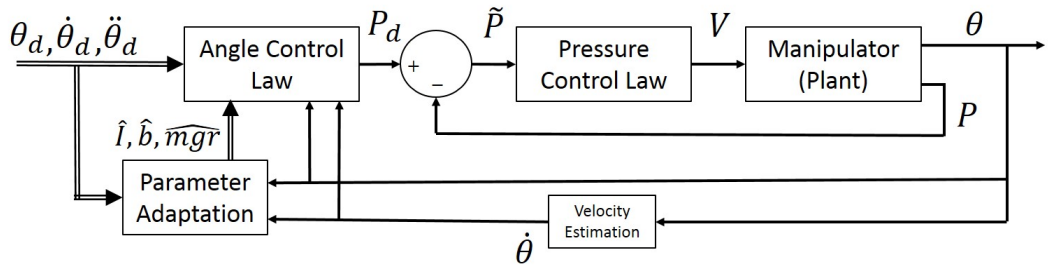


Figure 5.5: Diagram of adaptive sliding mode controller.

error metric modified to include a deadband:

$$s_\Delta = \begin{cases} s & s > \epsilon_{db} \\ 0 & \text{otherwise} \end{cases} \tag{5.15}$$

ϵ_{db} is a constant denoting the deadband width, and was set to 0.02. A diagram of the complete system is shown in Figure 5.5. Note that this approach does not necessarily estimate the unknown parameters exactly, but simply produces values that allow the system to follow the desired trajectory.

5.3.3 Adaptive Neural Network Control

The adaptive control strategy presented above cannot adapt the highly nonlinear, manipulator-specific equations relating pressure input to PAM force, or from PAM force to manipulator torque (due to the complex joint geometry). Parts of the manipulator model must be determined a priori, and cannot be adaptively updated using Slotine's framework. While it is possible to update several parameters, such as $\hat{I}$, $\hat{b}$, $\hat{mgr}$, and even the coefficients of $\hat{C}_2(\theta)$ if desired using the above adaptive method, the above strategy does not permit the adaptation of $\hat{C}_1(\theta)$. Using adaptive

sliding mode control, we must assume that $\hat{C}_1(\theta)$ is accurate when in fact, from Figure 5.2, we know there is some error between model and experiment. This motivates the use of neural networks, which employ a flexible mathematical framework to conform to the nonlinear system dynamics. In many cases, the application of neural networks renders a detailed system model unnecessary, which is typically a great benefit, though it comes at the expense of physical understanding and intuition of the system.

The neural network control law is composed of several terms relating the known functions of angle (and its derivatives) to unknown functions of angle:

$$P_d = \hat{H}(\theta)\ddot{\theta} + \hat{C}(\theta)\dot{\theta} + \hat{G}(\theta) - K_D \text{sgn}(s) \tag{5.16}$$

where the "effective" inertia, damping, and gravity terms are given respectively by:

$$\hat{H}(\theta) = \hat{C}_1(\theta)^{-1}\hat{I} \tag{5.17}$$

$$\hat{C}(\theta) = \hat{C}_1(\theta)^{-1}\hat{b} \tag{5.18}$$

$$\hat{G}(\theta) = \hat{C}_1(\theta)^{-1}(\hat{mgr}\sin\theta - \hat{C}_2(\theta)) \tag{5.19}$$

Using the above equations, we can approximate $H(\theta)$, $C(\theta)$, and $G(\theta)$ as nonlinear functions of angle, and adapt the estimates in response to system excitation.

The neural network architecture used to capture nonlinear plant behavior

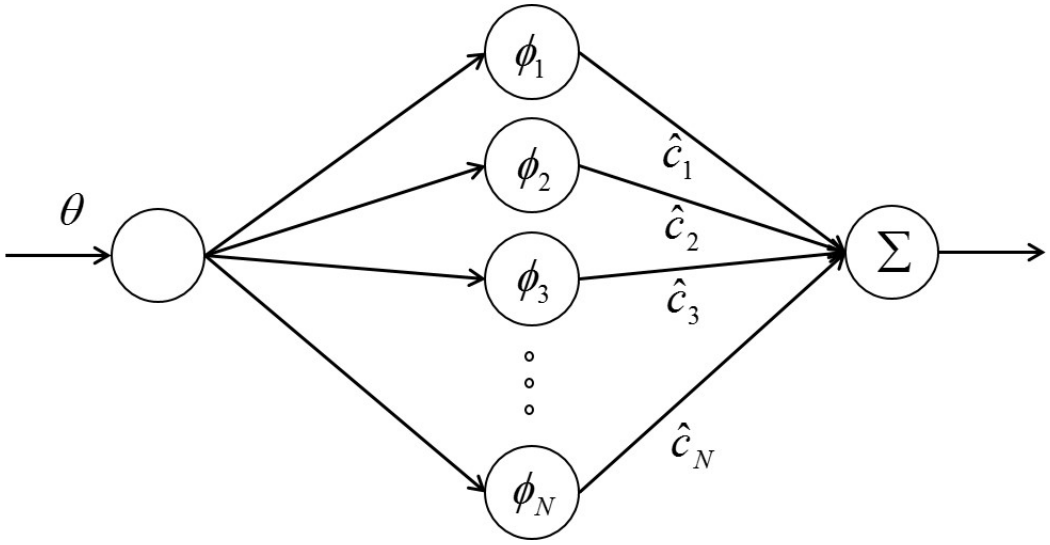


Figure 5.6: Single layer neural network structure.

was composed of a single layer of basis functions with corresponding weighting functions, similar to the approaches in Liu [174] and Sanner and Kosha [173]. A visual representation of the network is shown in Figure 5.6. Mathematically, the network approximation function for $H(\theta)$ is given by a summation of weighted basis function nodes:

$$\hat{H}(\theta) = \sum_{k=1}^{N} \hat{c}_{k,H} \phi(h\theta - k) \tag{5.20}$$

where k is the node index, h is the scale factor between nodes, N is the total number of nodes, $c_{k,H}$ is the kth weighting coefficient denoting the "height" of the kth node, and $\phi(h\theta - k)$ is the kth basis function. Identical formulas are used for $\hat{C}(\theta)$ and $\hat{G}(\theta)$. Triangular basis functions were chosen for their simplicity and ease of computation. Weighting coefficients $c_{k,H}$ were adjusted at each time step so that the network would converge to the desired function. The update law for the weighting function is given

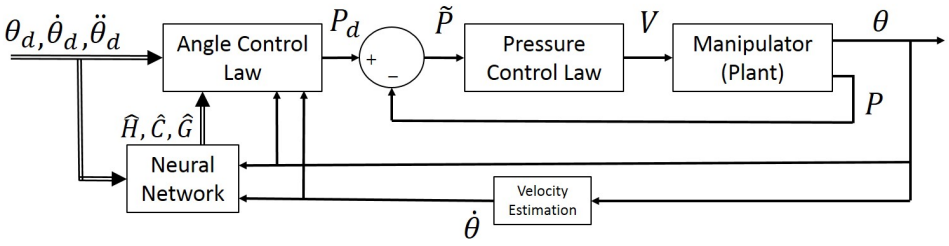


Figure 5.7: Diagram of adaptive neural network controller.

by:

$$\dot{\hat{c}}_{k,H} = -\gamma_H \phi(h\theta - k)\ddot{\theta}_r s_\Delta \tag{5.21}$$

$$\dot{\hat{c}}_{k,C} = -\gamma_C \phi(h\theta - k)\dot{\theta}_r s_\Delta \tag{5.22}$$

$$\dot{\hat{c}}_{k,G} = -\gamma_G \phi(h\theta - k) s_\Delta \tag{5.23}$$

where the γ terms are gains.

Figure 5.7 illustrates the neural network controller in detail. Its overall structure is very similar to that of the adaptive sliding controller, except the neural network outputs arrays corresponding to angle-dependent functions, rather than a few updated parameters.

5.4 Position Control Results

The controllers were implemented in MATLAB/Simulink, which interfaced with dSPACE software and hardware for data acquisition and real-time control.

Table 5.1: Parameter values of sinusoids in desired trajectory.

Index i	Amplitude A_i (deg)	Frequency ω_i (rad/s)
1	20	0.70
2	13	0.95
3	7	1.55
4	5	0.80

Results from the numerous trajectory-following experiments performed on the robotic manipulator demonstrate the utility of these distinct strategies.

5.4.1 Sliding Mode Control

The sliding mode controller was implemented first in experiments. The arm was commanded to follow a trajectory composed of several sinusoids and a small ramp. This desired trajectory (in degrees) is given by:

$$\theta_d = \sum_{i=1}^{4} A_i \cos \omega_i t + y_{tri} + 50 \tag{5.24}$$

where A_i and ω_i are the amplitude and frequency, respectively, of each sinusoid, and y_{tri} is a repeating triangular wave with a frequency of 0.16 Hz, a peak-to-peak amplitude of 20 deg, and a bias of 10 deg. Table 5.1 displays the parameter values of each sinusoid.

Figure 5.8 displays results from multiple sliding mode control experiments. Figure 5.8(a) illustrates the desired and acutal angle trajectories, Figure 5.8(b) shows angle error, and Figure 5.8(c) depicts the mean squared error (MSE) of each experiment as time progresses. Overall, results demonstrate that this controller

is capable of smooth, chatter-free motion. When the system model is accurate, including parameters $\hat{I}$, $\hat{b}$, and $\hat{mgr}$, then the controller cancels out most of the nonlinear dynamics. This leads to high accuracy trajectory-following. However, when these values are inaccurate, the system tends to over- or under-estimate the required pressure. For instance, in Figure 5.8, the blue curve corresponds to a controller with accurate measurements of joint inertia, damping, and mass. The red curve represents these values decreased by 90% (0.1x), and the green curve represents these values increased by 900% (10x). Surprisingly, the trajectory-following remains stable despite these extreme parameter estimates. However, it is clear that the experiment exhibiting the lowest error corresponds to the controller with accurate parameter measurements.

While sliding mode control is capable of smooth, accurate performance, the potential for poor estimation (which may be exacerbated with poor choice of controller gains K_D and λ) or dynamic variations in payload motivates the design of a controller that can adaptively update.

5.4.2 Adaptive Sliding Mode Control

As shown in Section 5.3.1, sliding mode control can be easily modified for parameter adaptation using the formulation developed by Slotine, with modifications for the additional nonlinearities in this PAM-actuated system ($C_1(\theta)$ and $C_2(\theta)$). The adaptive controller was tested several times for the same trajectory and utilizing the same controller gains as in non-adaptive sliding control. Each trial employed a

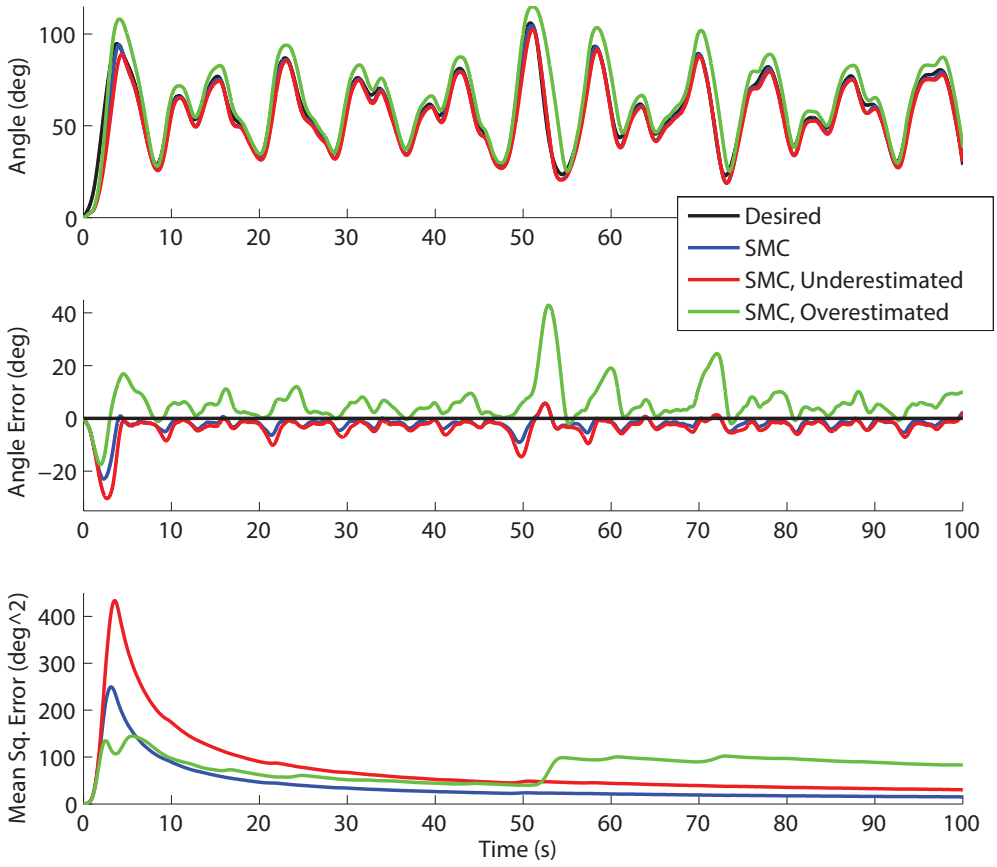


Figure 5.8: Sliding mode control results: (a) angle, (b) angle error, and (c) mean squared error.

different set of adaptation parameter gains, listed in Table 5.2. Note that the trajectory is sufficiently complex to satisfy the "persistence of excitation" requirements for an adaptive controller of this type [151].

Figure 5.9 displays the angle trajectories and error metrics associated with each trial. The results demonstrate that this adaptive controller is somewhat useful for improving trajectory-following after a "learning" period. However, there are underlying problems with the adaptation process.

The time-dependent adaptive parameter values obtained in each trial are shown

Table 5.2: Adaptation gains for adaptive sliding mode control.

	$\gamma_{\hat{I}}$	$\gamma_{\hat{b}}$	$\gamma_{\hat{mgr}}$
Trial 1	10	10	0.01
Trial 2	100	100	0.001
Trial 3	100	100	0.0001

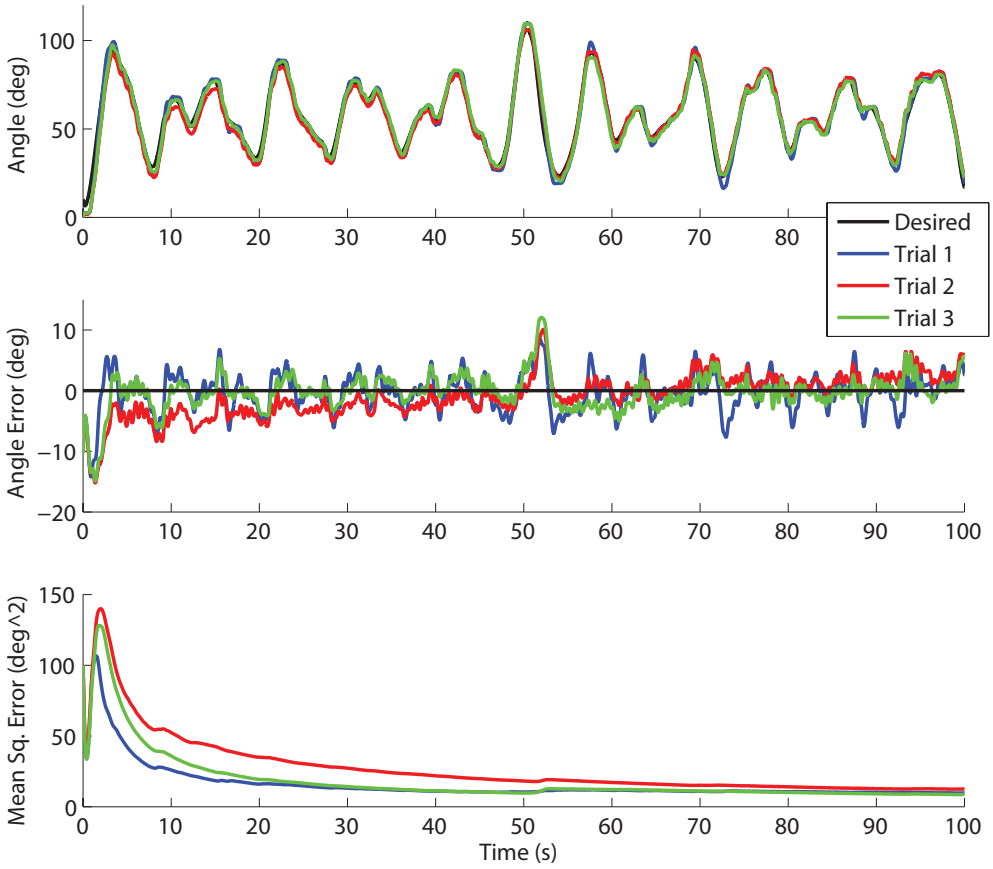


Figure 5.9: Adaptive sliding control results: (a) angle, (b) angle error, and (c) mean squared error.

in Figure 5.10. It is clear that parameter estimates are dependent upon choice of adaptive gains $\gamma_{\hat{I}}$, $\gamma_{\hat{b}}$, and $\gamma_{\hat{mgr}}$. Moreover, in most cases, the $\hat{I}$ and $\hat{b}$ terms do not converge. Inertia and damping play only a minor role when the system is moving slowly, so the trajectory is not affected; however, increasing the excitation frequency

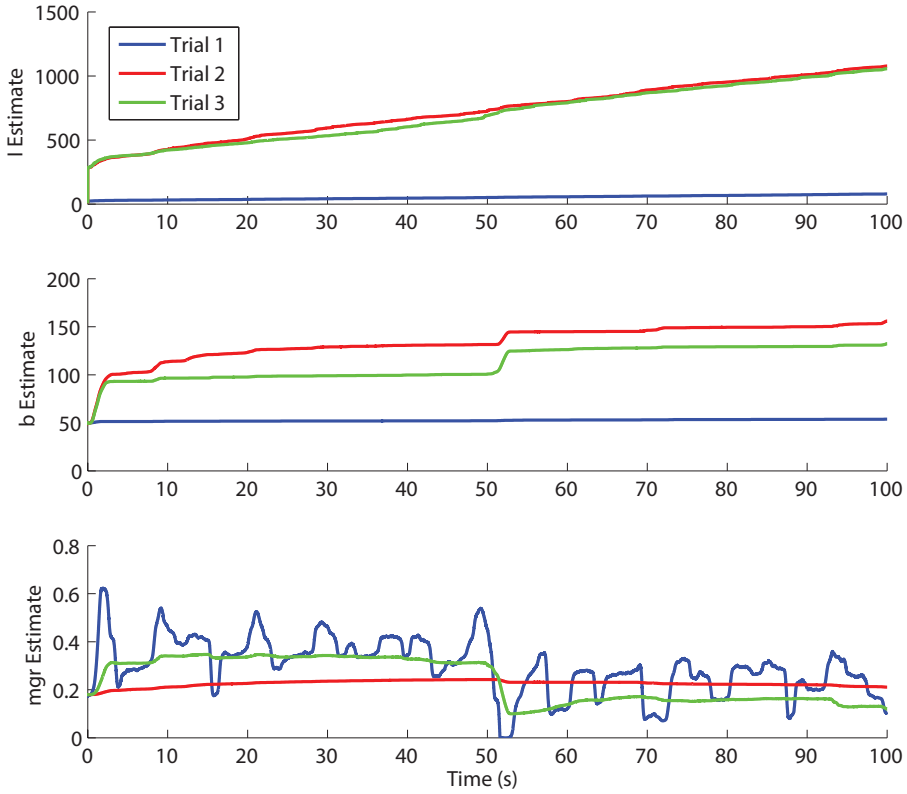


Figure 5.10: Parameter adaptation for three experiments, varying adaptation gains.

or further increasing the gains led to an unstable system. When the $\hat{mgr}$ update gain is high (blue curve), it is also unable to reach a steady-state. In fact, the $\hat{mgr}$ estimate exhibits angle dependence, most notably in Trial 1. This suggests that the joint nonlinearities, which were supposedly negated by the $C_1(\theta)$ and $C_2(\theta)$ terms, have not been fully accounted for. One potential solution to this problem is the use of adaptive neural networks, as was described previously.

5.4.3 Adaptive Neural Network Control

Figure 5.11 displays a trajectory-following experiment using the neural network approach. Again, the same trajectory is used; the complex waveform was sufficient to induce network learning. The network was initialized in two ways, with and without knowledge of an initial model. The blue curve displays the trajectory when the neural network has no initial knowledge of the system structure, $\hat{H}(\theta) = \hat{C}(\theta) = \hat{G}(\theta) = 0$, while the red curve corresponds to a network initialized with an educated guess using the simplified model. The results show that the angle error is consistently reduced as the neural network is trained on-line, regardless of initial parameterization.

Additional insight can be gained from observing the evolution of the adaptive functions $\hat{H}(\theta)$, $\hat{C}(\theta)$, and $\hat{G}(\theta)$ as time elapses. Figure 5.12 displays the adaptive functions that begin with no *a priori* information. Note that this system initially assumes zero inertia, damping, and mass, which is clearly an underestimate. As the experiment progresses, the functions are constructed. By 100 s, the adaptive functions have nearly converged because the trajectory is being followed with very low error. Figure 5.13 shows a similar test where *a priori* estimates of $\hat{H}(\theta)$, $\hat{C}(\theta)$, and $\hat{G}(\theta)$ are given. The final structures of these three functions are very similar to those gained from using no prior information.

The power of neural networks is clear: even with no knowledge of the PAM actuators or joint kinematics, functions that model the system dynamics may be quickly assembled and yield a smooth, accurate closed-loop response. However, when the networks are initially zero-valued, we observe that the ability to construct the

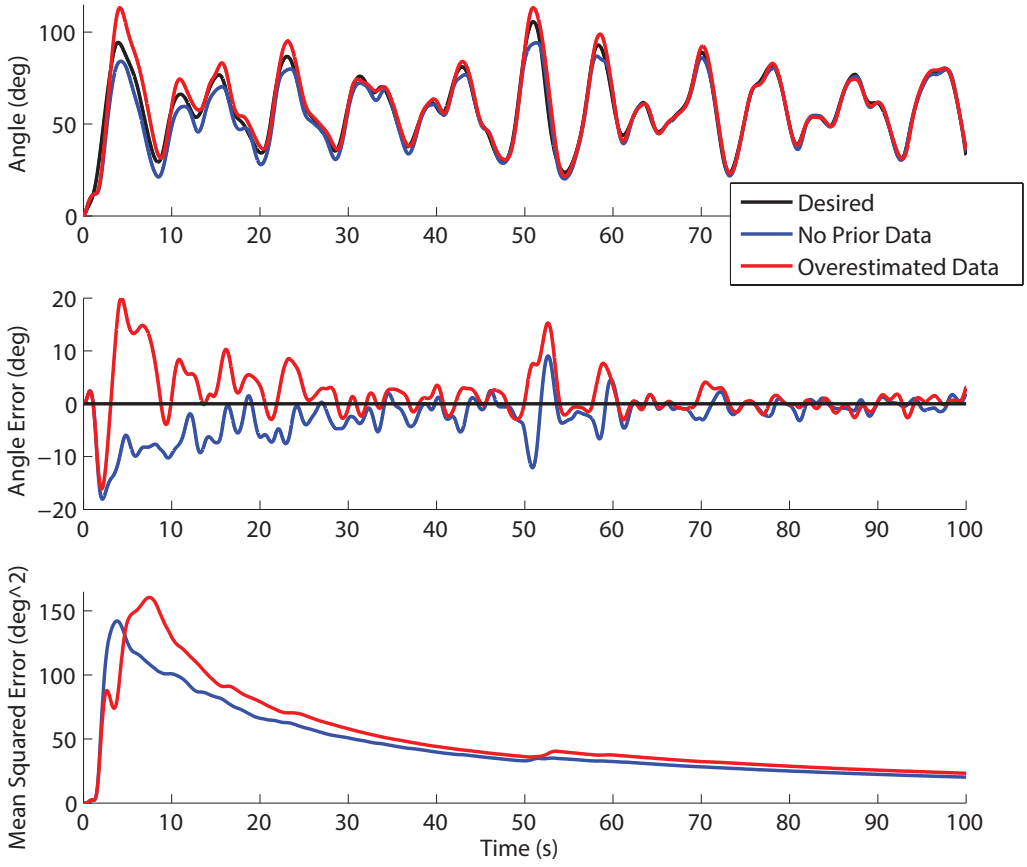


Figure 5.11: Adaptive neural network control for two distinct initial conditions; (a) angle, (b) angle error, and (c) mean squared error.

function at angles above 90 deg is limited. Sharp "peaks" and "valleys" often form on the cusp of the region where the network has been trained and where it has not, as shown in the G estimate of Figure 5.12, between 80 and 100 deg. When the desired arm trajectory reaches an angle corresponding to a "valley," the controller assumes low torque requirements, and gravity causes the arm to drop so that it does not reach the desired angle and cannot be tuned. In this manner, the system never builds up the capacity to learn high angles. The structure of the networks may be partially to blame: the triangular basis functions employed in the present work have

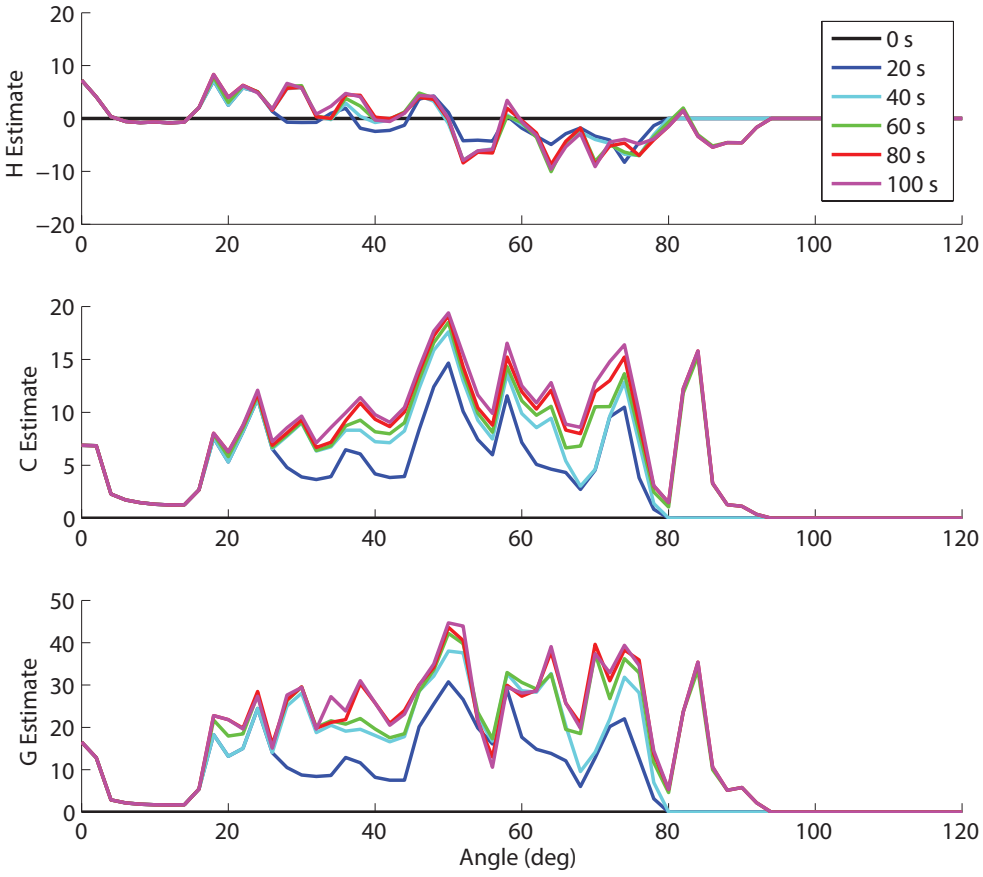


Figure 5.12: Neural network adaptation over 100 s, 50 lb payload, no prior information.

narrow support and tend to create sharp transitions as angle increases. This effect may be mitigated through the use of Gaussian basis functions, though this would be at the expense of increased complexity and computational load.

The neural network is able to learn the structure of systems with high payload variation. Figure 5.14 displays data from tests with 0 lb, 25 lb, and 50 lb payloads. From the 0 lb configuration to the 50 lb configuration, the inertia increases by a factor of 30. Generally, error increases with increasing payload. This trend partially arises because the network requires more time to "learn" functions with higher values.

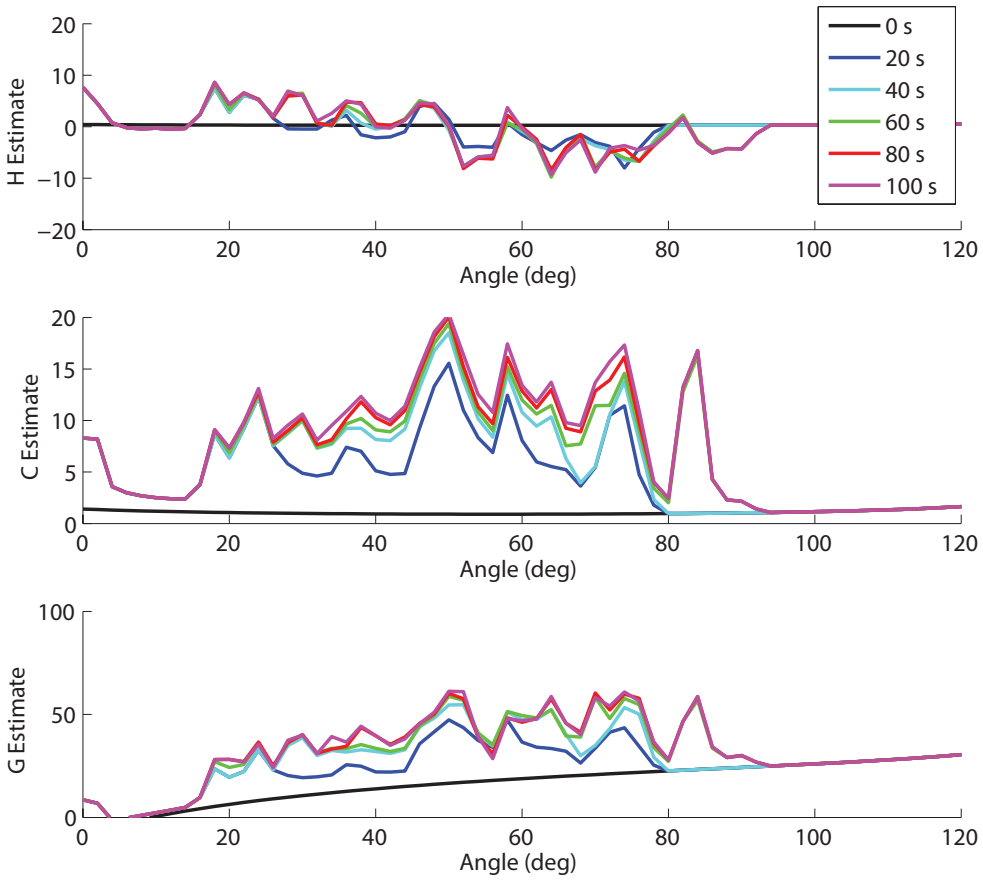


Figure 5.13: Neural network adaptation over 100 s, 50 lb payload, with model.

Additionally, as torque requirements increase, required pressure also increases, which is more difficult for the system to maintain. It is important to note that the internal pressure loop is a limiting factor in the system bandwidth.

Following adaptation of the neural networks to a particular payload, the payload can change, and adaptation to the new payload will occur. In order to demonstrate effects due to payload change, the controller was first tested with a light payload (15 lb), and the neural networks were initialized at zero (no prior information). After 100 s, the neural network structure in the system was saved. Subsequently the payload

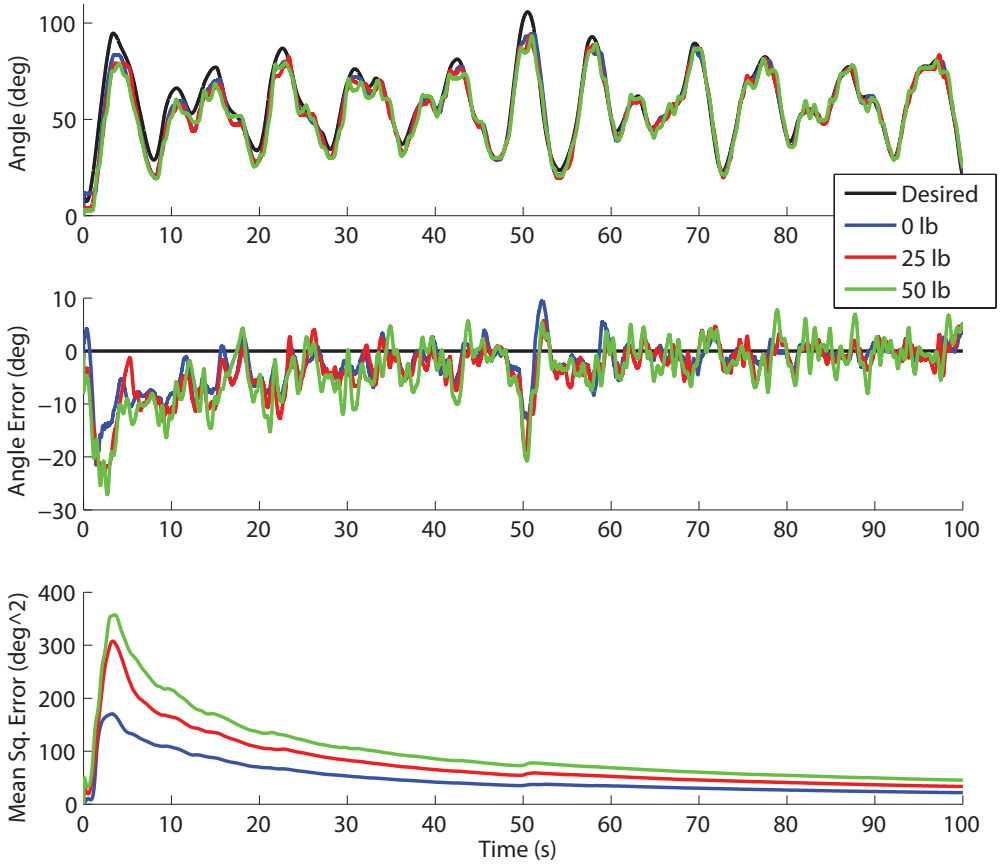


Figure 5.14: Adaptive neural network control, varying payloads; (a) angle, (b) angle error, and (c) mean squared error.

was increased to 50 lb, and the initial structure of the neural network was chosen to be the saved data from the 15 lb test.

Figure 5.15 displays the construction of the initial neural network from the 15 lb payload test. Figure 5.16 shows the adaptation from the neural network which starts with the final structure from Figure 5.15 and ends with a newly adapted network. As expected, the c_G function has an overall greater value, indicating that payload weight has increased.

Figure 5.17 shows the trajectory-following of the neural network controller

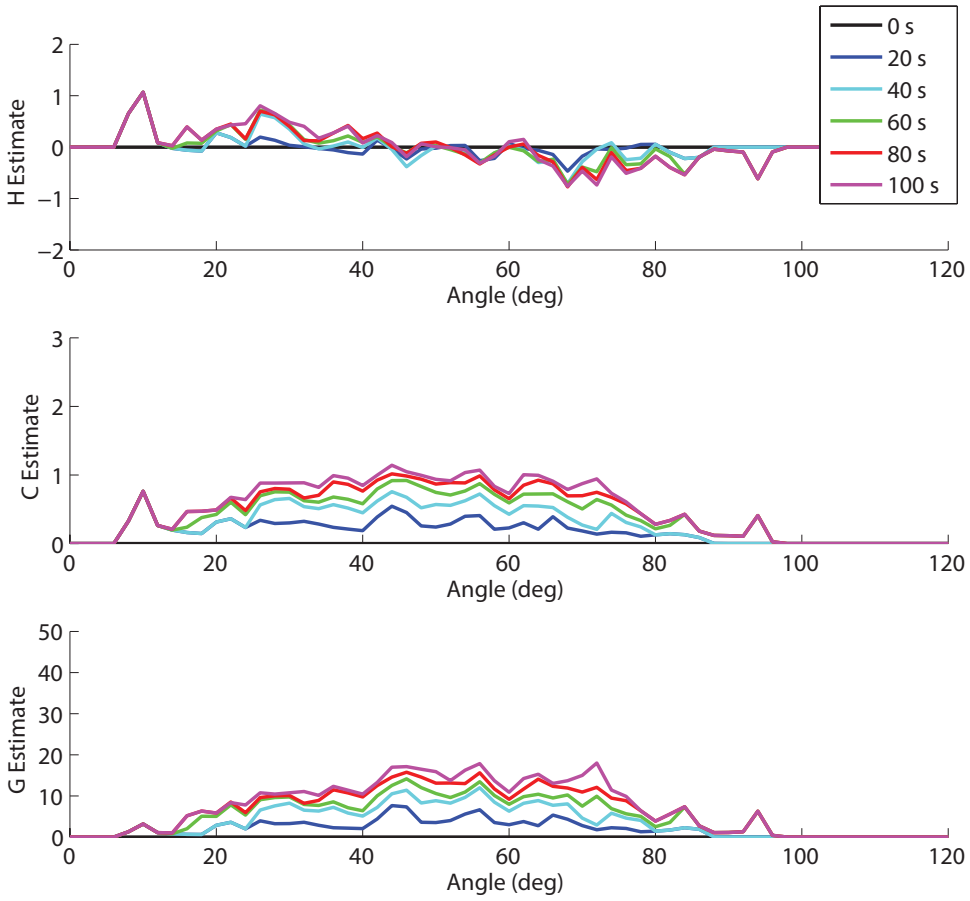


Figure 5.15: Neural network adaptation over 100 s, 15 lb payload, no prior information.

with a 50 lb payload, comparing the response from a neural network initialized with no prior data with a network pre-trained with a 15 lb payload. As expected, the mean-squared error is less for the system that has been pre-trained.

5.5 Discussion and Comparison of Controllers

Figures 5.19 and 5.20 compare four controllers following a complex sinusoidal trajectory and a lift-hold-return trajectory, respectively. In addition to the three controllers designed in this work, a cascaded PID controller (with angle and pressure

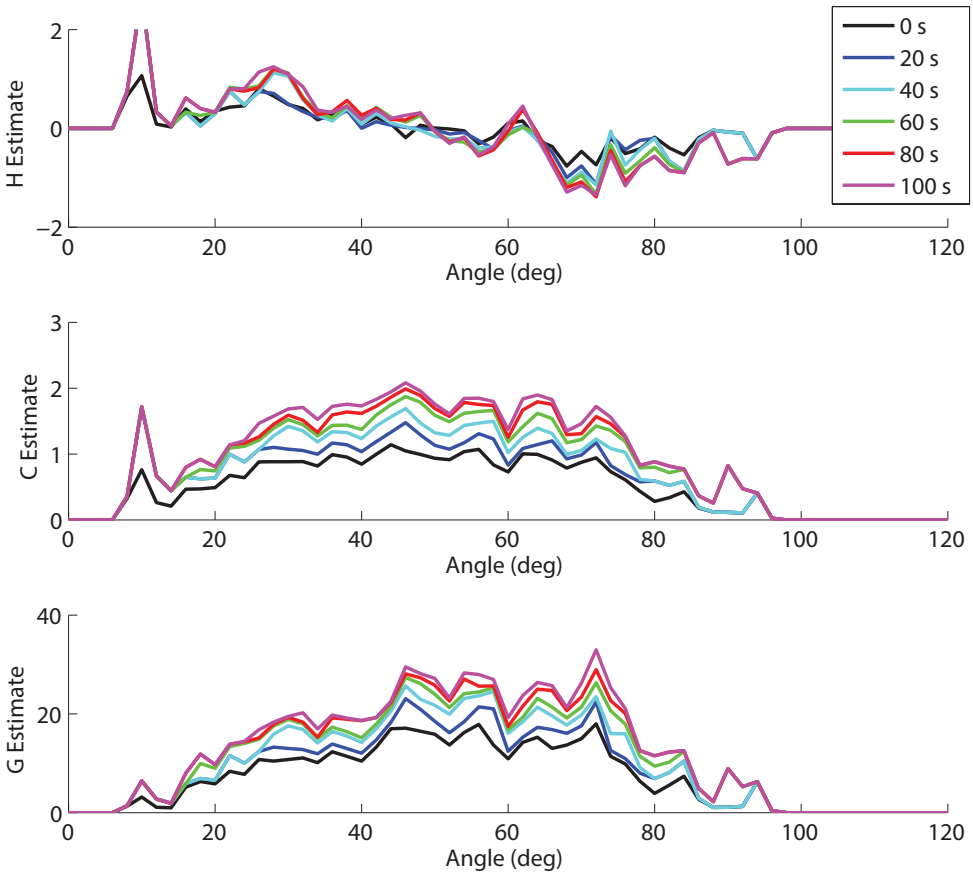


Figure 5.16: Neural network adaptation over 100 s, 50 lb payload, with network initialized from 100 s of training with 15 lb payload.

feedback) was added for comparison. A diagram of the controller is shown in Figure 5.18. For these comparisons, the two adaptive controllers were trained in previous experiments for 1000 s, and the resulting adaptive functions were saved. Therefore, the adaptive controllers begin with the ability to compensate for the system dynamics.

The mean squared error plot, Figure 5.19(c), illustrates that the trained adaptive controllers exhibit the highest cumulative accuracy by the time of trajectory completion. With accurate initial parameters, sliding mode control is more accurate than cascaded PID control, but less accurate than the two adaptive controllers. The

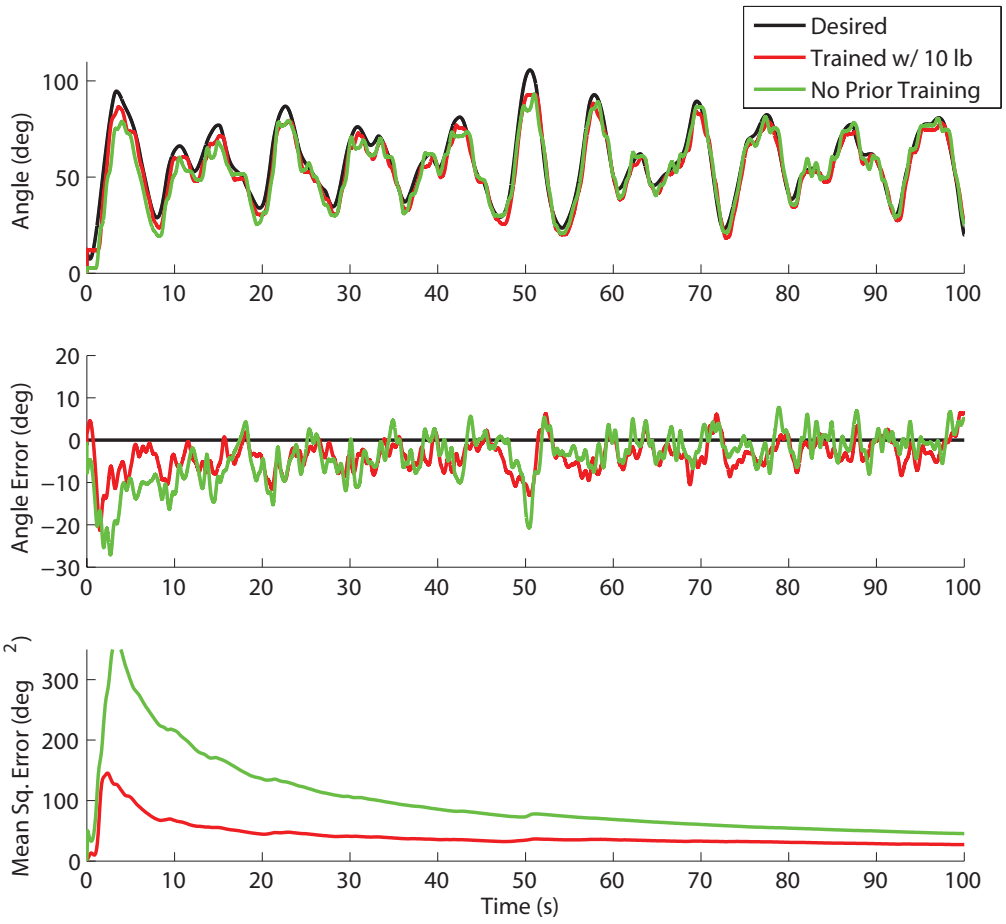


Figure 5.17: Adaptive neural network control, varying initial network structure; (a) angle, (b) angle error, and (c) mean squared error.

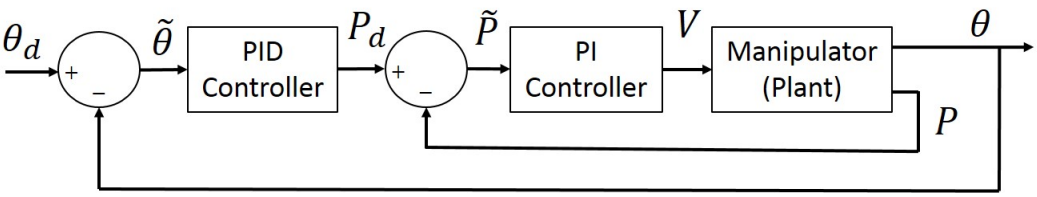


Figure 5.18: Diagram of a cascaded PID controller.

sliding mode controller and adaptive sliding mode controller trajectories both display low-amplitude, high-frequency content, which can be observed in Figure 5.19(b). Depending on the intended application, the vibration transmitted to the payload (e.g., an injured person) may be undesirable.

In Figure 5.20 similar results are observed. The adaptive sliding mode controller again provides the greatest accuracy, but sliding mode control is slightly more accurate than neural network control. However, this is primarily an artifact of the error caused by the neuro-controller's long rise time to the initial "resting" angle of 15 deg. After that initial rise, the steady-state error of the neural network control trajectory is considerably lower than both forms of sliding mode control. Also note that the adaptive and non-adaptive sliding mode controllers again sacrifice smoothness for accuracy during the return phase, illustrated by the minor oscillations between 15 and 20 s in Figure 5.20(a), which is not preferred for the intended application of human interaction, as stated previously. Overall, all of the advanced controllers provide good performance.

Considering the results of the previous section, it is clear that the proper selection of a control strategy depends upon the level of prior knowledge of the system and the intended application. If the system has been well characterized and parameters do not vary, then standard sliding mode control will likely suffice. Experiments employing the sliding mode controller were able to follow a complex waveform, and demonstrated robustness to large changes in model parameters.

If the system is poorly characterized, or is expected to confront dynamic changes in payload, an adaptive strategy is likely preferable. In many lifting tasks, particularly lifting humans for casualty extraction applications, the payload may shift. For this reason, it is important that an adaptive capability be added to the robot. The modified version of Slotine's adaptive sliding controller displayed some improvement over non-adaptive (standard) sliding mode control. However, the

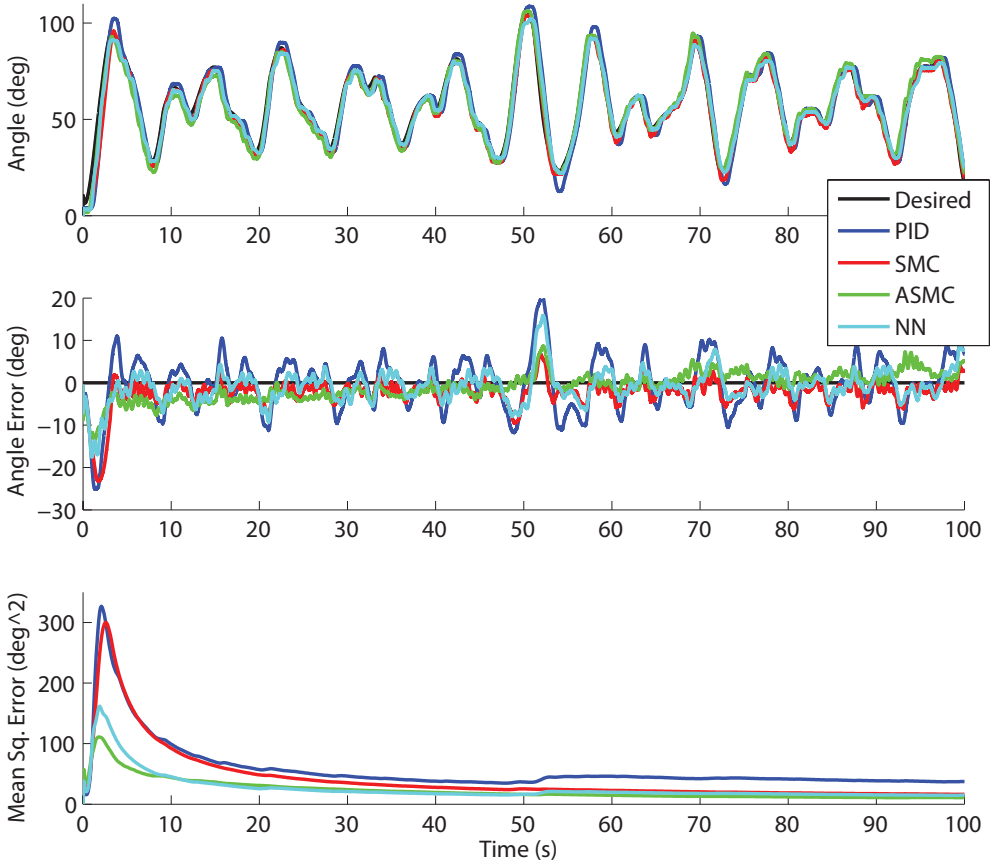


Figure 5.19: Comparison of control strategies, compound sinusoidal trajectory; (a) angle, (b) angle error, and (c) mean squared error.

system parameters were unrealistic and appeared to diverge; if the system runs for an extended duration, instability may occur. The neural network controller was designed to capture the dynamics of the PAMs and joint geometry that could not be captured in the adaptive sliding mode controller. In experimentation, the neural network controller was nearly as accurate as the adaptive sliding mode controller and showed strong signs of convergence, but required much less knowledge of the system structure than the adaptive sliding mode controller.

Although the neural controller is capable of adapting to nonlinear functions

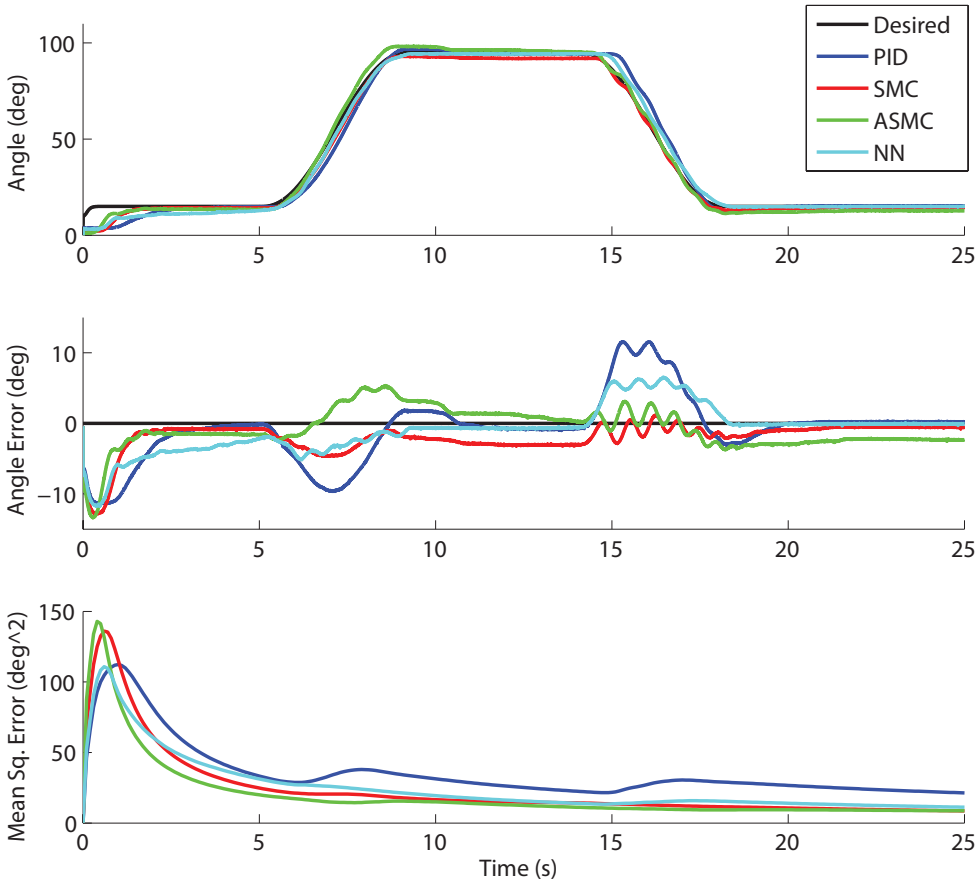


Figure 5.20: Comparison of control strategies, lift-hold-return trajectory; (a) angle, (b) angle error, and (c) mean squared error.

of joint angle, some nonlinearities which are not accounted for may persist. A key example of one such nonlinearity that will impact controller performance and convergence properties is hysteresis. Hysteresis is dependent on the displacement history, and implementing compensation in either of the present adaptive frameworks is difficult. Major improvements in trajectory-following performance are expected if hysteresis can be properly compensated. Hence, this will be the subject of future work.

Neural networks are an extremely useful form of control, particularly when

much of the system dynamics are unknown. The above results demonstrate that a network can be trained fairly quickly to recognize nonlinear functions of angle without any prior information to estimate the functions. Although the detailed kinematic and dynamic nonlinearities of a system may not be fully known, in some cases, it may be useful to initialize the neural controller with a rough estimate of $\hat{H}(\theta)$, $\hat{C}(\theta)$, and $\hat{G}(\theta)$. This can be achieved by assuming that PAM force behavior is characterized by the simple Gaylord model [23], and that the effective radius providing the actuation moment arm is constant or a linear function of angle. To this end, a supplementary experiment was conducted with initial estimates of the control law terms, Eqns. 5.17, 5.18, and 5.19. The approximation for $C_1(\theta)$ based on the Gaylord model is given by:

$$C_1(\theta) = \frac{3L(\theta)^2 - B^2}{4\pi N^2} r_{eff} \tag{5.25}$$

where $L = 5$ in is the length of the actuator (approximated as a linear function of θ), $B = 11.23$ in is braid length, $N = 0.9$ is the number of turns a single braid fiber makes around the PAM circumference, and $r_{\text{eff}} = 0.7$ in is the approximate effective radius from which PAM force is translated into joint torque.

Figure 5.21 displays results from two trajectory-following experiments, comparing the controller initialized with the Gaylord model to a controller with no prior information, as shown previously. The use of the Gaylord model slightly reduces the overall error.

Figure 5.22 illustrates the neural network adaptation of $\hat{H}(\theta)$, $\hat{C}(\theta)$, and $\hat{G}(\theta)$

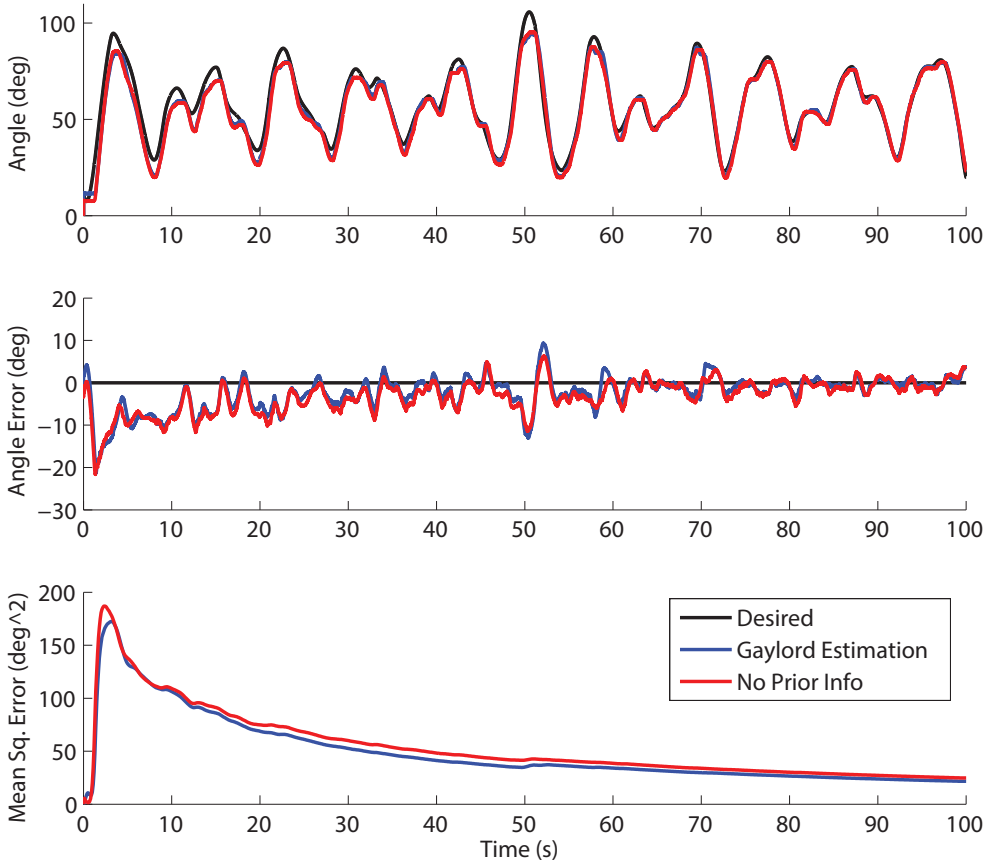


Figure 5.21: Adaptive neural network control, 0 lb payload, Gaylord model vs. no information.

using the Gaylord model to construct initial estimates. Adaptation of the $\hat{C}(\theta)$ and $\hat{G}(\theta)$ terms is clearly in the positive direction, signaling that the initial estimate provided by this model is low. Note that the Gaylord model typically overestimates force (especially at large contractions); thus, $C_1(\theta)$ is expected to be overestimated and $\hat{C}(\theta)$ and $\hat{G}(\theta)$ are underestimated as a result.

In order to perform complex manipulation tasks, potentially in three-dimensional workspaces, systems with multiple degrees-of-freedom are required. When extended to multi-dimensional systems, the principles of the three controllers will remain

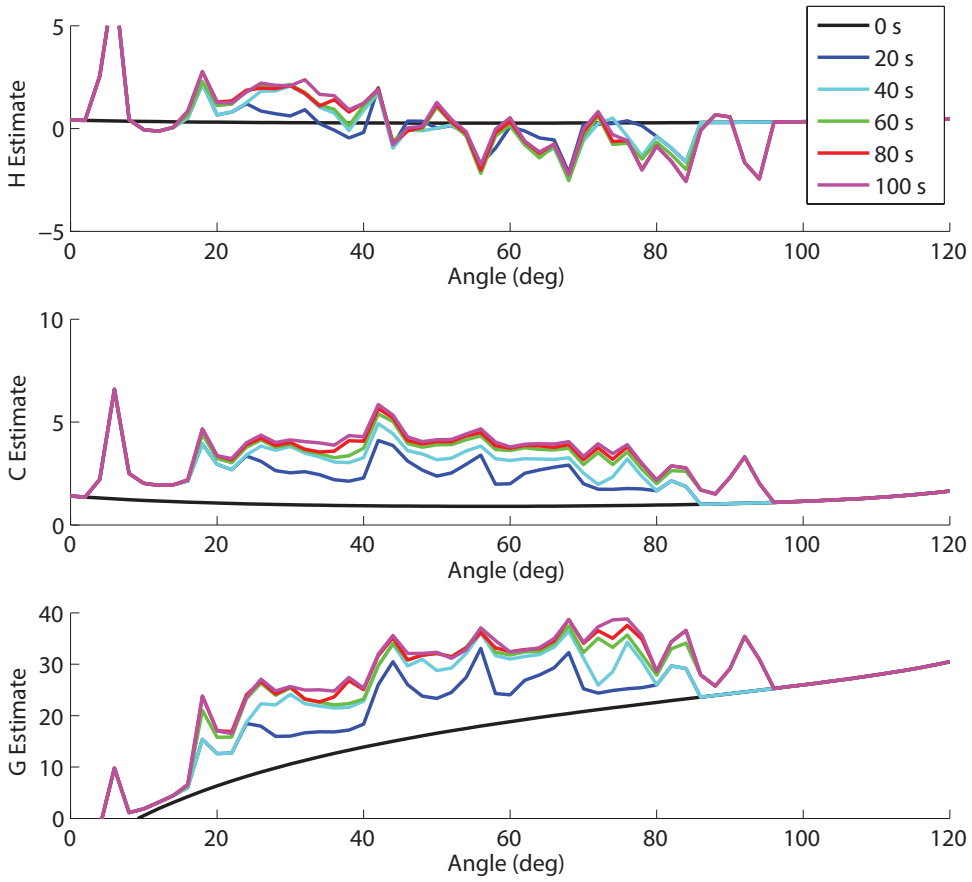


Figure 5.22: Neural network adaptation over 100 s, 0 lb payload, with Gaylord model.

applicable, but their complexity will increase (e.g., Coriolis forces will appear, inertia matrix will expand). In the case of neural network control, the networks themselves must become multi-dimensional functions of the various angle and angular velocity terms. The addition of a multi-dimensional network structure may impart a significant computational burden on the controller.

Lastly, it is important to note that, despite using a complex sinusoid, the frequency of actuation in the chosen trajectory was relatively low (maximum of 0.25 Hz), due to the intended application of lifting and carrying humans. In many other

manipulator applications, higher frequencies are required. High frequency motion will cause the inertia and damping to play a greater role in the dynamics, and will rely on the bandwidth of pressure feedback. Furthermore, additional high-frequency dynamics may be excited in the manipulator or the PAMs.

5.6 Conclusion

Three advanced control strategies were applied to the shoulder joint of a single degree-of-freedom PAM-actuated robotic manipulator. The controllers were evaluated in trajectory-following experiments, demonstrating different levels of accuracy for different situations. The standard sliding mode controller demonstrated robust trajectory-following, but to guarantee low error, parameter estimates such as arm inertia, damping, and mass were required to be known *a priori*. Because large payload variations are expected in the present manipulator application, the standard sliding mode controller was modified to include adaptation of payload-dependent parameters. While trajectory-following was improved, the underlying nonlinearities in the PAMs and joint kinematics were not fully addressed with this control structure. Therefore, a neural network controller was implemented to determine angle-dependent nonlinearities in the system while maintaining the ability to adapt to payload variations.

Results demonstrate the utility of all three of the nonlinear controllers, including improvements over cascaded PID control. Neural network control has great potential for learning and negating the complex nonlinearities present in a PAM-actuated

system. Future work may include hysteresis compensation, multiple degree-of-freedom experiments, and high-frequency motion experiments.

Chapter 6: Variable Recruitment

6.1 Introduction

Pneumatic artificial muscles (PAMs) are actuators known for their high specific work, natural compliance, flexibility, and extremely light weight. Also known as McKibben muscles, PAMs were developed in the 1950s to actuate orthotic devices for polio patients [23]. PAMs are composed of an elastomeric bladder surrounded by a helically-braided fiber sleeve. Pressurization of the soft bladder causes the braid fibers to reorient, generating contractile stroke in their typical configuration. As a result of their functional similarity to human muscle (decreasing length, increasing diameter), PAMs have been employed as the muscles in robotic arms [40, 160], legs [132, 137], and hands [178, 181].

Most PAM-based anthropomorphic robotic systems are designed with a single PAM working as an analog to a single human muscle. However, force buildup in human muscle is a complex phenomenon, developing on the level of small groups of muscle fibers called motor units [189]. In the human neuromuscular system, muscle force is adjusted by: (1) varying the firing rate of motor neurons, and (2) selective recruitment of motor units [191]. The activation of a single motor unit will create a distributed but weak signal; as force requirements increase, the number of

active motor units also increases. Motor units are generally recruited in order of smallest (slow, low-force, fatigue resistant) to largest (fast, high force, less fatigue resistant) [180]. Motor unit firing rate typically increases with increasing muscular effort, which helps smooth out the incremental force change as motor units are added [175].

Analogously, PAMs can be easily arranged in parallel and activated individually as torque requirements dictate. Although PAM research to date has mostly ignored variable recruitment, there are advantages to matching the form and function of natural muscles on the level of individual motor units. The main benefit of variable recruitment is the potential for improved efficiency over the entire range of anticipated force. When force requirements are low in a PAM-based system, a subset of the PAMs in a muscle "group" can be set to a relatively high pressure, while not pressurizing others, rather than activating all of the actuators at a lower pressure. Efficiency in a parallel PAM-based system is consequently improved for two major reasons. First, the energy required to overcome elastic bladder resistance is proportional to the number of PAMs employed. Therefore, if fewer PAMs are required, less energy is "wasted" to overcome bladder resistance. Second, pressure-dependent losses associated with compressible airflow in the pneumatic system can be exacerbated because high recruitment levels correspond to a larger gradient between source and actuator pressure as well as higher actuator "dead space" volume.

Despite the potential advantages of variable recruitment, research regarding the topic is limited. Odhner and Asada [194] explored the variable recruitment of multiple shape memory alloy (SMA) wires in a robotic arm to modulate force and

stiffness. By using multiple thin wires instead of one large wire, faster heat diffusion was achieved, and bandwidth was increased. However, efficiency was not quantified. Lorussi et al. [192] developed simulations of a dielectric elastomer muscle bundle. Huston et al. [190] explored concepts for hierarchical actuator systems, including designs that can improve precision, speed, efficiency, smooth motion, and redundancy. Repperger et al. [193] applied a bio-inspired control strategy to a single pneumatic muscle. The authors claim that individual "force twitches" mimic the control aspect of recruitment, but a single pneumatic muscle does not physically emulate variable recruitment.

In research highly relevant to the current study, Bryant et al. [179] constructed an actuator consisting of three small-diameter PAMs and three large-diameter PAMs in a parallel arrangement. Their results demonstrated that the two motor units can be activated separately or in unison to produce varying levels of force. The researchers hypothesized that efficiency improvements could result from variable recruitment, but measurements of actuator efficiency (ratio of output work to input energy) were left for future work.

To date, no known studies have investigated variable recruitment of pneumatic artificial muscles in practical robotics applications. The goal of the present research is to determine the practical value of a variable recruitment scheme in a robotic actuation system featuring a parallel arrangement of multiple equivalently sized PAM actuators. The exemplary robotic system chosen for this study was the shoulder joint of a robotic manipulator with heavy lifting capacity. First, a comparison of quasi-static actuator force behavior is presented for the candidate PAMs, showing that

fewer PAMs can produce greater force output for a given compressed air mass. Then, the efficiency of the manipulator joint is experimentally evaluated for different levels of recruitment. Simulations of the joint are also performed, validating experimental trends. Results demonstrate the benefits of variable recruitment and point toward the existence of an optimal recruitment strategy.

6.2 Preliminary Characterization and Analysis of Bladder Effects

A considerable source of efficiency loss during PAM force generation is the elastic resistance of the internal bladder. Previous studies have shown that the force behavior of a PAM actuator can be highly nonlinear as a result of bladder hyper-elasticity [27, 30]. Kothera et al. [35] modified an existing force balance model originally formulated by Ferraresi et al. [34] to better account for bladder effects and provide more accurate force estimates. Using this approach, PAM force is given by:

$$\begin{aligned} F = \frac{P}{4\pi N}(3L^2 - B^2) + P\left(\frac{V_B}{L} - \frac{tL^2}{2\pi RN^2}\right) \\ + \sigma_z \frac{V_B}{L} - \sigma_c \frac{tL^2}{2\pi RN^2} \end{aligned} \tag{6.1}$$

where P is PAM pressure, L is strained actuator length, R is strained actuator radius, t is strained bladder thickness, B is (constant) braid length, N is number of turns a braid fiber makes around the bladder, V_B is (constant) bladder volume, σ_z is axial stress, and σ_c is circumferential stress. The first term, known as the Gaylord force, is a function of actuator geometry. The second term accounts for the loss in force due to bladder thickness subtracting from actuator volume. The third and fourth

terms quantify the change in force due to bladder resistance.

In order to determine the effects of bladder resistance and motivate a variable recruitment strategy, force behavior was compared between "energy equivalent" actuator configurations. In these experiments, the force behavior of one PAM pressurized to a constant value was compared to two identical PAMs pressurized to half that value. The PAM(s) were contracted at constant pressure, and quasi-static force data was recorded. Following the ideal gas law, and assuming temperature is constant and PAM volume is independent of pressure (only a function of contraction), both configurations hold the same air mass for the same contraction. Therefore, the energy input between the two configurations can be considered equal and provide a baseline for comparison.

Measurements, however, show differences in force output. Figure 6.1 displays comparisons between single- and dual-PAM configurations at "low" pressure levels (2 PAMs @ 2 bar vs. 1 PAM @ 4 bar) and "high" pressure levels (2 PAMs @ 4 bar vs. 1 PAM @ 8 bar) using sample PAM A, with geometric and material properties listed in Table 6.1. Although quasi-static PAM force data exhibits direction-dependent hysteresis, contraction is the only motion in which positive work is being done by the PAM. Therefore, only the contractile portion of each curve is displayed. For any substantial amount of contraction, the force from a single PAM is greater than the force of two PAMs (at half pressure). Free contraction of the single PAM is also greater. These phenomena are mainly caused by PAM elasticity that resists circumferential expansion and axial contraction in a nonlinear manner. At low pressure, a high proportion of the stored energy is being spent to overcome bladder

Table 6.1: Geometric and material parameters for test PAMs.

Parameter	PAM A	PAM B
Diameter (cm [in])	2.5 [1.0]	1.9 [0.75]
Length (cm [in])	27.6 [10.9]	12.5 [4.9]
Braid Angle (deg)	73.5	75
Bladder Thickness (cm [in])	0.32 [0.125]	0.32 [0.125]
Bladder Material	Latex	Silicone
Shore Hardness	35A	25A

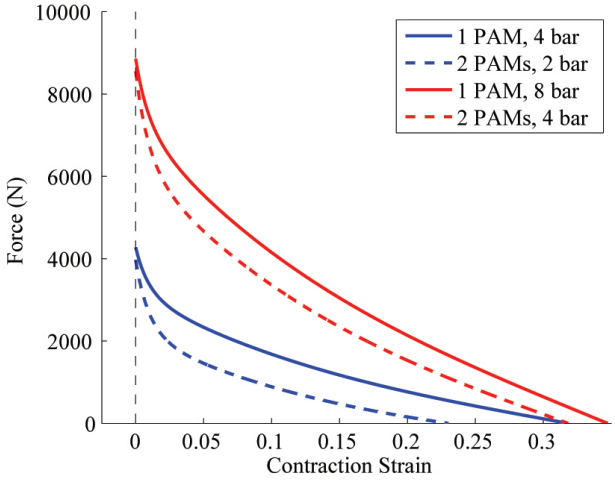


Figure 6.1: Comparison of single-PAM (full pressure) vs. dual-PAM (half pressure) force, PAM A.

resistance; as pressure increases, this proportion decreases, and the PAM becomes more efficient. Hocking and Wereley [27] noted that initiation pressure is required for the bladder to make substantial contact with the surrounding braid. This pressure "deadband" accounts for some of the force reduction in the dual-PAM configuration because two deadbands must be overcome instead of one. Results support using as few PAMs as possible to lift a given payload to maximize efficiency. As force requirements exceed the maximum force of the active PAM group, additional PAMs can be activated as needed. In other words, a variable recruitment scheme should be used.

Elasticity losses may be combated by fabricating PAMs with an extra-soft bladder. To illustrate the effects of a softer bladder, a second set of experiments were performed, with sample PAM B (see Table 6.1). This PAM has a silicone rubber bladder (Bluestar Bluesil V-330), with a lower Shore Hardness than the latex bladder used in PAM A [185]. Figure 6.2 shows force characterization data for two recruitment configurations at "high" and "low" pressure levels as in Figure 6.1. The reduction in force associated with using two PAMs is not nearly as dramatic for the silicone PAM (B) as was observed with the latex PAM (A). In fact, force loss does not occur until contraction reaches 5%. Although the different dimensions of these two sample PAMs make a direct comparison misleading, one would expect the PAM with a higher bladder thickness-to-diameter ratio (PAM B) to incur more losses if both PAMs used the same bladder material. Nevertheless, PAM B has better low-pressure performance because the bladder is softer. The minor difference in force output suggests that a softer bladder reduces the benefit of variable recruitment. However, in practical applications, one must consider not only quasi-static PAM force, but the efficiency of the dynamic system as a whole.

6.3 Variable Recruitment on a Robotic Manipulator

Several factors contribute to efficiency losses in PAM-actuated dynamic systems, many of which may affect a variable recruitment strategy. In addition to bladder elasticity, losses caused by airflow dynamics, excess actuator and tubing volume, friction, and damping may change with recruitment level. This section describes

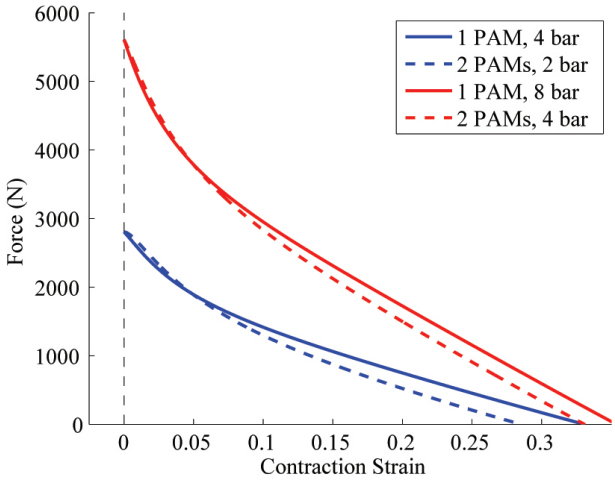


Figure 6.2: Comparison of single-PAM (full pressure) vs. dual-PAM (half pressure) force, PAM B.

the design and operation of a PAM-based robotic manipulator. In simulations and experiments, the efficiency of the entire system (pneumatics and arm mechanics) is measured at each level of motor unit activation in order to holistically evaluate variable recruitment.

The robotic actuation system employed in this work was the shoulder joint of the two degree-of-freedom planar manipulator shown in Figure 6.3. At maximum pressure (13 bar), the shoulder joint is capable of 850 Nm (630 ft-lb) of torque up to 90 deg, enough to lift a 95 kg (210 lb) tip payload with the 0.9 m (3 ft) arm fully outstretched. This joint is actuated by six latex bladder PAMs, all identical to PAM A (recall Table 6.1). The shoulder joint and actuators are shown in an exploded-view CAD model in Figure 6.4. The PAMs pull downward on an aluminum plate which slides vertically on linear bearings. Tendon links connect the plate to the shoulder joint shaft, which allows the PAMs to generate rotation. The PAMs act unidirectionally to lift the arm, while gravity acts in the opposing direction to

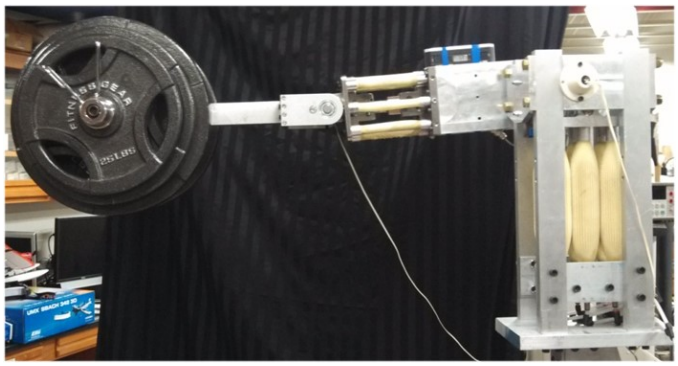


Figure 6.3: Robotic arm holding a 95 kg (210 lb) payload.

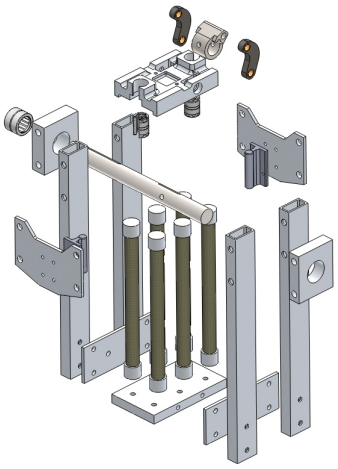


Figure 6.4: Exploded view of shoulder joint.

restore the arm to its resting angle when pressure is removed.

In the variable recruitment study by Bryant et al. [179], the total force of six PAMs actuated together was less than the sum of the forces produced by the individual motor units. The reason for this force reduction (mostly at low contraction) was unclear; however, the tightly packed configuration may have been a factor, as friction between PAMs can adversely affect force output, as can limitations on radial expansion imposed by the tight packing. In order to eliminate the effects of friction and resistance between PAMs in the present study, the actuators were given ample space (6.35 cm [2.5 in] diameter) to radially expand without interaction.

The PAMs are connected to a pressure source through a single proportional valve. This valve varies its orifice area in response to a voltage input (0-10 V). Voltage signals were produced in response to measured angle and pressure by dSPACE control hardware and software [186]. The PAMs were recruited in groups of two, and the number of active PAMs was varied off-line between (not during) tests by manually adjusting the tubing connections.

6.4 Variable Recruitment Simulations

Simulations were performed to predict the effects of variable recruitment and to justify experimental work. These simulations employed a detailed model of the robotic manipulator described in Section 6.3, including the pneumatic components used to channel pressurized air to the PAMs. Each simulation consisted of repeated lifting cycles along a prescribed trajectory. Payload weight and level of recruitment were varied, and system efficiency was determined for each test. This chapter describes the dynamic model used in simulation, the procedure completed to obtain reliable values of efficiency, and simulation results.

6.4.1 Dynamic Modeling

Figure 6.5 illustrates the system model used in simulation. This model describes the dynamics of the airflow and the dynamic response of the manipulator. First, voltage ε is input to the proportional valve, which controls the mass flow rate of air $\dot{m}$ from air source to PAMs (and in the case of deflation, from PAMs to the ambient

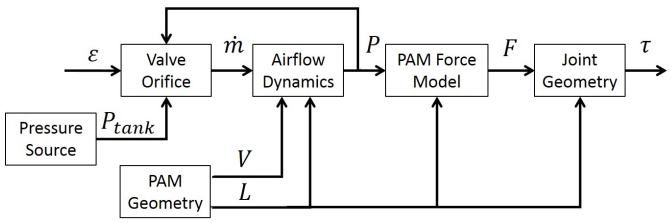


Figure 6.5: Diagram of PAM-based robotic system.

environment) by changing the size of the valve orifice. Mass flow into the PAM leads to pressure buildup, which generates PAM force. Pressurized PAMs, which are indirectly connected to the joint shaft, produce shoulder torque. Shoulder torque is a function of pressure and PAM contraction.

The system experiences compressible, potentially choked air flow through the variable-area valve orifice. A well-founded dynamic model of the pneumatic system must account for the compressibility of air, the heat transfer associated with mass flow into and out of the valve, changing PAM volume, and dead space in the PAMs. Dead space is the initial volume of the PAM that must be pressurized before motion begins. The air that occupies this space does no work but nonetheless requires energy to maintain pressure.

Some known but complex effects were neglected in this simulation. The Joule-Thomson effect, better known as "throttling," is an isenthalpic process (i.e. a process which is adiabatic, irreversible, and extracts no work) that causes the temperature of a non-ideal gas to drop as a function of the pressure gradient through an orifice [184]. While some cooling may occur as air passes through the valve, temperature change is minimal at the experimental range of pressures and is believed to have very little effect on overall efficiency. Therefore, we have opted to treat the air as an ideal gas.

Losses from tubing friction were also neglected.

In a pneumatic system with a sharp-edged variable-area orifice [187], the relationship between mass flow rate, pressure, and area is given by:

$$\dot{m}_{air} = \begin{cases} AC_d P_{us}\sqrt{\frac{2}{RT}}C_1, & \frac{P_{ds}}{P_{us}} < P_{cr} \\ \\ AC_d P_{us}\sqrt{\frac{2}{RT}}C_2, & \frac{P_{ds}}{P_{us}} \geq P_{cr} \end{cases} \tag{6.2}$$

In the above expression, $\dot{m}$ is mass flow rate, A is orifice area, and P_{us} and P_{ds} are the upstream and downstream pressures, respectively. Note that during PAM deflation, the upstream pressure corresponds to the PAM pressure, and the downstream pressure is the ambient room pressure. A lookup table provided by the valve manufacturer was used to determine orifice area for a given voltage input. The term C_d is a discharge coefficient capturing the losses in the orifice, $P_{cr} = (2/(\gamma+1))^{\gamma/(\gamma-1)}$ is the critical pressure separating subsonic and supersonic flow, and C_1 and C_2 are given by:

$$C_1 = \sqrt{\frac{\gamma}{\gamma-1}\left[\left(\frac{P_{ds}}{P_{us}}\right)^{\frac{2}{\gamma}} - \left(\frac{P_{ds}}{P_{us}}\right)^{\frac{\gamma-1}{\gamma}}\right]}$$

$$C_2 = \left(\frac{2}{\gamma+1}\right)^{\frac{1}{\gamma-1}}\sqrt{\frac{\gamma}{\gamma+1}} \tag{6.3}$$

where γ is the specific heat ratio of air.

Richer and Hurmuzlu [158] derived an expression for pressure change in a container of changing volume using the ideal gas law, conservation of mass, and

conservation of energy:

$$\dot{P} = \frac{R_{air}T}{V}\left(\alpha_{in}\dot{m}_{in} - \alpha_{out}\dot{m}_{out}\right) + \frac{P\dot{V}}{V}\alpha \tag{6.4}$$

where R_{air} is the specific gas constant for air, T is air temperature, and V_{air} is air volume in the PAMs. The coefficients $\alpha_{in} = 1.4$ and $\alpha_{out} = 1$ are estimates of specific heat ratio based on heat transfer as mass flows into and out of the valve, respectively. The parameter $\alpha = 1.2$ is the specific heat ratio corresponding to PAM volume change. From the above expression of pressure rate, time-varying pressure inside the PAMs can be determined by integration.

The mass flow exiting the air source implies decreasing source pressure. Using prior knowledge of the mass flow rate exiting the constant-volume tank at constant temperature, source pressure rate is given by:

$$\dot{P}_{tank} = \frac{R_{air}T}{V_{tank}}\dot{m} \tag{6.5}$$

Actuator force is given by Eqn. 6.1. For enhanced accuracy, it is assumed that the PAM exhibits a hyperelastic stress-strain relationship. Axial and circumferential stresses are empirically fit as fourth-order polynomial functions of axial and circumferential strain to well match the experimental data of PAM A, as in our earlier work [188].

PAM force is translated into joint torque through a complex, custom-designed joint geometry intended to maintain a fairly constant torque for a given pressure within the shoulder joint angle limits (15 deg to 120 deg). The details of the joint

geometry are inconsequential for this study, and are therefore omitted. Torque, like PAM force, is a function of pressure and actuator strain.

The dynamics of the one-degree-of-freedom manipulator are given by:

$$\tau = I\ddot{\theta} + G(\theta) + c\dot{\theta} + f\text{sgn}\theta \tag{6.6}$$

where I is the total (manipulator and payload) inertia, G is torque due to gravity, c is velocity-dependent damping, and f is torque due to Coulomb friction. Friction and damping in the joint were estimated empirically from test data.

6.4.2 Simulation Procedure

A detailed procedure was implemented to simulate manipulator motion and extract values of system efficiency. Simulations were designed such that they could be reproduced in actual experiments. In each simulation, the manipulator followed a time-periodic trajectory consisting of eight smooth lifting cycles. Each lifting cycle was composed of a 6 s cosine ramp from minimum to maximum angle, a 5 s hold at maximum angle, a 6 s cosine ramp back to the minimum angle, and a 5 s hold at minimum angle. This was regulated by a closed-loop cascaded proportional-integral (PI) controller with pressure and angle feedback. Figure 6.6 depicts the control architecture used in the simulations. Controller gains were set to ensure that the arm would reach the maximum desired angle smoothly and with negligible overshoot. This process was repeated for four payload weights and two maximum arm angles (50 deg and 90 deg). Test matrices for the two trajectories are shown respectively in

Table 6.2: Test matrix for variable recruitment, 50 deg max. angle.

Payload Weight	2 PAMs	4 PAMs	6 PAMs
0 kg (0 lb)	X	X	X
9 kg (20 lb)	X	X	X
18 kg (40 lb)	X	X	X
27 kg (60 lb)	X	X	X

Table 6.3: Test matrix for variable recruitment, 90 deg max. angle.

Payload Weight	2 PAMs	4 PAMs	6 PAMs
0 kg (0 lb)	X	X	X
9 kg (20 lb)	X	X	X
18 kg (40 lb)	-	X	X
27 kg (60 lb)	-	X	X

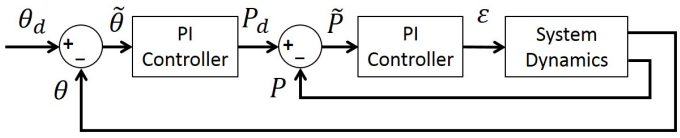


Figure 6.6: Diagram of cascaded PI control system.

Tables 6.2 and 6.3.

Total work output was calculated by summing torque multiplied by increments of angle. Because cycling the arm back to the initial angle yields a net work of zero and thus masks information about efficiency, increments of work were only summed if angle was increasing ($\Delta\theta_i > 0$):

$$W_{out} = \sum_{i=1}^{N_{\theta_+}} \tau_i \Delta\theta_{+,i} \tag{6.7}$$

where N_{θ_+} is number of positive work increments, τ_i is torque, and $\Delta\theta_{+,i}$ is (positive) change in angle.

Input energy was approximated by observing the change in initial and final

stored energy in the air source:

$$E_{in} = (P_i - P_f)\, V_{tank} \tag{6.8}$$

where P_i and P_f are initial and final pressure, and V_{tank} is the constant volume of the pressure source (15 L).

The efficiency of the cycling process was then determined by dividing output work by input energy:

$$\eta = \frac{W_{out}}{E_{in}} \tag{6.9}$$

It should be noted that the electrical efficiency of the compressor itself was not simulated and was excluded from the efficiency calculation. The compressed air source was set to the same initial pressure regardless of PAM number; therefore, in the present study, compressor efficiency had no bearing on a variable recruitment strategy.

6.4.3 Simulation Results

Figures 6.7 and 6.8 plot system efficiency for each set of simulations, illustrating the effects of different payload weights and numbers of PAMs. For each level of recruitment, system efficiency increases with payload mass. It is also clear that using fewer PAMs (when possible) increases system efficiency. The efficiency improvements are most beneficial at the lowest payloads. Overall, experimental results provide strong justification for a variable recruitment strategy.

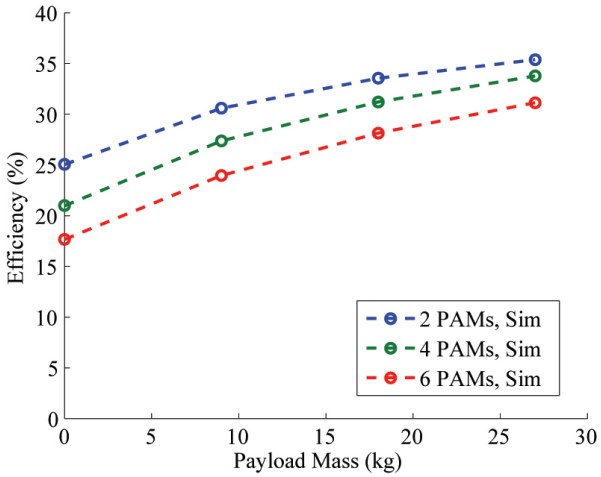


Figure 6.7: Efficiency of manipulator with variable recruitment, 50 deg max. angle.

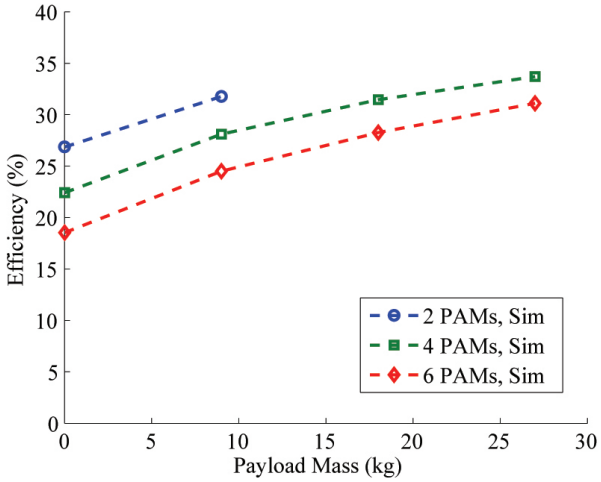


Figure 6.8: Efficiency of manipulator with variable recruitment, 90 deg max. angle.

The results from simulations suggest a strategy for adjusting recruitment level. At the lowest payloads, the fewest number of PAMs (a single motor unit) should be recruited to maximize efficiency. When payload weight requires torque greater than the capacity of a single motor unit, an additional motor unit can be recruited, and so on as torque requirements continue to increase, until all motor units are recruited. Figure 6.9 illustrates the most efficient number of motor units as payload changes, with simulations of the 90 deg trajectory extended to 63 kg (140 lb).

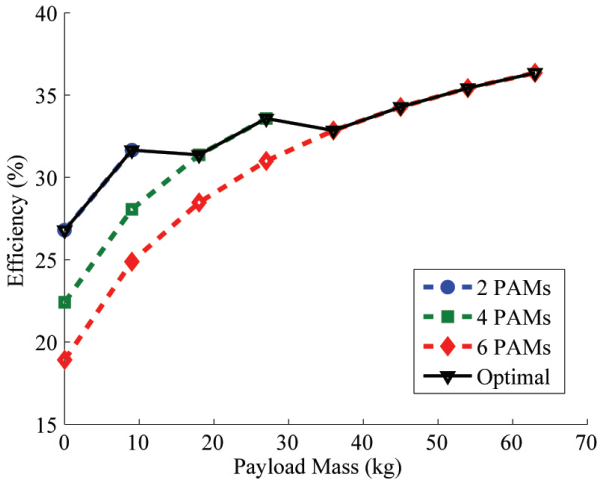


Figure 6.9: Maximizing efficiency through variable recruitment, simulations, 90 deg max. angle.

Motivated by the observations in Section 6.2, the implications of bladder stiffness were also explored. Simulations provide an opportunity to ignore the bladder effects by using only the Gaylord force term to model PAM force. Comparing simulations with and without elasticity in Figure 6.10, it is clear that bladder resistance plays a major role in reducing efficiency. Without axial or circumferential bladder stress (which is physically impossible, but helpful for illustration), the efficiency range jumps from 10-30% to 52-66%. Moreover, when elasticity is ignored in simulation, the importance of recruitment becomes less clear. For example, the 2-PAM configuration displays the greatest efficiency at zero payload, but becomes the least efficient at the maximum payload. As explained earlier, however, simulations treated air as an ideal gas, and unmodeled losses such as throttling may affect results. It is important to note, however, that softer bladders are more prone to fatigue and failure. A practical PAM-actuated system must strike a balance between efficiency and durability.

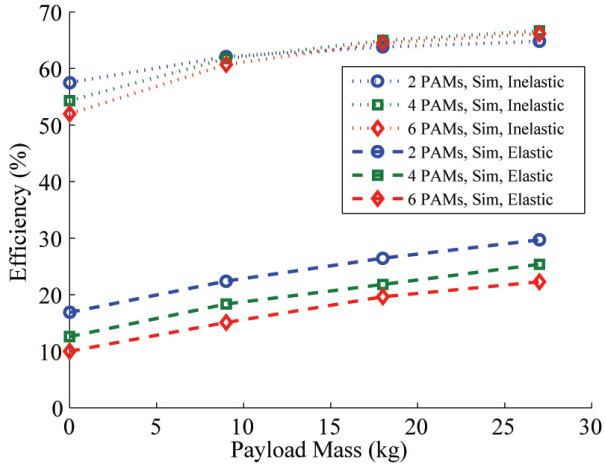


Figure 6.10: Efficiency of variable recruitment with and without bladder elasticity, simulations, 90 deg max. angle.

6.5 Variable Recruitment Experiments

Motivated by the results of simulations, experimental testing was performed on the manipulator. A comparison revealed similar trends between simulations and experiments. Using the combined results, the relationship between recruitment and efficiency was evaluated.

6.5.1 Experimental Procedure

In order to accurately measure arm efficiency, a detailed experimental procedure was developed and implemented. Experiments were performed in a manner that mirrored simulations. First, a specified payload mass (0, 9, 18, or 27 kg [0, 20, 40 or 60 lb]) was securely fastened to the end of the arm. Next, the compressed air tank was filled until an automatic stop was triggered (at 13.8 bar [200 psi]), and this "initial" pressure was recorded. At that point, the tank auto-start trigger was

turned off and arm cycling was begun immediately (to minimize the amount of air leakage) with a predetermined number of active PAMs. As in simulation, the arm trajectory was composed of eight smooth lift-hold-drop cycles regulated by a closed-loop cascaded proportional-integral (PI) controller, with pressure and angle feedback. Controller gains were set in a pre-test to ensure that the arm would reach the maximum desired angle smoothly and with negligible overshoot. During each test, pressure, angle, and valve voltage data were recorded. When the cycling was completed after 200 s, final tank pressure was recorded. Input energy, output work, and efficiency were calculated, as in simulation (see Section 6.4.2).

While the arm is capable of lifting payloads over 90 kg (200 lb), source pressure drops substantially during the cycling tests, causing the system to improperly follow the desired trajectory. This limited the maximum test payload to 27 kg (60 lb).

6.5.2 Experimental Results

Figure 6.11 depicts the time history of arm angle and estimated torque during an example experiment (18 kg [40 lb] payload, 2 PAMs activated), highlighting in red the areas where positive work is being produced. The lifting motions are smooth and repeatable despite the source pressure dropping during the tests. Applying Eqns. 6.7, 6.8, and 6.9 to each data set yields an approximation of manipulator efficiency.

Figure 6.12 displays simulation and experimental data for output torque vs. pressure for a sample test case (18 kg [40 lb] payload, 2 PAMs). The strong similarity between these hysteretic curves provides evidence that the joint and

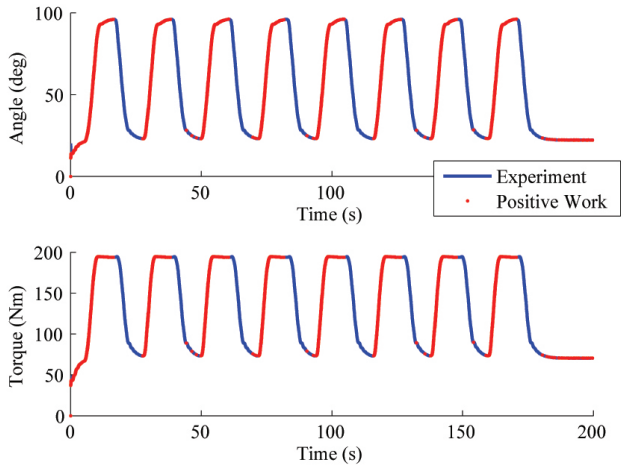


Figure 6.11: Angle and torque vs. time, 2 PAMs, 18 kg (40 lb) payload, 90 deg max. angle.

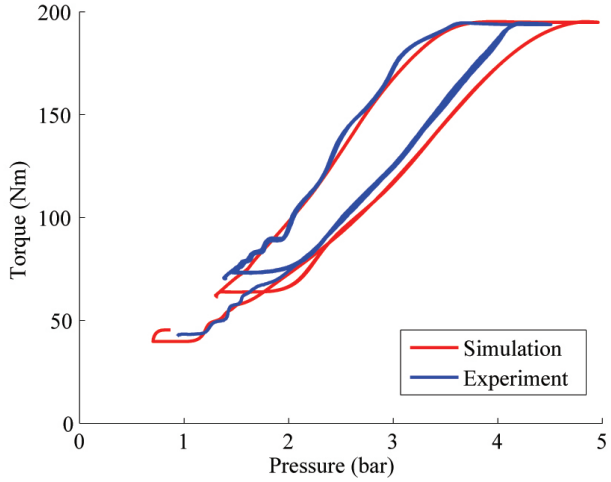


Figure 6.12: Torque vs. pressure, experiment and simulation, 2 PAMs, 18 kg (40 lb) payload.

actuator components of the system are modeled correctly.

Efficiency results from experiments display similarities with simulations. In Figure 6.13, we see that the use of fewer PAMs improves efficiency as in simulation, and efficiency increases with payload mass at about the same rate as in simulation. However, there is an offset between simulation and experimental data, likely caused by unmodeled losses.

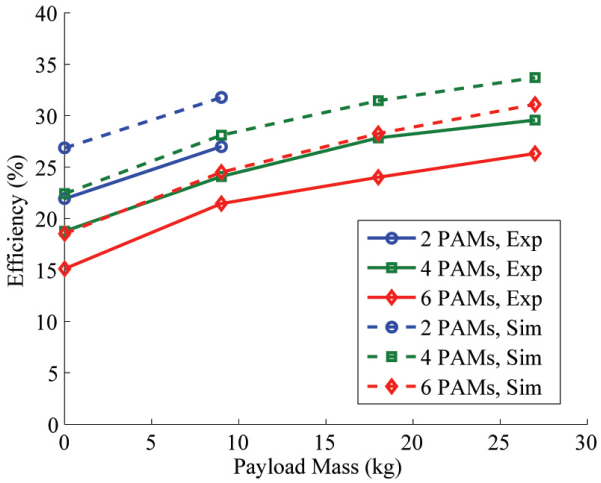


Figure 6.13: Efficiency of manipulator with variable recruitment, 90 deg max. angle.

Figure 6.14 shows that work output remains essentially constant for all levels of recruitment in both simulations and experiments. The discrepancy in efficiency between the two is caused by the difference in input energy consumed, as shown in Figure 6.15. The required energy for experiments is greater than simulations in each test case, suggesting that unmodeled losses which are not present in simulation can contribute to the efficiency. These unmodeled factors, which could include leakage, tubing losses, and temperature change, are difficult to accurately simulate but could be added in future work.

6.6 Discussion

Simulated and experimental results suggest a simple algorithm for achieving high efficiency via variable recruitment: Employ as few motor units as possible to satisfy torque requirements, and add/subtract motor units as torque requirements change. Implementation of the variable recruitment strategy will require a controller

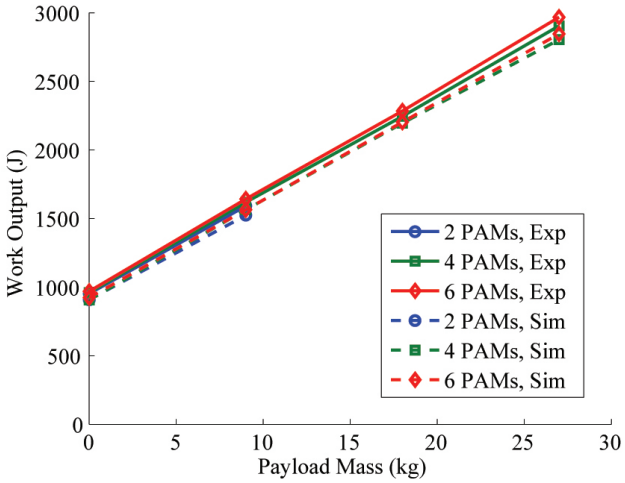


Figure 6.14: Work output of manipulator with variable recruitment, 90 deg max. angle.

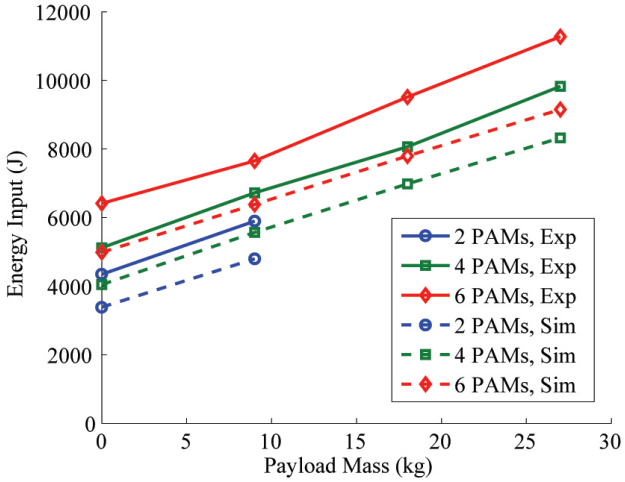


Figure 6.15: Energy input of manipulator with variable recruitment, 90 deg max. angle.

that activates motor units intelligently. The controller must be able to sense or predict torque requirements, and respond by creating smooth transitions when the discrete units are activated.

If there is *a priori* knowledge of expected payload, recruitment level can be planned. For instance, in a heavy-lifting scenario that consists of approaching and lifting a payload of known mass, only a small subset of motor units would require

activation during approach. Once contact is made with the payload, additional PAMs would then be recruited for lifting and manipulation. This strategy may benefit from a slight over-activation of motor units to compensate for unanticipated disturbances.

Alternatively, real-time adjustment of recruitment level may be desired to manipulate payloads of unknown weight or improve robustness to disturbances. In order to maintain stability and prevent shock to the payload while the system is in motion, transitions in recruitment level must be performed smoothly. One method of smoothly adding a motor unit is to use individual proportional valves for each motor unit and slowly ramp up the orifice area. This strategy is analogous to increasing the firing rate of individual motor units in human muscle. Furthermore, it is important to minimize "chatter" between recruitment levels, because each time a pressurized unit is deactivated, the air inside those PAMs will be lost to the environment.

One drawback to employing fewer PAMs at higher pressures is pressure saturation between the source and the PAMs. In the present system, this becomes an issue when the pressure gradient is less than 2 bar (30 psi). Saturation leads to limited manipulator power and speed, and degrades control. To reduce this effect, a higher source pressure and/or larger valve orifice(s) can be used. Alternatively, more PAMs can be recruited when a saturation threshold is reached. In this case, a precise control strategy must be implemented to ensure that transitions in recruitment can be performed smoothly, in concert with other recruitment algorithms, and without additional losses in efficiency.

Another consequence of a variable recruitment strategy is the buckling of

non-activated PAMs when the activated PAMs contract. Figures 6.16 and 6.17 show that PAMs which are not recruited will bend in arbitrary directions. Buckling can be eliminated by pre-tensioning the bladder during fabrication; however, braid will remain loose, carrying the risk of accelerated actuator fatigue. Bryant et al. [179] were able to keep PAM braid in place by embedding their PAM bundle in a silicone matrix; however, this dramatically decreased force output and free contraction for all levels of recruitment, and is not advisable if efficiency is important. In order to counteract fatigue while preserving high efficiency, alternative methods for containing the braid must be found.

6.7 Conclusion

A biologically-inspired variable recruitment architecture was explored in order to improve the efficiency of a robotic manipulator actuated by pneumatic artificial muscles. The actuators were arranged in a parallel bundle, and independently-controlled motor units were employed to emulate the structure and operation of human skeletal muscle. Simulations combining the pneumatic, mechanical, and control components of the robotic system were conducted, predicting efficiency increases as the number of activated motor units decreases. Nevertheless, motor units must be added as payload increases to satisfy torque requirements, implying the need to transition between recruitment levels. Experimental testing was performed on a robotic manipulator to validate simulations and to further evaluate a variable recruitment strategy. The experiments reproduced simulation trends across all tested



Figure 6.16: Two non-activated PAMs.

payloads. The offset error between experiment and simulation was attributed to unmodeled pneumatic losses such as leakage or throttling.

Further discussion regarding a variable recruitment strategy highlighted several challenges for future work. Full implementation of variable recruitment will require a control strategy that can select recruitment level, either via pre-planning or in real time. A real-time control strategy will require special attention to smooth transitions between recruitment levels and minimizing chatter. Additionally, the system should be designed to avoid or minimize the effects of pressure saturation

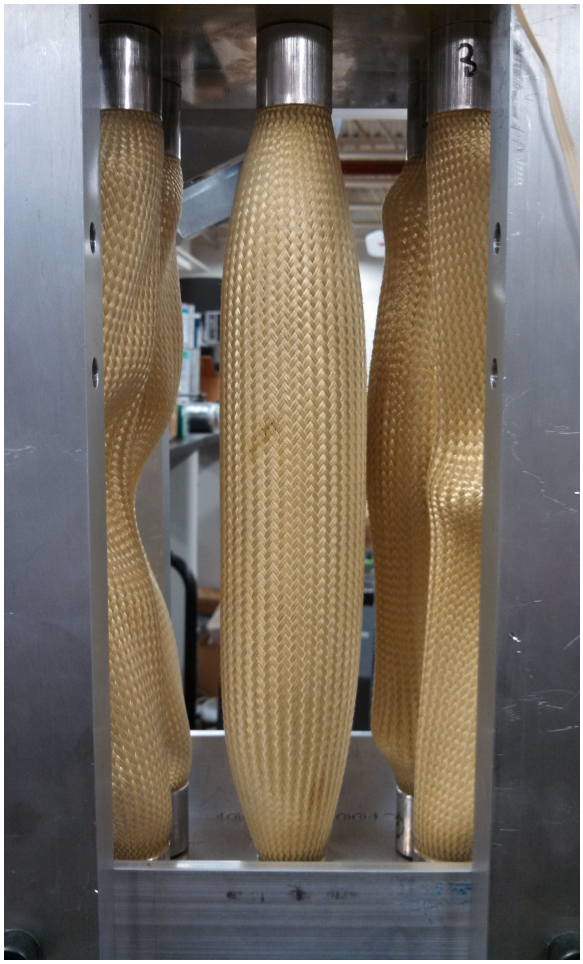


Figure 6.17: Four non-activated PAMs.

either through control or increasing source pressure. A variable recruitment control study is a natural extension of this work, and will be examined in the future. Lastly, a PAM design which eliminates bladder buckling and braid loosening due to variable recruitment is likely to improve actuator durability, and will also be considered in future work.

Chapter 7: Conclusion

7.1 Summary of Research and Key Conclusions

In this research, significant contributions were made toward the realization of robotic manipulation using lightweight, compliant pneumatic artificial muscles. Nonlinear PAM behavior, which has traditionally impeded the decision to use PAMs, was modeled accurately and in a manner that allows accurate predictions for simulation and motion control. Prototype robotic arms with several novel design features were designed, constructed, and experimentally evaluated. Substantial inroads have been made for improving arm control, including two types of adaptive control to improve the response to variations in payload. Lastly, a bio-inspired variable recruitment scheme was shown to increase manipulator efficiency, providing quantitative evidence that supports its use in control applications.

7.1.1 Pneumatic Artificial Muscle Modeling

An improved model of pneumatic artificial muscle behavior was developed that is applicable to both uni-directional and bi-directional (antagonistic) actuation schemes. Several refinements were applied to the well-known force balance derivation

in order to capture nonlinear PAM force behavior over the full range of actuator strain. This was achieved by combining a detailed model of the elliptic ends of the PAM in deformation with a hyperelastic stress-strain system identification procedure for nonlinear bladder effects. While the empirical modeling results are unique to each actuator and are not generally scalable, the model maintains predictive ability for untested pressure levels, which is very useful for model-based control applications.

7.1.2 Manipulator Proof-of-Concept and Joint Optimization

A two degree-of-freedom proof-of-concept demonstrator of a pneumatic artificial muscle-actuated robotic manipulator intended for lifting heavy payloads was designed, constructed, and experimentally tested. The manipulator featured a compact structure, natural compliance, and high specific force. Specific design choices included a tendon link-based joint structure that provided a direct connection from the PAMs to the arm linkage. As a consequence, the system exhibited virtually none of the slack typical of cable-driven systems, nor the backlash usually observed in geared systems. Moreover, the robotic joints featured bundles of small muscles in parallel. This was the result of an actuator sizing and scaling study that determined that multiple small muscles provided higher specific force capability than a single large muscle, as well as faster response and higher efficiency due to a reduced initial volume.

Following success with the proof-of-concept system, a second heavy-lift manipulator was designed by implementing a detailed joint optimization procedure for the

kinematics. The optimization minimized the area of the region where the available torque falls below a desired torque threshold, and heavily penalized joint geometries that could not meet the full range of motion. The genetic algorithm was run at multiple incremental pressure levels, until the optimization was able to meet torque requirements. In this way, torque performance was achieved with minimal pressure. Experimental data from the manipulator matched expected results, supporting the use of this kinematic design procedure.

7.1.3 Proof-of-Concept Manipulator Control Study

Several controllers were tested on the proof-of-concept manipulator and evaluated using a combined weighted metric to measure accuracy and smoothness. PID and fuzzy logic control were initially tested; however, these output feedback approaches were found to have unsatisfactory performance due to phase lag, oscillation, and overshoot. As a result, the PAM force model developed in Chapter 2 was combined with the kinematic and structural mechanics of the manipulator to form an inverse model feedforward component. When applied in parallel with PID or fuzzy feedback, the model-based controller was found to be considerably more accurate than output feedback alone, while maintaining smoothness.

7.1.4 Adaptive Control Study

In order to improve upon results from the initial control study, three advanced control strategies were developed and applied to the shoulder joint of a PAM-

actuated robotic manipulator for demonstration. The controllers were evaluated in trajectory-following experiments, demonstrating different levels of accuracy for different situations. The initial sliding mode controller showed robust trajectory-following, but to guarantee low error, parameter estimates such as arm inertia, damping, and mass were required to be known *a priori*. With the expectation of high payload variations in most manipulator applications, the sliding mode controller was modified to include adaptive capability of payload-dependent parameters. While trajectory-following was improved, the underlying nonlinearities in the PAMs and joint kinematics were not fully addressed by this adaptive control structure. Therefore, an adaptive neural network controller was applied to determine angle-dependent nonlinearities in the system while maintaining the ability to adapt to payload variations. Results demonstrated the utility of all three of the controllers, including improvements over cascaded PID control. In particular, neural network control has great potential for learning (and compensating for) the complex nonlinearities present in a PAM-actuated system.

7.1.5 Variable Recruitment

A biologically-inspired variable recruitment architecture was explored in order to improve the efficiency of a robotic manipulator actuated by PAMs. The actuators were arranged in a parallel bundle, and independently-controlled motor units were employed to emulate the structure and operation of human skeletal muscle. Simulations that combined the pneumatic, mechanical, and control components of the

robotic system were conducted, predicting an increase in efficiency as the number of activated motor units decreases. Motor units must be added as payload increases to satisfy torque requirements, implying the need to transition between recruitment levels. Experimental testing was performed on a robotic manipulator to validate simulations and to further evaluate a variable recruitment strategy. The experiments reproduced simulation trends across all tested payloads. The offset error between experiment and simulation was attributed to unmodeled pneumatic losses such as leakage, tubing friction, and throttling, though this error was minor.

7.2 Contributions to Literature

Improved actuator model: The PAM force model developed in this work combines model terms existing in literature with original contributions. Specifically, a completely new method was devised to account for the elliptical ends of the PAM, leading to a better estimation of geometric shape change and PAM force behavior. The empirically fit stress-strain relationship was extended to account for bladder-braid interaction in both positive and negative strain. When these two modifications were combined, force prediction accuracy was greatly improved.

Original manipulator design: This work is also the first known study to design a PAM-based manipulator with the intention of maximizing uni-directional torque over a large angular range of motion (90+ deg). To achieve this goal, the manipulator was constructed with unique design features such as parallel PAM arrangements, a tendon-link joint design, and pressure manifolds. Furthermore, the joint optimization

procedure used for kinematic design is an original approach adopted ensure that the joint can maintain high torque output from PAM actuators even as their force reduces as they contract.

Demonstration of novel nonlinear controller: Numerous control strategies have been applied in PAM literature; however, in the present work, a hybrid combination of modeling and adaptation is determined for PAM-based manipulator control. The new controller incorporates neural networks to determine unknown functions within expressions of the known system dynamics to create a hybrid neural network control law. This type of controller preserves some knowledge of the system structure without requiring knowledge of nonlinear PAM dynamics, joint kinematics, or payload.

Variable recruitment strategy: This is the first study to quantify the efficiency benefits of a variable recruitment strategy on a quasi-static PAM-actuated robotic manipulator. In addition, this study leveraged original work from the improved PAM actuator model to simulate variable recruitment, and to compare the simulations with corresponding experimental results with good accuracy.

7.3 Future Work

Several initiatives related to PAM-based manipulation would represent a natural extension of the work presented here. The work in this dissertation solves only a small portion of the challenges that need attention in order to propel the soft robotics field into a commercially viable industry. Even as soft actuation technologies mature, increasingly complex research will be necessary to expand human-robot interaction.

First, although the model introduced in Chapter 2 generates accurate PAM force predictions for untested pressure levels given some *a priori* data at other pressure levels, it cannot be used to predict PAM force for an entirely untested PAM. Such a model will require knowledge of the complex physical interaction between the bladder and braid, as well as the behavior of the bladder material itself. This has not been fully investigated in the literature, and is worthy of attention in future work.

In regards to Chapter 3, while the PAMs themselves are incredibly lightweight, little effort was made to minimize the mass of the manipulator itself. Several straightforward improvements could be made to increase the power-to-weight of the complete manipulator structure, or a structural optimization procedure could be designed. In order to lighten the skeletal structure of the arm, a lighter material such as carbon fiber composite or plastic could be used in place of solid metal; or perhaps inflatable segments (even PAMs) could be used as structural linkages, creating a fully-inflatable, highly portable, extremely human-friendly arm.

To improve upon the structural design in this research, a highly anthropomorphic PAM-based arm could be developed. For instance, the shoulder joint could be of ball-and-socket type, providing high dexterity without the singularities that arise from using multiple single-axis joints. Muscles might be placed and configured as they appear in the human body. In this way, a PAM-based robot could likely perform better in human-centric environments, for tasks like opening doors or reaching into tight spaces. Human-like "ballistic" motions such as throwing could also be attempted. A PAM-actuated hand could be added to enable grasping and manipulation.

Future control work with PAM-actuated systems could investigate hysteresis compensation, multi-degree-of-freedom control, high-frequency motion, and coordination with a visual system. Adaptive neural network control in Chapter 5 could be augmented with a more complex network that takes pressure and angular velocity as inputs in addition to angular position to improve learning and modeling ability, especially for high-frequency movements.

Full implementation of the variable recruitment strategy presented in Chapter 6 will require a control strategy that can select recruitment level, either via preplanning or in real-time. A real-time control strategy will require special attention to smooth transitions between recruitment levels and minimizing chatter. Additionally, the system should be designed to avoid or minimize the effects of pressure saturation either through control or increasing source pressure. A variable recruitment control study is a natural extension of this work, and will be examined in the future. Lastly, a PAM design that eliminates bladder buckling and braid loosening due to variable recruitment is likely to improve actuator durability, and will also be considered in future work.

Expanding upon the variable recruitment strategy, it should be possible to employ large numbers (hundreds) of miniature PAMs in muscle bundles. In addition to the complexity of regulating air to a large number of PAMs, the bundle approach was not taken in this work because of the weak performance of miniature PAMs using commercially available bladders. Commerically available bladders had high thickness-to-diameter ratios which restrict motion and degrade force. However, recent advancements in custom-bladder molding have produced thin, soft bladders, yielding

force-to-weight ratios that are comparable to the relatively larger PAMs employed in the present work [196].

Finally, PAMs could be employed in a safety-conscious, variable stiffness control strategy. This approach relies on an antagonistic actuator setup to increase stiffness when low velocity, fine motion is desired, and reduce stiffness to perform high velocity, low accuracy motions in scenarios where a stiff system would be unsafe. By intelligently selecting these characteristics, such a manipulator would be considerably safer to operate in the vicinity of humans or in direct contact with humans.

Bibliography

[1] J. E. Huber, N. A. Fleck, and M. F. Ashby. The selection of mechanical actuators. *Proceedings of the Royal Society of London A*, 453:2185–2205, 1997.

[2] B. K. Woods, M. F. Gentry, C. S. Kothera, and N. M. Wereley. Fatigue life testing of swaged pneumatic artificial muscles as actuators for aerospace applications. *Journal of Intelligent Material Systems and Structures*, 23(3):327–343, March 2012.

[3] J. M. Hollerbach, I. W. Hunter, and J. Ballantyne. Hollerbach_Hunter_Ballantyne_1992.pdf. *The Robotics Review*, 2:299–342, 1992.

[4] J. D. W. Madden, N. A. Vandesteeg, P. A. Anquetil, P. G. A. Madden, A. Takshi, R. Z. Pytel, S. R. Lafontaine, P. A. Wieringa, and I. W. Hunter. Artificial Muscle Technology: Physical Principles and Naval Prospects. *IEEE Journal of Oceanic Engineering*, 29(3):706–728, July 2004.

[5] Hstar Technologies. Robotic Nursing Assistant (RoNA) System.

[6] Vecna. BEAR Robot.

[7] M. Moran. Epochs in Endourology The da Vinci Robot. *Journal of Endourology*, 20(12):986–990, 2006.

[8] International Organization for Standardization. Robots and robotic devices – Safety requirements for industrial robots – Part 1: Robots.

[9] G. Pratt, M. Williamson, P. Dillworth, J. Pratt, K. Ulland, and A. Wright. Stiffness Isnt Everything. *Fourth International Symposium on Experimental Robotics, ISER*, 1995.

[10] M. Dadfarnia, N. Jalili, B. Xian, and D. M. Dawson. Lyapunov-based Piezoelectric Control of Flexible Cartesian Robot Manipulators. In *American Control Conference*, pages 5227–5232, 2003.

[11] V. Bundhoo. *Design and evaluation of a shape memory alloy-based tendon-driven actuation system for biomimetic artificial fingers*. PhD thesis, University of Victoria, 2009.

[12] S. Dilibal, E. Guner, and N. Akturk. Three-finger SMA robot hand and its practical analysis. *Robotica*, 20(2):175–180, April 2002.

[13] F. Carpi, R. Kornbluh, P. Sommer-Larsen, and G. Alici. Electroactive polymer actuators as artificial muscles: are they ready for bioinspired applications? *Bioinspiration & Biomimetics*, 6(4):045006, December 2011.

[14] Q. Pei, M. A. Rosenthal, R. Pelrine, S. Stanford, and R. D. Kornbluh. Multi-functional electroelastomer roll actuators and their application for biomimetic walking robots. In Yoseph Bar-Cohen, editor, *SPIE Smart Structures and Materials*, pages 281–290, July 2003.

[15] G. Pratt. Low impedance walking robots. *Integrative and comparative biology*, 42(1):174–81, February 2002.

[16] A. Bicchi and G. Tonietti. Fast and Soft-Arm Tactics: Dealing with the Safety-Performance Tradeoff in Robot Arms Design and Control. *IEEE Robotics and Automation Magazine*, pages 22–33, 2004.

[17] J. W. Hurst, J. Chestnutt, and A. Rizzi. An actuator with mechanically adjustable series compliance.

[18] J. Versace. A Review of the Severity Index. Technical report, Ford Motor Co., 1971.

[19] D. W. A. Brands. *Predicting brain mechanics during closed head impact - numerical and constitutive aspects*. PhD thesis, Technische Universiteit Eindhoven, 2002.

[20] H. Kazerooni and T. B. Sheridan. Robust Compliant Motion for Manipulators , Part I : The Fundamental Concepts of Compliant Motion. *IEEE Journal of Robotics and Automation*, RA-2(2):83–92, 1986.

[21] S. Haddadin, A. Albu-sch, A. de Luca, and G. Hirzinger. Collision Detection and Reaction : A Contribution to Safe Physical Human-Robot Interaction. *IEEE/RSJ International Conference on Intelligent Robots and Systems*, pages 22–26, 2008.

[22] Rethink Robotics. Baxter: A unique robot with unique features.

[23] H. Schulte. The Application of External Power in Prosthetics and Orthotics. Technical report, National Academy of Sciences, Washington, D.C., 1961.

[24] R. H. Gaylord. Fluid Actuated Motor System and Stroking Device, 1958.

[25] A. H. Morin. Elastic Diaphragm, US Patent No. 2642091, 1953.

[26] B. Solano, J. Laloy, and C. Rotinat-Libersa. Compact and Lightweight Hydraulic Actuation System for High Performance Millimeter Scale Robotic Applications: Modeling and Experiments. *ASME 2010 Conference on Smart Materials, Adaptive Structures and Intelligent Systems*, pages 405–411, 2010.

[27] E. G. Hocking and N. M. Wereley. Analysis of nonlinear elastic behavior in miniature pneumatic artificial muscles. *Smart Materials and Structures*, 22(1):014016, January 2013.

[28] S. Davis and D. G. Caldwell. Biologically inspired damage tolerance in braided pneumatic muscle actuators. *Journal of Intelligent Material Systems and Structures*, 23(3):313–325, September 2011.

[29] Z. Zhang and M. P. Philen. Pressurized artificial muscles. *Journal of Intelligent Material Systems and Structures*, 23(3):255–268, September 2011.

[30] B. Tondu. Modelling of the McKibben artificial muscle: A review. *Journal of Intelligent Material Systems and Structures*, 23(3):225–253, March 2012.

[31] C. P. Chou and B. Hannaford. Measurement and Modeling of McKibben Pneumatic Artificial Muscles. *IEEE Transactions on Robotics and Automation*, 12(1):90–102, 1996.

[32] G. Klute and B. Hannaford. Accounting for Elastic Energy Storage in McKibben Artificial Muscle Actuators. *ASME Journal of Dynamic Systems, Measurement, and Control*, 122(2):386–388, 2000.

[33] N. Tsagarakis and D. G. Caldwell. Improved modelling and assessment of pneumatic muscle actuators. In *Proceedings 2000 ICRA. Millennium Conference. IEEE International Conference on Robotics and Automation. Symposia Proceedings (Cat. No.00CH37065)*, volume 4, pages 3641–3646. IEEE, 2000.

[34] C. Ferraresi, W. Franco, and A. M. Bertetto. Flexible Pneumatic Actuators: A Comparison between The McKibben and the Straight Fibres Muscles. *Journal of Robotics and Mechatronics*, 13(1):56–63, 2001.

[35] C. S. Kothera, M. Jangid, J. Sirohi, and N. M. Wereley. Experimental Characterization and Static Modeling of McKibben Actuators. *Journal of Mechanical Design*, 131(9):091010, 2009.

[36] R. S. Rivlin. Large Elastic Deformations of Isotropic Materials. I. Fundamental Concepts. *Philisophical Transactions of the Royal Society of London*, 240(822):459–490, 1948.

[37] J. E. Adkins and R. S. Rivlin. Large Elastic Deformations of Isotropic Materials. IX. The Deformation of Thin Shells. *Philisophical Transactions of the Royal Society of London*, 244(888):505–531, 1952.

[38] A. D. Kydoneifs. Finite Axisymmetric Deformations of Initially Cylindrical Reinforced Membranes. *Rubber Chemistry and Technology*, 45(6):1677–1683, 1972.

[39] Y. Shan, M. P. Philen, C. E. Bakis, K. Wang, and C. D. Rahn. Nonlinear-elastic finite axisymmetric deformation of flexible matrix composite membranes under internal pressure and axial force. *Composites Science and Technology*, 66(15):3053–3063, December 2006.

[40] B. Tondu, S. Ippolito, J. Guiochet, and A. Daidie. A Seven-degrees-of-freedom Robot-arm Driven by Pneumatic Artificial Muscles for Humanoid Robots. *The International Journal of Robotics Research*, 24(4):257–274, April 2005.

[41] D. G. Caldwell, G. A. Medrano-Cerda, and M. Goodwin. Control of pneumatic muscle actuators. *IEEE Control Systems Magazine*, 15(1):40–48, 1995.

[42] K. Ahn and H. Nguyen. Intelligent switching control of a pneumatic muscle robot arm using learning vector quantization neural network. *Mechatronics*, 17(4-5):255–262, May 2007.

[43] J. Wu, J. Huang, Y. Wang, K. Xing, and Q. Xu. Fuzzy PID control of a wearable rehabilitation robotic hand driven by pneumatic muscles. In *2009 International Symposium on Micro-NanoMechatronics and Human Science*, pages 408–413. IEEE, November 2009.

[44] T.-J. Yeh, M.-J. Wu, T.-J. Lu, F.-K. Wu, and C.-R. Huang. Control of McKibben pneumatic muscles for a power-assist, lower-limb orthosis. *Mechatronics*, 20(6):686–697, September 2010.

[45] X. Zhu, G. Tao, B. Yao, and J. Cao. Adaptive Robust Posture Control of Parallel Manipulator Driven by Pneumatic Muscles With Redundancy. *IEEE/ASME Transactions on Mechatronics*, 13(4):441–450, August 2008.

[46] S. Ganguly, A. Garg, A. Pasricha, and S.K. Dwivedy. Control of pneumatic artificial muscle system through experimental modelling. *Mechatronics*, 22(8):1135–1147, 2012.

[47] H.C. Nho and P. Meckl. Intelligent feedforward control and payload estimation for a two-link robotic manipulator. *IEEE/ASME Transactions on Mechatronics*, 8(2):277–283, June 2003.

[48] M. M. Fateh and A. Izadbakhsh. Robust Control of a High-Speed Manipulator in State Space. *International Journal of Aerospace and Mechanical Engineering*, 1(1):38–43, 2007.

[49] K.D. Young, V.I. Utkin, and U. Ozguner. A control engineer's guide to sliding mode control. *IEEE Transactions on Control Systems Technology*, 7(3):328–342, 1999.

[50] J.-J. Slotine. On the Adaptive Control of Robot Manipulators. *The International Journal of Robotics Research*, 6(3):49–59, 1987.

[51] P. Carbonell, Z. P. Jiang, and D. W. Repperger. Nonlinear control of a pneumatic muscle actuator: backstepping vs. sliding-mode. In *Proceedings of the 2001 IEEE International Conference on Control Applications*, volume 2, pages 167–172. IEEE, 2001.

[52] D. Cai and Y. Dai. A sliding mode controller for manipulator driven by artificial muscle actuator. *Electronics and Communications in Japan (Part III: Fundamental Electronic Science)*, 86(11):57–64, November 2003.

[53] J. H. Lilly. Adaptive tracking for pneumatic muscle actuators in bicep and tricep configurations. *IEEE Transactions on Neural Systems and Rehabilitation Engineering*, 11(3):333–339, September 2003.

[54] A.S. Nouri, C. Gauvert, B. Tondu, and P. Lopez. Generalized variable structure model reference adaptive control of one-link artificial muscle manipulator in two operating modes. In *Proceedings of IEEE International Conference on Systems, Man and Cybernetics*, volume 2, pages 1944–1950. IEEE, 1994.

[55] K. Xing, J. Huang, J. He, Y. Wang, Q. Xu, and J. Wu. Sliding mode tracking for actuators comprising pneumatic muscle and torsion spring. *Transactions of the Institute of Measurement and Control*, 34(2-3):255–277, July 2010.

[56] X. Shen. Nonlinear model-based control of pneumatic artificial muscle servo systems. *Control Engineering Practice*, 18(3):311–317, March 2010.

[57] H. Aschemann and D. Schindele. Sliding-Mode Control of a High-Speed Linear Axis Driven by Pneumatic Muscle Actuators. *IEEE Transactions on Industrial Electronics*, 55(11):3855–3864, November 2008.

[58] K. Braikia, M. Chettouh, B. Tondu, P. Acco, and M. Hamerlain. Improved Control Strategy of 2-Sliding Controls Applied to a Flexible Robot Arm. *Advanced Robotics*, 25(11-12):1515–1538, January 2011.

[59] S. F. Brown. Ruber muscles take robotics one step further. *Rubber Developments*, 37(4), 1984.

[60] B. Tondu, V. Boitier, and P. Lopez. Naturally compliant robot-arms actuated by McKibben artificial muscles. *IEEE International Conference on Systems, Man, and Cybernetics*, 3:2635 – 2640, 1994.

[61] M. Eichhorn, C. Ament, and T. Nguyen. Modelling of the 4-Axis Kinematic Manipulator AirArm Driven by Pneumatic Muscle Actuators. In *IEEE International Conference on Control and Automation*, pages 1301–1307, 2009.

[62] G. Tuijthof and J. Herder. Design, actuation and control of an anthropomorphic robot arm. *Mechanism and Machine Theory*, 35(7):945–962, July 2000.

[63] D. G. Caldwell, G. A. Medrano-Cerda, and M. Goodwin. Characteristics and adaptive control of pneumatic muscle actuators for a robotic elbow. In *Proceedings of the 1994 IEEE International Conference on Robotics and Automation*, pages 3558–3563. IEEE Comput. Soc. Press, 1994.

[64] K. Yaegashi, N. Saga, and T. Satoh. Control of Robot Arm Using Pneumatic Artificial Muscle with Spherical Joint. *IEEE International Conference on Mechatronics and Automation*, July:1093–1098, 2005.

[65] I. Walker, D. Dawson, T. Flash, F. Grasso, R. Hanlon, W. Kier, C. Pagano, C. Rahn, and Q. Zhang. Continuum Robot Arms Inspired by Cephalopods. *Unmanned Ground Vehicle Technology*, 5804:303–314, 2005.

[66] D. Trivedi, A. Lotfi, and C. D. Rahn. Geometrically exact dynamic models for soft robotic manipulators. *2007 IEEE/RSJ International Conference on Intelligent Robots and Systems*, pages 1497–1502, October 2007.

[67] Shadow Robot Company. Air muscle, left hand, and arm integration.

[68] J.-Y. Nagase, N. Saga, T. Satoh, and K. Suzumori. Development and control of a multifingered robotic hand using a pneumatic tendon-driven actuator. *Journal of Intelligent Material Systems and Structures*, 23(3):345–352, September 2011.

[69] R. Q. van der Linde. Design, analysis, and control of a low power joint for walking robots, by phasic activation of McKibben muscles. *IEEE Transactions on Robotics and Automation*, 15(4):599–604, 1999.

[70] R. W. Colbrunn, G. M. Nelson, and R. D. Quinn. Modeling of braided pneumatic actuators for robotic control. *Proceedings 2001 IEEE/RSJ International Conference on Intelligent Robots and Systems. Expanding the Societal Role of Robotics in the the Next Millennium (Cat. No.01CH37180)*, 4:1964–1970, 2001.

[71] B. Verrelst, R. van Ham, B. Vanderborght, F. Daerden, D. Lefeber, and J. Vermeulen. The Pneumatic Biped Lucy Actuated with Pleated Pneumatic Artificial Muscles. *Autonomous Robots*, 18:201–213, 2005.

[72] D. Shin, I. Sardellitti, and O. Khatib. A hybrid actuation approach for human-friendly robot design. In *2008 IEEE International Conference on Robotics and Automation*, pages 1747–1752. IEEE, May 2008.

[73] R. M. Robinson, C. S. Kothera, B. K. S. Woods, R. D. Vocke, and N. M. Wereley. High Specific Power Actuators for Robotic Manipulators. *Journal of Intelligent Material Systems and Structures*, 22(13):1501–1511, September 2011.

[74] Y.-L. Park, B.-R. Chen, N. Perez-Arancibia, D. Young, L. Stirling, R. J. Wood, E. C. Goldfield, and R. Nagpal. Design and control of a bio-inspired soft wearable robotic device for ankle-foot rehabilitation. *Bioinspiration & biomimetics*, 9(1):016007, January 2014.

[75] X. Li, H. Xia, and T. Guan. Development of Legs Rehabilitation Exercise System Driven by Pneumatic Muscle Actuator. In *International Conference on Bioinformatics and Biomedical Engineering*, pages 1309–1311. IEEE, May 2008.

[76] V. L. Nickel, D. L. Savill, J. Karchak, and J. R. Allen. Synthetically Powered Orthotic Systems. *The Journal of Bone and Joint Surgery*, 47(3), 1965.

[77] U.S. Scientists Triggered First A-Bomb 15 Years Ago.

[78] J. M. Winters. Braided artificial muscles: Mechanical properties and future uses in prosthetics/orthotics. *Proceedings of the 13th Annual RESNA Conference*, pages 173–174, 1990.

[79] S. D. Prior, P. R. Warner, A. S. White, J. T. Parsons, and R. Gill. Actuators for Rehabilitation Robots. *Mechatronics*, 3(3):285–294, 1993.

[80] D. G. Caldwell and N. Tsagarakis. Biomimetic actuators in prosthetic and rehabilitation applications. *Technology and Health Care*, 10(2):107–20, January 2002.

[81] N. G. Tsagarakis and D. G. Caldwell. Development and Control of a Soft-Actuated Exoskeleton for Use in Physiotherapy and Training. *Autonomous Robots*, 15:21–33, 2003.

[82] T. Noritsugu, M. Takaiwa, and D. Sasaki. Power Assist Wear Driven with Pneumatic Rubber Artificial Muscles. *2008 15th International Conference on Mechatronics and Machine Vision in Practice*, pages 539–544, December 2008.

[83] J. Ueda, D. Ming, V. Krishnamoorthy, M. Shinohara, and T. Ogasawara. Individual muscle control using an exoskeleton robot for muscle function testing. *IEEE Transactions on Neural Systems and Rehabilitation Engineering*, 18(4):339–50, August 2010.

[84] M. Jordan, D. Pietrusky, M. Mihajlov, and O. Ivlev. Precise position and trajectory control of pneumatic soft-actuators for assistance robots and motion therapy devices. *2009 IEEE International Conference on Rehabilitation Robotics*, pages 663–668, June 2009.

[85] P. Jamwal, S. Xie, and K. Aw. Design Analysis of a Pneumatic Muscle Driven Wearable Parallel Robot for Ankle Joint Rehabilitation. In *IEEE/ASME Int. Conf. Mechatronics and Embedded Systems and Applications*, pages 403–408, 2010.

[86] M. Chandrapal. *Intelligent Assistive Knee Orthotic Device Utilizing Pneumatic Artificial Muscles*. PhD thesis, University of Canterbury, Christchurch, New Zealand, 2012.

[87] B. K. S. Woods, C. S. Kothera, and N. M. Wereley. Wind Tunnel Testing of a Helicopter Rotor Trailing Edge Flap Actuated via Pneumatic Artificial Muscles. *Journal of Intelligent Material Systems and Structures*, 22(13):1513–1528, October 2011.

[88] B. K.S. Woods, C. S. Kothera, and N. M. Wereley. Whirl Testing of a Pneumatic Artificial Muscle Actuation System for a Full-Scale Active Rotor. *Journal of the American Helicopter Society*, 59(2):1–11, 2014.

[89] L. D. Peel, J. Mejia, B. Narvaez, K. Thompson, and M. Lingala. Development of a Simple Morphing Wing Using Elastomeric Composites as Skins and Actuators. *Journal of Mechanical Design*, 131(9), 2009.

[90] E. Bubert. *Highly-Extensible Skin for a Variable Wing-Span Morphing Aircraft Utilizing Pneumatic Artificial Muscle Actuation*. PhD thesis, University of Maryland, 2009.

[91] R. D. Vocke, C. S. Kothera, A. Chaudhuri, B. K. S. Woods, and N. M. Wereley. Design and testing of a high-specific work actuator using miniature pneumatic artificial muscles. *Journal of Intelligent Material Systems and Structures*, 23(3):365–378, January 2012.

[92] P. Beyl. *Design and control of a knee exoskeleton powered by pleated pneumatic artificial muscles for robot-assisted gait rehabilitation*. PhD thesis, 2010.

[93] K. Ahn and H. Anh. Design and implementation of an adaptive recurrent neural networks (ARNN) controller of the pneumatic artificial muscle (PAM) manipulator. *Mechatronics*, 19(6):816–828, September 2009.

[94] A. D. Deshpande, Z. Xu, M. J. V. Weghe, B. H. Brown, J. Ko, L. Y. Chang, D. D. Wilkinson, S. M. Bidic, and Y. Matsuoka. Mechanisms of the Anatomically Correct Testbed Hand. *IEEE/ASME Transactions on Mechatronics*, 18(1):238–250, February 2013.

[95] D. Trivedi and C. D. Rahn. *Soft Robotic Manipulators: Design, Analysis, and Control*, pages 141–167. DEStech Publications, 2012.

[96] I. Sardellitti, J. Park, D. Shin, and O. Khatib. Air muscle controller design in the distributed macro-mini (DM2) actuation approach. In *IEEE/RSJ International Conference on Intelligent Robots and Systems*, pages 1822–1827. IEEE, October 2007.

[97] R. M. Robinson and N. M. Wereley. Control of a Heavy-Lift Robotic Manipulator. In *AIAA Structures, Structural Dynamics, and Materials Conference*, pages 1–14, Honolulu, Hawaii, 2012.

[98] W. Liu and C. R. Rahn. Fiber-Reinforced Membrane Models of McKibben Actuators. *Journal of Applied Mechanics*, 70(6):853, 2003.

[99] C. O. Horgan and G. Saccomandi. Phenomenological Hyperelastic Strain-Stiffening Constitutive Models for Rubber. *Rubber Chemistry and Technology*, 79(1):152–169, 2006.

[100] T. Hesselroth, K. Sarkar, P.P. van der Smagt, and K. Schulten. Neural network control of a pneumatic robot arm. *IEEE Transactions on Systems, Man, and Cybernetics*, 24(1):28–38, 1994.

[101] S. D. Prior and A. S. White. Measurements and simulation of a pneumatic muscle actuator for a rehabilitation robot. *Simulation Practice and Theory*, 3(2):81–117, September 1995.

[102] D. G. Caldwell, O. Kocak, and U. Anderson. Multi-armed dexterous manipulator operation using glove/exoskeleton control and sensory feedback. In *IEEE/RSJ International Conference on Intelligent Robots and Systems*, pages 567–572, 1995.

[103] C. Ferraresi, W. Franco, and A. Bertetto. Straight Fibres Pneumatic Muscle: An Actuator with High Traction Force. In *Sixth Scandinational Conference on Fluid Power*, Tampare, Finland, 1999.

[104] D. A. Kingsley and R. D. Quinn. Fatigue life and frequency response of braided pneumatic actuators. *Proceedings 2002 IEEE International Conference on Robotics and Automation*, 3:2830–2835, 2002.

[105] Y. K. Lee and I. Shimoyama. A multi-channel micro valve for micro pneumatic artificial muscle. In *IEEE International Conference on Micro Electro Mechanical Systems (Cat. No.02CH37266)*, pages 702–705. IEEE, 2002.

[106] H. Kobayashi, Y. Ishida, and H. Suzuki. Realization of all motion for the upper limb by a muscle suit. *RO-MAN 2004. 13th IEEE International Workshop on Robot and Human Interactive Communication (IEEE Catalog No.04TH8759)*, pages 631–636, 2004.

[107] M. van Damme, B. Vanderborght, R. van Ham, B. Verrelst, F. Daerden, and D. Lefeber. Proxy-Based Sliding Mode Control of a Manipulator Actuated by Pleated Pneumatic Artificial Muscles. In *IEEE International Conference on Robotics and Automation*, pages 10–14, 2007.

[108] E. Benson. *Investigation of a Cable-Driven Parallel Mechanism for Pressure Suit Arm Resizing and Motion Assistance*. PhD thesis, University of Maryland, 2007.

[109] N. Saga and T. Saikawa. Development of a Pneumatic Artificial Muscle Based on Biomechanical Characteristics. *Advanced Robotics*, 22(6-7):761–770, January 2008.

[110] H. Aschemann and D. Schindele. Nonlinear Model-Based Control of a Parallel Robot Driven by Pneumatic Muscle Actuators. In *New Approaches in Automation and Robotics*, pages 26–40. I-Tech Education and Publishing, Vienna, Austria, 2008.

[111] M. van Damme, B. Vanderborght, R. van Ham, F. Verrelst, B.and Daerden, and D. Lefeber. Sliding Mode Control of a 2DOF Planar Pneumatic Manipulator. *Journal of Dynamic Systems, Measurement, and Control*, 131(2):021013, 2009.

[112] F. Stulp, I. Kresse, A. Maldonado, F. Ruiz, A. Fedrizzi, and M. Beetz. Compact models of human reaching motions for robotic control in everyday manipulation tasks. *2009 IEEE 8th International Conference on Development and Learning*, pages 1–7, 2009.

[113] C. S. Kothera, B. K. S. Woods, and N. M. Wereley. Dynamic modeling of Mckibben pneumatic artificial muscles for antagonistic actuation. *2009 IEEE International Conference on Robotics and Automation*, pages 182–187, May 2009.

[114] B. Tondu, K. Braikia, M. Chettoulr, and S. Ippolito. Second Order Sliding Mode Control for an Anthropomorphic Robot-Arm driven with Pneumatic Artificial Muscles. *IEEE-RAS International Conference*, pages 47–54, 2009.

[115] O. Khatib and M. Cutkosky. Design methodologies of a hybrid actuation approach for a human-friendly robot. *2009 IEEE International Conference on Robotics and Automation*, pages 4369–4374, May 2009.

[116] D. Schindele and H. Aschemann. Trajectory tracking of a pneumatically driven parallel robot using higher-order SMC. In *2010 15th International Conference on Methods and Models in Automation and Robotics*, pages 387–392. IEEE, August 2010.

[117] M. de Volder and D. Reynaerts. Pneumatic and hydraulic microactuators: a review. *Journal of Micromechanics and Microengineering*, 20(4):043001, April 2010.

[118] T. Vo-Minh, T. Tjahjowidodo, H. Ramon, and H. van Brussel. A New Approach to Modeling Hysteresis in a Pneumatic Artificial Muscle Using The Maxwell-Slip Model. *IEEE/ASME Transactions on Mechatronics*, 16(1):177–186, February 2011.

[119] J. Romano and K. Hsiao. Human-Inspired Robotic Grasp Control With Tactile Sensing. *IEEE Transactions on Robotics*, 27(6):1067–1079, 2011.

[120] J. Jalani, N. Mahyuddin, G. Herrmann, and C. Melhuish. Active robot hand compliance using operational space and Integral Sliding Mode Control. *2013 IEEE/ASME International Conference on Advanced Intelligent Mechatronics*, pages 1749–1754, July 2013.

[121] F. Daerden and D. Lefeber. Pneumatic Artificial Muscles : actuators for robotics and automation. *Smart Materials and Structures*, 47(1):11–21, 2002.

[122] B. Hannaford. Measurement and modeling of McKibben pneumatic artificial muscles. *IEEE Transactions on Robotics and Automation*, 12(1):90–102, 1996.

[123] J. Lilly and L. Yang. Sliding Mode Tracking for Pneumatic Muscle Actuators in Opposing Pair Configuration. *IEEE Transactions on Control Systems Technology*, 13(4):550–558, 2005.

[124] T. Nguyen, C. Ament, and M. Eichhorn. A Nonlinear Control Design of the 4-Axis Kinematic Manipulator AirArm Driven by Pneumatic Muscle Actuators. *IEEE International Conference on Control and Automation*, pages 2341–2347, 2009.

[125] B. Wang, W. Zhou, Y. Jin, H. Xu, and H. Ke. Modeling and Characteristics Analysis of Intelligent Pneumatic Muscle with Shape Memory Alloy Braided Shell. *2009 International Asia Conference on Informatics in Control, Automation and Robotics*, pages 3–7, February 2009.

[126] H. Jahanabadi, M. Mailah, M. Z. Zain, and H. M. Hooi. Active Force with Fuzzy Logic Control of a Two-Link Arm Driven by Pneumatic Artificial Muscles. *Journal of Bionic Engineering*, 8(4):474–484, December 2011.

[127] C. Semini, N. Tsagarakis, E. Guglielmino, F. Cannella, and D. Caldwell. Design of HyQ-a Hydraulically and Electrically Actuated Quadruped Robot. *Journal of Systems and Control Engineering*, pages 1–20, 2011.

[128] B. Vanderborght. Exploiting Natural Dynamics to Reduce Energy Consumption by Controlling the Compliance of Soft Actuators. *The International Journal of Robotics Research*, 25(4):343–358, April 2006.

[129] H. Seraji. A new class of nonlinear PID controllers with robotic applications. *Journal of Robotic Systems*, 15(3):161–181, March 1998.

[130] F. Daerden and D. Lefeber. The concept and design of pleated pneumatic artificial muscles. *International Journal of Fluidic Power*, 2(3):41–50, 1999.

[131] N. Tsagarakis and D. G. Caldwell. A 7 dof pneumatic Muscle Actuator (pMA) powered Exoskeleton n. *IEEE Workshop on Robot and Human Interaction*, 1999.

[132] R. W. Colbrunn. *Design and Control of a Robotic Leg with Braided Pneumatic Actuators*. PhD thesis, Case Western Reserve University, 2000.

[133] K. Balasubramanian and K. S. Rattan. Fuzzy logic control of a pneumatic muscle system using a linearing control scheme. *IEEE Fuzzy Information Processing*, pages 432–436, 2003.

[134] S. Davis, N. Tsagarakis, J. Canderle, and D. G. Caldwell. Enhanced Modelling and Performance in Braided Pneumatic Muscle Actuators. *The International Journal of Robotics Research*, 22(3-4):213–227, March 2003.

[135] D. Sasaki, T. Noritsugu, M. Takaiwa, and H. Yamamoto. Wearable power assist device for hand grasping using pneumatic artificial rubber muscle. *RO-MAN 2004. 13th IEEE International Workshop on Robot and Human Interactive Communication (IEEE Catalog No.04TH8759)*, pages 655–660, 2004.

[136] A. Hildebrandt, O. Sawodny, R. Neumann, and A. Hartmann. Cascaded control concept of a robot with two degrees of freedom driven by four artificial pneumatic muscle actuators. In *American Control Conference*, pages 680–685, 2005.

[137] J. Vermeulen. Trajectory Planning for the Walking Biped "Lucy". *The International Journal of Robotics Research*, 25(9):867–887, September 2006.

[138] S. Davis and D. G. Caldwell. pneumatic Muscle Actuators for Humanoid applications - Sensor and Valve Integration. *IEEE/RAS International Conference on Humanoid Robots*, pages 456–461, 2006.

[139] T. Thanh and K. Ahn. Nonlinear PID control to improve the control performance of 2 axes pneumatic artificial muscle manipulator using neural network. *Mechatronics*, 16(9):577–587, November 2006.

[140] Y. Karayiannidis, G. Rovithakis, and Z. Doulgeri. Force/position tracking for a robotic manipulator in compliant contact with a surface using neuro-adaptive control. *Automatica*, 43(7):1281–1288, July 2007.

[141] M. Mihajlov, O. Ivlev, and A. Gräser. Modelling and Identification for Control Design of Compliant Fluidic Actuators with Rotary Elastic Chambers : Hydraulic Case Study. In *The International Federation of Automatic Control*, pages 10492–10497, 2008.

[142] J. Nakanishi, R. Cory, M. Mistry, J. Peters, and S. Schaal. Operational Space Control: A Theoretical and Empirical Comparison. *The International Journal of Robotics Research*, 27(6):737–757, June 2008.

[143] M. Raibert, K. Blankespoor, G. Nelson, and R. Playter. BigDog, the Rough-Terrain Quadruped Robot. In *The International Federation of Automatic Control*, pages 6–9, 2008.

[144] S. Q. Xie and P .K. Jamwal. An iterative fuzzy controller for pneumatic muscle driven rehabilitation robot. *Expert Systems with Applications*, 38(7):8128–8137, July 2011.

[145] H. Anh and K. Ahn. Hybrid control of a pneumatic artificial muscle (PAM) robot arm using an inverse NARX fuzzy model. *Engineering Applications of Artificial Intelligence*, 24(4):697–716, June 2011.

[146] J. Fishel and G. Loeb. Bayesian exploration for intelligent identification of textures. *Frontiers in neurorobotics*, 6(June):4, January 2012.

[147] G. Andrikopoulos, G. Nikolakopoulos, and S. Manesis. Pneumatic artificial muscles: A switching Model Predictive Control approach. *Control Engineering Practice*, 21(12):1653–1664, December 2013.

[148] H. Li, K. Kawashima, K. Tadano, S. Ganguly, and S. Nakano. Achieving Haptic Perception in Forceps Manipulator Using Pneumatic Artificial Muscle. *IEEE/ASME Transactions on Mechatronics*, 18(1):74–85, February 2013.

[149] N. S. Pollard and R. C. Gilbert. Tendon arrangement and muscle force requirements for human-like force capabilities in a robotic finger. In *Proceedings 2002 IEEE International Conference on Robotics and Automation*, volume 4, pages 3755–3762. IEEE, 2002.

[150] Z. Wu, X.-Q. Bao, V. K. Varadan, and V. V. Varadan. Light-weight robot using piezoelectric motor, sensor and actuator. *Smart Materials and Structures*, 1(4):330–340, December 1992.

[151] J.-J. E. Slotine and W. Li. *Control of Multi-Input Physical Systems*, pages 392–436. Prentice Hall, 1991.

[152] M. Knestel, E. P. Hofer, S. K. Barillas, and R. Rupp. The Artificial Muscle as an Innovative Actuator in Rehabilitation Robotics. In *17th IFAC World Congress*, pages 773–778, Seoul, Korea, 2008.

[153] O. H. Yeoh. Some Forms of the Strain Energy Function for Rubber. *Rubber Chemistry and Technology*, 66(5):754–771, 1993.

[154] M. P. King and E. B. Rapacki. Human Extraction Rescue Robot: Material Handling Methodology Proof-of-Concept Prototype (Athena). Technical report, Northeastern University, Boston, MA, 2007.

[155] G. K. Klute, J. M. Czerniecki, and B. Hannaford. Artificial Muscles: Actuators for Biorobotic Systems. *The International Journal of Robotics Research*, 21(4):295–309, April 2002.

[156] K. C. Wickramatunge and T. Leephakpreeda. Study on mechanical behaviors of pneumatic artificial muscle. *International Journal of Engineering Science*, 48(2):188–198, February 2010.

[157] B. Tondu and P. Lopez. The McKibben muscle and its use in actuating robot-arms showing similarities with human arm behaviour. *Industrial Robot: An International Journal*, 24(6):432–439, 1997.

[158] E. Richer and Y. Hurmuzulu. A High Performance Pneumatic Force Actuator System Part 1 - Nonlinear Mathematical Model. *ASME Journal of Dynamic Systems, Measurement, and Control*, 122(3):416–425, 2001.

[159] C. C. Gordon, T. Churchill, C. E. Clauser, J. T. Mcconville, I. Tebbetts, and R. A. Walker. 1988 Anthropomorphic Survey of U.S. Army Personnel: Methods and Summary Statistics. Technical report, US Army Natick Research, Development, and Engineering Center, Natick, MA, 1988.

[160] B. Hannaford, J. M. Winters, C. P. Chou, and P. H. Marbot. The anthroform biorobotic arm: a system for the study of spinal circuits. *Annals of biomedical engineering*, 23(4):399–408, 1995.

[161] Anonymous. Foster-miller unveils talon robot that detects chemicals, gases, radiation, and heat. *Industrial Robot*, 32:99–100, 2010.

[162] S. Lightner and R. Lincoln. The Fluidic Muscle: A "New" Development. *The International Journal of Modern Engineering*, 2, 2005.

[163] P. Beater. *Pneumatic Drives: System Design, Modeling, and Control*. Springer, 2007.

[164] K. Passino. *Fuzzy Control*. Addison Wesley Longman, 1998.

[165] L. Sciavicco and B. Sciliano. *Modeling and Control of Robot Manipulators*. Springer, 2000.

[166] D. Shin, I. Sardellitti, and O. Khatib. A hybrid actuation approach for human-friendly robot design. In *IEEE International Conference on Robotics and Automation*, pages 1747–1752. IEEE, May 2008.

[167] W.-F. Xie. Sliding-Mode-Observer-Based Adaptive Control for Servo Actuator With Friction. *IEEE Transactions on Industrial Electronics*, 54(3):1517–1527, June 2007.

[168] Y. Zhu and P. R. Pagilla. Adaptive Controller and Observer Design for a Class of Nonlinear Systems. *Journal of Dynamic Systems, Measurement, and Control*, 128(3):712, 2006.

[169] T. Vo Minh, T. Tjahjowidodo, H. Ramon, and H. Van Brussel. Cascade position control of a single pneumatic artificial muscle-mass system with hysteresis compensation. *Mechatronics*, 20(3):402–414, April 2010.

[170] A. Rezoug, B. Tondu, M. Hamerlain, and M. Tadjine. Adaptive Fuzzy Nonsingular Terminal Sliding Mode Controller for Robot Manipulator Actuated by Pneumatic Artificial Muscles. In *IEEE International Conference on Robotics and Biomimetics*, volume 18, pages 334–339, 2013.

[171] D. Repperger, C. Phillips, and M. Krier. Controller Design Involving Gain Scheduling for A Large Scale Pneumatic Muscle Actuator. In *IEEE International Conference on Control Applications*, pages 285–290, 1999.

[172] R. Sanner and J.-J. Slotine. Gaussian networks for direct adaptive control. *IEEE transactions on neural networks / a publication of the IEEE Neural Networks Council*, 3(6):837–863, 1992.

[173] R. Sanner and M. Kosha. A mathematical model of the adaptive control of human arm motions. *Biological Cybernetics*, 80(5):369–382, 1999.

[174] K-C. Liu. *Adaptive friction compensation in robot manipulators using multiresolution neural networks*. PhD thesis, 1998.

[175] C. J. De Luca. Control Properties of Motor Units. *The Journal of Experimental Biology*, 115:125–136, March 1985.

[176] A. Nardone, C. Romano, and M. Schieppati. Selective Recruitment of High-Threshold Human Motor Units During Voluntary Isotonic Lengthening of Active Muscles. *Journal of Physiology*, 409:451–471, 1989.

[177] H. S. Milner-Brown, R. B. Stein, and R. Yemm. The Orderly Recruitment of Human Motor Units During Volunatary Isometric Contractions. *Journal of Physiology*, 230:359–370, 1973.

[178] I. Boblan, R. Bannasch, H. Schwenk, F. Prietzel, L. Miertsch, and A. Schulz. A Human-like Robot Hand and Arm with Fluidic Muscles: Biologically Inspired Construction and Functionality. In *Embodied Artificial Intelligence*, pages 160–179. Springer, 2003.

[179] M. Bryant, M.A. Meller, and E. Garcia. Toward Variable Recruitment Fluidic Artificial Muscles. In *ASME Conference on Smart Materials, Adaptive Structures and Intelligent Systems*, pages 1–8, 2013.

[180] E. Henneman, G. Somjen, and D. O. Carpenter. Functional Significance of Cell Size in Spinal Motoneurons. *Journal of Neurophysiology*, 28(3):560–580, 1965.

[181] F. Rothling, R. Haschke, J. J. Steil, and H. Ritter. Platform Portable Anthropomorphic Grasping with the Bielefeld 20-DOF Shadow and 9-DOF TUM Hand. In *2007 IEEE/RSJ International Conference on Intelligent Robots and Systems*, pages 2951–2956. IEEE, October 2007.

[182] A. St Clair Gibson and T. D. Noakes. Evidence for Complex System Integration and Dynamic Neural Regulation of Skeletal Muscle Recruitment During Exercise in Humans. *British Journal of Sports Medicine*, 38(6):797–806, December 2004.

[183] N. K. Vø llestad. Measurement of human muscle fatigue. *Journal of Neuroscience Methods*, 74(2):219–27, June 1997.

[184] D. G. Miller. Joule-Thomson Inversion Curve, Corresponding States, and Simpler Equations of State. *Industrial & Engineering Chemistry Fundamentals*, 9(4):585–589, November 1970.

[185] Freeman Manufacturing and Supply Company. Bluestar silicone rubber specifications.

[186] dSPACE. DS1104 Controller Board.

[187] D. Ben-Dov and S. E. Salcudean. A Force-Controlled Pneumatic Actuator. *IEEE Transactions on Robotics and Automation*, 11(6):906–911, 1995.

[188] R. M. Robinson, C. S. Kothera, and N. M. Wereley. Nonlinear analysis of quasi-static response of pneumatic artificial muscles for agonistic and antagonistic actuation modes. In *Proc. SPIE*, volume 8686, pages 868604–868604–15, 2013.

[189] Z. Erim, C. J. de Luca, K. Mineo, and T. Aoki. Rank-ordered regulation of motor units. *Muscle & nerve*, 19(5):563–73, May 1996.

[190] D. Huston, B. Esser, G. Spencer, D. Burns, and E. Kahn. Hierarchical Actuator Systems. In *SPIE Smart Structures and Materials*, pages 311–319, 2005.

[191] D. A. Winter. *Biomechanics and Motor Control of Human Movement*. John Wiley and Sons, Inc., Hoboken, New Jersey, 4 edition, 2009.

[192] F. Lorussi, A. Tognetti, F. Carpi, A. Mazzoldi, and D. De Rossi. Recruited dielectric elastomer motor units as a pseudomuscular actuator. In *SPIE Smart Structures and Materials*, pages 464–467, 2003.

[193] D. W. Repperger, C. A. Phillips, A. Neidhard-Doll, D. B. Reynolds, and J. Berlin. Actuator design using biomimicry methods and a pneumatic muscle system. *Control Engineering Practice*, 14(9):999–1009, September 2006.

[194] L. Odhner and H. Asada. Scaling up shape memory alloy actuators using a recruitment control architecture. *Robotics and Automation (ICRA)*, 2010.

[195] E. Azizi and T. J. Roberts. Variable gearing in a biologically inspired pneumatic actuator array. *Bioinspiration & Biomimetics*, 8(2):026002, June 2013.

[196] G. Wang, N. M. Wereley, and T. Pillsbury. Non-linear quasi-static model of pneumatic artificial muscle actuators. *The International Journal of Robotics Research*, 25(8), 2014.